UNIVERSITY OF SOUTHAMPTON

FACULTY OF SCIENCE

PHYSICS

A LOW ENERGY GAMMA RAY IMAGING TELESCOPE IN THE ENERGY RANGE 0.2-10MeV

by

Faraydoon Ahmad Younis

A thesis submitted for the degree of
Master of Philosophy

November 1989

Chapter 1

1 The present status of low energy gamma ray astronomy.

1.1 Introduction.

1.2 The mechanisms of gamma ray production.

1.2.1 Blackbody radiation.
1.2.2 Synchrotron emisson.
1.2.3 Inverse Compton scattering.
1.2.4 Bremsstrahlung radiation.
1.2.5 Electron-positron annihilation.
1.2.6 Decay of Π° mesons.
1.2.7 Nuclear gamma ray emission.

1.3 Galactic gamma ray astronomy.

1.3.1 Diffuse galactic emission.
1.3.1.1 Diffuse galactic continuum.
1.3.1.2 Diffuse galactic lines.
1.3.2 Galactic centre region and the 511 keV line.
1.3.3 Localized galactic sources.
1.3.3.1 Cos-B sources.
1.3.3.2 " GEMINGA " the source that is not there.
1.3.3.3 Radio pulsars.
1.3.4 Transient sources.
1.3.4.1 Gamma ray bursts.
1.3.4.2 Supernovae and Supernovae remnant.

1.4 Extragalactic gamma ray astronomy.

1.4.1 Active galactic nuclei.
1.4.2 Cosmic diffuse radiation.

Chapter 2

2 A review of the instrumentation techniques used in low energy gamma ray astronomy.

2.1 Introduction.

2.2 The contribution to the background level of low energy gamma ray telescopes.

2.2.1 Cosmic diffuse gamma rays.
2.2.2 Vertical atmospheric radiation.
2.2.3 Neutron induced background.
2.2.4 Spallation induced background.
2.2.5 Locally produced gamma rays.

2.3 Methods of detecting gamma ray photons.

2.3.1 Scintillation counters.
2.3.2 Solid-state detectors.

2.4 Development of low energy gamma ray telescopes.

2.4.1 Unshielded detectors.
2.4.2 Passively shielded detectors.
2.4.3 Actively shielded detectors.

2.5 Current techniques employed in low energy gamma ray telescopes.

2.5.1 Compton telescopes.
2.5.1.1 MISO telescope.
2.5.1.2 MPI telescope.
2.5.2 Coded aperture mask telescopes.
2.5.2.1 ZEBRA telescope.
2.5.2.2 GRIP telescope.

Chapter 3

Chapter 4

Chapter 5

Chapter 6

Chapter 7

7 A satellite development of the ZEBRA telescope : GRASP.

UNIVERSITY OF SOUTHAMPTON

ABSTRACT

FACULTY OF SCIENCE
PHYSICS

Master of Philosophy

A LOW ENERGY GAMMA RAY IMAGING TELESCOPE IN THE ENERGY RANGE 0.2-10MeV

by

Faraydoon Ahmad Younis

A telescope has been developed that is operating in the low energy range of the gamma ray spectrum. It is capable of generating gamma ray images of the sky with a precision of arc minutes in the energy range 0.2-10MeV. The telescope is based on a position sensitive detector and a coded aperture mask. It has a fully coded field of view of 7.0°*7.7° and a partially coded field of view of 12.8°*14.3°.

The detection plane comprises of an array of position sensitive detectors that is shielded from undesired events. These units are capable to locate the position of interaction of gamma ray photons of energy 662 keV to a precision of 2.1cm(F.W.H.M). The energy resolution at this particular energy is 11%.

The coded aperture imaging technique employed allows the simultaneous observation of more than one source in the field of view.

The thesis is based on the performance of the position sensitive detectors as well as the overall imaging quality of the telescope.

PREFACE

ZEBRA telescope is a low energy gamma ray telescope developed under the supervision of an international collaboration that comprise the following groups:

Istituto di Fisica Cosmica, Milano, Italy.

Istituto Astrofisica Spaziale, Frascati, Italy.

Laboratorio TESRE, Bologna, Italy.

Department of Physics, Southampton University, England.

The author was involved in the development of the position sensitive detectors, the calibration and the determination of the performance of the position and anticoincidence detectors. The thesis is also aiming to highlights the overall performance of the telescope.

Chapter 1

1 The present status of low energy gamma ray astronomy.

1.1 Introduction.

Gamma ray astronomy is the last window of the electromagnetic spectrum to be opened. All other branches from radio to x-ray have been widely open and enormous astronomical knowledge has been provided through them, and has been developed. The emission of the electromagnetic radiation from this region is in the energy range of $(10^5\text{-}10^{12})$eV which mainly arises from the interaction of extremely energetic particles with matter,magnetic fields or photons. There are many astrophysical objects such as Supernovae explosions and their remnants, Black holes, Radio galaxies, Seyfert galaxies, Neutron stars and Quasars that are candidate for emitting gamma rays.

The development of gamma ray astronomy has been quite slow comparing with other fields of astronomy for two fundamental reasons. Firstly, the low flux of the high energetic gamma ray photons and secondly, the enormous penetration power of these photons which are difficult to detect by their interaction with traditional detecting medium.

The low energy region of this window of astronomy, (0.2-10.0) MeV, is of particular astrophysical significance because of the appearance of gamma ray lines. The recognition of these lines, their intensities and widths can provide a unique identification of nuclear species at the source and reveal the detailed dynamics of the involved emission processes.

Gamma ray photons suffer negligible absorption or scattering while they travel in space and can reach the solar system from the galactic centre and the dense region around the centre of active galaxies.

In this chapter, the first part is designated to a description of the mechanisms involved in the production of gamma ray photons. Meanwhile the second part present the current status of gamma ray astronomy regarding galactic and extragalactic gamma ray sources.

1.2 The mechanisms of gamma ray production.

There are many physical mechanisms which contribute to the production of gamma ray radiation. A number of authors have discussed this matter in detail such as Stecker 1971, Chupp 1976 and Hillier 1984. An astrophysical shock, like a supernovae explosion, can provide a hot gas or a relativistic electrons or may be both. These could be a major source of gamma or x-ray emission. Fig.1.1 illustrates, schematically, the emission mechanisms that may occur when a hot gas or relativistic electrons are produced. A description of these mechanisms is given in the following sections.

1.2.1 Blackbody radiation.

Any astrophysical object sufficiently hot, behaving as a blackbody can give gamma ray photons and the required temperature for the mechanism is $10^8 k < T < 10^{10} k$. The number of photons emitted from a unit area of a blackbody per second at $T(k)$ temperature according to "Plank's formula" is:

$$N(Eg) = 9.9*10^{40} . E_\gamma^2 \left(exp(1.2*10^{10} . \frac{E\gamma}{T}) - 1 \right)^{-1} ph\ cm^{-2}\ s^{-1}\ MeV^{-1} \quad (1.1)$$

According to "Wien's law" the maximum position of this distribution is at:

$$E_{max}\ (MeV) = 4.7*10^{-10}\ T(k) \quad (1.2)$$

and the average photon energy is:

$$E_{aver}\ (MeV) = 2.7\ kT = 2.3*10^{-10}\ T(k) \quad (1.3)$$

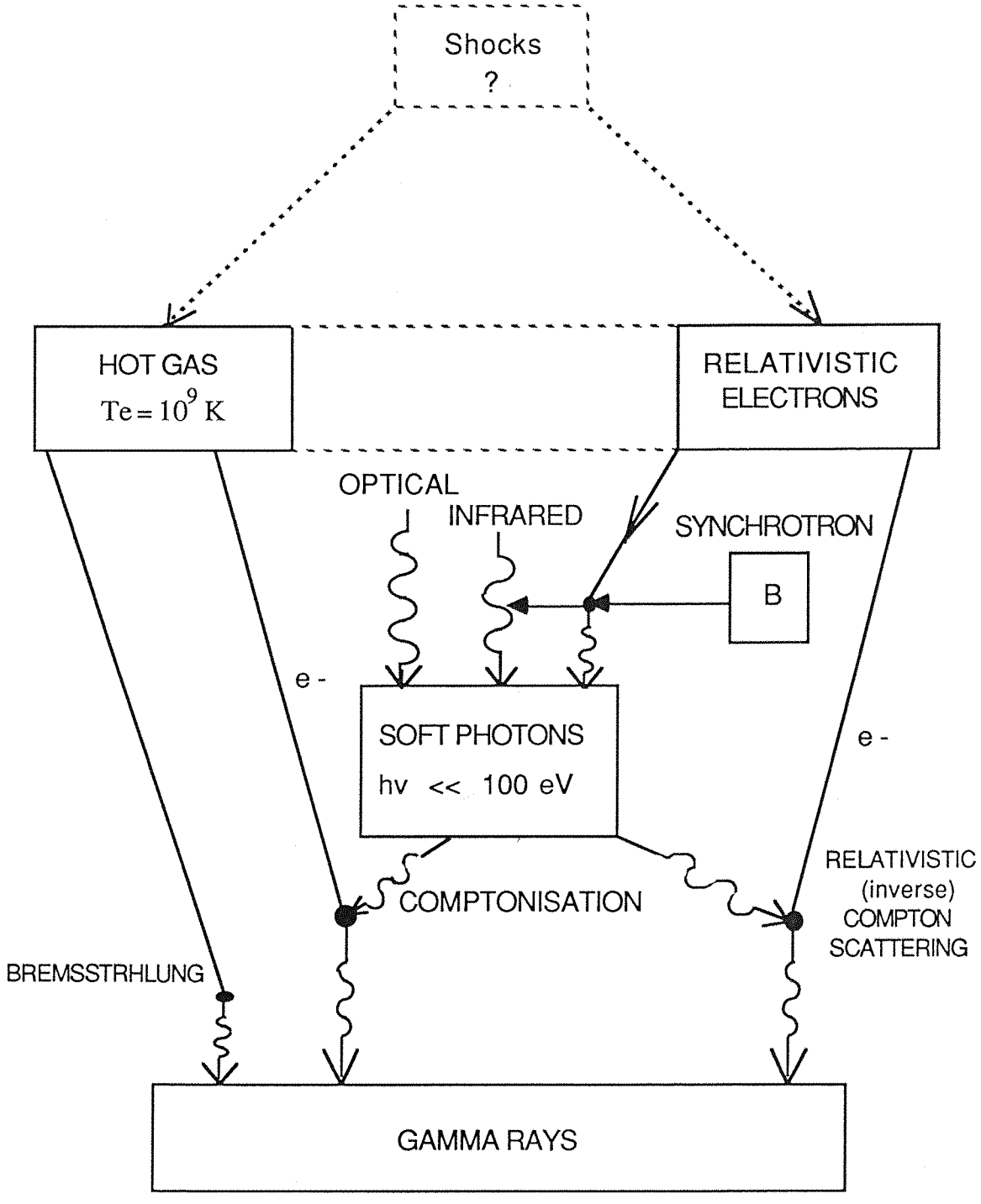

Figure(1.1) Possible pathways for gamma ray emission (from Fabian and Rees 1980)

1.2.2 Synchrotron emission.

Synchrotron radiation is emitted when a charged particle moves spirally in a magnetic field. The correspondent magnetic force is given by:

$$F = \frac{q(v*B)}{c} \qquad (1.4)$$

where (v) is the velocity of the charged particle, (B) is the magnetic field strength and (c) is the speed of light.
The mechanism of synchrotron radiation production is responsible for the general x-ray emission of less than 30 keV from the Crab Nebula and the radio emission from the Jupiter (Chupp 1976).
The characteristic frequency emitted by a single electron above which the emitted radiation becomes negligible is given by:

$$\nu_s = \frac{3 e \gamma 2 \ B}{4 \Pi m_o c^2} (Hz) \qquad (1.5)$$

where (γ) is the Lorentz factor for the electron and equal to $(\frac{E}{m_o c^2})$.
The frequency distribution of the emitted radiation is a symmetric function with a maximum at :

$$\nu_{max} = \frac{0.87 \ e \ \gamma^2 \ B}{4 \Pi m_o c^2} \qquad (1.6)$$

The energy of the photon at the maximum of the distribution is expressed by:

$$E_{\gamma(max)} = 0.29 \ h\nu_s = 5*10^{-15} \gamma^2 \ (MeV) \qquad (1.7)$$

In order to produce gamma ray photons in the MeV energy range, very energetic electrons or a strong magnetic field is required.
The total power emitted over all frequencies for a single charged particle of mass $(M)$and (Z) charge can be given by :

$$P_S = -\frac{dE}{dt} = 0.98*10^{-3} \cdot \left(\frac{B^2 (Z^2 mo)^2}{M^2}\right) .\left(\frac{E}{Mc^2}\right)^2 \cdot (eV\ s^{-1}) \quad (1.8)$$

*For an electron $(M=m_o)$, therefor the power can be given :

$$_eP_S = 10^{-3} B^2 \gamma^2 \quad (eV\ s^{-1}) \qquad (1.9)$$

*For a proton with the same energy the power can be given :

$$_pP_S = \frac{m_o}{M_p}4.{}_eP_S = 10^{-3}\ {}_eP_S \qquad (1.10)$$

Ginzburg (1969) evaluated the gamma ray energy spectrum of the case of a power law spectrum of electrons trapped in a random magnetic field of dimension (L), volume (V) and (R) distance from the observer. The formula is given bellow :

First the density of the trapped electron can be given by :

$$N(E) = KE^{-\alpha}\ dE\ (e\ cm^{-2}) \qquad (1.11)$$

assuming that $(R>>L)$ the flux can be expressed by :

$$F_\gamma = 3.27*10^{-2}\ a(\alpha).\left(\frac{keV_B^{(\alpha+1)/2}}{R^2}\right).\left(\frac{2.59*10^{-2}}{E_{MeV}}\right)^{(\alpha+1)/2}$$
$$ph\ cm^{-2}\ s^{-1}\ MeV^{-1} \qquad (1.12)$$

where (R) is the distance from the source and $a(\alpha)$ is the coefficient which depends on the exponent (α) in the electron spectrum.

1.2.3 Inverse Compton scattering.

This is an exactly parallel situation to the Compton effect, in which a highly energetic particle transfers momentum to a low energy photon and endows it with a large momentum and energy. Thus the energy of the scattered photon is on average, $(\frac{E}{m_o c^2})^2$ times greater than the photon energy before scattering (Ginzburg 1969). For an isotropic photon distribution two cases can be considered :

i) $\gamma E_\gamma << m_o c^2$

ii) $\gamma E_\gamma >> m_o c^2$

where (γ) is the Lorenz factor and (m_o) is the rest mass of electron.

In the first case, $E_\gamma << m_o c^2$, the average energy of the produced gamma ray is given by (Stecker 1974) and take the following form :

$$< E'_\gamma > = \frac{4}{3} \gamma^2 < E_\gamma > \qquad (1.13)$$

where $< E_\gamma >$ is the average photon energy of the target photon.

For the case in which a power law electron distribution (as given by equation 1.11) incident on an isotropic photon field, the gamma ray emission spectrum is :

$$\frac{dN_\gamma}{dE'_\gamma} \alpha E'^{-(\alpha+1)/2}_\gamma \qquad (1.14)$$

In the second case, $\gamma E_\gamma >> m_o c^2$, the energy of the scattered photon is proportional to the energy of the incident electron :

$$E'_\gamma \alpha E_e \qquad (1.15)$$

The mechanism in which relativistic electrons, inverse Compton scatter their own produced synchrotron photons to higher level of energies is called Synchrotron self-Compton.

1.2.4 Bremsstrahulng radiation.

When a charged particle is accelerated or decelerated in the Colomb field of another charged particle, Bremsstrahlung radiation is emitted. The total power emitted by a single particle is proportional to the square of the charge of the scatterer and inversely proportional to the square of the mass of the incident particle (Rybicki and Lightman 1979) . This leads to a conclusion that the electron bremsstrahulng emission is of the order (10^6) times more intense than the proton bremsstrahlung of the same energy. The energy range of the emitted photon by a single electron is starting from (Zero) up to (Maximum) corresponding to the total kinetic energy of the electrons (Evans 1955).
For incident non thermal electron spectrum of the form of equation (1.11), Fazio 1967 shows that the spectrum of the emitted photon is :

$$\frac{dN_\gamma}{dE_\gamma} \alpha E_\gamma^{-\alpha} \; ph\ cm^{-2}\ s^{-1}\ MeV^{-1} \qquad (1.16)$$

where (α) is the spectral index of the electron distribution and (E_γ) is the photon energy in MeV.

The electromagnetic radiation of a sufficiently hot plasma can extend up to the x-ray and gamma ray spectral region. If the emitting volume is optically thick to its own radiation, then the spectrum is given by Plank's law as given in section 1.2.1.
The number of photons emitted by a unit area of a blackbody per second at $T(k)$ temperature is given by :

$$N(E_\gamma) = 9.9*10^{40}\ E^2_\gamma \left(exp(1.2*10^{10}.\frac{E_\gamma}{T}) - 1\right)^{-1}\ ph\ cm^{-2}\ s^{-1} MeV^{-1} \quad (1.17)$$

where (E_γ) is the photon energy in MeV.

The maximum of the photon distribution is given by "Wien's law" of equation 1.2 and the average photon is :

$$E = 2.3*10^{-10}\ T(k) \quad (MeV) \qquad (1.18)$$

The required temperature for gamma ray photons is in the range of $(10^8\text{-}10^{10})k$.

The bremsstrahlung emission from a thermal distribution of electrons in a hot optically thin plasma was studied by (Tucker and Gould 1966) and (Blumenthal and Tucker 1974). The differential photon spectrum is :

$$\frac{dN_\gamma}{dE_\gamma} \alpha\ G(E_\gamma kT) e^{-(E_\gamma/kT)} \quad ph\ cm^{-2}\ s^{-1}\ MeV^{-1} \qquad (1.19)$$

Where (E_γ) is the photon energy, $G(E_\gamma kT)$ is the temperature averaged Gaunt factor and (T) is the gas temperature.

1.2.5 Elecrton-positron annihilation.

One of the most interesting examples of particle-matter interaction is the electron-positron annihilation in which at least two gamma rays are produced. The (511 keV) annihilation lines in solar flares could be a result of one of the following cases :

1. Free annihilation of positrons with electrons.
2. Formation and decay of positronium.

In the first case, the formation of the (511 keV) line depends on the positrons source, their propagation in the solar atmosphere and the density and the temperature of the ambient medium in which they decelerate.
Free electron-positron annihilation at rest produce two equal gamma rays of (511 keV) each and will have equal amount of energy, if only they are emitted perpendicular to the centre of mass of the system of the two particles (Stecker 1971).
An outline of all the possibilities of positron decay which leads to a gamma ray emission is shown in fig.1.2.
There are three possibilities for the annihilation of relativistic positrons, (a) escape from the Sun, (b) annihilation in flight and(c) decelerate to thermal energies via interaction with magnetic fields or interaction with ambient matter.
The positrons which annihilate in flight, produce (511 keV) line emission. These are not observed at (511 keV) but appear as gamma ray continuum due to "Doppler broadening". The positrons which do not annihilate in flight or escape from the Sun, can lose their energy by collision and ionization and thus be thermalised. If these thermal positrons annihilate freely, they produce two gamma rays of (511 keV), otherwise they go via positronium. These emission can be observed as discrete gamma ray lines since

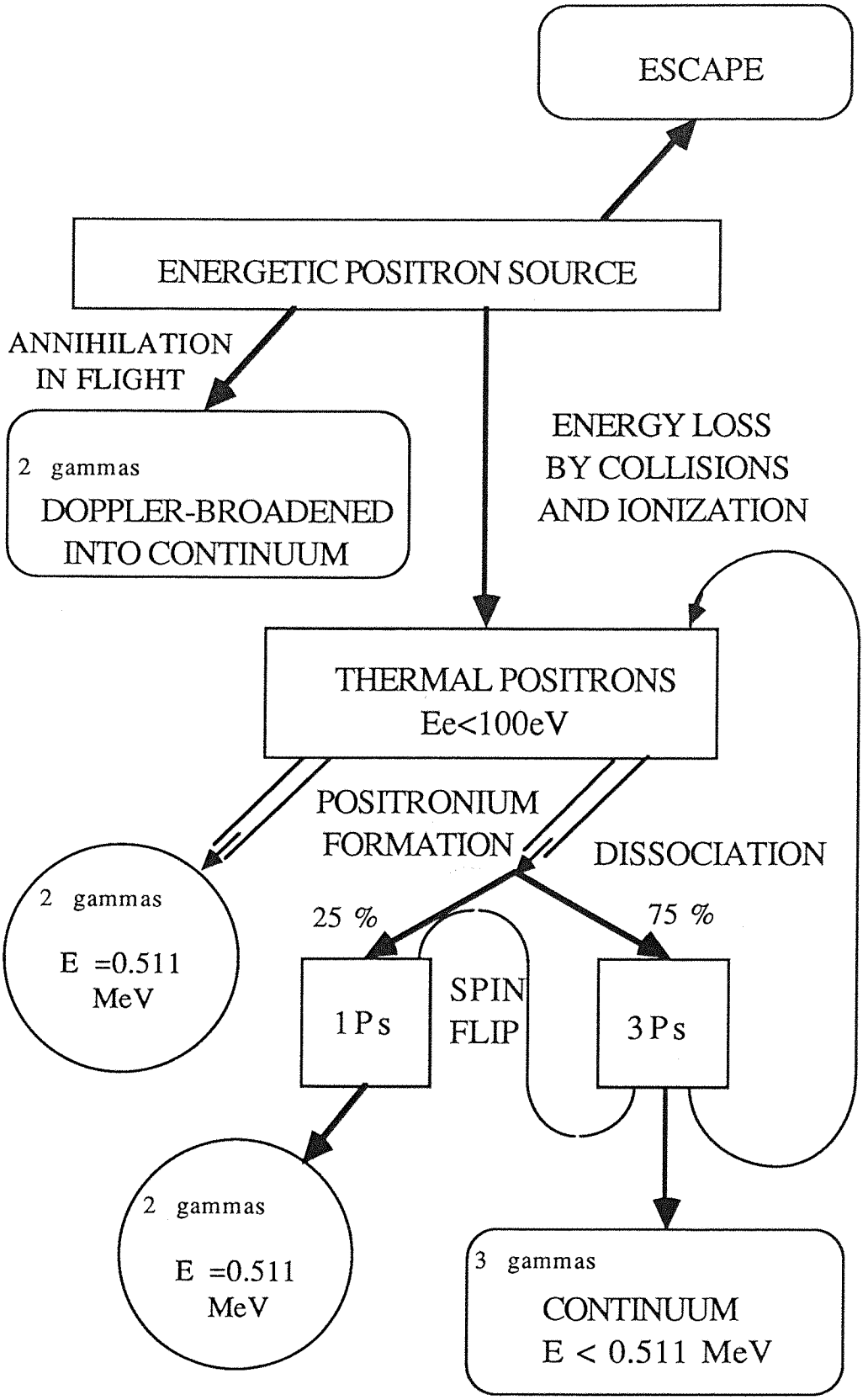

Figure(1.2) Possible methods of positron decay leading to gamma ray emission(from Crannel et al, 1975)

the annihilation occur at thermal energies and there is a very little Doppler broadening.

When a positron slows down while it pass through matter, it may join an electron and built an electron-positron system called "Positronium P_S" which last for a very short time before combining to produce annihilation radiation. If their spins are in opposite directions, the atom will be in (^1S) state otherwise (^3S) state. The first state has a short lifetime of ($1.2*10^{-10}$ sec.) while the second has a longer lifetime of ($1.4*10^{-7}$ sec.).

The annihilation of the first state produce two (511 keV) gamma rays but the second state annihilation emits three gamma ray photons simultaneously each with energy less than (511 keV).

About 25% of the positronium is going through the single state and 75% through the triple state. The energy threshold for positronium formation is 6.8 eV.

Positrons that have a leading role in this mechanism of generating gamma ray photons, can themselves be generated by a number of mechanisms such as the decay of positively charged mesons created in cosmic ray collisions.

1.2.6 Decay of Π° mesons.

Π° mesons are created in the collisions of cosmic rays with interstellar matter. These neutral pions are unstable and decays into two gamma rays. Also the interaction of high energy particles generate Π°. Here some examples of such interactions are given :

$$P + P \text{ -------> } n\,\Pi^\circ \qquad (1.20)$$

and

$$P + \alpha \text{ -------> } n\,\Pi^\circ \qquad (1.21)$$

where (n) is the multiplicity which may become significant during solar flares (Fichtel and Trombka 1981).

Then gamma ray production follows

$$\Pi^{\circ} \text{ -------> } 2h\nu \qquad (1.22)$$

Another example of the Π° mesons production is the matter anti-matter annihilation which eventually give rise to two gamma rays as a result of the Π° decay :

$$P + \bar{P} \text{ ---------> } bosons$$

$$\text{-------> } \Pi^{\circ}$$

$$\text{-------> } 2\gamma$$

$$(1.23)$$

1.2.7 Nuclear gamma ray line emission.

As a result of the interaction of energetic particles with ambient matter, gamma ray lines are produced ranging from *(10 keV to 20 MeV)* (Ramaty et al 1979). The spectral structure of these gamma ray lines depend on the composition and energy spectrum of the initial energetic particles and the physical state of the ambient medium.
Many astrophysical sites are candidate for the emission of these lines such as, solar flares, the interstellar medium, neutron stars, blackholes, supernovae remnants and nuclei of galaxies.
There are many physical mechanisms which can give rise to gamma ray lines, here is a summery of them :

1. The annihilation of positrons that have been slowed down with interstellar electrons given (511 keV) lines.
2. The decay of the long lived nuclei which in turn emit gamma rays. The details of the expected lines from this mechanisms given by (Clayton 1973).
3. The interaction of low energy cosmic rays with interstellar gas and dust grains leading to exited nuclei which eventually emit gamma rays through electromagnetic deexcitation of an exited state.

4. Cyclotron line emission in strong magnetic field which is due to the transition in the energy levels of electrons in the presence of a magnetic field (Hayles 1982).

1.3 Galactic gamma ray astronomy.

1.3.1 Diffuse galactic emission.

1.3.1.1 Diffuse galactic continuum.

The collision between cosmic rays and protons, nuclei of atoms and molecules of interstellar gas generates pions of all charges (Π^+ , Π^-, and Π°). The (Π^- and Π^+) mesons decay into (μ^- and μ^+) and later into positrons and electrons with relativistic energies. The Π° mesons decay into almost two gamma rays.
Gamma rays can be produced by the decay of (Π°) mesons , bremsstrahlung from energetic cosmic ray electrons, inverse Compton scattering electrons interacting with photon field and synchrotron radiation of high energy electrons passing through magnetic fields.
The Cos-B map of the galactic plane is shown in fig1.3. It indicates that it is a rich source of gamma ray emission (Mayer-Hasselwander et al 1982). The conclusion of this satellite observations suggest that gamma ray radiation above 100 MeV results from the decay of mesons. At energies less than 100 MeV, it is suggested that either inverse Compton scattering or bremsstrahlung process make a significant contribution to the total gamma ray intensity. The situation for the galactic centre is shown in fig.1.4 (Sacker and Schonfelder 1984) .
At MeV energies, the explanation of the diffuse energy spectrum is rather complicated. This is due to the only existence of upper limits and the contribution of gamma ray lines to the overall flux. The energy spectrum shown in fig.1.4 contains only the mean fluxes of energy band intervals and it is very likely that gamma ray lines have contributed to it.

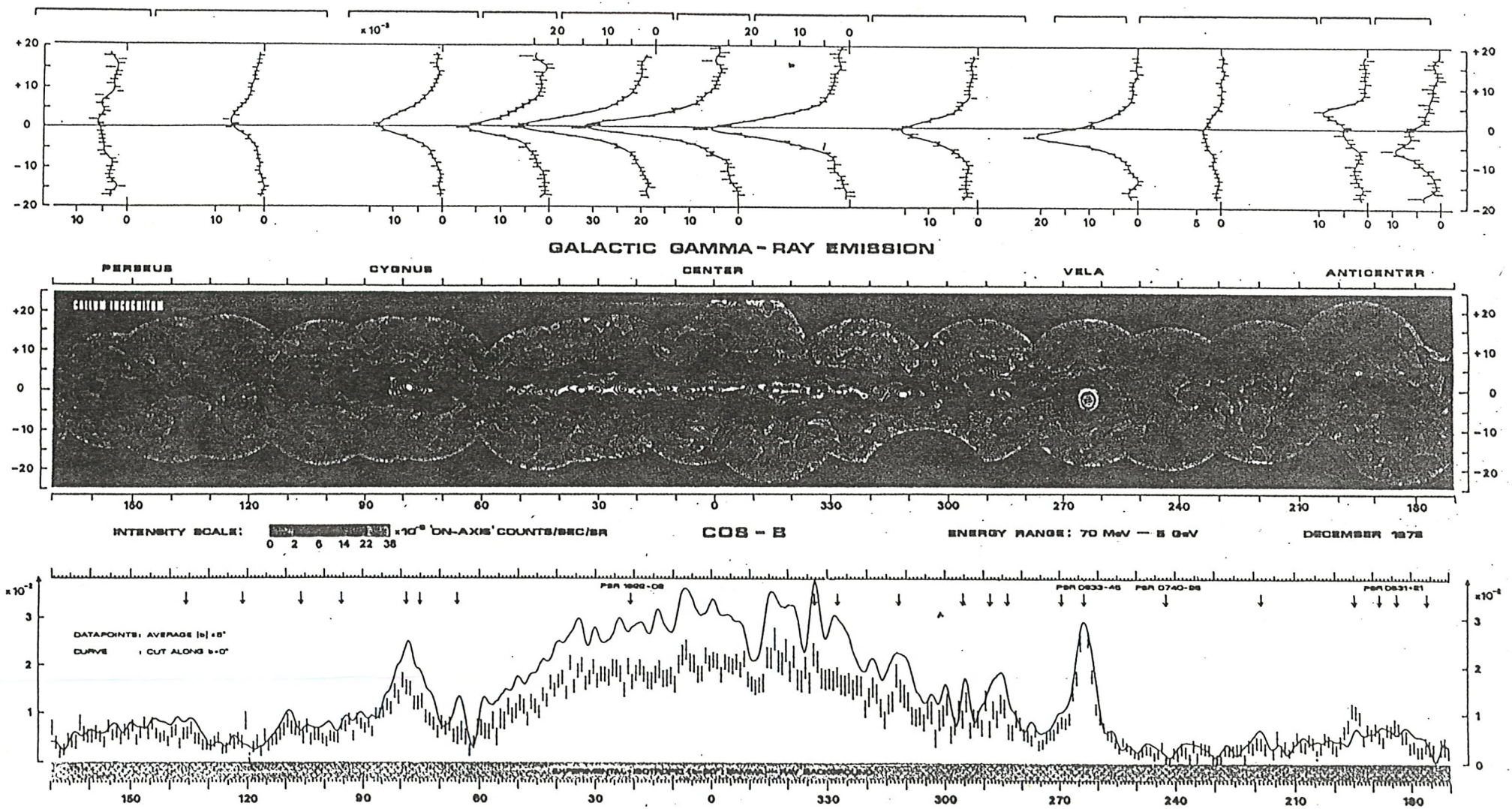

Figure (1.3) The map of the galactic plane presented by Cos-B satellite from Mayor-Hasselwander et al 1982.

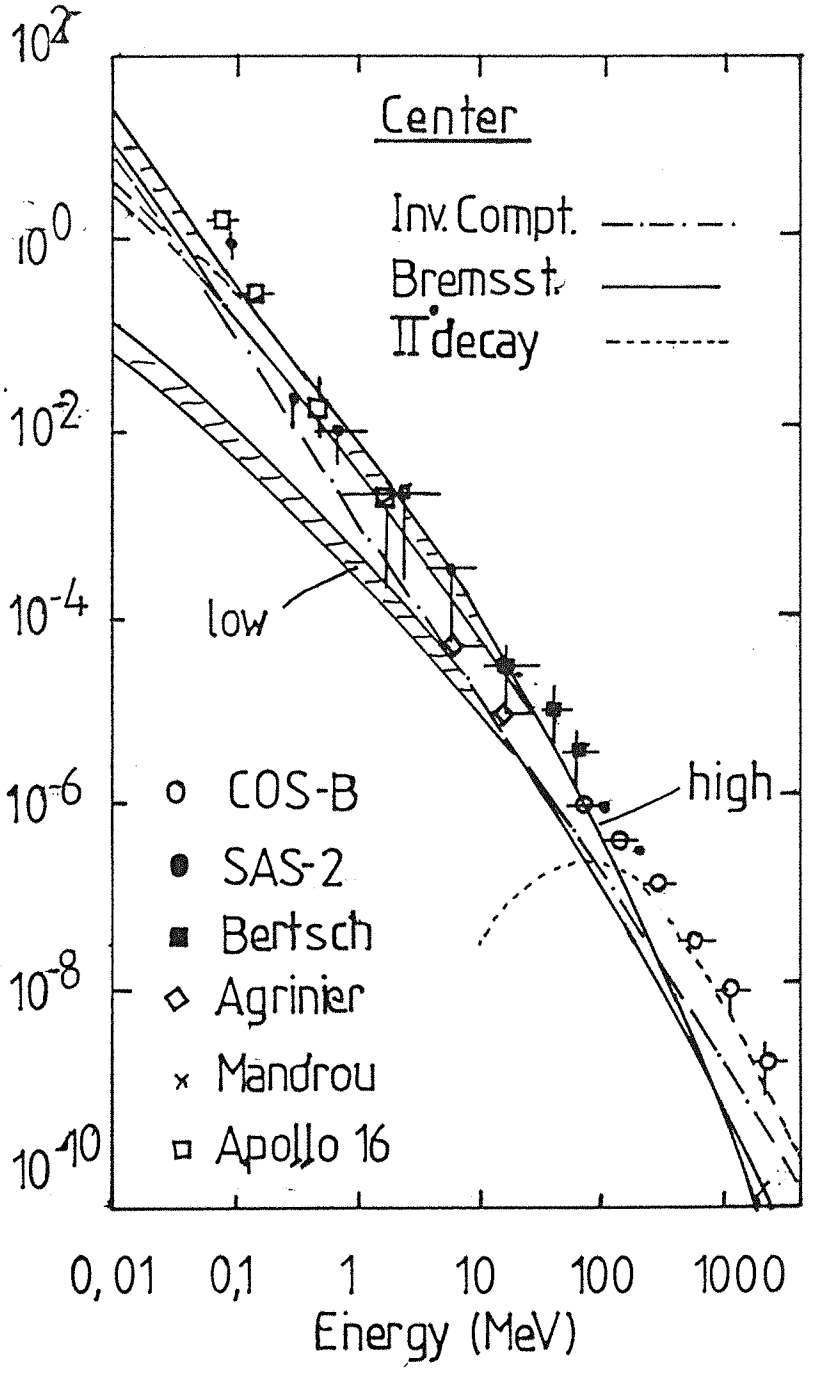

Figure (1.4) Broad band gamma-ray measurements of the gelactic centre region. (Sacker and Schonfelder 1984).

1.3.1.2 Diffuse galactic lines.

The interactions of low energy cosmic rays in the interstellar medium are expected to give rise to gamma ray lines from few keV to few tenth of MeV (Ramaty et al 1979). Fig.1.5 shows the predicted line emission spectrum. Two of the most interesting lines are the (6.129 MeV) from ^{16}O and the (4.44 MeV) from ^{12}C resulting from de-excitation of nuclei in interstellar grains.
Two more interesting lines are the (1.809 MeV) of ^{26}Al and the (0.511 MeV) line. The first line result from the decay of ^{26}Al in the interstellar medium (Ramaty and Lingenfelter 1977) and the second from positron annihilation. Both lines have been detected and reported by many authors (Mahoney et al 1984, MacCallum et al 1987, Leventhal et al 1978 and Share et al 1988).
The ^{26}Al decays into ^{26}Mg with a half life of $7.4*10^5$ yr. The intensity of the detected line has been measured to be $(4.8+1.0)*10^{-4}$ ph. $cm^{-2}.s^{-1}.$ rad^{-1}.(fig.1.6). The origin of this large amount of ^{26}Al is hard to explain. The explosion of novae and supernovae can only contribute to a fraction of this amount. Prantzos et al 1986 have suggested that Wolf-Rayet stars (WR) are most likely to be the real candidate for it. The (511 keV) line has been discussed in the galactic centre section.

1.3.2 Galactic centre region.

The centre of our galaxy has been shown to be a very strong radio and infrared source. In the gamma energy range, the (511 keV) annihilation line is the most interesting and puzzling line reported from this region. The line was reported initially by (Johnson et al 1972) and later confirmed by many authors. A total of 17 different balloon and satellite observations, including the recent SMM results, have confirmed the existence of this source (Leventhal 1987).

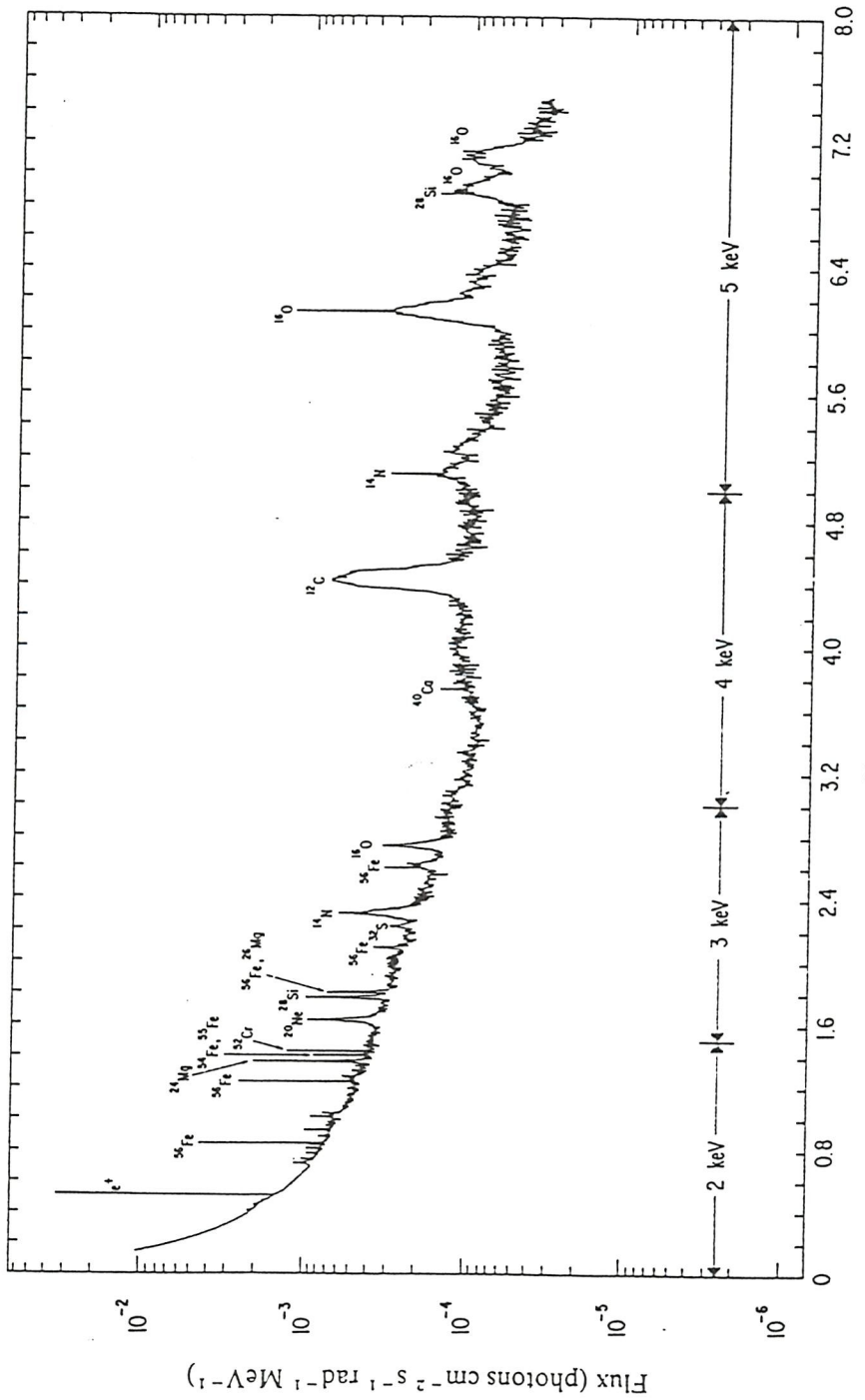

Figure (1.5) The predicted line emission spectrum given by Ramaty et al 1979.

The autumn of 1979 and the spring of 1980 observations of HEAO-3 satellite of this line show a change in the intensity of the source by a factor of (3). Fig.1.7 shows the 1979 observation of the (511 keV) line having an intensity of $(1.85\text{-}0.21)*10^{-3}$ ph.cm^{-2}.s^{-1}. Also the continuum spectrum of the 1980 observation is shown in fig.1.8. This continuum spectrum below the (511 keV) line has barely changed during the same period . Bildsten and Zurek 1988 claims that Compton scattering of the line and high energy radiation provide a natural explanation for the little change detected in the continuum spectrum.

In conclusion it appears that the galactic centre is a harbor for a soft gamma ray source. Future experiments with higher sensitivities may lead to a better explanation of this source.

1.3.3 Localized galactic sources.

1.3.3.1 Cos-B sources.

The successful ESA satellite Cos-B, which was launched for the first time in 1975, has given a clear map of the galactic distribution of gamma ray emission. This experiment was finally switched off on 1982 completing 64 observations (Pollock et al 1985). The scientific objective of this mission was to study extraterrestrial gamma ray radiation of energies above (30 MeV). A full description of the experiment is given by (Bignami et al 1975).

Most of the observations were devoted to the study of the galactic disk. Many gamma ray maps were presented and one of them was given earlier in this chapter (fig.1.3). The Cos-B catalog of gamma ray sources presented by (Swanenburg et al 1981) contains 25 sources (Table 1.1). The latitude profile of the galactic plane is dominated by three isolated bright sources : 2CG263-02 , 2CG184-05 and 2CG195+04. The first two sources have been unambiguously identified with the Crab and Vela pulsars respectively (Bennett et al 1977).

The Crab pulsar has been observed essentially over the whole electromagnetic spectrum, from radio up to gamma ray. Fig 1.9 summarize measurement of this pulsar "light curve" at various wavelengths (Bignami and Hermesen 1983). Despite of similarity in

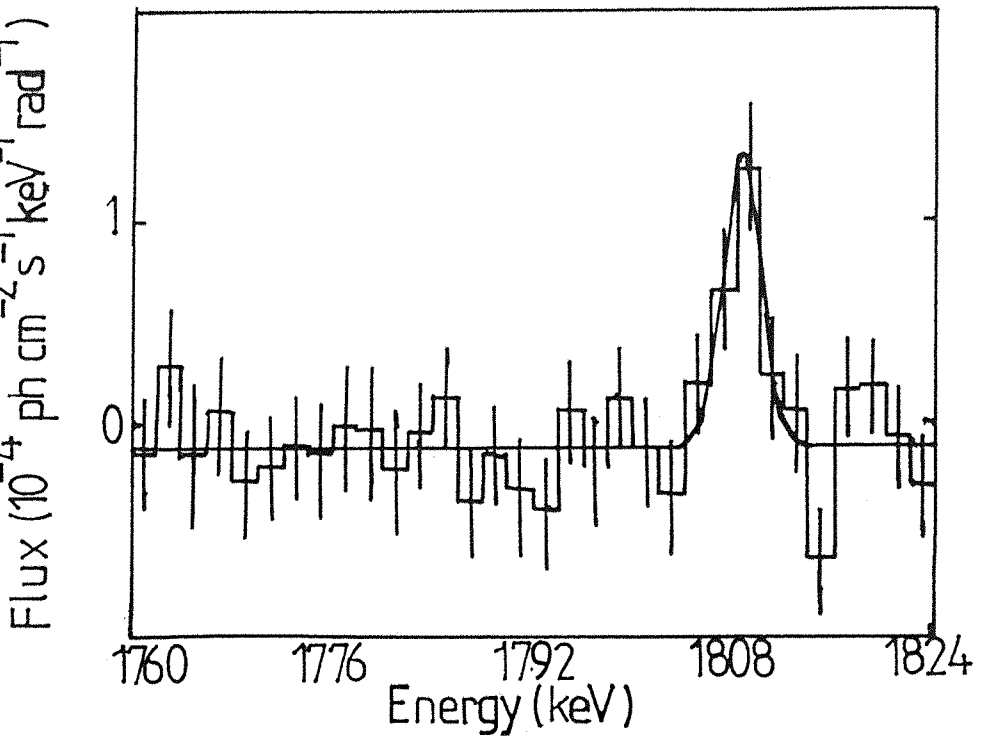

Figure (1.6) The galactiv emission near 1809 kev. (From Mahoney et al 1984

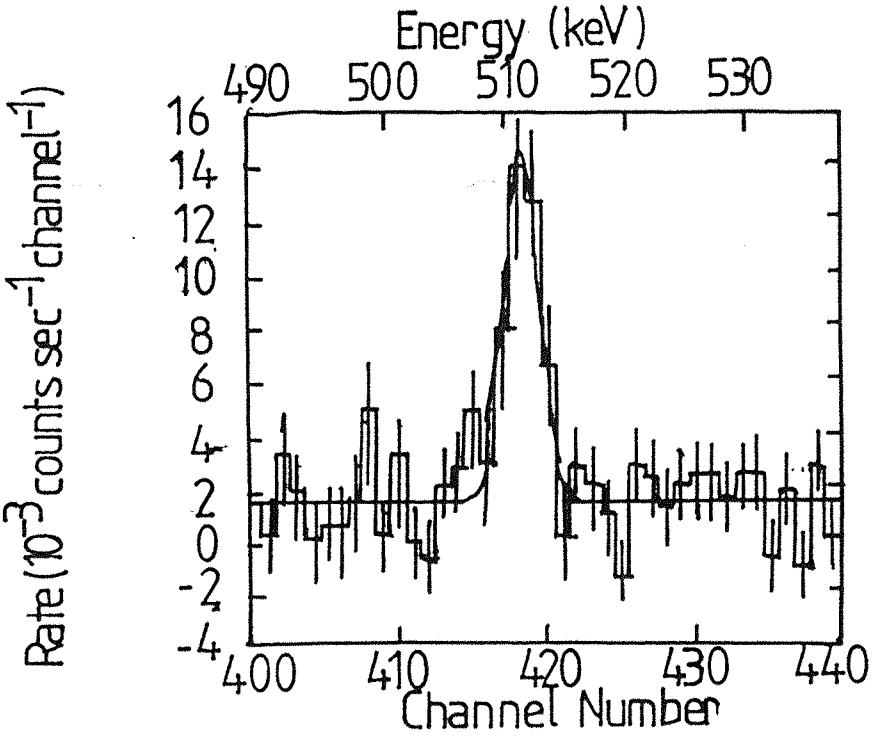

Figure (1.7) The galactic emission near 511 Kev. (From Riegler et al 1981).

Table (1.1)

The 2CG Catalogue of Gamma Ray Sources Observed by Cos-B

(From Swanenburg et al 1980)

Source Name	No. of observations	Position (degrees) l	Position (degrees) b	Flux E>100 MeV (10-6 ph.cm-2s-1)	Spectral Prarameter	Identifications
2CG006-00	3	6.7	-0.5	2.4	0.39±0.08	.....
2CG010-31	1	10.5	-31.5	1.2	.....	.....
2CG013+00	4	13.7	+0.6	1.0	0.68±0.14	.....
2CG036+01	3	36.5	+1.5	1.9	0.27±0.07	.....
2CG054+01	3	54.2	+1.7	1.3	0.20±0.09	.....
2CG065+00	4	65.7	0.0	1.2	0.24±0.09	
2CG075+00	5	75.0	0.0	1.3	.....	.....
2CG078+01	5	78.0	+1.5	2.5	.....	.....
2CG095+04	3	95.5	+4.2	1.1	.....	.....
2CG121+04	3	121.0	+4.0	1.0	0.43±0.12	.....
2CG135+01	3	135.0	+1.5	1.0	0.31±0.10	.....
2CG184-05	4	184.5	-5.8	3.7	0.18±0.04	PSR 0531+21
2CG195+04	3	195.1	+4.5	4.8	0.33±0.04	.....
2CG218-00	3	218.5	-0.5	1.0	0.20±0.08	.....
2CG235-01	2	235.5	-1.0	1.0	.....	.....
2CG263-02	4	263.6	-2.5	13.2	0.36±0.02	PSR 0833-45
2CG284-00	1	284.3	-0.5	2.7	.....	.....
2CG288-00	1	288.3	-0.7	1.6	.....	.....
2CG289+64	2	289.3	+64.6	0.6	0.15±0.07	3C273
2CG311-01	2	311.5	-1.3	2.1	.....	....
2CG333+01	3	333.5	+1.0	3.8	.....	.....
2CG342-02	5	342.9	-2.5	2.0	0.36±0.09	.....
2CG353+16	4	353.3	+16.0	1.1	0.24±0.09	r Oph
2CG356+00	1	356.5	+0.3	2.6	0.46±0.12	.....
2CG359-00	3	359.5	-0.7	1.8	.....	.....

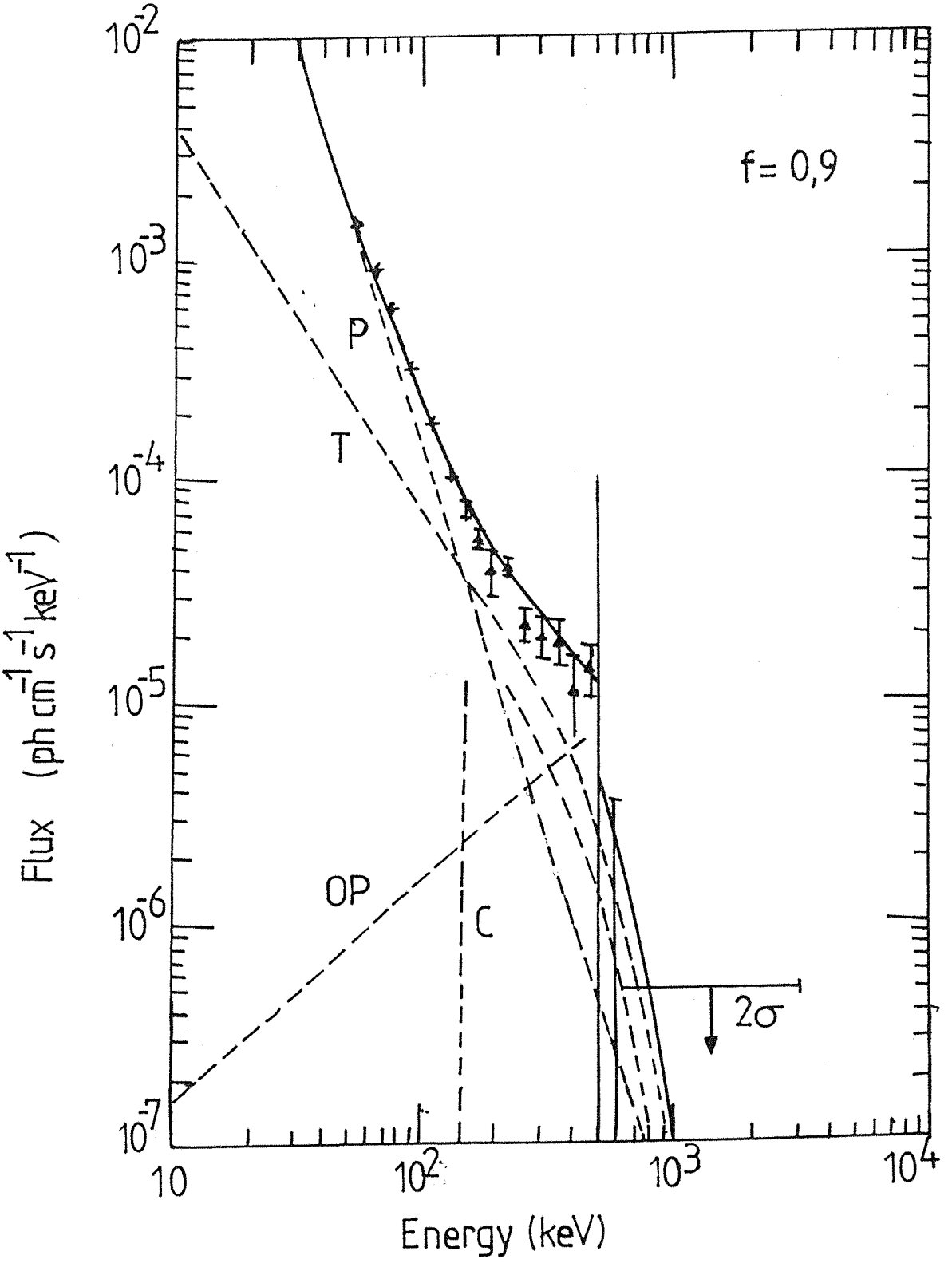

Figure (1.8) The continuum spectrum of position annihilation line. (From Riegler et al 1981).

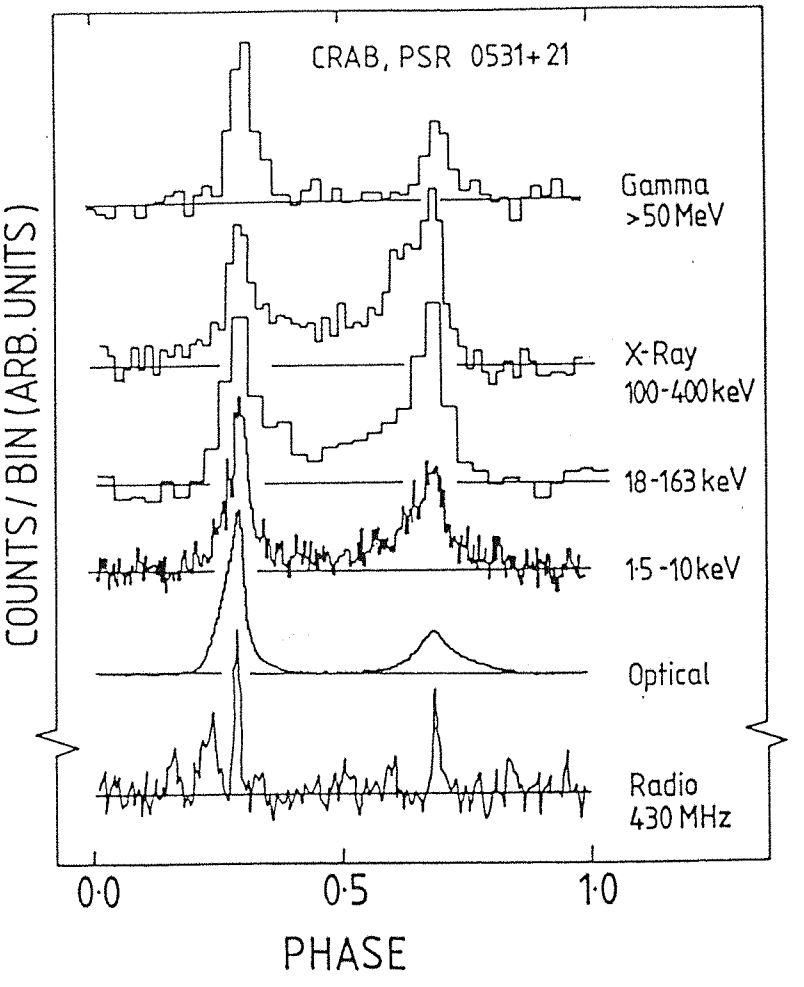

Figure (1.9) Light curves for PSR 0531 + 21 at various wavelengths. Gamma-ray data summation of five COS-B observations (248).

the width of the two pulses at all wavelengths, except radio, there are a number of differences :

(i) The ratio of the intensity of the interpulse to the main pulse is a function of wavelength. Cos-B has provided evidence that above (50 MeV) this ratio is variable on a time scale of years (Wills 1981).
(ii) The valley between the pulses has a wavelength dependent magnitude.

The Vela pulsar is the strongest gamma ray source in the sky. Its flux above (100 MeV) has been evaluated to be $1.3*10^{-5}$ $ph.cm^{-2}.s^{1}$.. The Cos-B light curve for this pulsar together with the distribution detected at optical and radio wavelength is shown in fig.1.10 (Wills et al 1980).
A part from the two sources (Crab and Vela) only two other sources from Cos-B catalog have been identified. The 2CG289+64 and 2CG353+16. the first is associated with the QSO 3C273 and the second with the ρ Ophiuchi cloud complex (Bignami et al 1981, Bignami and Morfill 1980).
The Cos-B error box containing 3C273 is estimated to be of the order of 2.5 square degrees and the probability of a chance coincidence is roughly 10.
The ρ−Oph cloud is a complex region containing different classes of potential gamma ray emitting objects. No direct understanding of the source emission will be gained until a survey of this region of the sky is achieved by an instrument with a fine angular imaging capability.
The source 2CG195+4 or "GEMINGA" is a very interesting scorch and have been left to be discussed separately in the following section.
There are two other Cos-B sources namely the 2CG078+01 and 2CG075+00 near the edges of Cygnus X complex and another one 2CG013+00 near the H_{II} region M17 (Pollock et al 1985) but without any confirmation of their identification.

1.3.3.2 " GEMINGA" The source that is not there.

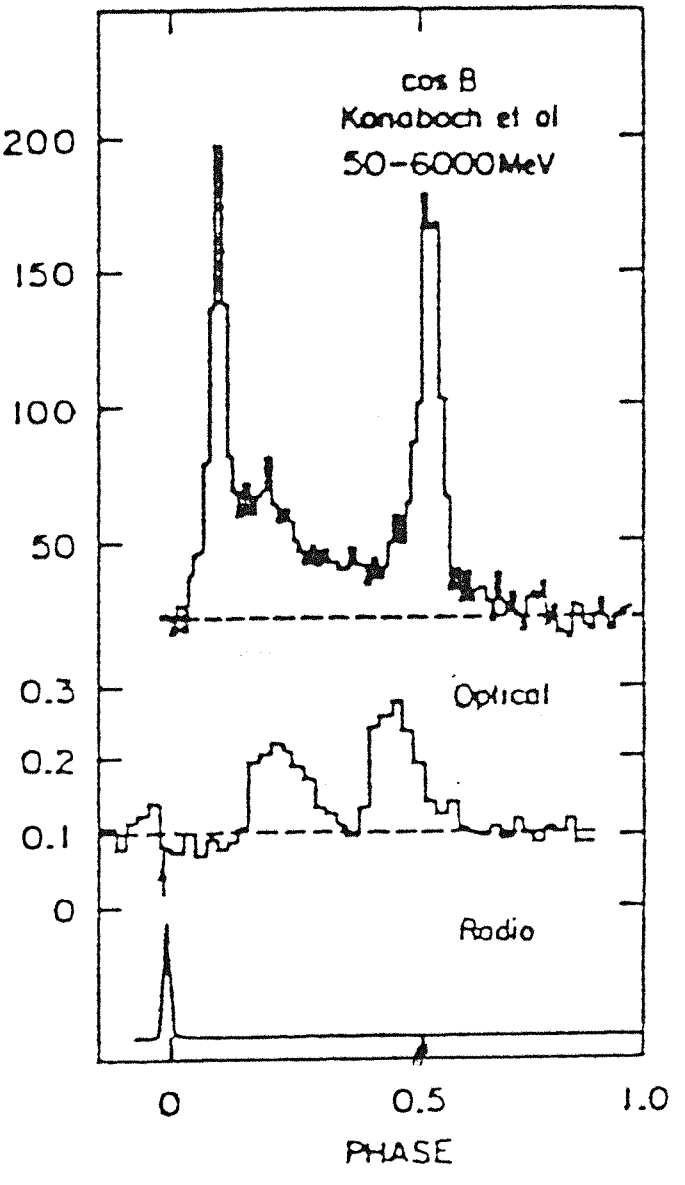

Figure (1.10) Light curves for the Vela pulsar at various wave-lengths from Willis et al 1980.

This is a mysterious gamma ray source discovered by SAS-2 group (Fichtel et al 1975) and latter confirmed by Cos-B group (Swanenburg et al 1981). 2CG195+04 or Geminga is the second brightest gamma ray source at energy more than (100 MeV) after the Vela pulsar. Its flux over (35 MeV) is grater than 10^{-5} ph.cm^2.s^{-1}..
Bignami et al 1983 have identified this source with a nearby (= 100pc) X-ray source IE0630+178. The SAS-2 group have claimed detecting periodicity (P = 59 sec) in the emission of gamma rays (Thompson et al 1977). This was confirmed by (Bignami et al 1984) using Einstein and Exosat data and the latter also associate the identification of Geminga with the event 437 AD witnessed by the Chinese (Zyskin and Mukanov 1983).
The poor angular resolution of the past telescopes created difficulties in the identification of this object. There might be something in common between Geminga and the rest of the unidentified Cos-B sources. Only future experiments with better angular resolution may answer the question about the origin of "Geminga".

1.3.3.3 Radio pulsars.

Two of the most common radio pulsars exist are the Crab and Vela pulsars. In the early 70's, it was discovered that both are very bright gamma ray sources (Kniffen et al 1974). After this discovery, it was clear that neutron stars are one of the best candidates for the emission of gamma rays.
During the last decade many authors have reported lines from the Crab pulsar. A narrow line at (73 keV) was first reported in 1979 by (Ling et al 1979). This was latter confirmed by (Strickman et al 1982) and (Manchanda et al 1982). Two other lines at (400 keV) and (1050 keV) were reported by (Leventhal et al 1977) and (Ayre et al 1983) respectively.
The last two lines were observed recently by the DGT telescope of New Hampshire. McConnell et al 1987 have placed (3σ) upper limits of $3.2*10^{-3}$ and $1.9*10^{-3}$ ph.cm^{-2}.s^{-1}. for the two lines

respectively. Also the Crab spectrum has been determined and described by a power law with a best fit of $5.1*10^{-3}\ E^{-1.88}$ ph.cm^{-2}.s^{-1}.MeV^{-1} .
Meanwhile the observation and imaging of the Crab by the GRIP telescope (Althouse et al 1987) has not given any confirmation about the existence of any gamma ray lines.

1.3.4 Transient sources.

1.3.4.1 Gamma ray bursts.

Gamma ray bursts (GRB) were detected for the first time in 1967 by a telescope designed to study interplanetary scintillation of compact radio sources but their discovery were not published until 1973 (Klebesadel et al 1973). So far several hundred GRB have been fully analyzed and a few hundred more have been detected and are under analysis.
GRB are generated by neutron stars with very strong magnetic fields roughly (10^{12} -10^{15}) G. Gamma ray emission and absorption have been detected from GRB. Two spectral line features have been reported by (Teegarden et al 1980), a broad line at (420 keV) and a narrow one at (740 keV). They have suggested that the first line is the redshifted (511 keV) and the second one is the redshifted first exited state of the Fe (E=847keV). Also an absorption line feature at (50 keV) has been reported by (Mazets et al 1981).
GRB have three main features :

(i) Most of them have a continuum spectrum which can be approximated to the shape of thermal bremsstrahlung emission ;

$$dN = A\ dE^{-1}\ exp(\frac{-E}{k\,T})dE \qquad (1.24)$$

(ii) Many GRB spectra contains cyclotron absorption or/and redshifted annihilation line.
(iii) Continuum and line radiation both experience strong spectral variability.

All these unique characters make GRB a good target for astronomers to investigate them. A typical spectrum of a GRB is shown in fig.1.11.

1.3.4.2 Supernovae and Supernovae remnant.

Supernovae remnant and Supernovae explosion are fundamental matters in astrophysics. The expected gamma ray lines produced in the decay of radioactive isotopes during the event of an explosion emphasis on the significance of these objects.
Ramaty and Lingenfelter 1979 have given a list of the decay chains from the nucleosynthesis during the explosion (Table 1.2).
Two of the most promising lines are the features at (0.847 and 1.238 MeV) resulting from the following decay :

$$^{56}Ni \text{ -------> } ^{56}Co \text{ -------> } ^{56}Fe \qquad (1.25)$$

These lines were detected from SN1987A by the gamma ray spectrometer (GRS) on board NASA's Solar Maximum Mission (SMM) and reported by (Matz et al 1988). Their fluxes were estimated to be $(1\text{-}25)*10^{-3}$ and $(6\text{-}2)*10^{-3}$ $ph^{-1}.cm^{-2}.s^{-1}$. respectively.
Gamma ray lines resulting from the above decay chain can be detected for years after the explosion.There are also three lines at (0.068 , 0.078 and 1.156) MeV which could be detected from the following decay :

$$^{44}Ti \text{ -------> } ^{44}Sc \text{ -------> } ^{44}Ca \qquad (1.26)$$

These above three lines could be traced from young supernovae in our galaxy over the past 100 years.
The predicted line at (1.809 MeV) from the decay :

$$^{26}Al \text{ -------> } ^{26}Mg \qquad (1.27)$$

has been discused in detail in section 1.3.1.2.

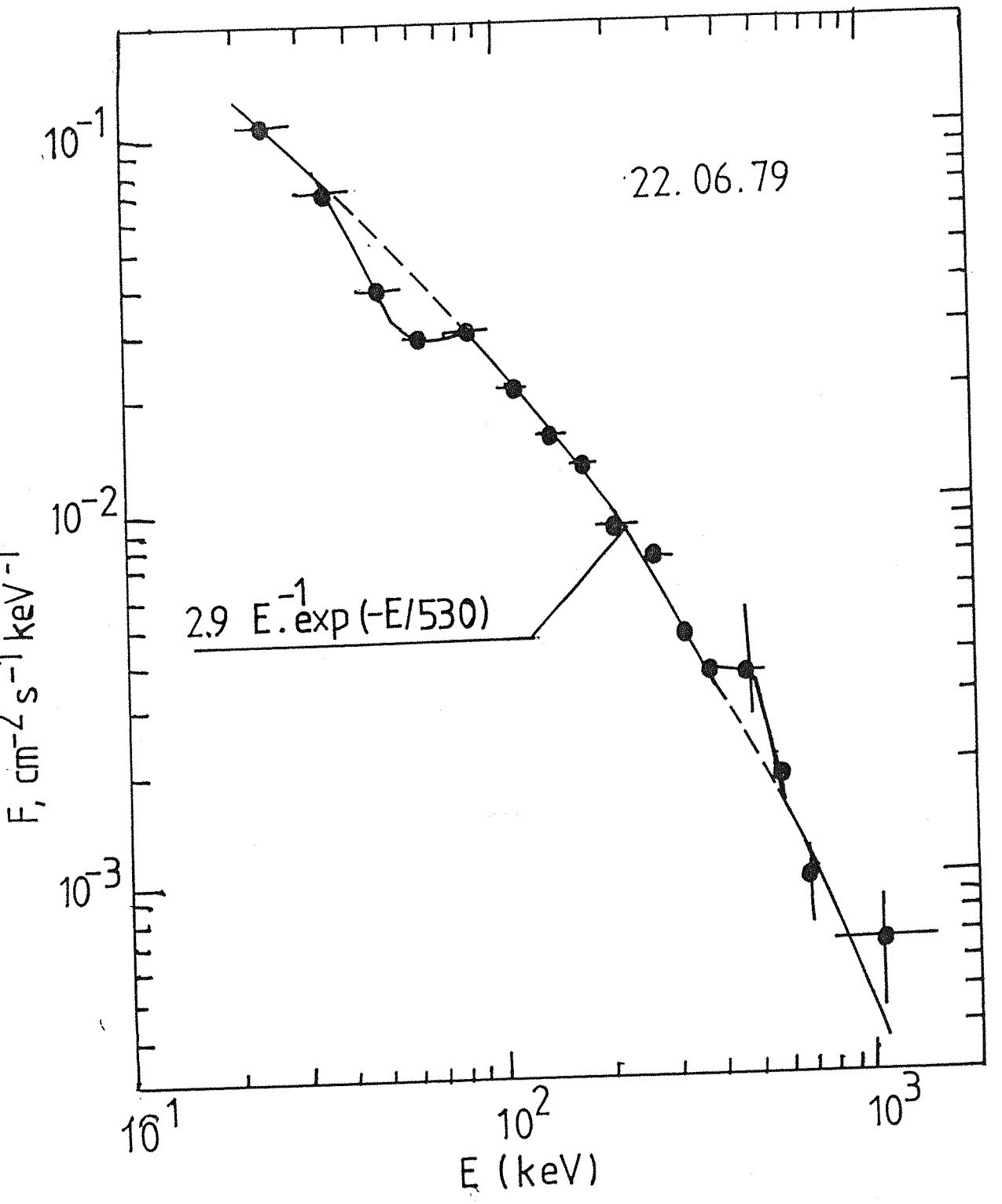

Figure (1.11) The spectrum of a gamma-ray burst with an emission live at 460 KeV and an absorption line at 50-70 KeV.

Table(1.2)
The decay chains from the nucleosynthesis in supernovae
(From Ramaty and Lingenfelter 1979)

Decay chain	Mean life (y)	Q/Q(^{56}Ni)	Energy	Positrons or photons per disintegration
^{56}Ni → ^{56}Co → ^{56}Fe	0.31	1	e^+	0.2
			0.847MeV	1
			1.238MeV	0.7
^{57}Co → ^{57}Fe	1.1	$2*10^{-2}$	0.122MeV	0.88
			0.014MeV	0.88
^{22}Na → ^{22}Ne	3.8	$5*10^{-3}$	e^+	0.9
			1.275MeV	1
^{44}Ti → ^{44}SC → ^{44}Ca	68	$2*10^{-3}$	e^+	0.94
			1.156MeV	1
			0.078MeV	1
			0.068MeV	1
^{60}Fe → ^{60}Co → ^{60}Ni	$4.3*10^5$	$1.5*10^{-4}$	1.322MeV	1
			1.173MeV	1
			0.059MeV	1
^{26}Al → ^{26}Mg	$1.1*10^6$	$1.5*10^{-4}$	e^+	0.85

The frequency of supernovae explosions in our galaxy is averaged by one in every 30 years. This should lead to the location of a number of supernovae sites.

1.4 Extragalactic astronomy.

1.4.1 Active galactic nuclei (AGN).

Many gamma ray sources have been associated with several classes of AGN. Some examples of the brightest objects are the Seyfert galaxies NGC4151 and MCG8-11-11, the Quasar 3C273, the Radio galaxy Cen-A and the peculiar galaxy NGC1275 (Bassani and Dean 1983).

The Seyfert galaxy NGC4151 is not only the best studied galaxy at gamma ray energy range but also has been thoroughly investigated over the entire range of the electromagnetic spectrum (fig.1.12). The MISO telescope had a great interest in this particular object. It observed this galaxy three times between 1979 and 1980. The obtained spectrum is shown in fig.1.13 (Boella et al 1984).
The data from the first observation favour a power law spectrum of a spectral index of (1), while the last data was fitted with a power law spectrum of (α=1.5).
All the available data from observing this object over the gamma ray energy range indicate for a variable output over a large time scale and this was confirmed by the 1979 observation of MISO.
Comparing all the different experimental data, a variation of typically a factor of (3-10) over a long time scale (years) can be appreciated. Meanwhile the shortest time scale for intensity variation can be considered to be around six months or less.

The Quasar 3C273 is a nearby quasar known to be one of the brightest optically. Its luminosity has been measured to be (L_x = $1.7*10^{46}$ erg.s^{-1}) in the (0.5-4.5)keV energy band (Dean and Ramsden 1981). The spectral steepens sharply from the x-ray to the gamma ray region. The slope is changing from 1.4 in the hard x-ray region to 2.7 in the high energy gamma ray region (Fig. 1.14).

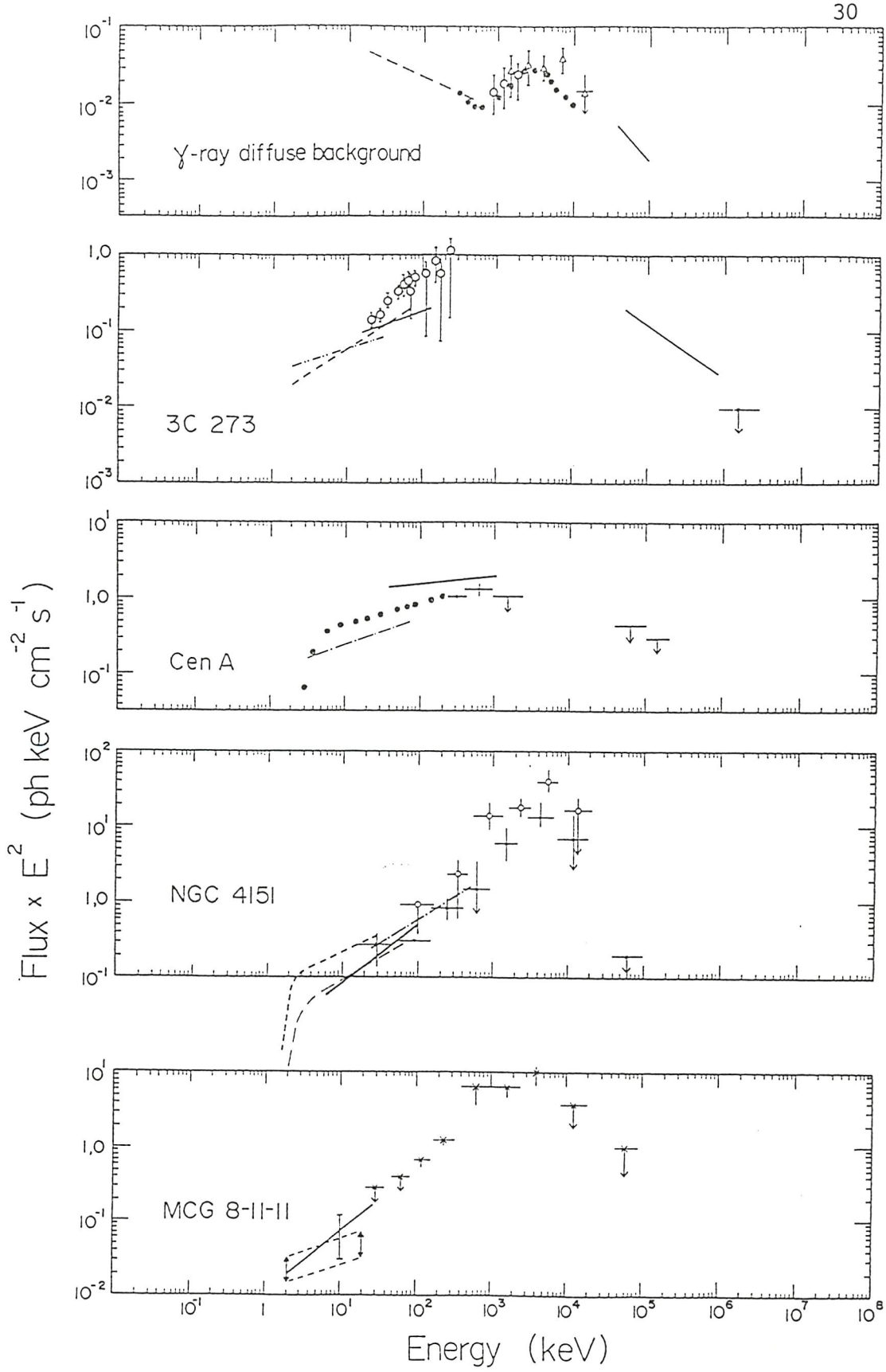

Figure (1.12) The power output of some galactic and extragalactic sources.

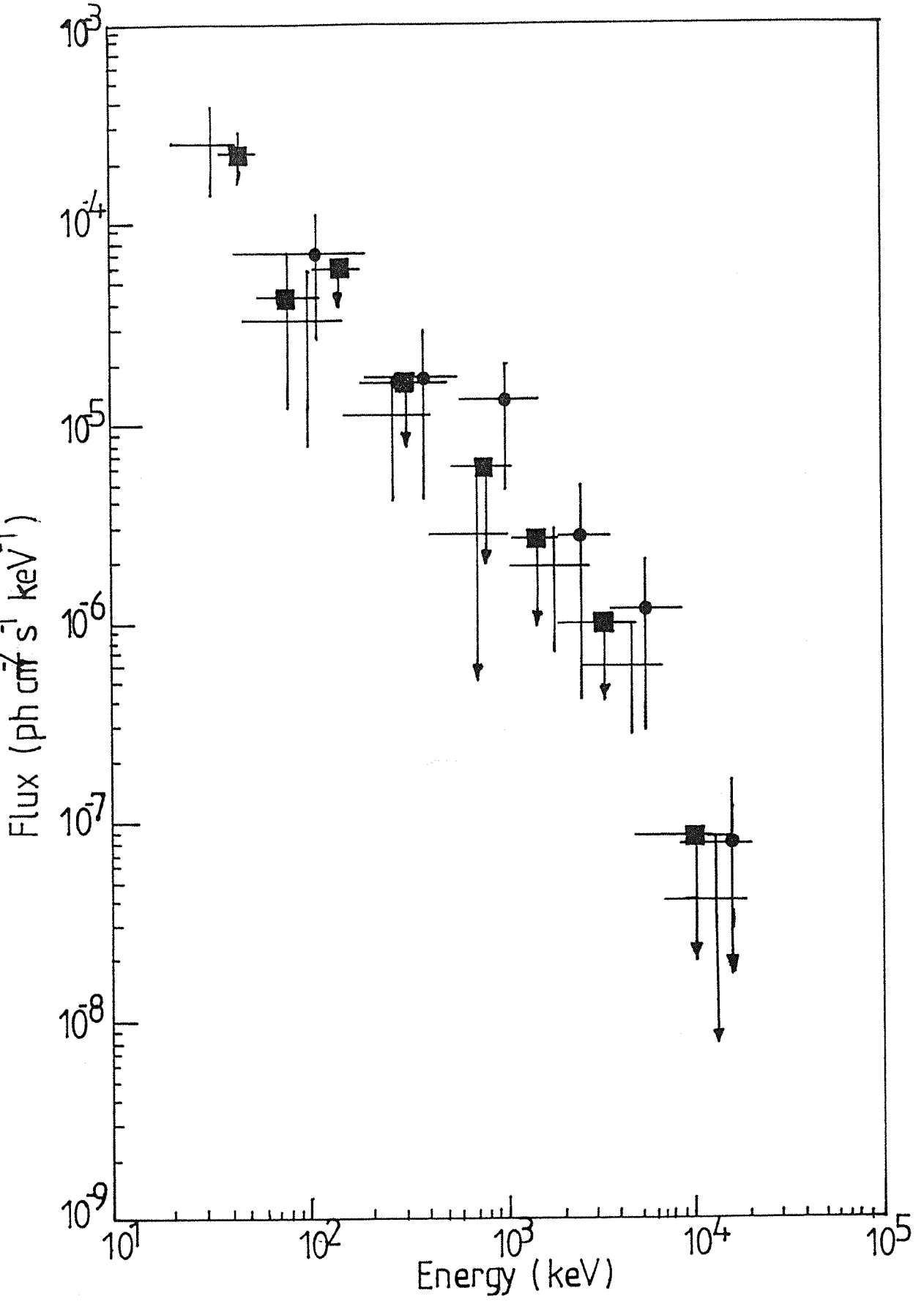

Figure (1.13) The NGC4151 energy spectrum observed by the MISO telescope. (From Boella et al 1984).

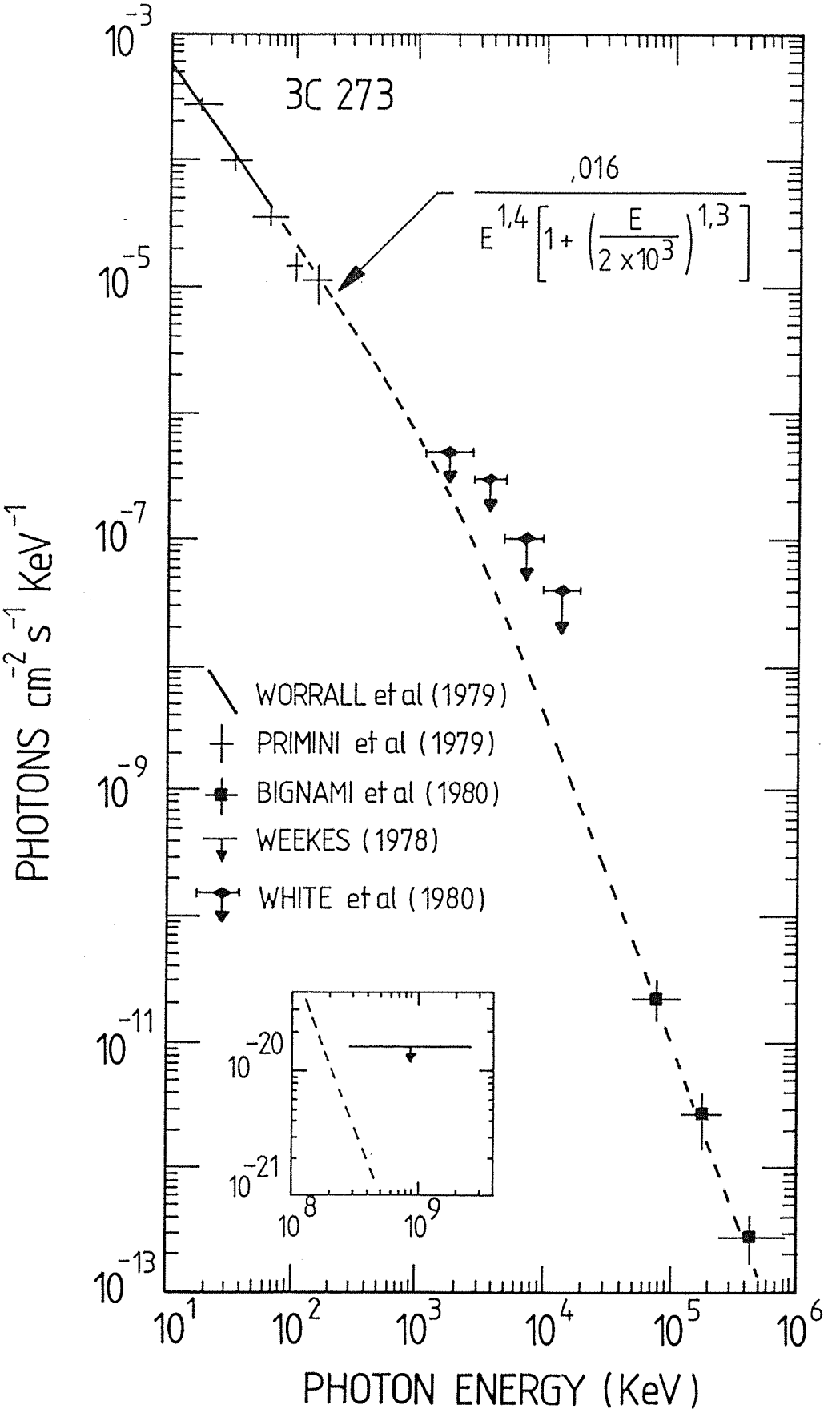

Figure (1.14) The differential high energy photon spectral results from several experiments as a function of energy for 3C 273. The dashed curve is given by the equation shown in the figure.

There is a well known variability of the output at the x-ray energy range of this quasar (Worrall et al 1979) but no variability in flux was observed in the gamma ray energy range according to Cos-B data. This could be due to the fact of sparse gamma ray data.

The Radio galaxy Cen-A is the nearest active galaxy in the sky and is the brightest extragalactic source both at x-ray and radio. It was one of the first extragalactic object to be identified as an x-ray source (Bowyer et al 1970).
Observations show the variability in the intensity of the source also imply changes in the spectral index. The available data indicates that the x-ray intensity of Cen-A has varied by a factor of (5) from 1971-1976. A two fold increase in only (6) days in 1973 was reported by (Winkler and White 1975).
Hall et al 1976 observed Cen-A at energies between 30 keV and 12MeV. Their spectrum was fitted with a power law of (1.9) spectral index. The fascinating thing about this observation was the detection of two gamma ray lines at (1.6)and(4.5) MeV with fluxes of $(3.4\pm1.0)*10^{-3}$ and $(9.9\pm3.0)*10^{-3}$ $ph.cm^{-2}.s^{-1}$. respectively.
Cen-A was observed by the MPI telescope and the spectrum was fitted with a spectral index of (2) as shown in fig.1.15 (Ballmos et al 1987). This spectrum at MeV energies is well connected to the x-ray region with practically constant slope.
Since the upper limit s above (35 MeV) from Cos-B and SAS-2 are so valid, there must be some sort of steepen in Cen-A's spectrum somewhere beyond (20 MeV) in order to meet the upper limits. This spectrum places the maximum luminosity of this galaxy in the MeV range and this provide an interesting question about the size of the source and the radiation mechanism which is involved.
Cen-A has a jet structure at other wavelengths. Since it is close and bright with a large angular extent, it may produce a valuable prototype for the study of possible gamma ray jet structure in active galactic nuclei. The jet structure of this galaxy as seen at x-ray wavelength by the Einstein observatory is shown in fig.1.16.

1.4.2 Cosmic diffuse radiation.

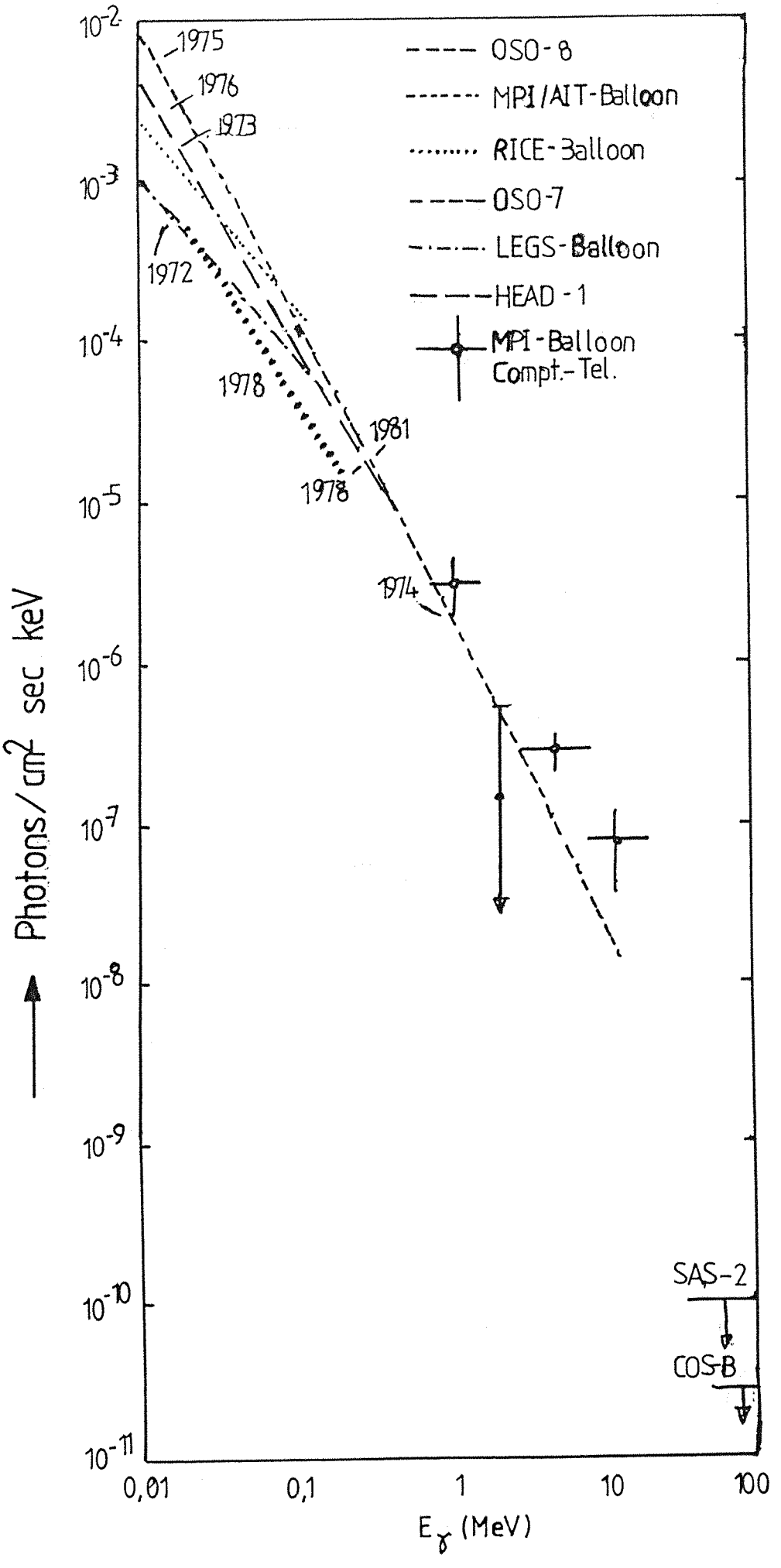

Figure (1.15) The Cen-A energy spectrum given by V. Ballmoos et al 1987.

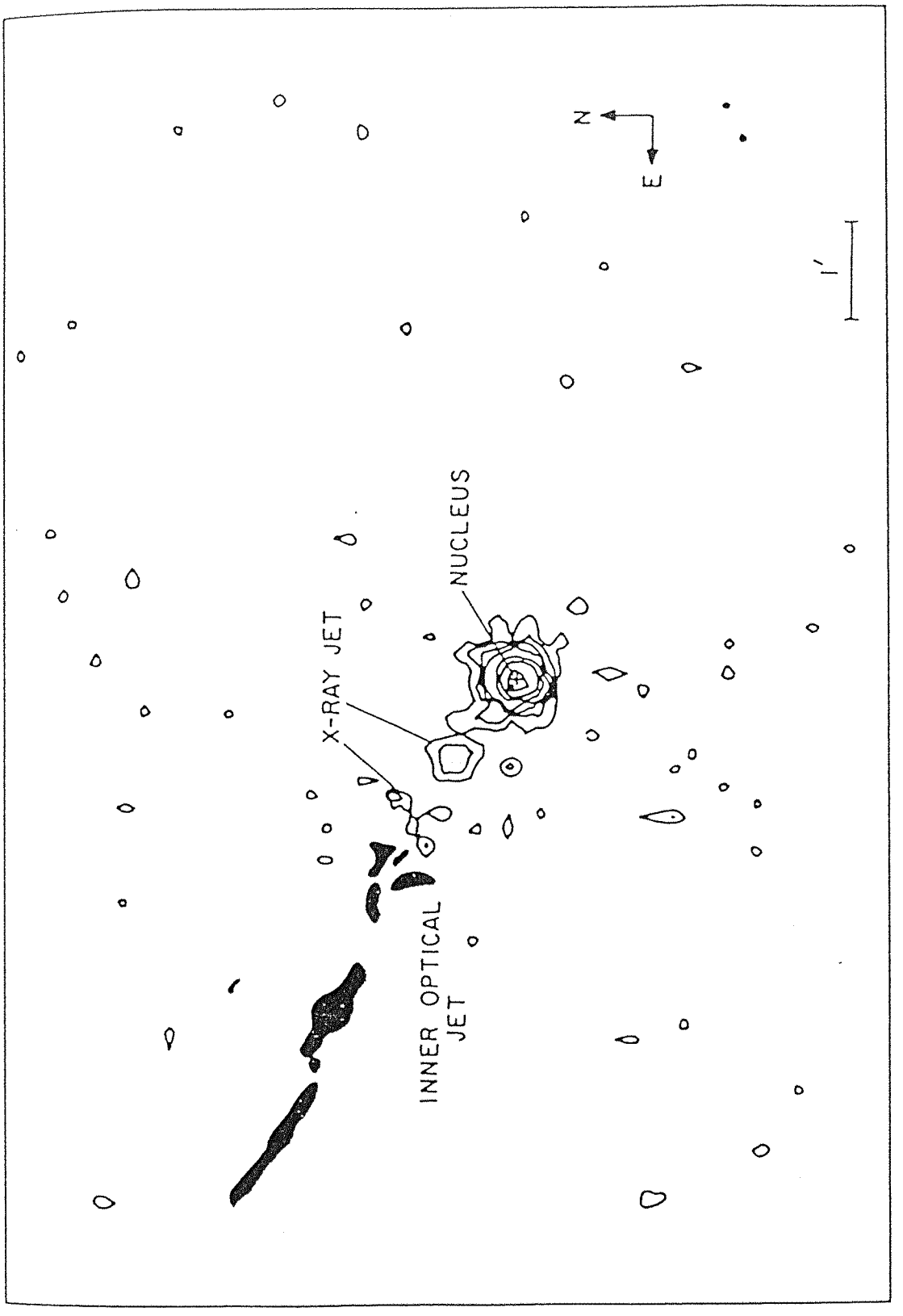

Figure (1.16) A soft X-ray image of Cen-A clearly showing the X-ray jet.

SAS-2 results has provided evidence for the existence of diffuse extragalactic flux. This indicate of high latitude fluxes over the expected contributions of the interaction of galactic cosmic rays with the interstellar medium.

There is no doubt about the existence of extragalactic flux in the x-ray energies and its magnitude is considerable. The gamma ray spectrum can be fitted well to the x-ray data and this is a proof that the gamma rays are from extragalactic origin. Fig.1.17 shows the spectrum of diffuse x and gamma rays (Fictel and Trombka 1981). There is a "bump" around few MeV which has drawn the attention of many astronomers. This feature was first presented by the Apollo satellite observations with a greater magnitude than shown. The reason was due to induced radioactivity in the experiment detection plane. The style of this spectrum ties with the obtained spectrums of NGC4151 and MCG8-11-11 of MISO telescope.

Many authors have put forward suggestion to the interpret the "bump" of the spectrum. Ginzburg 1968 thought that it was due to the decay $(P+P\text{-------}>\Pi^{\circ})$ produced in the universe at early epoch. While Stecker 1969 went further and said that the responsible interaction is $(P\bar{P})$ and not (PP).

Strong et al 1974 provided another explanation which suggest that the bump is due to the interaction of extragalactic origin cosmic rays with the 2.7k microwave background in early epoch.

Finally if cosmic rays were from an extragalactic origin, having the same intensity every where in the universe, a higher gamma ray flux would be generated from their interactions with the extragalactic gas (Said et al 1982). Therefore it is very likely that cosmic rays are generated in active galaxies in clusters.

A gamma ray telescope with good angular imaging capability may help to confirm the origin of this diffuse flux.

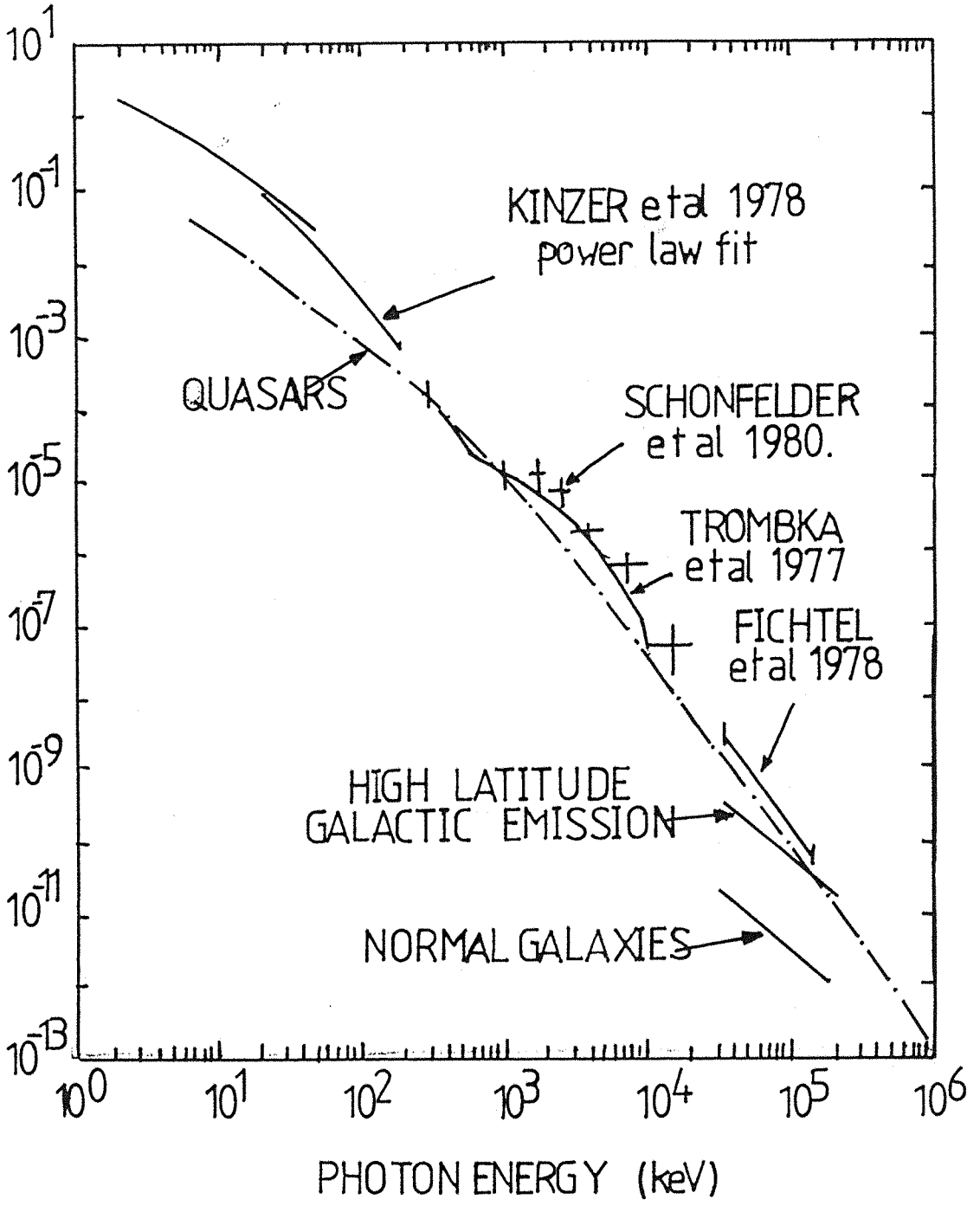

Figure (1.17) The estimated diffuse gamma-ray spectra for quasars and normal galaxies compared with some experimental data from (Fichtel and Trombka 1981).

Chapter 2

2 A review of the instrumentation techniques used in low energy gamma ray astronomy

2.1 Introduction

In this chapter the design of experiment for low energy gamma ray astronomy is considered. Also the instrument background has been discussed since they play a major role in the overall consideration of any experiment. The determination of the background level is an extremely foreboding task for the prediction of the sensitivity of the telescope. Therefore it is important to discuss the factors that contribute to the overall background level of any experiment in this particular range of the electromagnetic spectrum.
The development of the techniques used in detecting low energy gamma rays since the early days up to date are also discussed.

2.2 The contributions to the background level of low energy gamma ray telescopes

The main problem in detecting the considerably weak flux of gamma ray sources, is the pretending of the atmosphere to be a gamma ray source itself. This source of background is due to the interaction of cosmic radiation with the atmosphere. Also the atmosphere works as an attenuator for the gamma ray photons. To achieve any significant astronomical measurements, these problems and other factors that contribute to the total background level must be well considered before. All these factors are discussed in the following sections.

2.2.1 Cosmic diffuse gamma rays

The cosmic background flux given by (Vedrenne, 1978) can be expressed by :

$$D(E) = 87.4\ E^{-2.3}\quad ph\ cm^{-2}\ s^{-1}\ keV^{-1}\ sr^{-1} \qquad (2.1)$$

This only if the doubtful bump at MeV energies is ignored. Schonfelder et al 1980 support the existence of this bump. According to Schonfelder, the spectrum above 5 MeV is very steep (namely E^{-3}). At lower energies, the data is in good agreement with the SAS-2 measurements (fig.2.1).
The cosmic diffuse flux contribute to the background level in two ways. firstly, photons that enter the unshielded entrance aperture of a telescope and interact in the main detection plane. Secondly, photons that pass through the shield without interaction and reach the detection plane depositing their energies. In the case of a collimated telescope, the major contribution will be due to the second mechanism.
For a balloon-borne gamma ray telescope, the contribution of the cosmic diffuse background to the total background level is of secondary importance. This is mainly due to :

(i) The cosmic diffuse gamma rays are attenuated by residual atmosphere above floating altitudes.
(ii) The earth atmosphere is a bright source of diffuse photons which swamp the cosmic photons.

2.2.2 The vertical atmospheric radiation

The earth atmosphere is an intense source of gamma rays resulting from the interaction of cosmic ray particles with the surrounding gas. The vertical atmospheric component has been calculated by (Schonfelder et al 1980)(fig.2.2) and can be represented by :

$$F_\gamma = (6\text{-}1)*10^{-3}\ E^{-(1.65-0.15)}\quad ph\ cm^{-2}\ s^{-1}\ MeV^{-1}\ g^{-1}\ sr^{-1} \qquad (2.2)$$

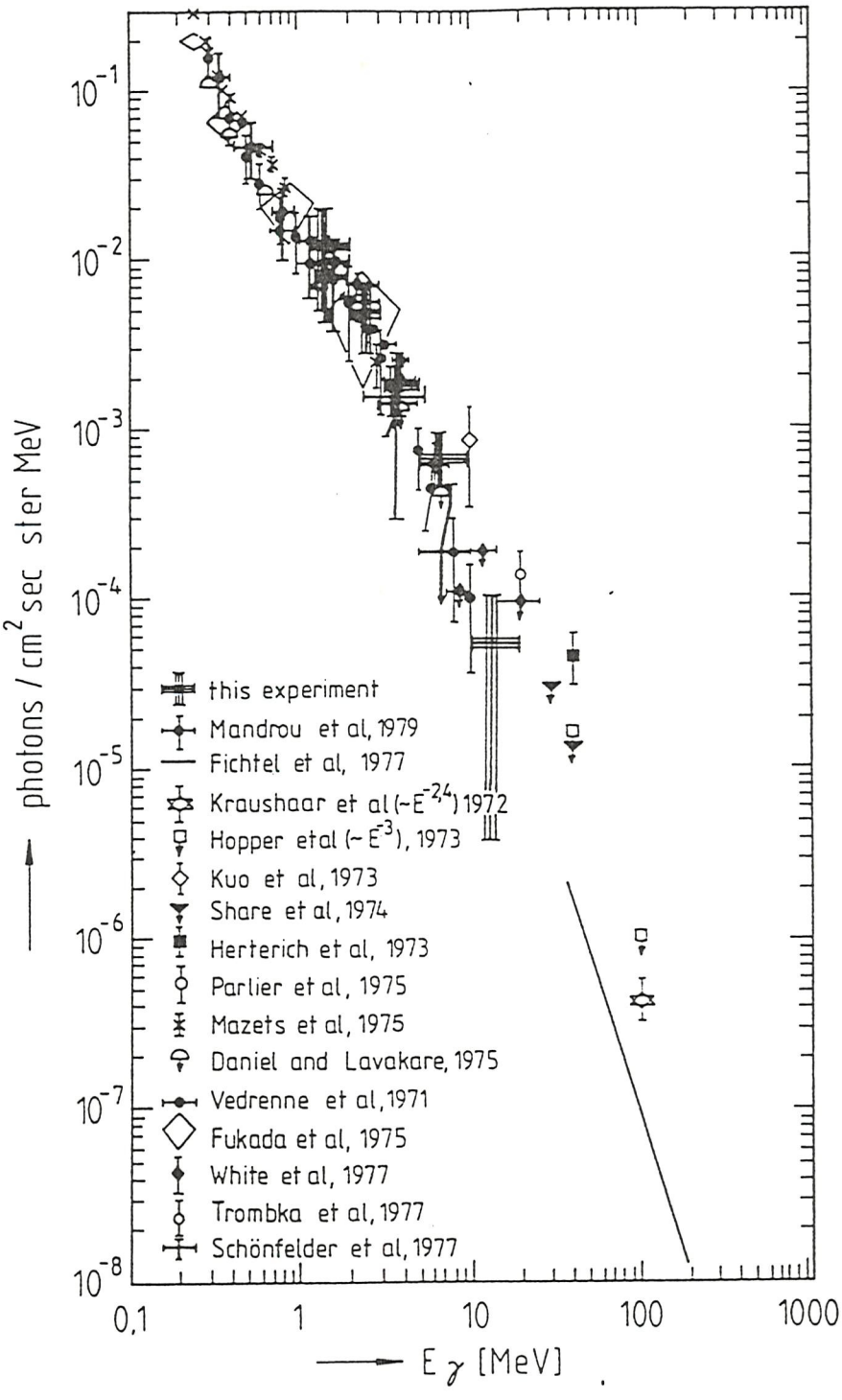

Figure (2.1) The spectrum of the diffuse cosmic gamma-ray component. (From Schonfelder et al 1980).

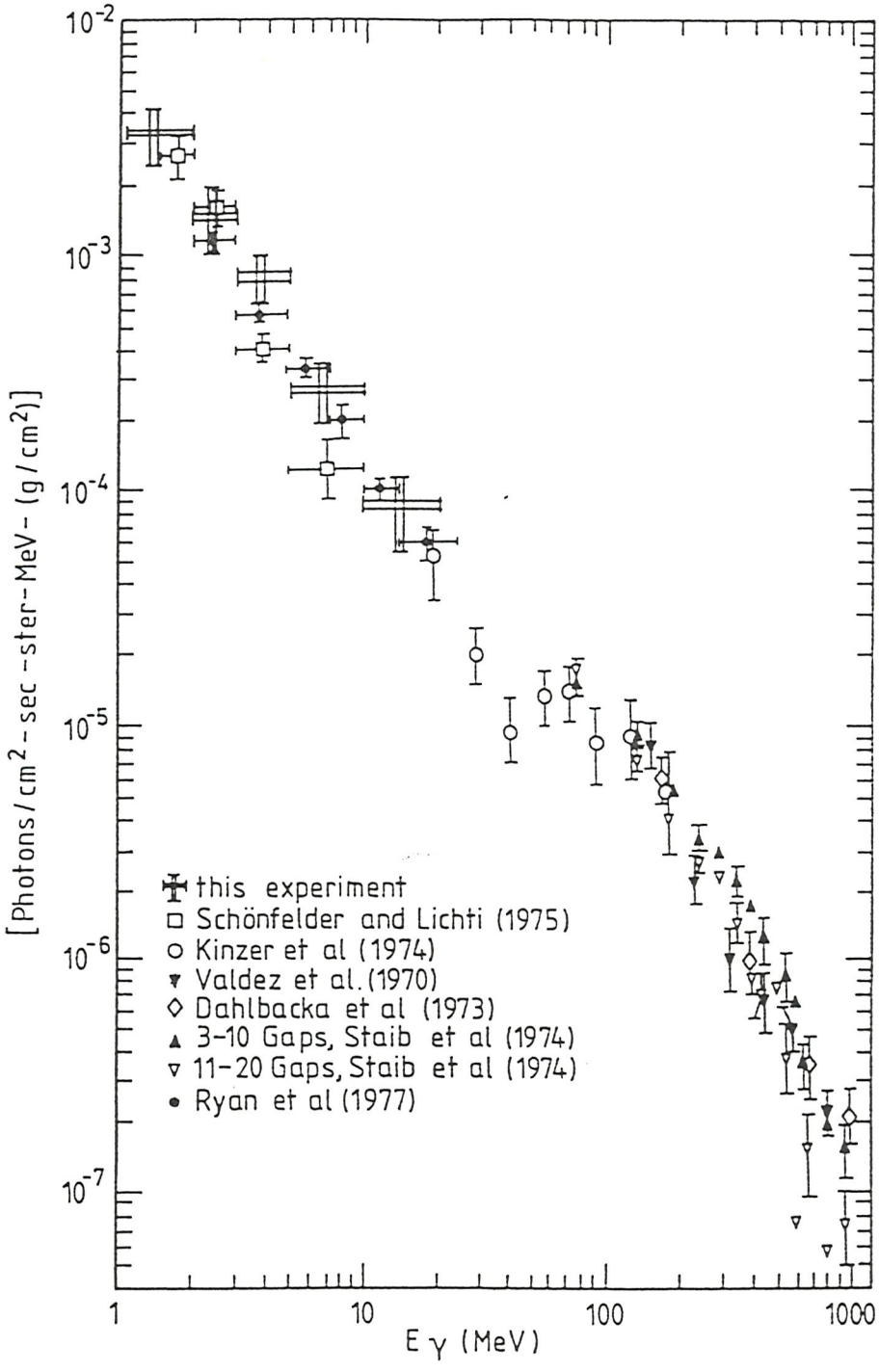

Figure (2.2) The spectrum of the vertical atmospheric gamma-ray component from Schonfelder et al 1980.

At energies above 50 MeV, this background is due to the decay of Π° produced by nuclear collisions of cosmic ray particles in air. Below this energy, the background is dominated by the bremsstrahlung of relativistic electrons (Beuermann 1971).
These undesired photons contribute to the background level of any balloon or satellite experiment. Their presence effect any astronomical measurements by reducing the sensitivity of the experiment and also increase the uncertainty in the evaluation of cosmic diffuse background spectrum.

2.2.3 Neutron induced background

Background events are generated by the interaction of cosmic rays with atmospheric nuclei. This process will rise a flux of neutrons. In this section, the background derived from the interaction of these neutrons through the body of the spacecraft is discussed.
There are two ways that neutrons can deposit their energies in the detection plane.
Firstly, they can be absorbed by the ^{127}I or ^{23}Na nuclei of the NaI crystal. Most of them undergo radiation capture at the ^{127}I nuclei since it has a larger cross-section of neutron absorption than the ^{23}Na. Also the ^{128}I product has a half-life of 25 min. comparing with the 25 hours of the ^{24}Na product which never reach equilibrium in a typical balloon flight. Therefore, gamma ray photons can be created via the reaction :

$$^{127}I\ (n,\ \gamma)\ ^{128}I \qquad (2.3)$$

Many gamma ray energies, and their extensive interactions, have been recorded by (Archer et al 1966).
Secondly, neutrons can undergo inelastic scattering at ^{127}Inucleus and cause background events. The two lowest levels of ^{127}I to be excited by this effect can contribute in the emission of gamma rays at (58, 203) keV energies.

2.2.4 Spallation induced background

This source of background events is derived from the interaction of high energy cosmic ray protons with the detection plane of the experiment resulting spallation products. An energy spectrum, for energies below 10^5eV, can be approximated to the following form :

$$N(E)\,dE \;\alpha\; E^{-2.6}{}_p\,dE \qquad (2.4)$$

where E_p is the energy of the proton. Generally, the veto pulse are made as long as possible to reduce these type of events. However, this cannot eliminate all these undesired events since the time associated with most of these photons are longer than the veto pulse.

An estimation of this background level has been reported by (Baker et al 1979) using a beam of 2GeV protons for irradiating the detection plane for a typical flight period. Two main period were apparent for the decay of spallation products of half-lives roughly (17 and 53) min. . The first product is probably comes from the contribution of the isotopes ^{119}I(19min.), ^{120}Sb(15.9min.) and ^{116}Sb(15min.). The second product may come from the contribution of ^{120}I(80min.), ^{117}Te(61min.), ^{116}Sb(60min), ^{121}Xe(38.8min.)and^{115}Sb(31min.).

2.2.5 Locally produced gamma rays.

The interaction of cosmic rays with the body of a spacecraft generate gamma ray photons as well as neutrons. These photons penetrate the rest of the spacecraft, the anticoincidence system then interact in the detection plane. Measuring this background level is not an easy task and depends on the geometry of the spacecraft. However, the total number of photons produced by this process is smaller than the contribution of the cosmic diffuse component.

2.3 Methods of detecting gamma ray photons

Low energy gamma ray photons are detected mainly by using either scintillation counters or solid state devices on which electrons are ejected when photons are interacting the material of the detectors. In our region of interest, the main mechanism that dominate this interaction is the Compton effect regardless the type of material used for the detectors (fig.2.3).
Telescopes designed for the detection of gamma rays have problems regarding measuring the direction of motion for the photons. Also photons may suffer few Compton scattering before coming to rest and soon their original direction of motion is lost. Therefore design of telescopes directional sensitive is not an easy task.
The cross-section for Compton effect is not very large and to achieve an efficient experiment, a massive detection plane is required which is mechanically is not highly desirable for many reasons.

2.3.1 Scintillation counters

There are three main process that a gamma ray may experience while interact on a scintillator detector. These are the photoelectric effect, Compton scattering and pair production. By any of these mechanisms, the photon lose part or entire energy in the scintillator. This energy will be converted to high energy electrons and subsequently the crystal suffer ionization by the movement of electrons through it. These detectors are normally viewed by photomultiplier tubes or diodes which produce large pulse of electrons. The materials that available as scintillators are either inorganic like NaI and CsI crystals or organic like plastic scintillators. Chosing the type of scintillator is highly dependent on the objective of the experiment.
The coupling of photomultiplier tubes to the scintillators are of great importance since it effects the energy resolution of the detector. Three different ways are employed (fig.2.4) for this purpose :

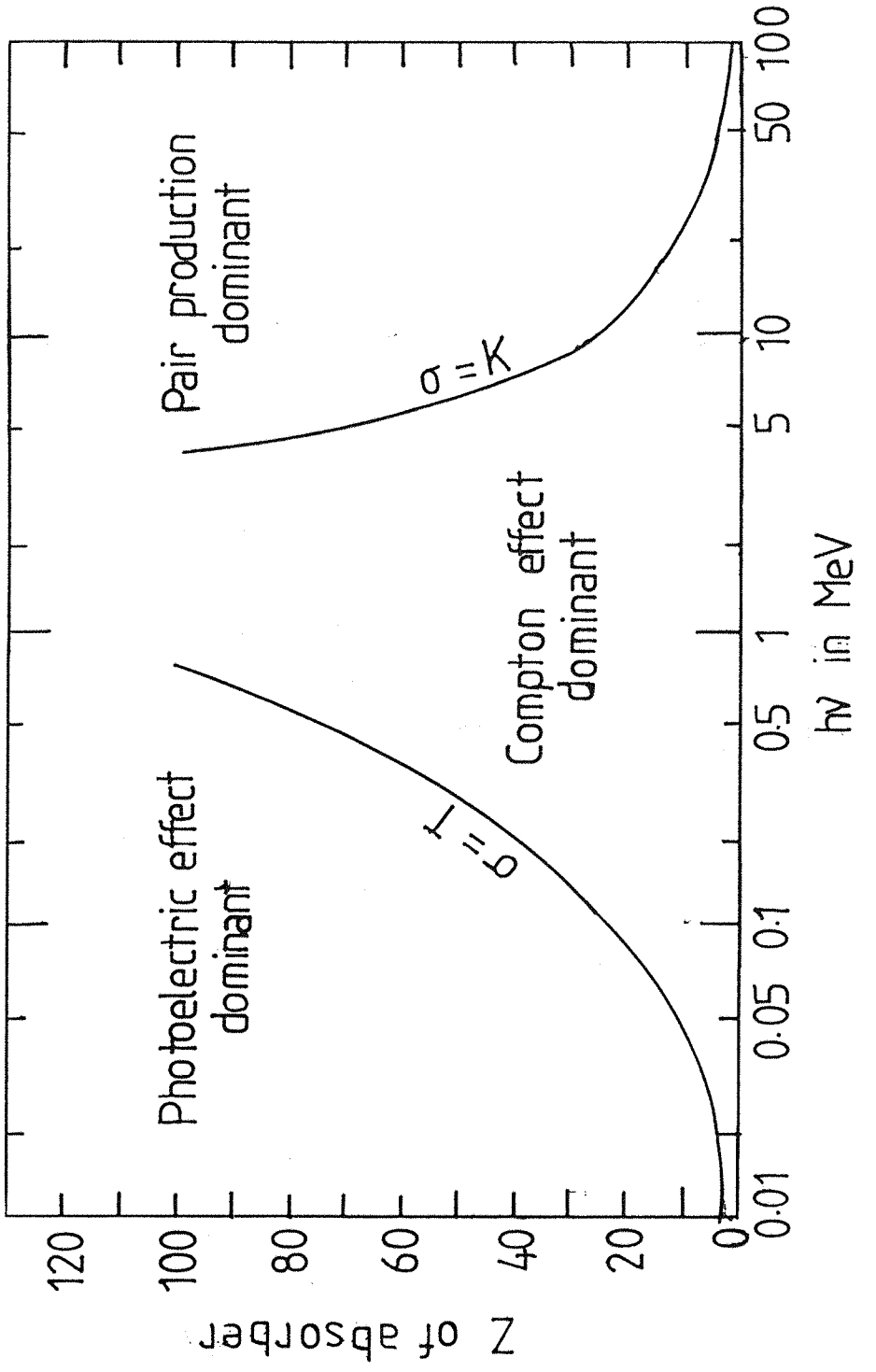

Figure (2.3) The major forms of gamma matter interaction as a function of gamma-ray energy and atomic number of the involved material. (From Evans 1955).

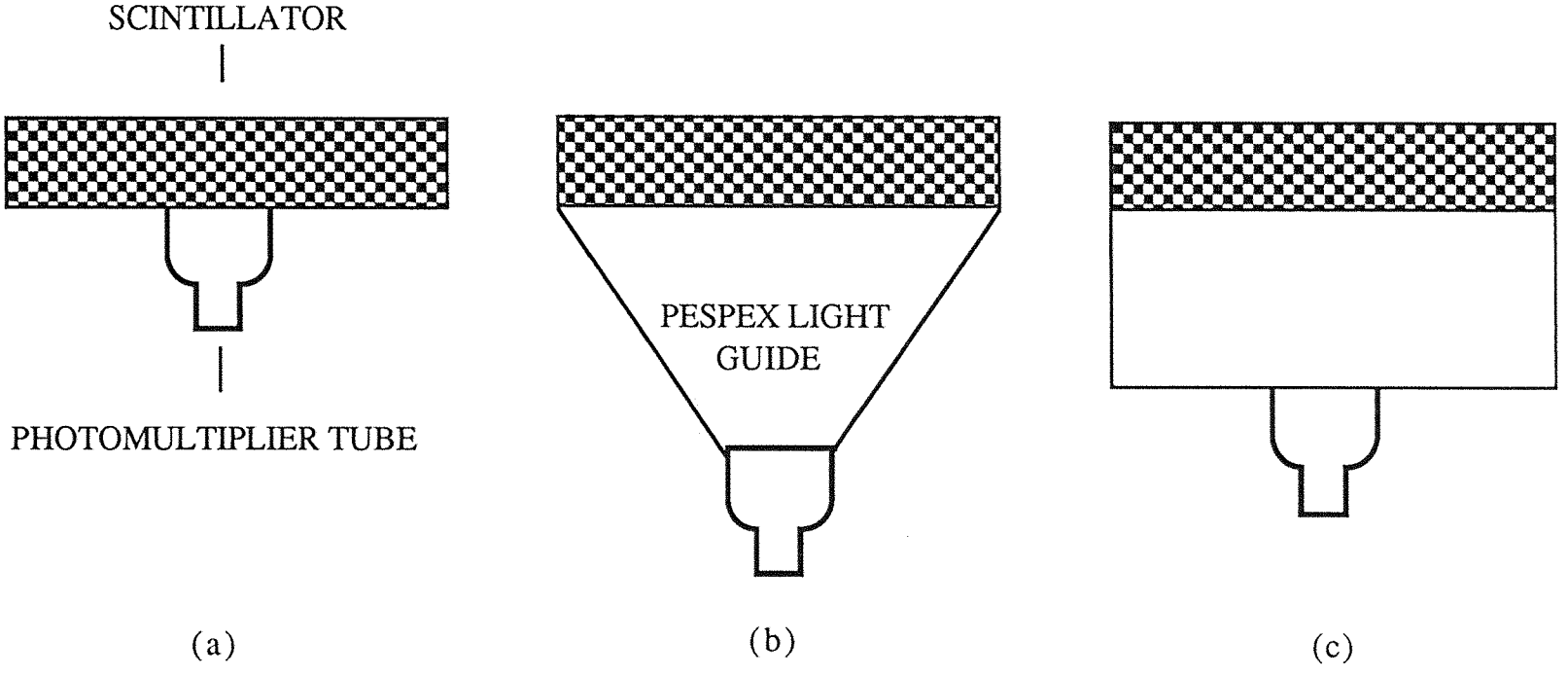

Figure (2.4) Different methods of optically coupling a photomltiplier tube to a large scintillator: (a)direct coupling;(b)coupling through a Perspexlight guide;(c)coupling through a diffuse light box (from Hillier,1984)

1. Optical contacts.
2. Light pipes.
3. Diffuse light boxes.

The first option is excellent when the size of the crystal is rather small. In this case, the efficiency of the light collection by the photomultipliers is high (roughly 90%). When the size of the crystal is large, uniformity of light collection by the tube will become more difficult. In such circumstances, the second and third methods are used. The second method provides high uniformity of light collection but the mass of the light guide is a matter of concern. While the third method provides a uniform light collection but with much less efficiency.

2.3.2 Solid state detectors

This type of detectors are used when energy resolution has got priority than other characteristics such as efficiency. Mainly, solid state detectors are constructed from Lithium drifted Germanium or Silicon. One of the disadvantages of these detectors is to be operated at low temperatures to get maximum energy resolution. Germaniums are used more since they have a high atomic number which means a higher cross-section for photoelectric absorption.
In this type of detector, photons lose their energies in the form of electron-hole pairs. The number of these carriers are fairly high but the total collected charges are not. Therefore, charge amplifiers with high gain and low noise must follow the detectors. The noise of these amplifiers are dictating the energy resolution of the detectors which are in the range of 3keV.

2.4 Development of low energy gamma ray telescopes

One of the most effective method for reducing the ambient background level is to shield the detection plane from this type of particles. It is highly desirable to chose such material that has a high cross-section of interaction for these particles. In the following section, a review for the past and present techniques employed in the design of low energy gamma ray telescopes is presented.

2.4.1 Unshielded detectors

The major problem in employing unshielded detectors is the very high counting rate recorded by the detectors and the very small signal to noise ratio expected from a gamma ray source. An example of this type of detector is the experiment constructed at Bristol University (Sale 1970)(fig.2.5). The purpose of the experiment was to measure gamma ray emission from pulsar. This technique was soon followed by shielded detectors.

2.4.2 Passively shielded detectors

As it was discussed in the beginning of this chapter, the major problem in designing gamma ray telescopes is the background flux produced by cosmic radiation.
Passive shielding is treating this problem by surrounding the detection plane with massive inert material, such as lead, because of its high stopping power for gamma ray photons.
An example of this kind of shielding is the LEG1 telescope of Southampton University (Lovett 1973). In this experiment it was found that the background counting rate, with the existence of the passive shield, is higher than without it. This is due to the fact that when the shield is exposed to cosmic rays and neutrons, it becomes itself a bright source of undesired gamma rays, neutrons and β particles. Also genuine gamma rays may suffer Compton scattering before depositing their energies on the detector giving false information about their origin.

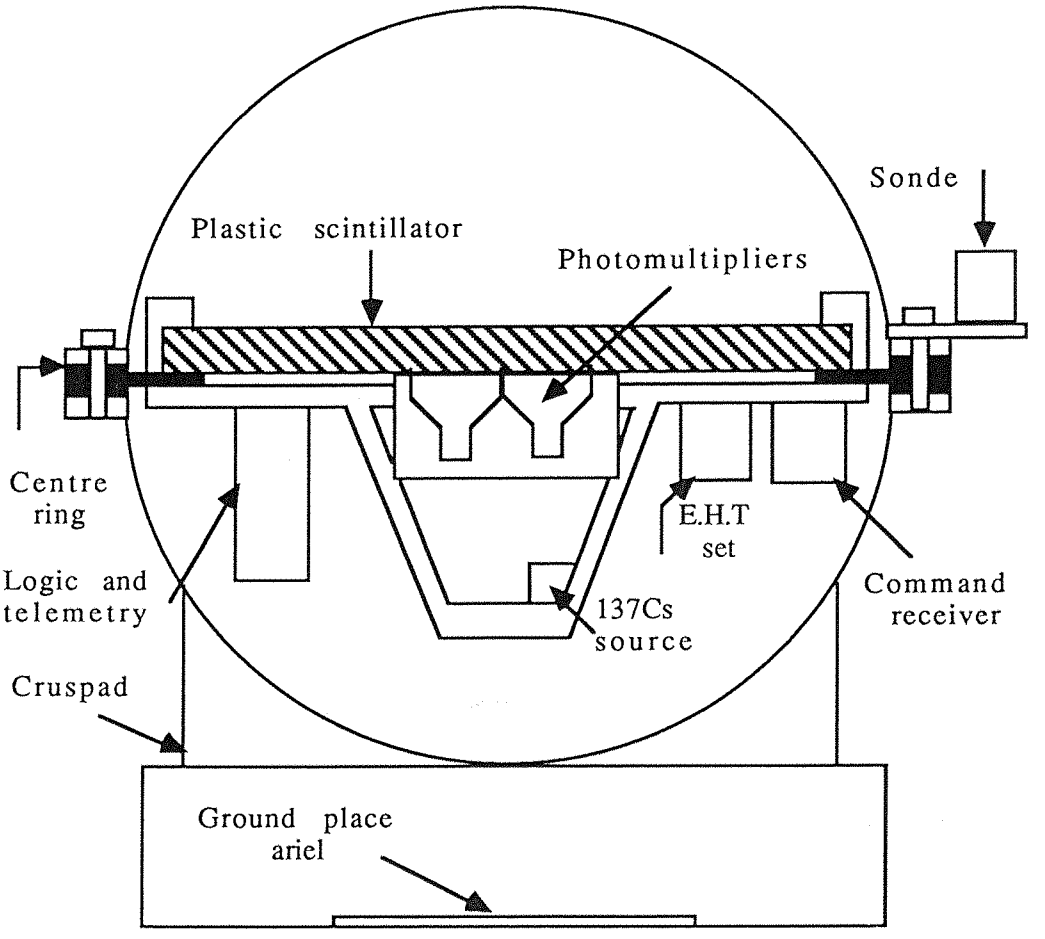

Figure(2.5) A schematic diagram of the unshielded counter built at Bristol University to measure gamma ray emission from pulsars (from Sale 1970)

2.4.3 Actively shielded detectors

The background generated on the central detector due to the existence of passive shield can be tremendously reduced if the shield itself consist of a detector works in anti-coincidence with the central detector. This technique is known as "Active shielding". The only disadvantage of this method is the high cost of the shield rather than its weight.

One of the early examples of actively shielded experiments is the telescope built by the Rice University group (Walraven et al 1975, Johnson and Haymes 1873). This experiment was designed to operate in the 56keV-12MeV energy range. It consist of a central NaI(Tl) detector surround by an active collimator with a field of view of 15° F.W.H.M.. A thin plastic scintillator which covers the aperture complete the shielding and protect the central detector from undesired particles. The shield operates in anti-coincidence with the central detector. A schematic diagram of this telescope is shown in(fig2.6).

2.5 Current techniques employed in low energy gamma ray telescopes

2.5.1 Compton telescopes

This type of technique used in the design of low energy gamma ray telescopes utilizes the Compton scattering process. Usually it consists of two levels of detectors separated by some distance. The basic principle is illustrated in (fig.2.7). An identified photon is the one undergo two interactions in both detectors (Schonfelder et al 1982).

The gamma ray photon with energy E_γ suffers Compton scattering in the upper detector transferring the energy E'_e to an electron. When the scattered photon with energy E'_γ interact on the second

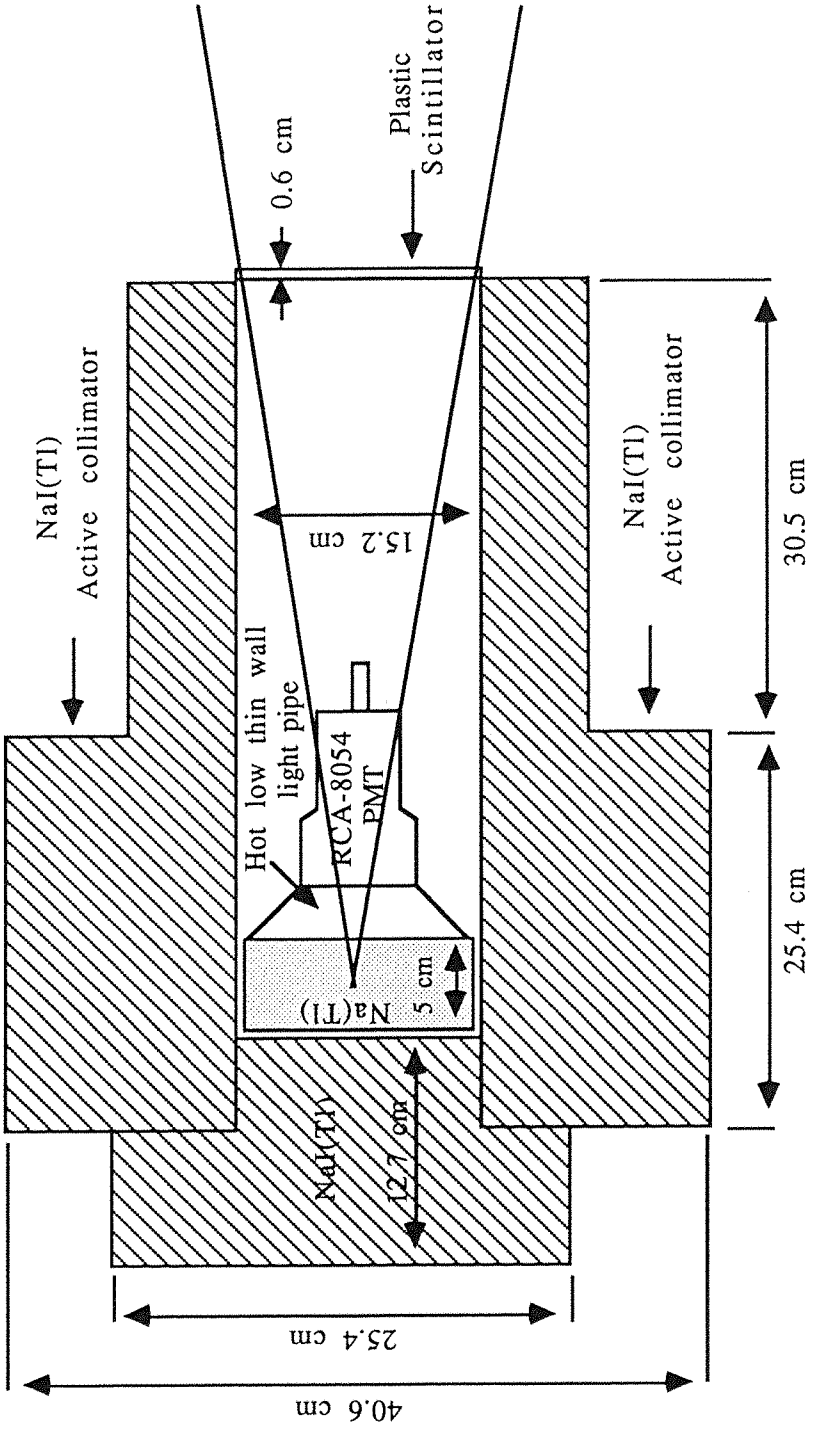

Figure(2.6) A schematic diagram of the actively collimated gamma ray detector built by the Rice University group (from Walraven et al 1975)

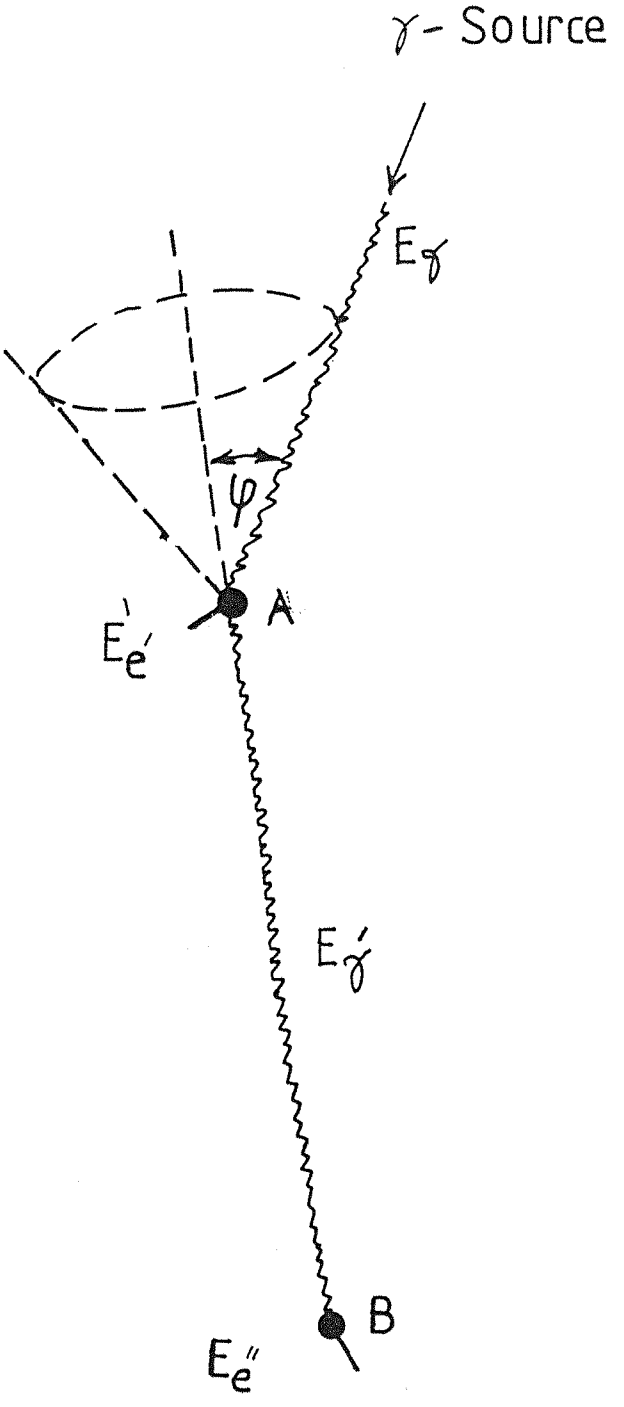

Figure (2.7) Principle of measurement in a Compton telescope.

detector losing E''_e energy. Measuring E'_e and E''_e can lead to the identification of the two parameters $\overline{E_\gamma}$ and $\overline{\Phi}$:

$$\overline{E_\gamma} = E'_e + E''_e \qquad (2.5)$$

$$Cos\ \overline{\Phi} = 1-(\frac{m_o c^2}{E''_e}) + m_o c^2.(E'_e+E''_e) \qquad (2.6)$$

If the scattered photon is totally absorbed in the second detector, then ($E_\gamma \equiv \overline{E}_\gamma$) and ($\Phi \equiv \overline{\Phi}$) which are the energy of the incident photon and its scattering angle. Under such circumstances, the location A and B are also known and the arrival direction of the incident photon is lying on the surface of a cone with an angle of 2Φ. This cone surface is called the "Circle Event". Therefore it is possible to draw a circle for each event. All totally absorbed gamma ray photons will intersect and this define astronomical source position.

2.5.1.1 MISO telescope

A schematic view of the Milan-Southampton telescope (MISO) detector is shown in (fig2.8). The central detector consist of a liquid scintillator (NE311) as the top detector (S1) and a large (NaI) crystal as the bottom detector. These detectors are completely surrounded by a plastic anticoincidence jacket (A1) and separated by an independent anticoincidence counter (A3). S1 and S2 are roughly 27cm in diameter, 10cm thick and separated by a distance of 3cm. The top detector S1 provides the target for the incoming photons to scatter at. Then the scattered photons interact in S2. A full description of the telescope is given by (Baker et al 1979). The presence of the anticoincidence detector A3 plays a major role in vetoing the charged particles passed from S1 to S2.
The central detection system is semi-actively shielded from atmospheric gamma rays by a sandwich of lead/plastic scintillator A4 and A5. A slatted lead collimator situated inside this intense

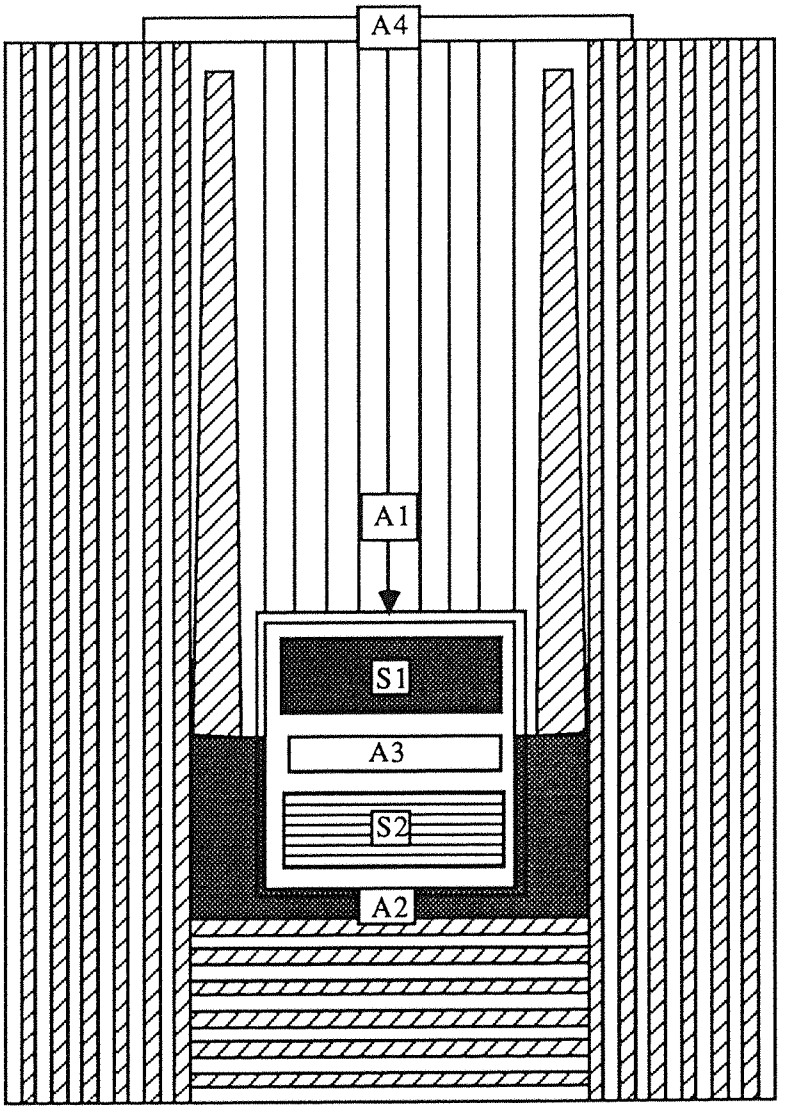

Figure(2.8) A schematicview of the MISO telescope built by the Anglo-Italian collaboration; ☐ Plastic, ▩ NE 311, ▤ NaI, ▨ Pb (from Boella et al 1984)

semi-actively shield, provide an angular resolution of 3°*3° F.W.H.M..

The bottom half of the central detection system is surrounded by a shell which contains a mixture of boron, tungsten and lithium set in a wax moderator to absorb unwanted neutrons. The complete Compton coincidence signature is :

$$S1.S2 \quad (A1+A2+A3+A4+A5) \qquad (2.7)$$

It is expected that this system will increase the sensitivity and decrease the background level of the telescope. The threshold of S1 and S2 are set to 25 keV and 150 keV respectively. This enable the system to respond to photon events that deposit energy in the 0.2-20 MeV range.

This experiment was successfully flown from Palestine, Texas(U.S.A.) in May1977, October1978, September1979 and finally May 1980. During these flights many galactic and extragalactic sources were observed. A full catalogue of this data is given by (Boella et al 1984).

2.5.1.2 MPI telescope

Max-Plank-Institute telescope (MPI) is a low energy balloon borne Compton telescope designed to perform in the energy range (1-20)MeV. The early version of this telescope was flown in 1973 and 1974 (Schonfelder and Litchi 1974, Sconfelder et al 1977) aiming to investigate the diffuse cosmic and atmospheric gamma ray components.

The telescope consists of an array of low-Z material organic liquid scintillator (NE213) as the top detector and a high-Z material NaI(Tl) as the bottom detector(fig.2.9). The two detectors are separated by a distance of (1.2 m.). The liquid scintillator and the NaI planes consist of 16 cells of (15*15*15cm.) and 32 blocks of (15*15*7.5cm.) respectively. Each unit is viewed by a photomultiplier tube. The two detector assemblies are surrounded by an anticoincidence shield of plastic scintillator (NE110). For the purpose of calibration, two radioactive sources are located between both detector

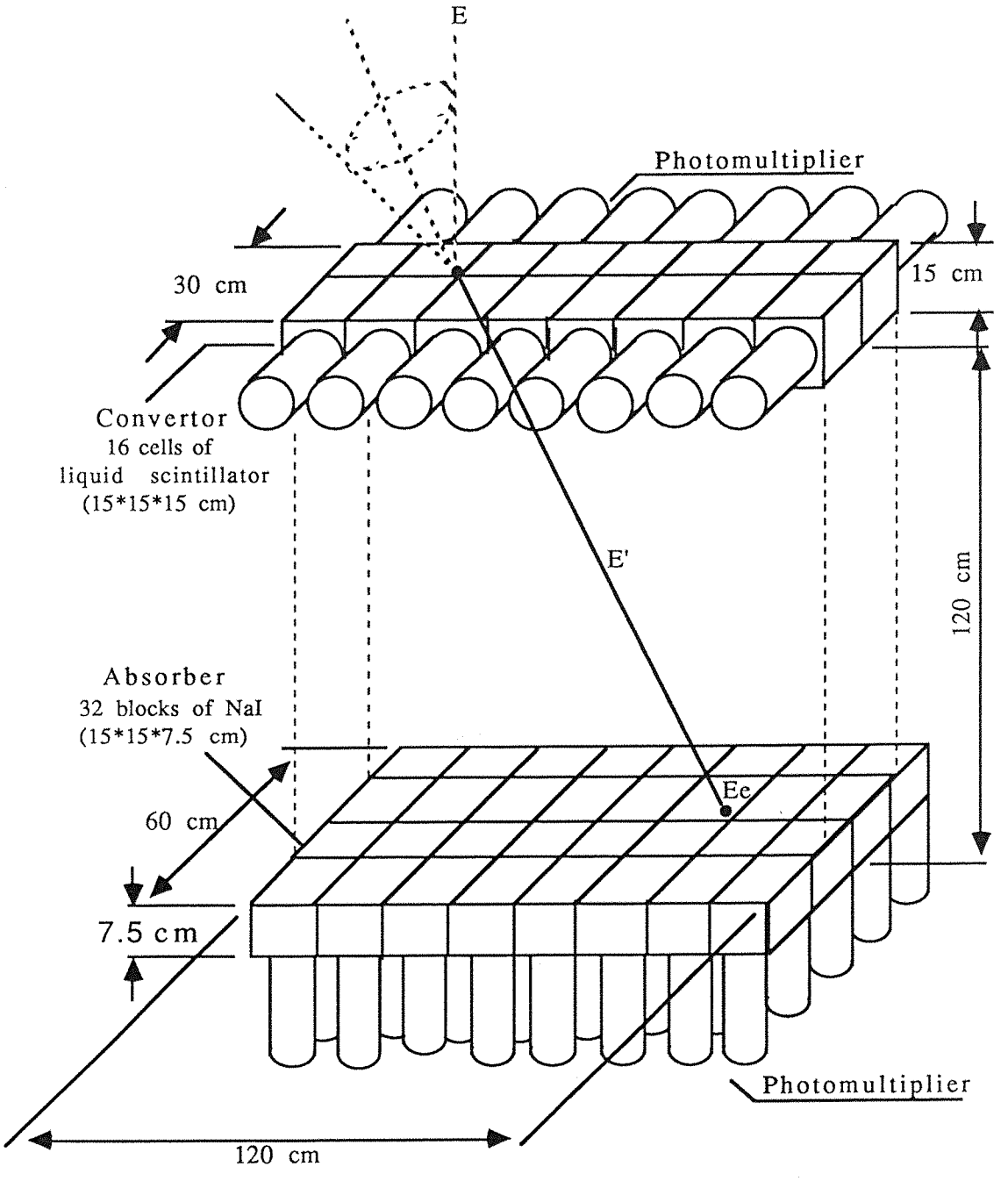

Figure(2.9) A schematic view of the Compton telescope of the Max-Plank Institue (from Schonfelder et al 1982)

assemblies outside the beam of scattered gamma rays. A detailed description of this experiment is given by (Schonfelder et al 1982). For each event the following parameters are measured :

(i) Energy of Compton electron in the top detector (E'_e).
(ii) Energy loss in the bottom detector (E''_e).
(iii)Location of scattering event in both detectors (triggered units).
(iv)The pulse shape of the photomultiplier tube pulse in the top detector.
(v) Time-of-flight of the scattered gamma ray photon from the top to the bottom detector.
(vi) Absolute time of the event.

The pulse shape and the time-of-flight measurements are performed in order to reject background events. The quantities E'_e, E''_e and the interaction position of the photons in both detectors determine the energy and angular resolution of the telescope.
It was suggested by (Grumplinger and Schonfelder 1979) to apply the Anger camera principle to locate the interactions in both detectors due to the rather overall poor angular resolution of the telescope. This suggestion was eventually applied and an updated version of the telescope is described by (Diehl 1988). This new version was selected to be one of the four experiments on board NASA's gamma ray observatory (GRO) satellite due to launch early 1990s. The other three experiments are the EGRET, OSSE and BASTE.
Finally, the Compton telescope method which has been pioneered by the Max-Plank institute group in the early 70s has been a success in this branch of astronomy.

2.5.2 Coded aperture masks

Coded mask imaging systems can be considered as an extension of the pin-hole camera in which a coded mask plane that contain transparent and opaque regions used instead of a single hole. This technique was originally introduced by (Dicke, 1968) and (Abbles, 1968) are capable of achieving the best angular resolution in the

range of interest. The mask is positioned some distance away from a position sensitive detection plane. A point source cast a shadow of the mask pattern on the detection plane. The data can be deconvolved and an image of the source can be reconstructed. A full description of coded mask imaging is given in chapter 3.

2.5.2.1 ZEBRA telescope

The detection plane of this imaging telescope is constructed from an array of NaI(Tl) crystal elements each viewed by two photomultiplier tubes. A similar array of NaI crystals are positioned underneath serving as the anticoincidence system. Chapter 4 is designated to a full description of the telescope.

2.5.2.2 GRIP telescope

This gamma ray imaging payload (GRIP) experiment is a balloon borne telescope designed to operate in the energy range of (30keV-5MeV). The telescope features a rotating hexagonal coded aperture mask and a thick NaI scintillation camera.
A schematic view of the telescope is given in (fig2.10). The shielded detection system is separated from the mask by (2.5cm.). The detection plane consist of a NaI camera plane (41cm.) in diameter and (5cm.) thick. This detector is viewed by nineteen (3 inch) photomultiplier tubes which are individually pulse height analyzed. The shielding system consist of (12) plastic scintillator modules which form a cylinder (roughly 16cm. thick) surrounding the whole detection system. Each module is viewed by a (5 inch) tube. The bottom part of the NaI camera is shielded by an identical NaI camera. An ^{241}Am source is fixed 1m. above the coded mask for calibration purposes.
The mask is made of lead hexagonal (2cm.) thick and (2.5cm.) across (flat-to-flat) cells mechanically supported by a honeycomb structure. The mask consists of 1000 opaque and 1000 transparent cells.
During observation, the mask is continuously rotated to impose a time modulation of gamma ray signals at each location of the detector. Since the mask pattern is not symmetric, rotation of the

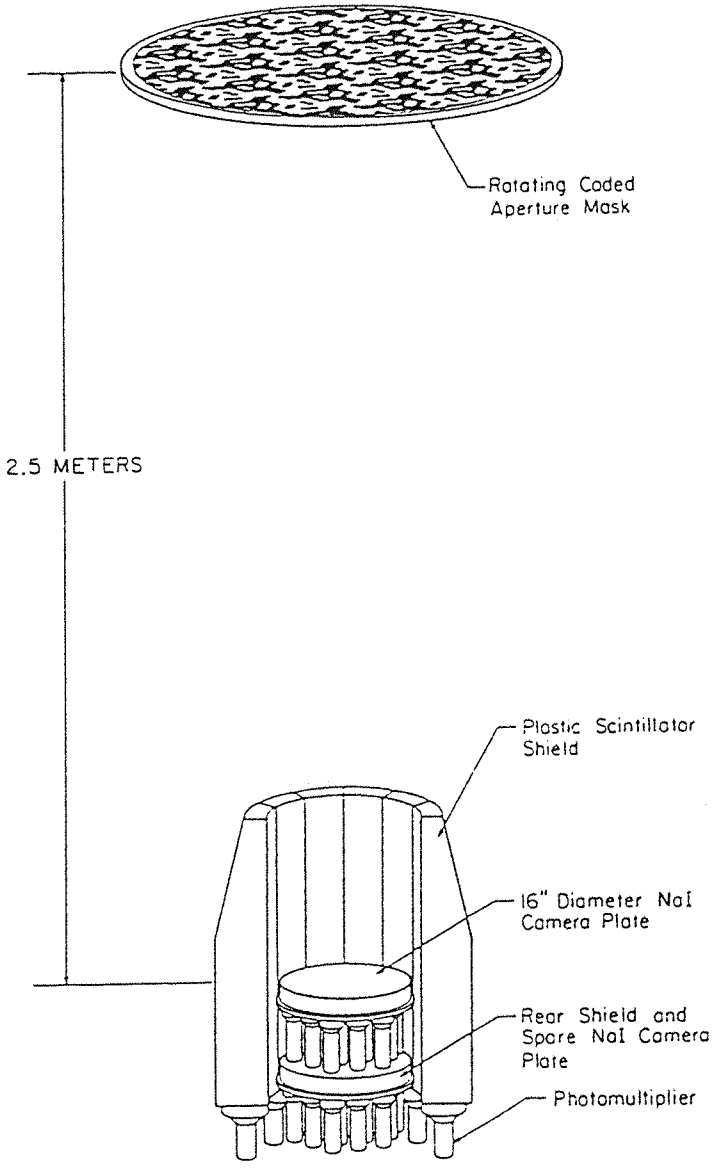

Figure (2.10) The GRIP telescope .

mask under (60 degree) allows the gamma ray signal at each detector position to be modulated with a 50% duty cycle. This leads to a total background subtraction every (20 sec.) assuming that the mask is rotated with (1rpm) rotation rate. Continues rotation of the mask is also extending the field of view to 20 degrees which automatically increase the number of pixels imaged by a factor of (10). The parameters of this telescope is given in table (2.1) and a full description of the telescope is given by (Althouse et al 1985) and (Althouse et al 1987).

This experiment was flown for the first time on October 1986 from Palestine, Texas (U.S.A.). The first observation program was including the Quasar 3C273, the galactic centre, the Crab and Cygnus region (Althouse et al 1987).

Table 2.1 The GRIP Telescope
(From Althouse et al 1985)

Primary Detector	:	41cm * 5cm NaI Anger Camera. Position Resolution ; < 5 mm rms (0.1-5 MeV).
Shield	:	Back Plate ; 5cm NaI. Side ; 16cm plastic scintillator.
Mask	:	Haxagonal URA ; 2000 cells (2.5cm). Rotation Rate ; 1 rpm. Spacing ; 2.5m from the NaI detector. Size ; 1.2m diameter * 2cm (Pb).
Energy Range	:	0.03-5 MeV.
Energy Resolution	:	8.3 keV FWHM at 50 keV. 70 keV FWHM at 1 MeV.
Imaging	:	Resoution ; 0.6° (1070 pixels in 20° FOV) Angular Localization ; 3 arc min (10σ source).

Chapter 3

3 Imaging with coded aperture mask.

3.1 Introduction.

In the gamma ray energy range of the electromagnetic spectrum, imaging is not an easy process mainly due to two reasons. Firstly, the weak flux of the sources and secondly, the difficulties in focusing the photons. This is very much applicable in the low energy range of the spectrum.

At high energies (E_γ>50 MeV) , the main process that dominate the interaction process of gamma ray photons with matter was the pair production. These photons, traditionally, have been detected using spark chambers (Bignami et al 1975) or drift chambers (Mckechnie et al 1977). Here the direction of the gamma ray photon can be measured either by evaluating the direction of the electron-positron pair created in the pair production effect or by extrapolating back the spark tracks.

At energies less than 30 MeV, Compton scattering effect dominate the interaction process. In this region of the spectrum images have been taken using double Compton telescopes (Schonfelder et al 1982, Hartman et al 1983). This type of instrument, as described in section (2.5.1) , uses two different detectors separated by some distance. The energy and position of the incident photon can be evaluated from the energy deposited in both detectors and the position of interactions. These instruments suffer from a lack of good angular resolution (typically half to few degrees).

In recent years "Coded Mask" systems have been employed in low energy gamma ray astronomy. This technique has already been a success and giving promising results in the field of x-ray astronomy (Skinner et al 1987). This method employs a plate which consist of an array of opaque and transparent elements known as "Coded Mask" fixed between the source fluxes and a position sensitive detector.

This technique is an extension of pin hole camera with increased aperture transmission while retaining the angular resolution of a small hole. If there are (N) pinholes in the mask, the picture will

consist of (N) overlapping images of the object. This technique can improve the signal to noise ratio for a point source object by a factor of roughly (N) comparing to the single pinhole camera (Fenimore and Cannon 1978) and this is very encouraging.
Another advantage of this technique is that the source and the background counts are space multiplexed. Therefore the major problem of time independent background counting rate is eliminated.
In this chapter a description of coded mask imaging technique is given with some of the general problems associated with it.

3.1 The basic principle of coded mask imaging.

In coded mask imaging, a gamma ray source (or source element) cast a shadow of the aperture on the detection plane. The recorded image on the detection plane is an overlapping of many shadows. The position and the intensity of the shadow depends on the position and intensity of the source object. The basic steps of coded mask imaging is shown in (fig.3.1).
If an object distribution is considered to as O(x,y) and the aperture transmission as A(x,y), then the spatial distribution of the detected flux can be described by :

$$P(x,y) = A(x,y) * O(x,y) + N(x,y) \qquad (3.1)$$

where N(x,y) is the noise that is not modulated by the aperture and (*) is the correlation or convolution operator. An estimate $\hat{O}(x,y)$ of the object O(x,y) can be obtained by filtering the shadowgram P(x,y) with a suitable decoding function G(x,y) :

$$\hat{O}(x,y) = \left[A(x,y) * O(x,y) + N(x,y)\right] * G(x,y) \qquad (3.2)$$

If the decoding function G(x,y) is chosen such as that the system point spread function, G(x,y)*A(x,y), is a delta function a perfect image can be reconstructed.

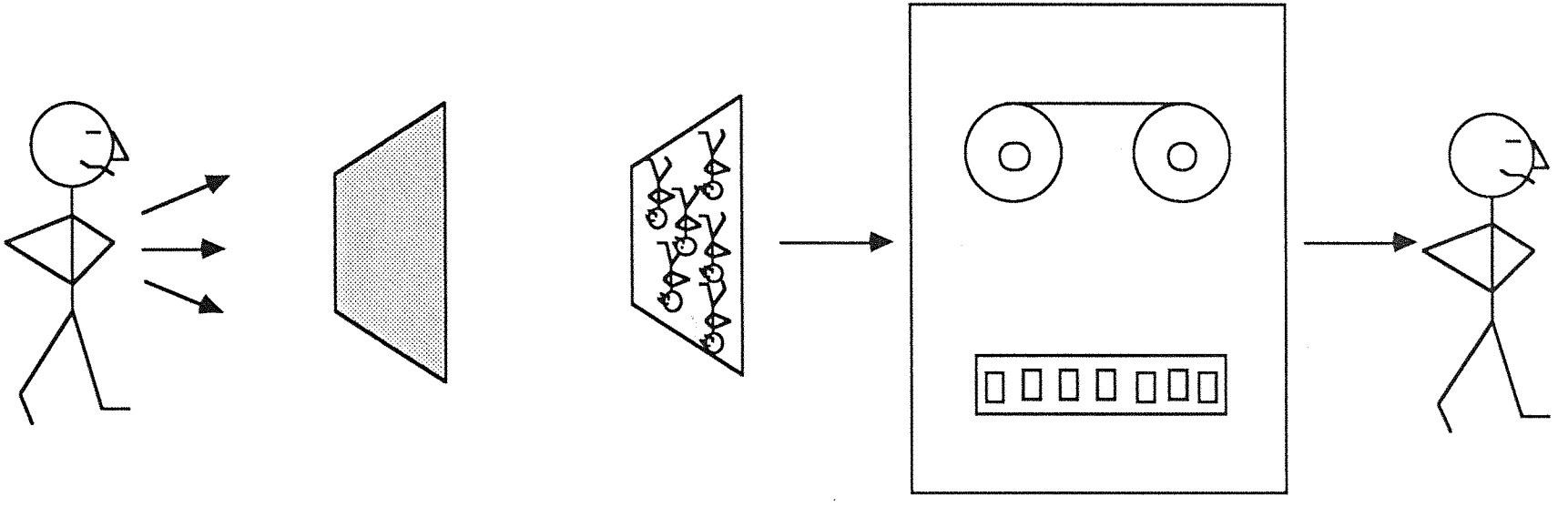

Figure(3.1) The basic principle of coded aperutre imaging (from Fenimore and Cannon 1980)

3.3 The development of coded aperture masks.

3.3.1 Fresnel zone plate.

Mertz and Young in 1961 introduced for the first time the Fresnel zone plate (FZP) as a coded aperture system for x-ray astronomy. This technique was implemented successfully in x and gamma ray tomografic imaging but never was a success in the field of high energy astronomy (Caroli et al 1987).
FZP consists of a series of concentric rings with opaque regions having the ability of focusing coherent light to a point. If the radius of the innermost ring is (R_0), then the radius of the (N^{th}) ring can be given by :

$$R_n = R_o N \qquad (3.3)$$

The total opaque region is equal to the total transparent region resulting a transmission factor of roughly 50%. This technique has the property of an autocorrelation function that approximates the delta function. The best approach to the ideal case is to increase the number of rings.
The transmission function of the (FZP) is proportional to the cosine of the radius (R).

$$A(R) \ \alpha \ cos\,(R^2) \qquad (3.4)$$

A typical (FZP) pattern of three opaque regions with its autocorrelation function is shown in (fig.3.2 a,b).
In an ideal case, the autocorrelation function consist of a single peak and a flat background. Practically, the discretized transmission function produces a poor point spread function and the autocorrelation function is consisting of a single peak surrounded by many concentric lobes as illustrated in (fig.3.2 b). Although this problem of the existence of the lobes can be eliminated (Woods et al 1975) but the poor point spread function will remain as it is.

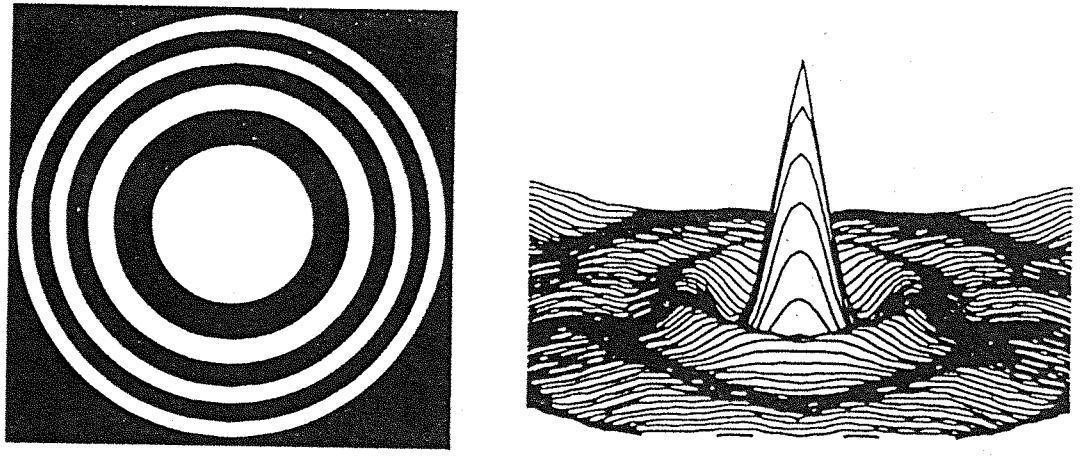

Figure (3.2a, b) (a) A Fresnel Zone Plate (FZP) pattern with three opaque rings and (b) its autocorrelation function.

3.3.2 Random pinhole arrays.

When (Dicke 1968) and (Abbel 1968) independently suggested the use of coded mask aperture in x-ray and gamma ray astronomy, they proposed the use of (Random pinhole arrays). In this case the aperture consists of an opaque plate with randomly positioned pinholes with an overall transmission of roughly 50%.
The autocorrelation is a delta-like function and the imaging is ideal. however, the main problem in using this type of mask is the disagreement between the resolution and the sensitivity. The sensitivity of the telescope is determined by the amount of flux arriving the detection plane, therefore, it is essential to have reasonably large pinholes in the plate. Meanwhile, the angular resolution is also governed by the size of the holes and to achieve a high angular resolution, it is required to employ small holes!
The autocorrelation for a typical random pinhole arrays mask consists of a large central peak surrounding by strongly marked sidelobes structure as shown in (fig.3.3 a,b).
It is clear why this kind of mask has not placed itself in the field of high energy astronomy.

3.3.3 Non-uniformly redundant arrays.

The first coded aperture mask capable of producing perfect images of sources distribution was the non-uniformly redundant arrays introduced by Golay (1970). The autocorrelation is a delta function with no sidelobes up to some large values of (L) (the distance between a pair of holes is 2L).
This technique is based on the theory that no more than one pair of holes is separated by the same distance. Therefore this method severely restrict the number of possibilities of array configuration. This means that for a desired large field of view with no loss of angular resolution, a very large mask is required. In all cases this technique provide a poor sensitivity which is a very important factor in the consideration of designing any telescopes.
These are the reasons for the failure of this type of masks in the desired field of astronomy. However, applications have been made

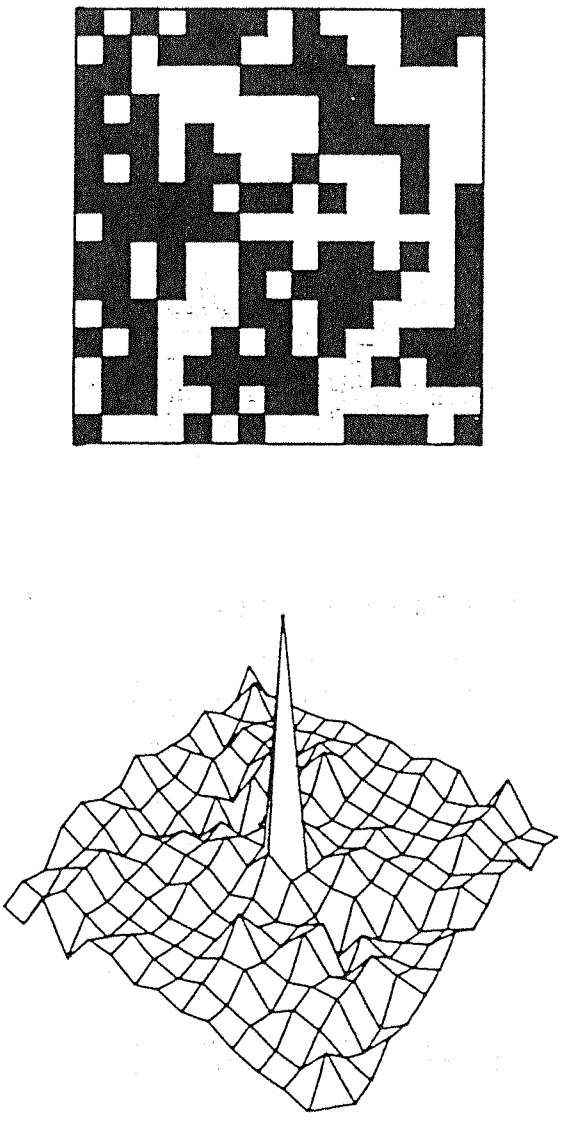

Figure (3.3) A 15 x 15 elements mask pattern with 50% transparency with its autocorrection function. (From Caroli et al 1987).

in nuclear medicine (Fleming and Goddard 1984) and infrared astronomy (Aitken 1981).

3.3.4 Uniformly redundant arrays.

The uniformly redundant arrays (URA) has the combination characteristics of high transmission of the random arrays and the flat sidelobe of the non redundant pinhole arrays. The high transmission property of this pattern means a better capability of imaging low intensity x and gamma ray sources and the flat sidelobes property means that there will be no noise to swamp low intensity sources.
The name of this type of arrays was chosen because the number of times that a particular separation distance for a pair of holes in a pattern occurs is constant for every possible separation. This kind of pattern which was originally introduced by (Fenimore and Cannon 1978) is based on the use of cyclic difference set (Baumert 1971).
To reconstruct a perfect object image taken by a URA, Fenimore and Cannon 1978 developed two process. One is the "Balanced correlation" method and the other is the "Mosaicking" method.

3.3.4.1 Balanced correlation.

In the early days of using random pinhole arrays, it was assumed that the aperture arrays must be the same of the decoding arrays. Therefor the decoding process became one of autocorrelation. In this case the autocorrelation features a central peak with a finite width and a pyramidal structure underneath the peak. This causes a severe degradation of spatial resolution especially for low intensity sources.
Brown 1972 introduced a method to solve this problem known as the "Mismatch process" in which the transmission function was defined to be 50% and replaced the zeros of the binary aperture array by (-1). This method was generalized for any transmission

function, not necessarily 50%, by Fenimore and Cannon 1978. The improvement was achieved by introducing the following array for (G) :

$$G(x,y) = 1 \qquad \text{if } A(x,y) = 1 \qquad (3.5)$$

$$= \frac{-\rho}{(1-\rho)} \qquad \text{if } A(x,y) = 0 \qquad (3.6)$$

where (ρ) is the transmission function.

3.3.4.2 Mosaicking.

To achieve a better use of the detection plane and to record enough information to reconstruct an image, Fenimore and Cannon 1978 suggested that the coded mask pattern should be "Mosaicked". In such case, the aperture consists of a two cycle of the original pattern in each direction. An advantage of this technique is that the detector need to be only as large as one cycle of the mask pattern as shown in (fig.3.4). In this way, the object or the object elements which are in the field of view will contribute to cast a shadow of the mask pattern in the detection plane. As long as these contributions can complete one cycle of the basic pattern, there will be enough data to unfold the object with a point spread function equal to a delta function.

Sources outside the field of view of the telescope will be partially coded and their imperfect reconstructed image will be described as "Vignetted".

In medical coded aperture imaging the latter problem does not exist due to the positioning of the sources in the complete field of view.

In general, URA is either based on a twin prime or m-sequences. The twin primes are sets classified by $N = p * q$ where p and q are both prime numbers and $p-q = 2$. In the m-sequence arrays (N =

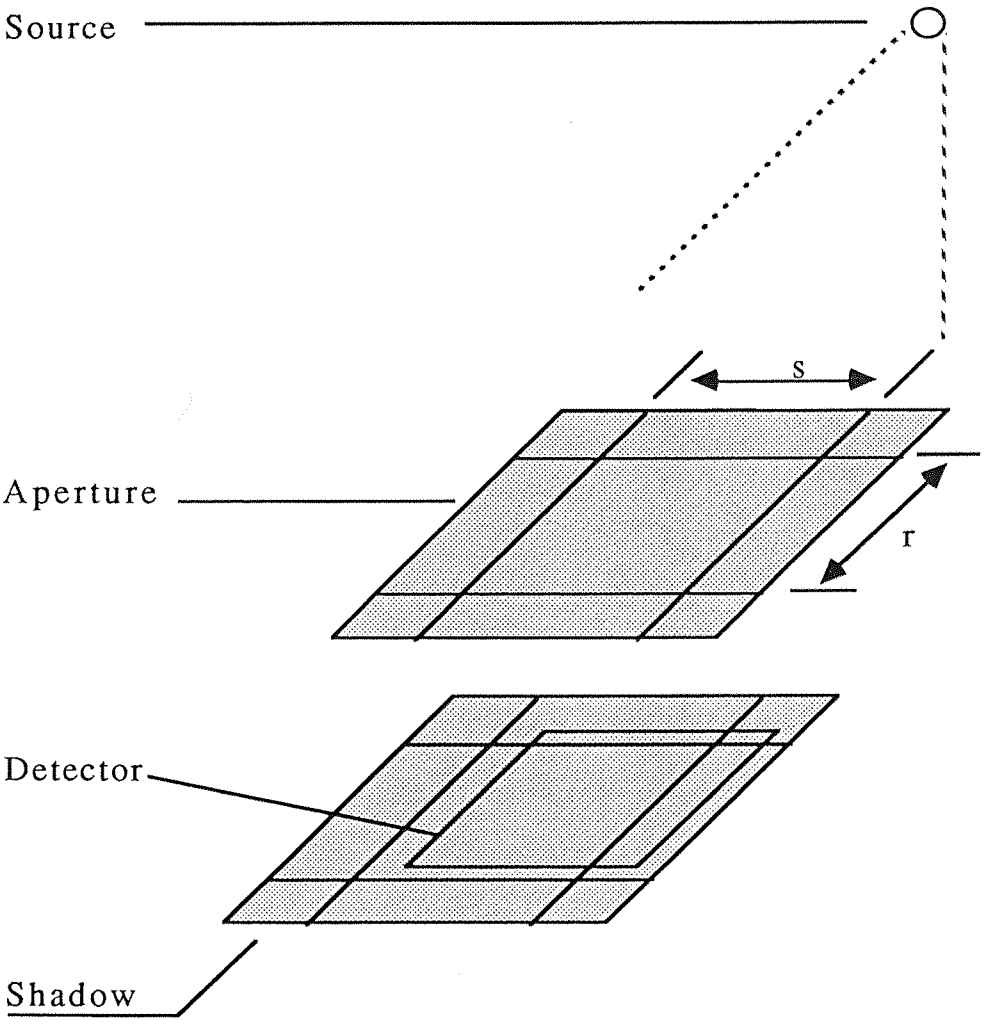

Figure(3.4) The configuration of a coded aperture system based on the employment of 4 cycles of the mask design (from Fenimore and Cannon 1980)

2^m-1) where m is an integer>1 and the dimensions can be given by (p =2^m/2-1) and (q = 2^m/2+1).
As it was mentioned earlier that the uniformly redundant arrays have many advantages over the random pinhole arrays but their only disadvantages is that the size of the mask is limited. Typical examples of the twin primes are 5*3 , 11*13 and of m-sequences are 7*9 , 15*17. Fig3.5 illustrates some different mask patterns. Also the fully mosaicked mask of the ZEBRA telescope based on a 9*7 pattern is shown in (fig.3.6).

3.3.5 Hexagonal uniformly redundant arrays.

Up to mid 80's, most of the uniformly redundant array masks were constructed on rectangular lattices. In 1985, Finger and Prince have introduced URA's constructed on Hexagonal lattices. This type of URA is very much suitable for use in the field of gamma ray astronomy to generate high quality images under high level background circumstances. This is mainly due to two reasons :

(i) They are almost 50% open which leads to an optimum sensitive instrument.
(ii) They are antisymmetric upon rotation by 180° (open cells exchange with closed cells except the central cell).

The latter property in which the mask is rotate to a near antimask position allows perfect background subtraction.
This type of mask pattern is based on a Skew-Hadamard sequence with N = 4m-1 , M = 2m-1 and λ = m-1 where (N and m) are integers.
A typical hexagonal uniformly redundant mask pattern is given in (fig.3.7) which has the order of (N=151).

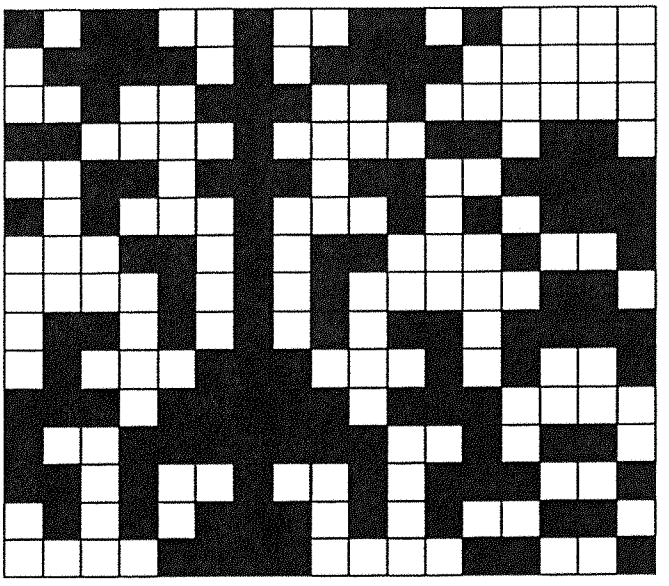

(a)

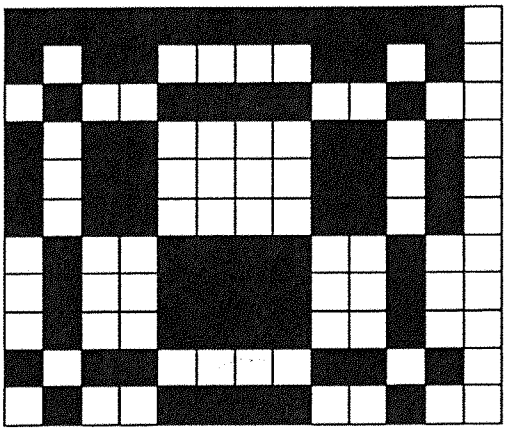

(b)

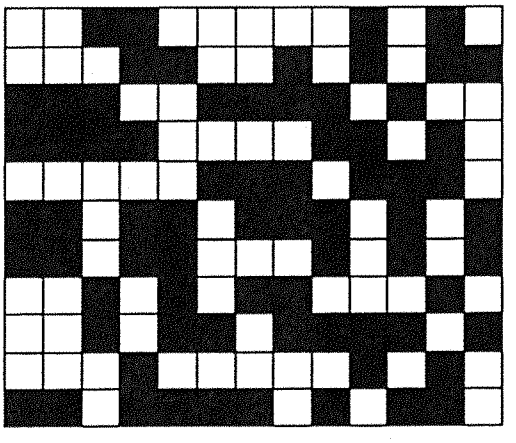

(c)

Figure(3.5) Three different types of coded aperture masks ; (a) is a random pattern. (b) is based on a twin-prime. (c) is based on an m-sequence.

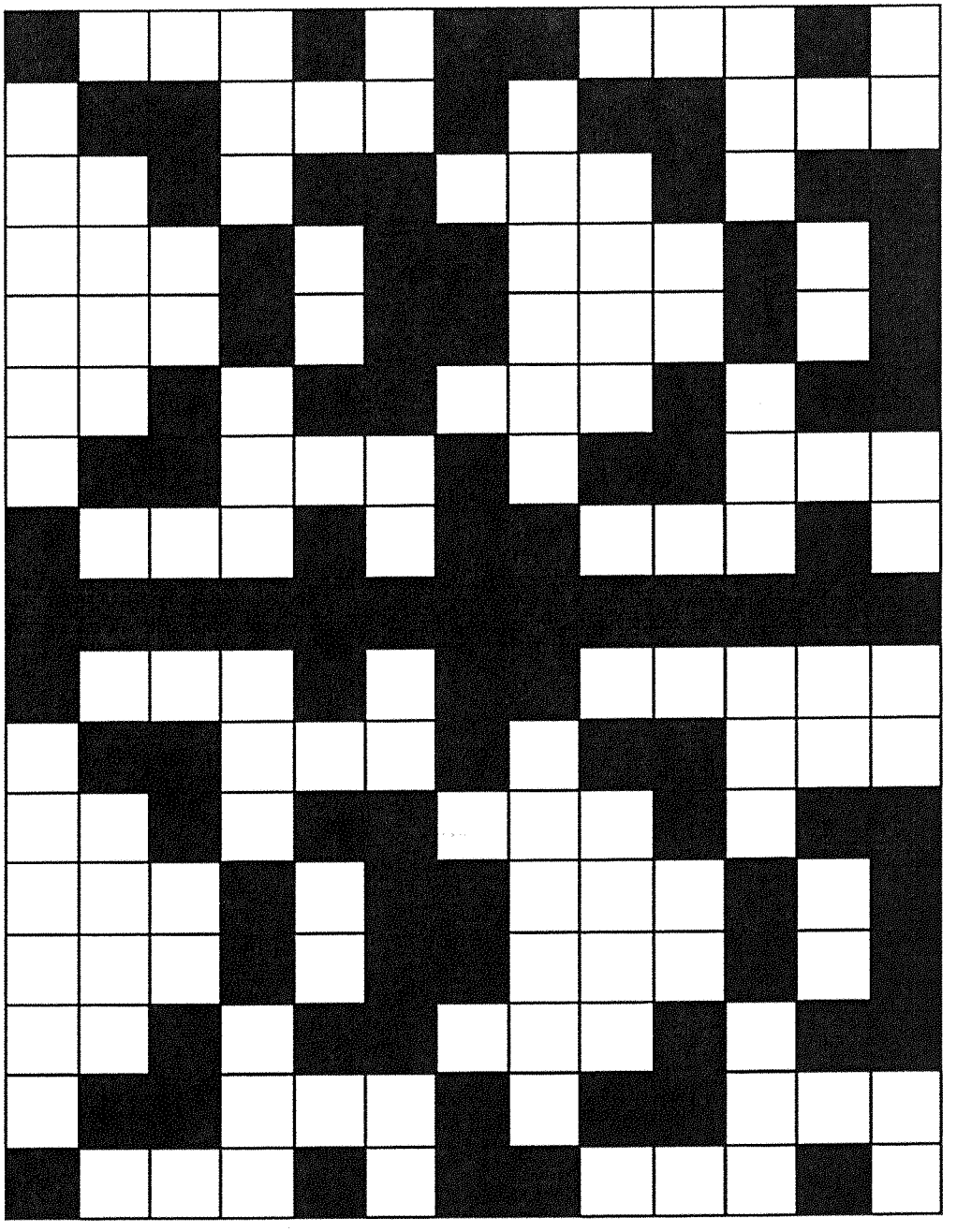

Figure (3.6) The full coded apertue mask of ZEBRA telescope

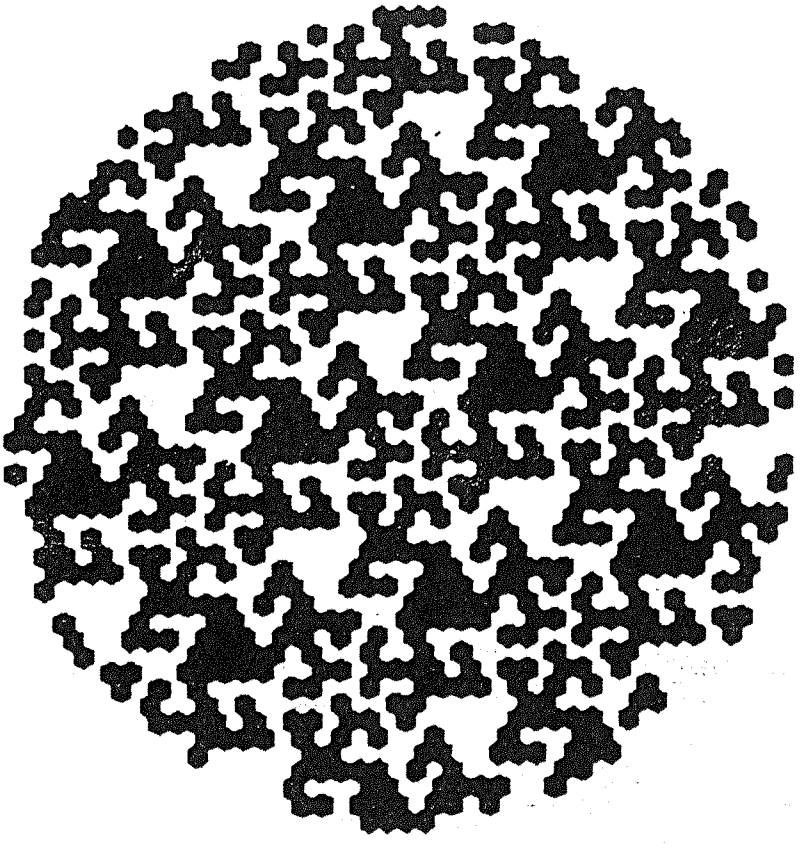

Figure (3.7) An HURA of order 151.

3.4 Aberrations in coded mask imaging.

So far it has been demonstrated that coded mask imaging in gamma ray astronomy has been a great success and high quality imaging of the sky at this particular range of the electromagnetic spectrum cloud be produced. Nevertheless, there are few obstacles in the way of producing quality images. These obstacles are related both to the mask and to the detection plane. In the following sections a brief description of them in given.

3.4.1 Mask performance.

The opaque elements of any mask are typically made of substances such as Tungsten which has a high stopping power for gamma ray photons (roughly 90% attenuation at 1 MeV energy). This percentage decreases with the increase of energy. Therefore at high energies, the mask elements will be less efficient and more photons penetrate the mask elements. This leads to a reduction in the imaging quality.
Also to support a mask , mechanically, it requires some kind of structure, typically a honeycomb of Carbonfiber. This leads to a non-perfect transmission of the desired photons and once again the quality of the images is reduced.

3.4.2 Positional resolution of the detector.

To reconstruct a true image, the image must be folded with the detector response. A finite positional resolution within the detection plane results in reduction of the amplitude of the point spread function and an increase in its width in additional to create sidelobes in the image.
Charalambous et al 1984 have given the degradation in the peak height over the mean background level as a function of the ratio of the mask element sizes to detector resolution (fig.3.8). It can be seen that in both cases of one and two dimensional masks that the functions fall away rapidly as the positional error increases. It is clear that even with mask element size as small as (2σ) of the resolution, the signal to noise ratio is reduced by roughly 30% for

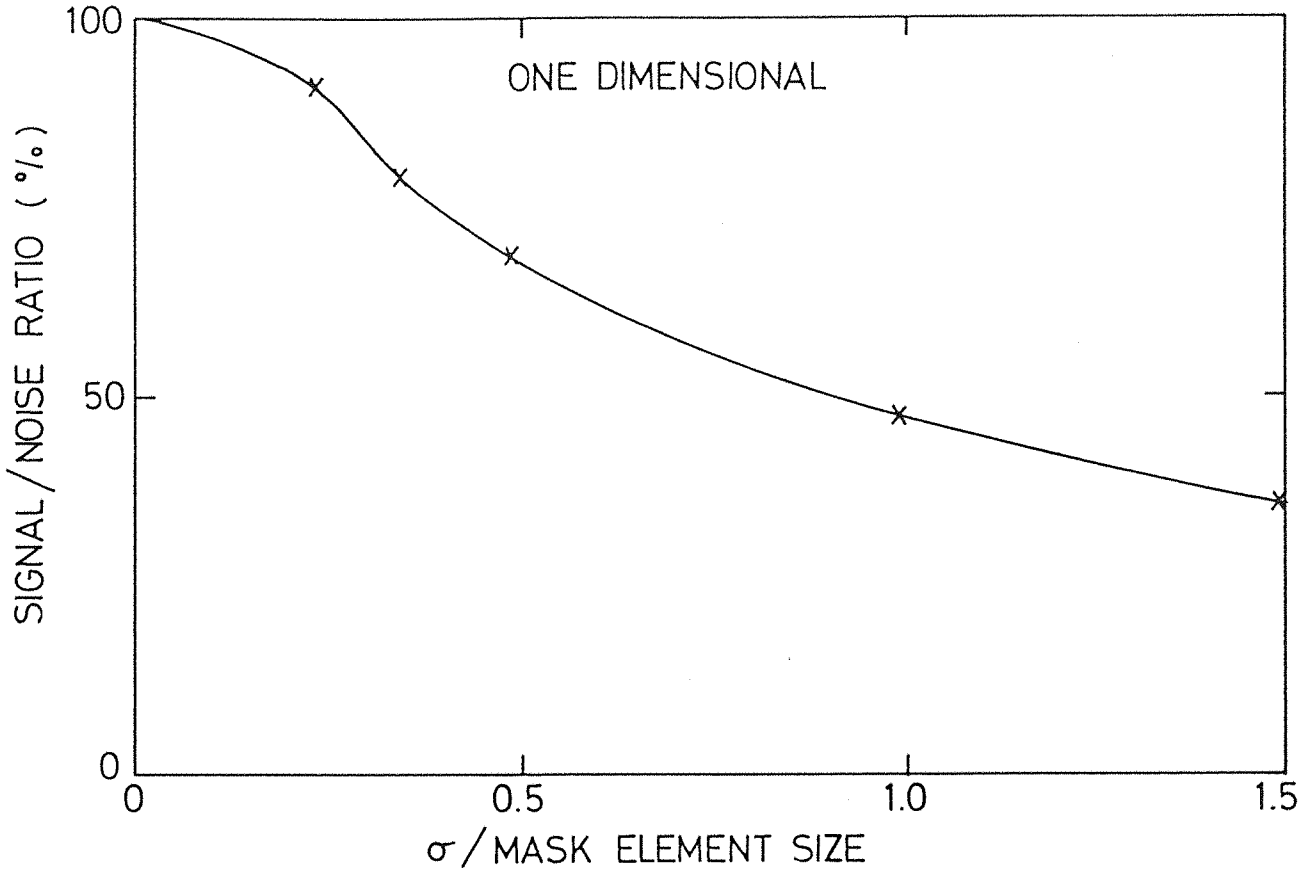

Figure (3.8) The signal loss in a one and two dimensional coded aperture system as a function of detector positional resolution.

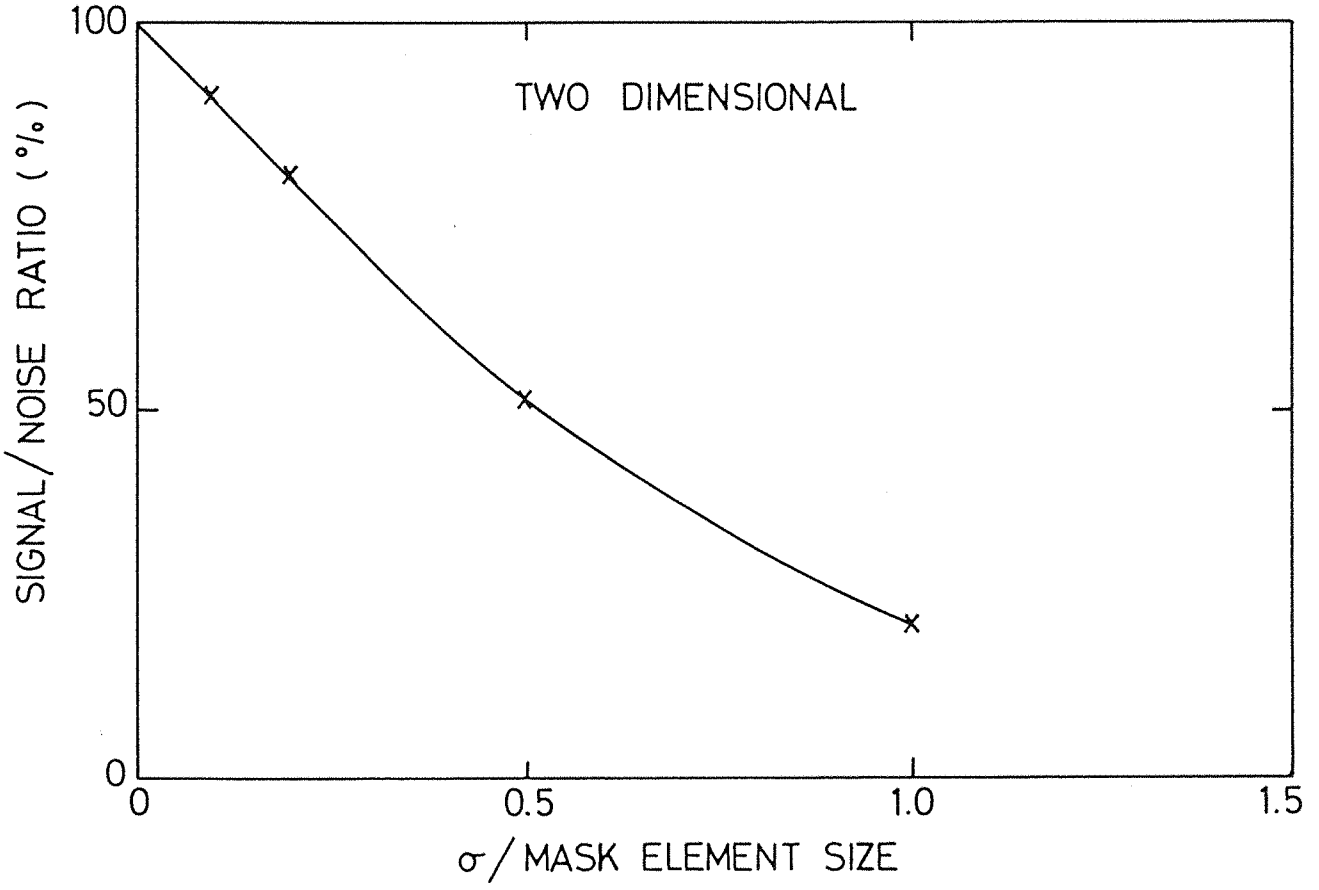

the case of the two dimensional mask which means a less quality imaging.

3.4.3 Non-uniform background distribution.

A non uniformly distributed background counting rate on a detection plane has a rolling effect on the deconvolved image which leads to an improper identification of source position and intensity. A typical image taken by a detection plane with a non-uniform background is shown in (fig.3.9). To identify a source correctly, a suitable detailed data analysis on both the final image and the row count rate data is required.

3.4.4 Vignetting of sources.

Sources outside the field of view of a telescope will cast a partially coded shadow of the mask into the detection plane. These sources are known as "Vignetted sources". It is very difficult to isolate a telescope from this kind of sources. The reconstructed image of this incomplete data consist of a peak with false intensity superimposed over a very high non uniform background as shown in (fig.3.10). The intensity of the peak is related to the area of the encoded data. Caroli et al 1987 suggested that this effect could be removed by means of :

(i) Employment of advanced deconvolution methods.
(ii) A statistical analysis of the recorded shadowgram.
(iii)Decoding each image by a correlation with suitably altered arrays to distinguish vignetted sources from others.

3.5 Conclusion.

The first part of this chapter was an introduction to the basic principles of coded mask imaging and its developments over the years up to date. The second part was dedicated to the general

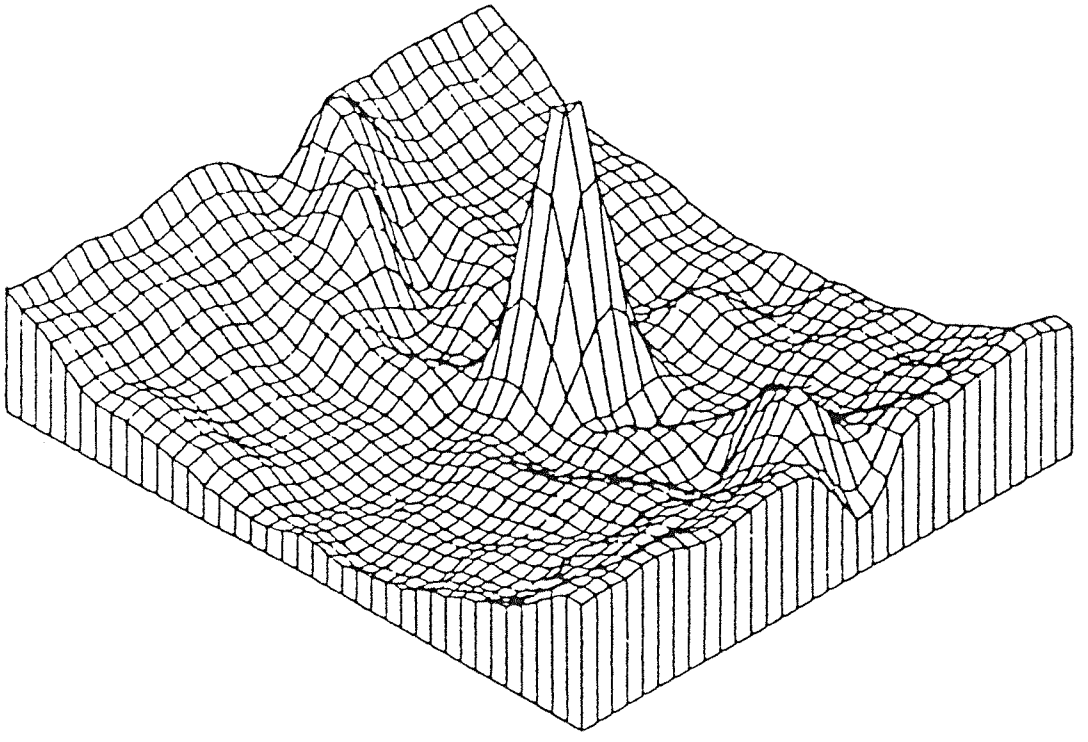

Figure (3.9) An image of a point source that was formed with a sinusoidal detection plane background.

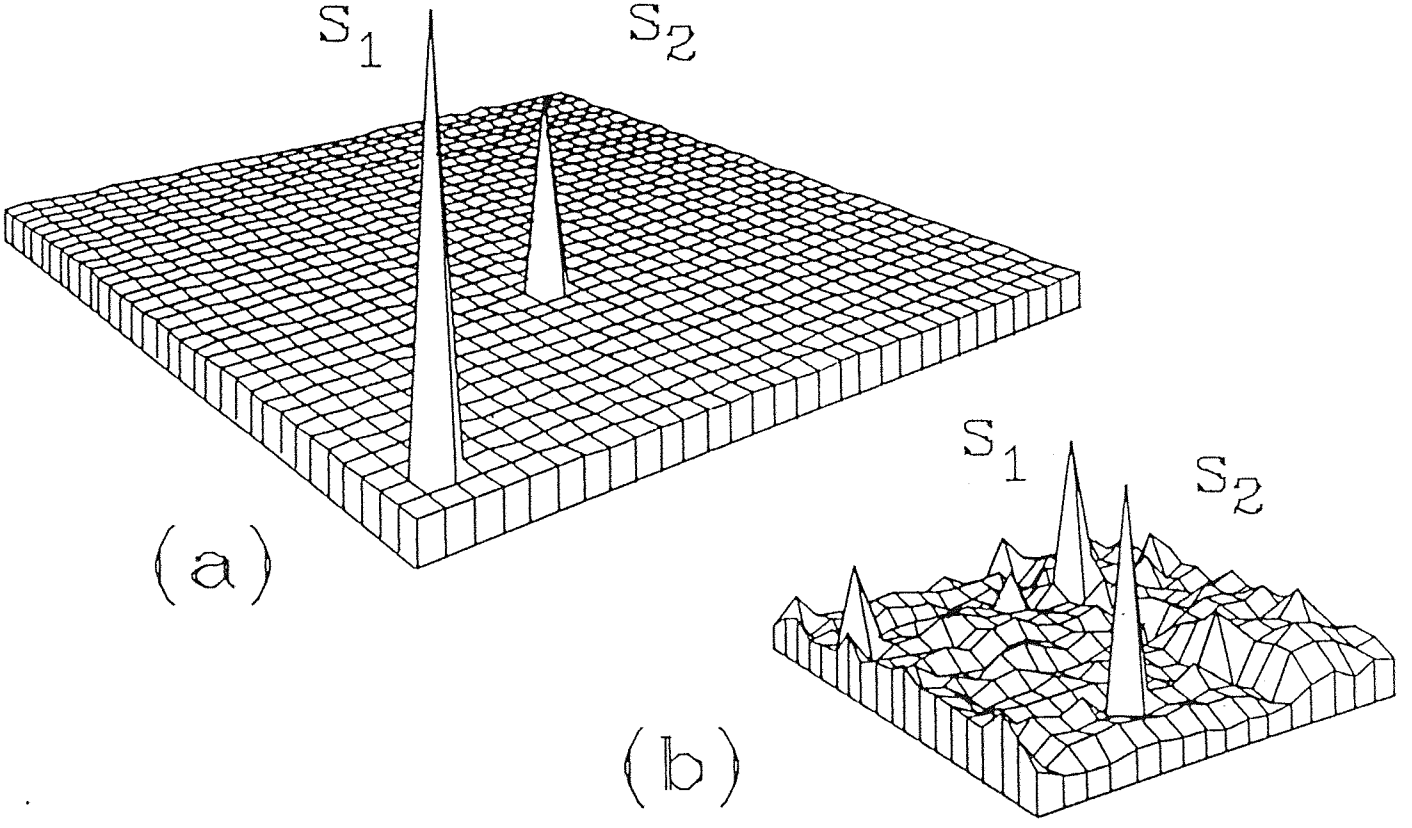

Figure (3.10) Effect of source vignetting: (a) true position and intensity of two sources, one (S_2) in the FCFV and the other (S_1) in the PCFV. (b) reconstructed image of the FCFV using correlation (assuming no detector background). From Caroli et al 1987.

problems related to the employment of coded mask imaging in gamma ray astronomy.

It is obvious that the wide range of mask patterns available leads to the design of many different types of telescopes for the field of x and gamma ray astronomy.

Chapter 4

4 An overall description of the low energy gamma ray telescope, "ZEBRA".

4.1 Introduction.

ZEBRA is a low energy gamma ray imaging telescope designed to produce fine angular resolution images of the sky in the energy range (0.2-10.0) MeV. The experiment features a coded aperture mask separated by some distance from an actively shielded detection plane
The mask is based on a 2*2 mosaic of 9*7 uniformly redundant arrays. The fully coded field of view is (8*8.8) degrees. The capability of this instrument of simultaneous measurements of source and background flux suppress time dependent background.
The mask and the detection plane are mounted on a steering platform capable of pointing to a specific target with an accuracy of (0.5) degrees. An artistic impression of the experiment is given in (fig4.1). A full description of the telescope is given by (Villa et al 1987).

4.1 The coded mask.

The coded mask is fixed at (3.5 meters) from the detection plane. The material used for constructing the mask is Tungsten. This is due to its high atomic number (Z=74) and good stopping power for gamma ray photons. The mask is sandwiched between two sheets of Carbonfiber honeycomb structure to provide mechanical support (Carbonfiber has a high transparency to gamma ray photons).
The thickness of the mask elements is limited by two factors. Firstly the weight which is a mechanical consideration. Secondly, they might up to certain degree form as a collimator. The optimum thickness of these elements was found to be (2 cm.) using a Monte-Carlo simulation (Butler et al 1984).
The mask pattern chosed for ZEBRA is based on a 9*7 uniformly redundant array. There are several factors that influence the

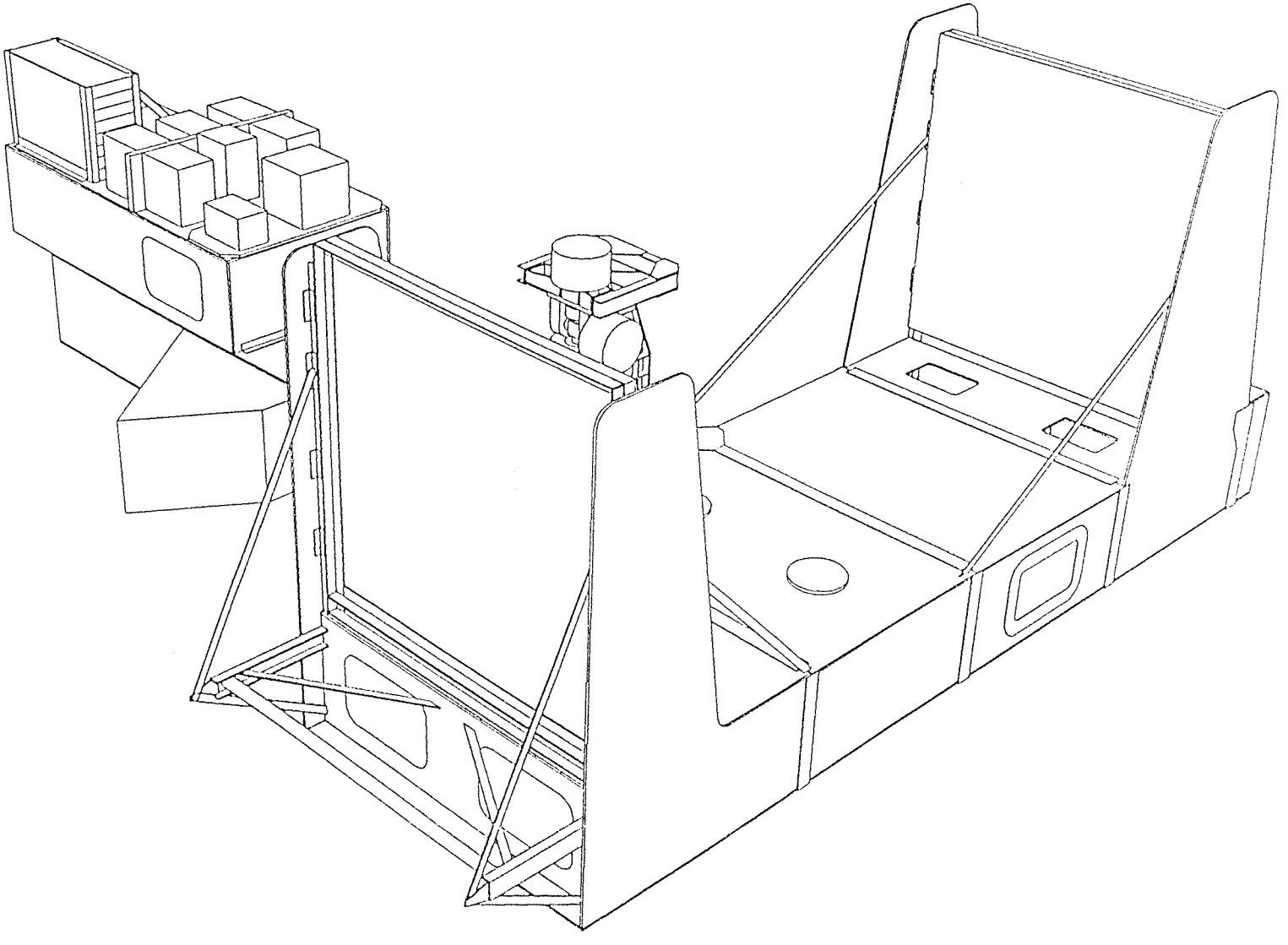

Figure (4.1) An artistic impression the the ZEBRA telescope in the first flight configuration.

choice of the mask. Gil 1986 has given a list of possible mask patterns and the reason for chosing this particular pattern of ZEBRA. The mask is formed by a four times replication of the 9*7 pattern. One line and one column at the boarders are reduced in order to avoid ambiguities. The basic mask pattern has the same size of the detectors (60*49 cm.) which allows each source, on the field of view, to cast a different shadow on the detection plane. The mechanical characteristics of the mask is given in fig.(4.2).

4.3 The detection plane.

The detection plane of the ZEBRA telescope is constructed of nine position sensitive NaI(Tl) detectors of dimensions (55*5.8*5 cm.) (total detection area of (2500 cm^2). These detectors are individually viewed by two two inchs Hamamatsu photomultiplier tubes. The position sensitive detectors are actively shielded from bellow and the sides by means of thirteen anti-coincidence detectors. These detection units are described in detail in Chapter5. A (6 mm.) thick plastic scintillator fixed above the detection plane completes the shielding system. A schematic view of the detection plane is given in fig.(4.3). Each position sensitive bar operates in anti-coincidence with the adjacent bar. In this way, the position sensitive detectors are not only operate as main detection units but also as a shield for each other.
When a gamma ray photon interact on a position detector, the N^{th} of fig.(4.3) for example, it can be counted as a valid event only if the coincidence signal from the two photomultiplier tubes of the N^{th} bar is not associated with any other signal from the surrounding bars or the plastic scintillator. The logic criterion for the acceptance of an event is :

$$\gamma_N = N.\overline{((C\text{-}1)+(C7+(C+1)+(N+1)+(N\text{-}1)+P1+P2)} \qquad (4.1)$$

4.4 The electronic system.

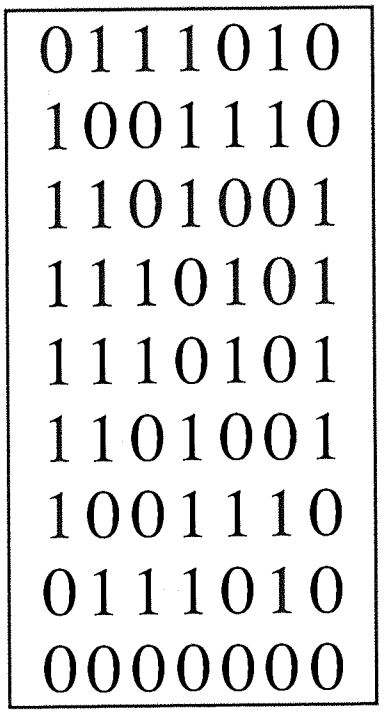

Figure (4.2) The ZEBRA telescope mask pattern:
1=Empty pixel,0=Tungsten pixel

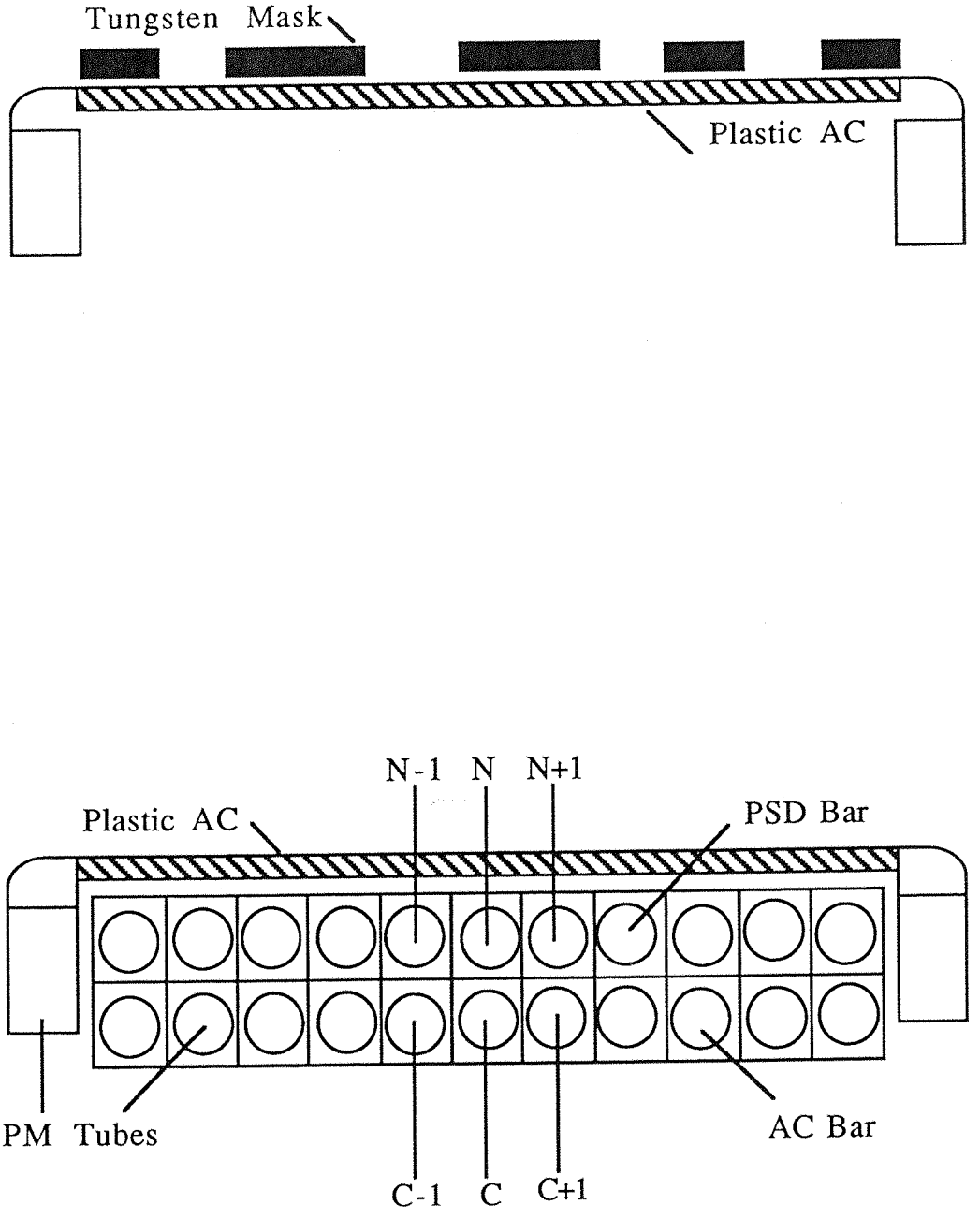

Figure(4.3) A schematic view of the ZEBRA detection plane with the associated coded aperture mask

The flight electronics system mainly consist of three units; the Front End Electronics(FEE) , the Digital Processing Electronics(DPE) and the Telecommand and Telemetry Data Handling(TTDH).
The FEE interface with the detectors and handle the data to the DPE then the received data is processed. The TTDH organize the transmission of the processed data to the ground. A block diagram of the electronics system is given in fig.(4.4).

4.4.1 Data processing electronics.

The photomultiplier tubes and their associated high tensions (H.T.) with the preamplifiers all together form an interface between the detection plane and the electronics system.
These H.T.'s are independently adjusted for the desired gains by a telecommand from the ground station. These units are equipped with digital to analog convertors employed to translate the data words send by the ground station for controlling their gains.
The output signals from the tubes are passed via noise filter to the preamplifier line driver circuits. Then the preamplified signals are passed to the Front End Electronics

4.4.1.1 Front End Electronics (FEE).

The signals provided by the preamplifiers will be transferred to the Front End Electronics. Here discrimination levels are supplied for the incoming pulses then valid events will be converted into a digital form. A block diagram of the Front End Electronics package is show in fig.(4.5)
The two signals from each position sensitive detector are combined, after passing through amplifiers and shapers, to give the energy deposited in that particular bar using the formula :

$$E_\gamma = k.\sqrt{E_L.E_R} \qquad (4.2)$$

This output will pass through discriminator to check weather the energy deposited is within the energy range (0.2-10.0) MeV or not. Since each detector is operating as Compton anticoincidence for the

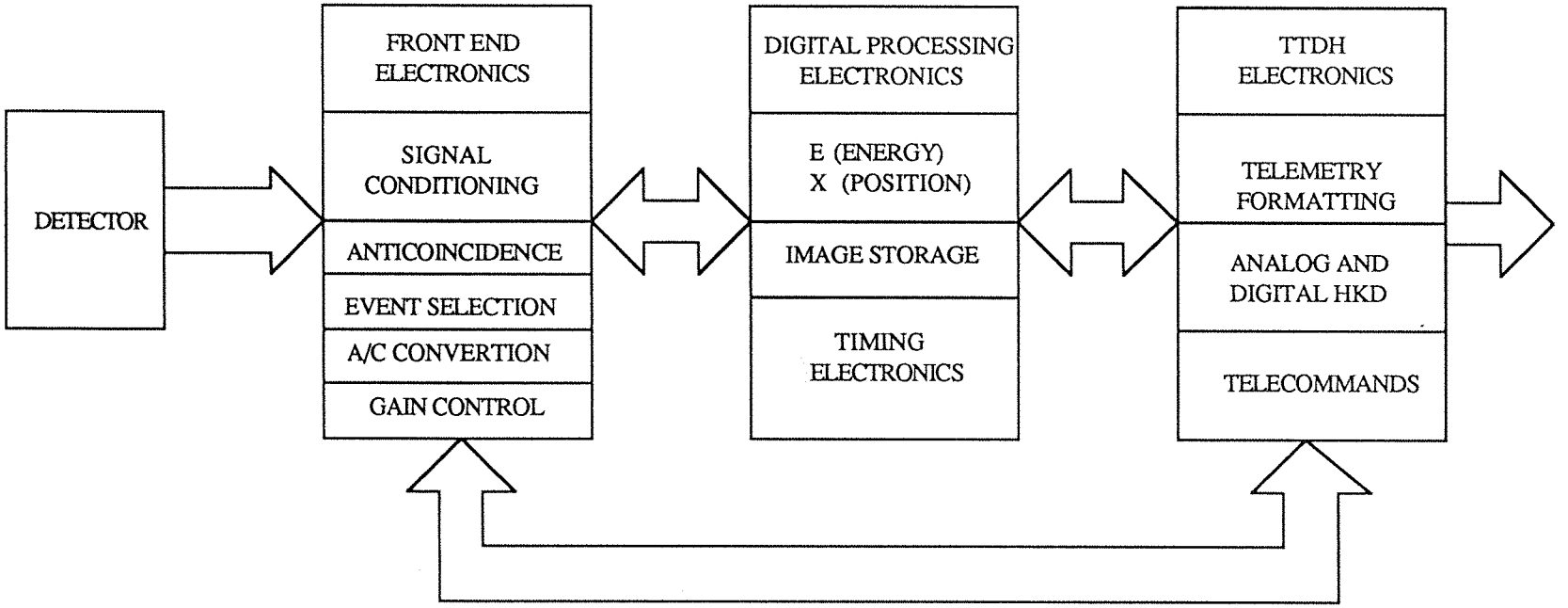

Figure (4.4) The ZEBRA flight electronics

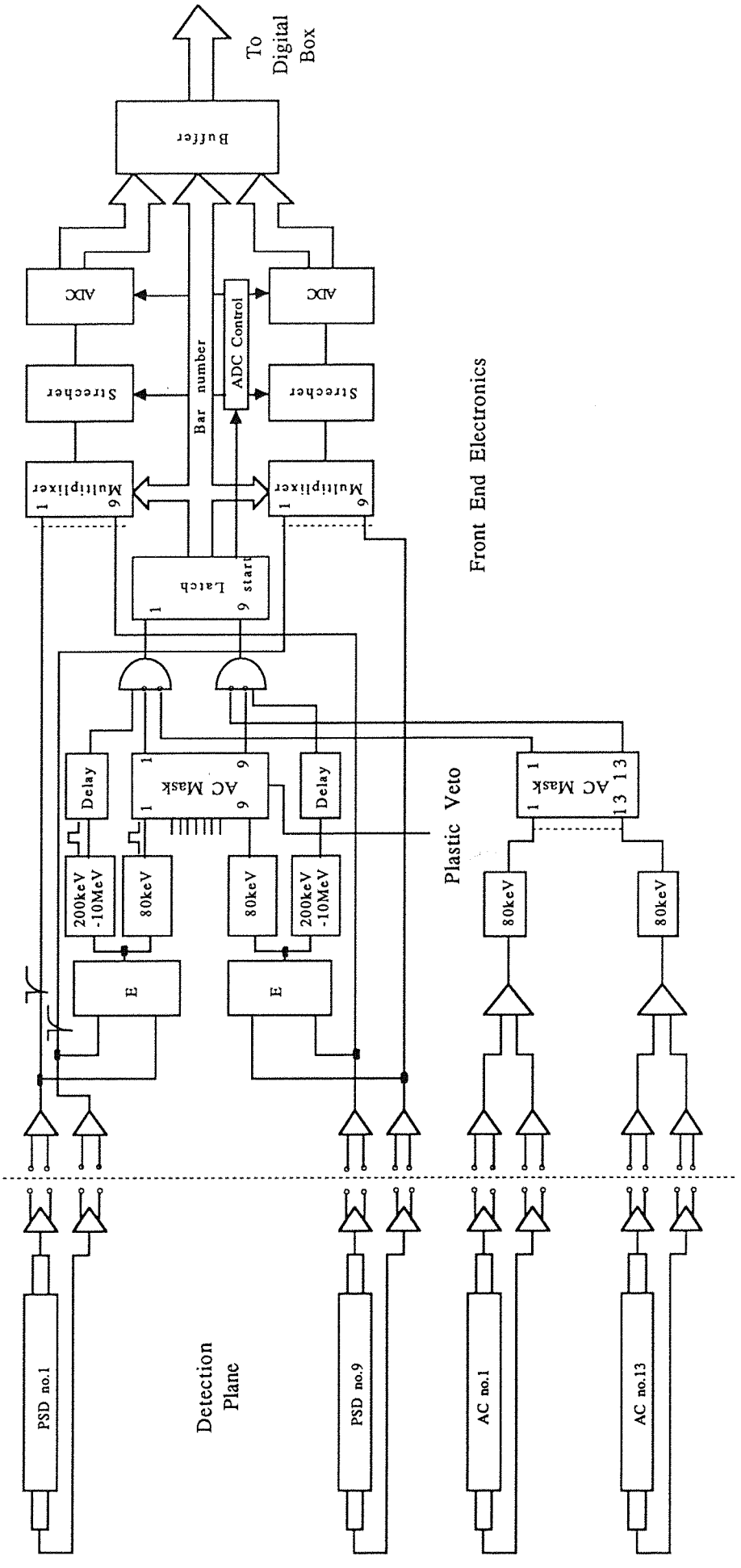

Figure(4.5) A schematic diagram of the ZEBRA Front End Electronics

adjacent bars, the pulses are passed through (80) keV discriminators which set the lower threshold level for the Compton anticoincidence. These Compton discriminator outputs are fed to a logic mask to determine weather there is coincidence with the neighboring detectors and the plastic scintillator.
In the case of the anticoincidence bars, the output signals of the two photomultiplier tubes are summed and fed into 80 keV discriminators. The outputs are supplied to another logic mask which determines which set of detectors is shielded by each anticoincidence bar.
The outputs of the two logic masks and the (0.2-10.0) MeV discriminators are gated to check for the overall valid event criterion given in section (4.3). The resultant pulse is latched to give the bar number and to select the two correspondent detector signals via an analog multiplexer switch. Then the signals are stretched and subsequently are digitized by two individual 12 bit analog to digital converters. The outputs are then passed to the Digital Processing Electronics package.

4.4.1.2 Digital Processing Electronics (DPE).

A block diagram of the Digital Processing Electronics is given in fig(4.6). At this stage there will be enough information to calculate the energy and position of each event. Then the data is stored in a block of memory. Also the timing information is kept in some sort of memory.
The digitalized signals from the Front End Electronics are first converted to arithmetic values using a look-up table EPROM. Here the 16-bit microcomputer employ its facilities to calculate the energy and position of each event using the formulas :

$$E_\gamma = \frac{e^{\alpha L/2}.\sqrt{E_L E_R}}{(P/E_o)} \qquad (4.3)$$

$$X_\gamma = \frac{ln\,(E_R/E_L)}{2\alpha} \qquad (4.4)$$

For the non-linearity of the position detectors, fine corrections are applied using look-up tables previously prepared for each detector.

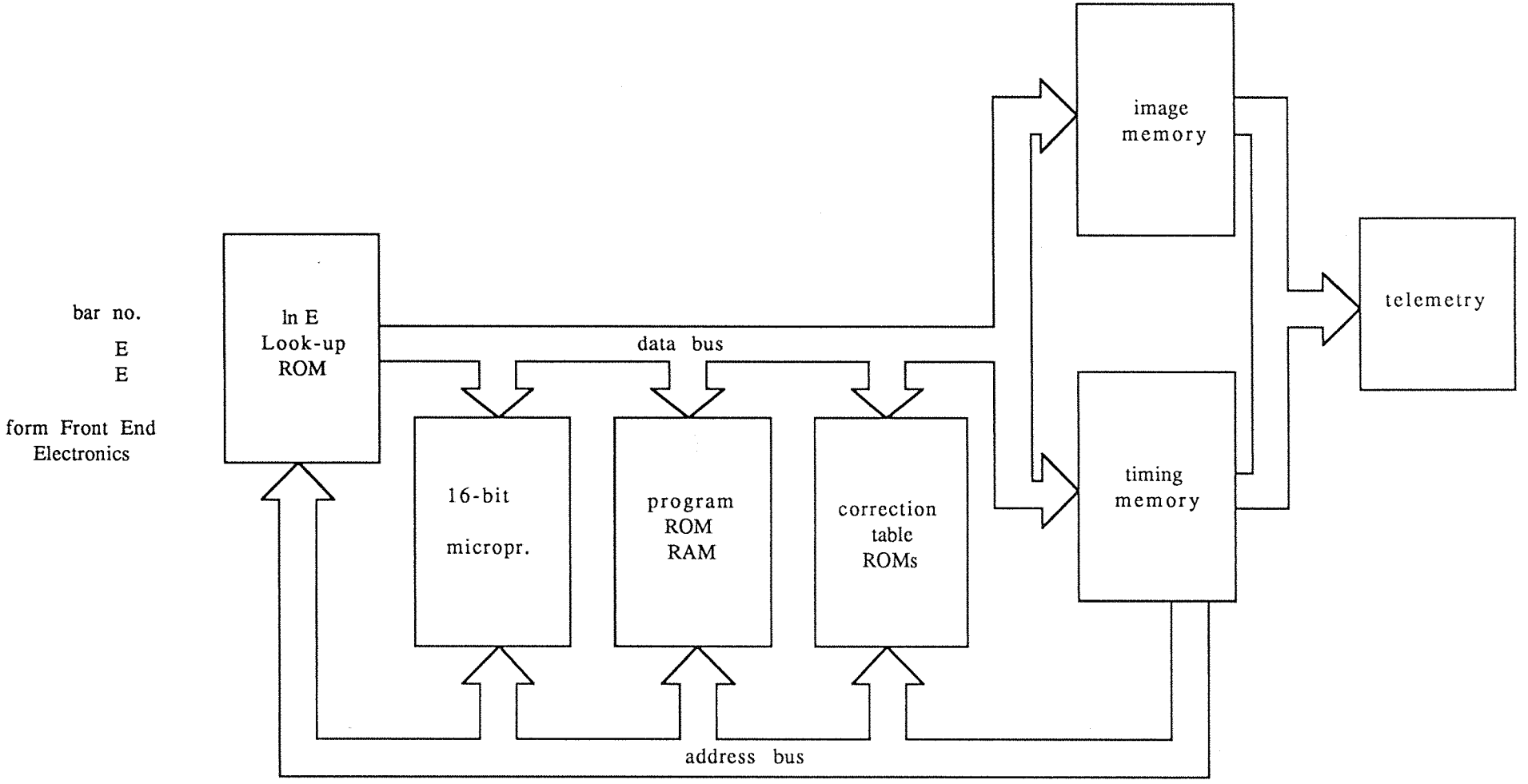

Figure (4.6) A block diagram of the digital processing unit of the ZEBRA detection plane

The resulting data is stored in two memory banks, one for the timing mode and the other for the image mode which are explained later on.

4.4.1.3 Telecommand and Telemetry Data Handling (TTDH).

The Telecommand and Telemetry Data Handling unit organizes the accumulated data to be telemetry formatted and then transmitted to the Ground Station. Also it arranges the distribution of telecommands coming from the Ground Station.
A telemetry format consist of a sub-frame with (64) frames of (32) words of (16) bits each. The data stored in the memory banks are transmitted in (128) subframes which is one scientific record.
All the commands coming from the Ground Station will be received by a decommulator onboard that distributes the telecommands to the telescope electronics, the star sensor and the steering electronics.

4.4.2 Operational modes.

The telescope is operating either on the image mode or the time mode. In the case of the image mode, the energy data E_γ , the position data x and the bar number are stored in a matrix over an interval of 100 seconds. The telemetry bit rate corresponding to this data is : 128(pixels) * 128(energy bins) * 9(bars) * 12(bits ADC resolution) or about 1.8 Mbits.s^{-1} .
In the timing mode, all the position data and most of the energy data is sacrificed to determine a presice time of the arrival of the gamma ray photons. The energy data is divided into (5) channels : (0.2-0.48)MeV , (0.48-1.44)MeV , (1.44-4.0)MeV , (4.0-7.0)MeV and (7.0-10.0)MeV. Every (1) millisecond, events are scaled into these energy bins. A (3) bit scaler is employed for each bin which allows the system to handle 10^4 counts. s^{-1}.. Therefore the telemetry rate is : 3(bit scaler)* 4(energy bins)* 1000(milliseconds) or 12 kbits.s^{-1}..

4.4.3 In-flight calibration.

In order to generate high quality images of the sky, the detection plane must be kept in calibration constantly during flight. To achieve this goal, a collimated ^{241}Am source is fixed 3cm. from both ends of each position sensitive detector. The 60 keV x-rays are not seen by the detection electronics since they are bellow threshold but are seen by the calibration electronics system. The spectra of these sources are accumulated over the integration time and then send via the telemetry format to the Ground Station along the image and timing data. The data will be analyzed continuously to monitor the reference positions. Any detected displacement will lead to the application of correction via telecomand organized by the Ground Station.

4.5 The steering platform.

ZEBRA platform, as show in fig.(4.1) is designed by the collaboration of Southampton University and Rutherford Appleton Laboratories (RAL). It is based on a three axis gyro stabilized gimbal system capable of pointing in the direction of a given target with a real time accuracy of (0.5)arc min'.s The platform can be divided , for demonstration, into three sections.

The first section is the Aluminum honeycomb structure that holds the coded mask and the detection plane. This section is about (4)m. long. The structure is rigid enough to maintain the arc minute angular resolution during flight under any circumstances (altitude and temperature differential). To monitor any distortion of the platform, an optical system is employed to monitor the displacement and if required, correction can be made to the recorded images.

The second section is the Aluminum structure based on the other side of the gimbal system. This section provides the necessary location for all the various subsystems associated with the telescope such as flight electronics, platform electronics, star sensor, telemetry package, batteries..etc. The arrangement is made in such

away to have the centre of gravity set at the centroid of the gimbal system.

The third and last section is the three axis gimbal system. The gimbal drive unit incorporates three torque motors and drive shafts to provide the three axis movements, azimuth, elevation and roll (Farman and Hardie 1986).

A two axis magnetometer is used for the initial steering of the platform to sense position in azimuth and a three axis accelerometer to sense position in elevation and roll. When the telescope set in a particular position, a 3 axis rate gyro is switched on for maintaining stabilization.

To obtain the absolute pointing direction with a precision of 30 arc seconds, a second sensor is required. For this purpose a star sensor, based on a CCD array sensor, has been developed to fillful this requirement.

Finally, a Ferranti 3 axis inertial gyro is switched on into the position control loop stabilizing the system to (1) arc minute per (30) minute period.

4.6 The Ground Support Equipments.

The Ground Support Equipments for the ZEBRA imaging telescope is a self contained system based on a PDP 11/23 computer. Its primary task to format and record both laboratory and inflight data on magnetic tapes but also performing the following tasks :

1. Recording the formatted data coming from the flight electronics.
2. Performing "Quick-look" data analysis on the images taken and displaying them on the graphic terminals continuously during flight.
3. Analyzing the calibration data and displaying them.
4. Providing the "House-keeping" data on display.
5. Continuous controlling of the photomultiplier gains.
6. Straggling "Back-up" data during flight.
7. Arranging telecomands to be sent to the on-board flight electronics.

Fig.(4.7) shows a typical presentation format of the Ground Support Equipments. The data is from a collimated ^{137}Cs source fixed above the centre of the central bar. Upper left is the counts distribution per bar pixel. Lower left is the top view of the c/r level curves of the whole detection plans. Upper right is the energy spectrum for that particular bar and finally, the lower right is the count rate distribution across the (9) position bars.

4.7 The performance of the telescope.

4.7.1 Spectral resolution.

Energy and positional resolution of the ZEBRA telescope have been evaluated using the calibration data given in Chapter 5. The energy resolution was measured for each single bar in (5) different positions along the bar for (6) different energy sources. The average energy resolution was calculated for each bar and then the overall resolution of the whole detection plane was evaluated. The result is fitted with a power law spectra as shown in fig.(4.8) and can be presented by :

$$\frac{\Delta E}{E}\,(F.W.H.M.) = 1.9\,(E)^{-0.44} \qquad (E \text{ in keV}) \qquad (4.5)$$

In the same way the positional resolution was evaluated as shown in fig.(4.9) and can be presented by :

$$\Delta x\,(F.W.H.M.) = 31\,(E)^{-0.41} \qquad (E \text{ in keV}) \qquad (4.6)$$

4.7.2 Image quality.

To evaluate the imaging quality of the ZEBRA telescope, a series of test images were taken including point and extended sources. A fully assembled position sensitive detection plane was operated in

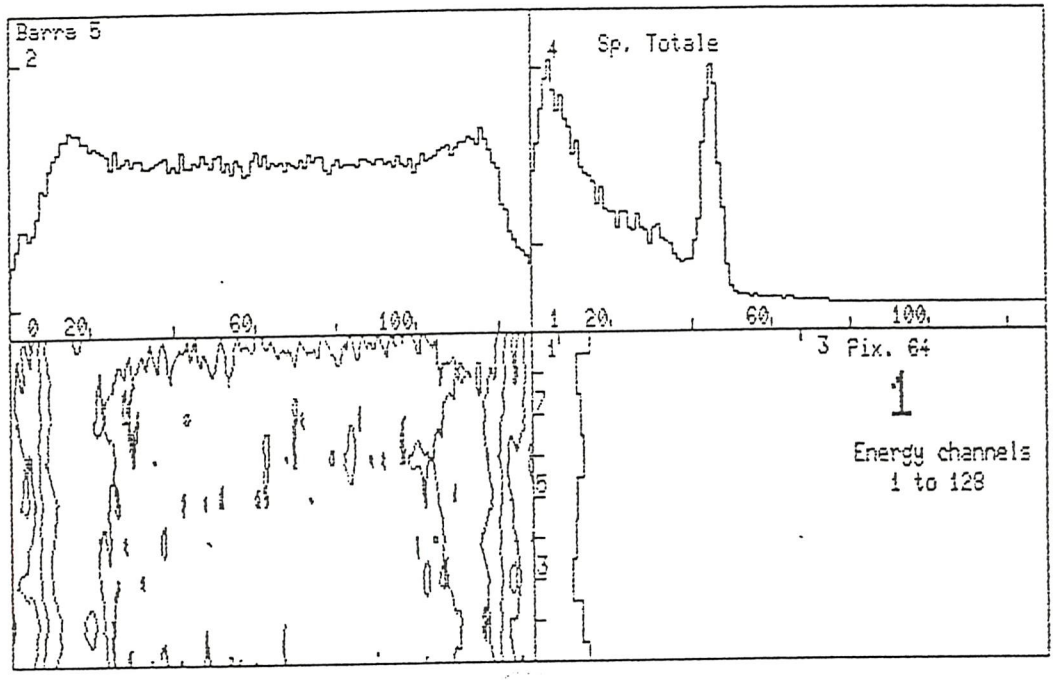

Figure (4.7) The GSE presentation for a collimated Cs^{137} source.

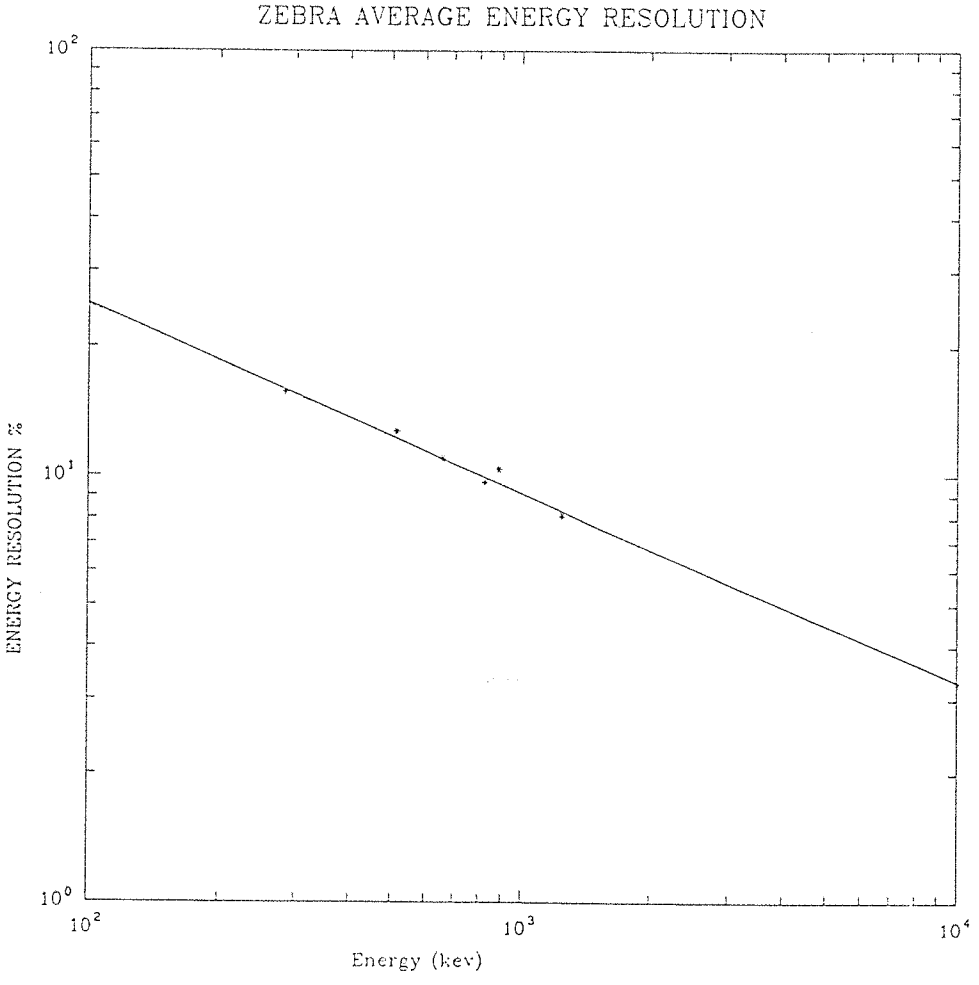

Figure (4.8) The average energy resolution for the detection plane of ZEBRA as a function of energy.

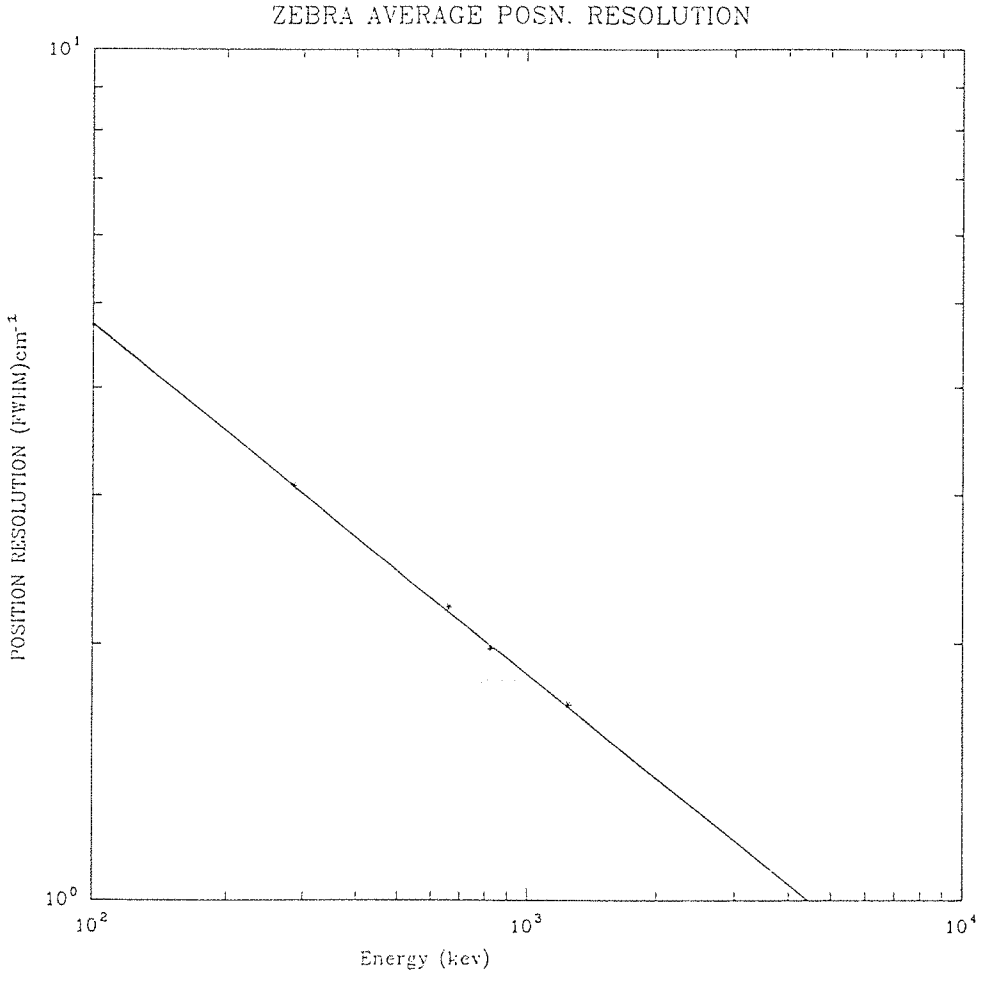

Figure (4.9) The average position resolution for the detection plane of ZEBRA telescope as a function of energy.

conjunctions with a CAMAC PDP 11/24 computer system in order to record spectral and positional data from interacting of gamma ray photons. A half size 9*7 pattern mask were used to create images from a series of gamma ray sources within the energy range (0.5-2.6) MeV (Butler et al 1985, Dean et al 1987).

The imaging configuration of the detection plane and the mask is shown in fig.(4.10). Data from the detection plane was collected via the CAMAC system and then processed by the PDP 11/24 computer fig.(4.11). The logic unit generates a gate only when the following criterion is satisfied :

$$Gate = N.(N-1).(N+1) \qquad (4.8)$$

where (N) is the coincidence signal from the (N^{th}) bar and (N-1), (N+1) are the signals from the neighboring bars of the (N^{th}) bar.

Two types of gamma ray sources were used for the evaluation of the imaging quality;point sources and extended sources. For these imaging tests, the detection plane was calibrated using a collimated ^{137}Cs source placed at three different positions along the bar. An energy look-up table was evaluated for each position sensitive detector to provide a uniform spectral response both down the length of the bars and between the entire set.

In the case of point source imaging, a powerful ^{137}Cs source with an intensity of 100μci was employed for the objective of this test. The source was fixed at more than 80 different positions on the object plane.

Images were accumulated for 10^5 events (which is roughly equivalent of $1.5*10^4$ source counts). The data were binned in (128) energy bins. 112 of these bins are corresponding to the central (49) cm. active region of the detectors. A straight forward analysis of this 9*112 data set and the 9*7 mask pattern allowed reconstruction of the source distributions; Fig(4.12) shows a typical image obtained from these tests.

To simulate an extended source, a point source was rotated within the field of view of the detection plane with different radiuses. Many images were taken. Fig.(4.13) illustrates the quality of a rotated ^{137}Cs sources with a radius of 20 cm.

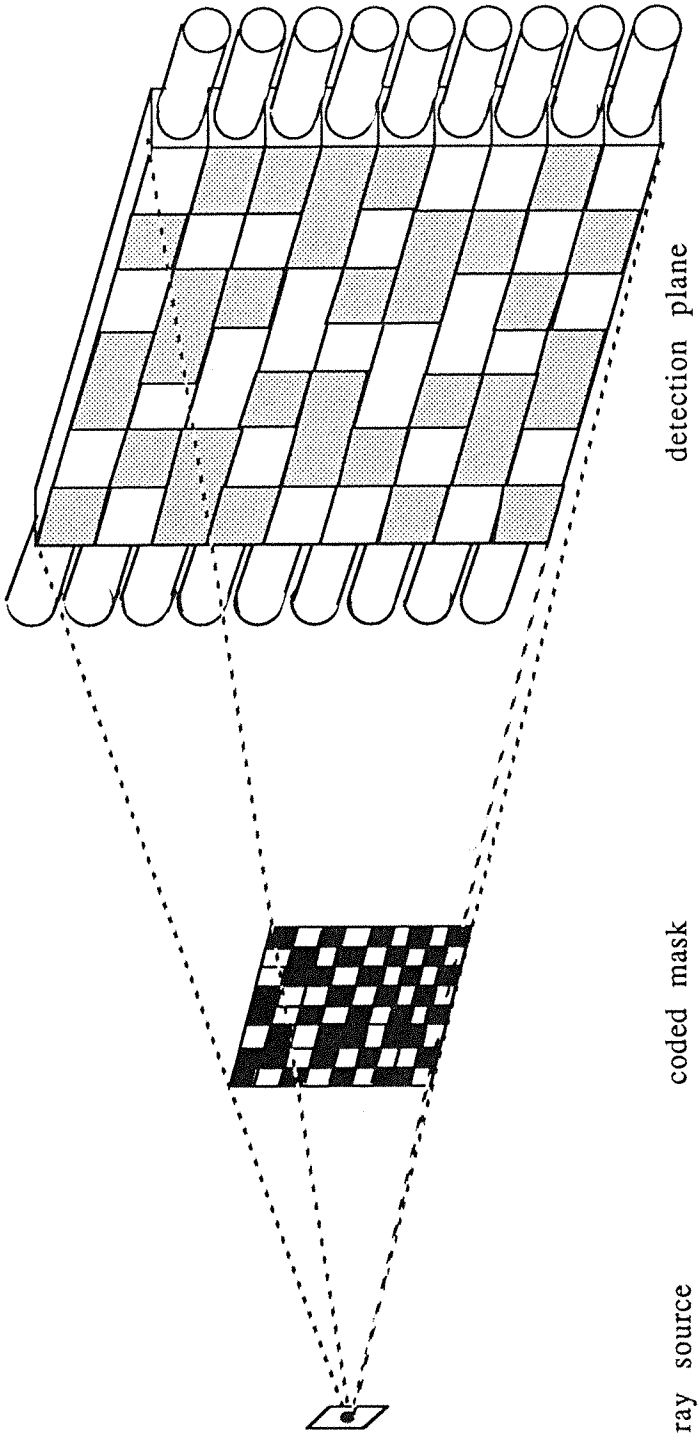

Figure(4.10) The geometrical arrangement of the laboratory imaging tests

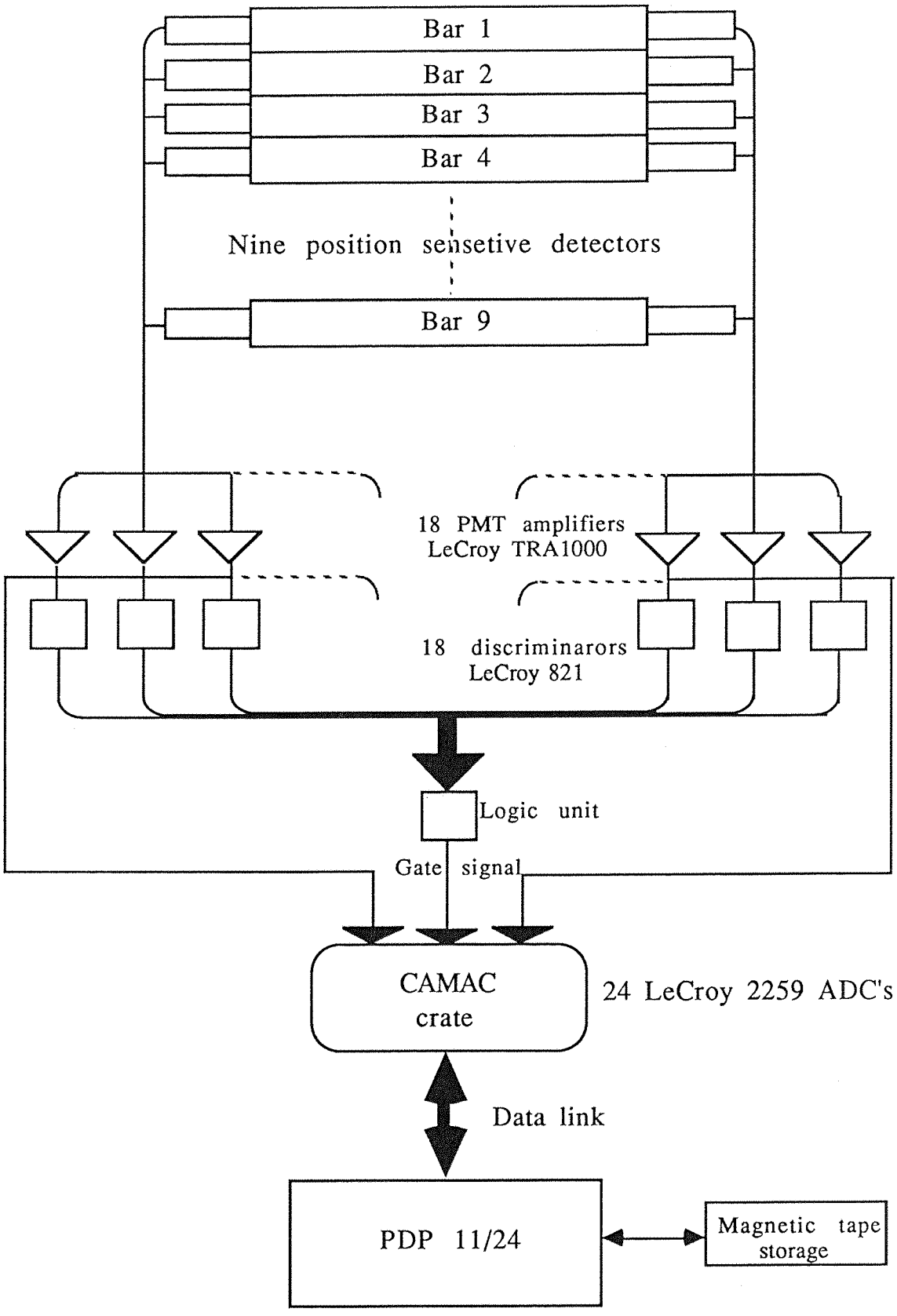

Figure (4.11) The experimental set-up of the nine bars imaging.

Figure (4.12)

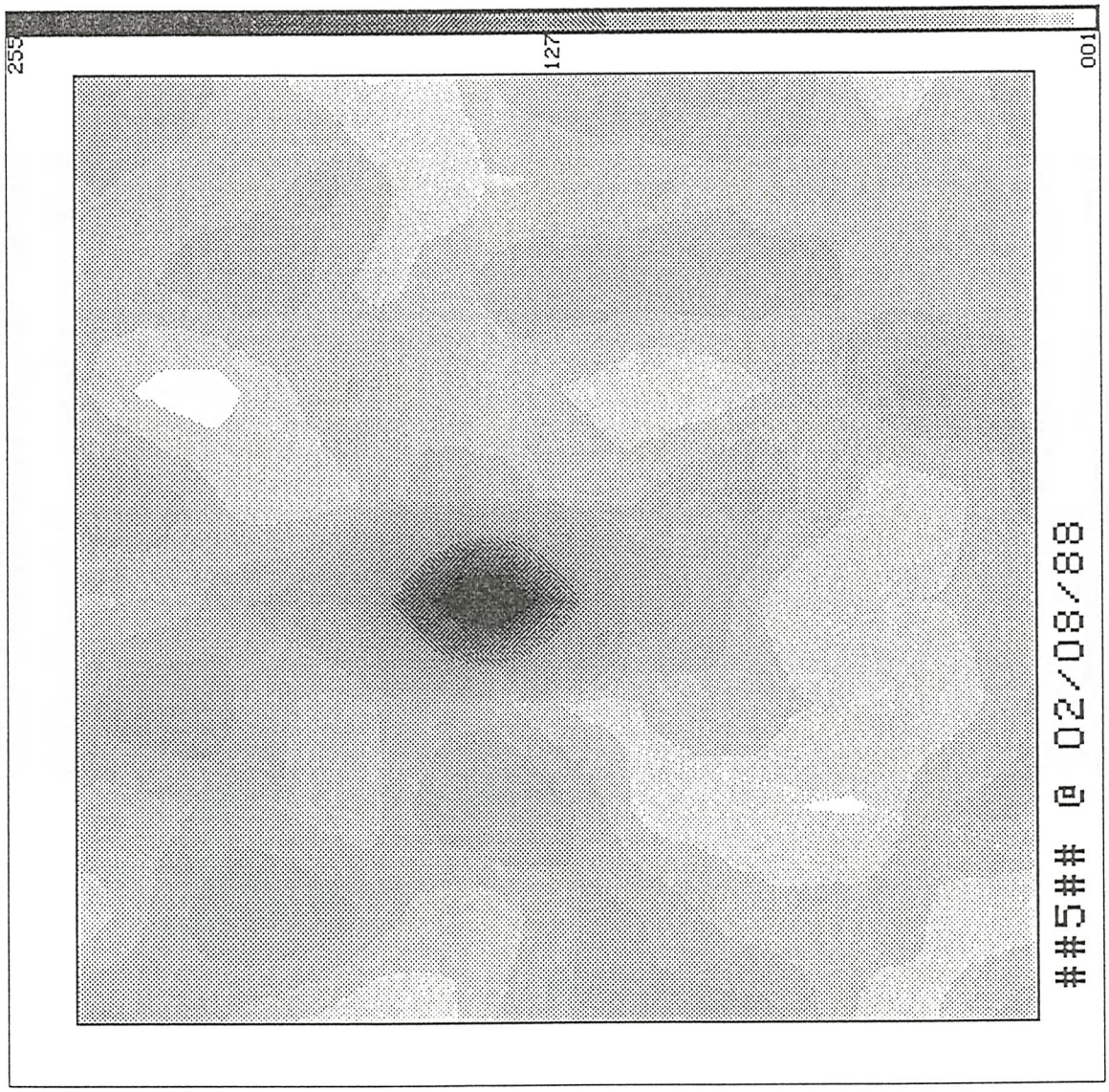

137Cs point source image : simple deconvolution ## ZEBRA – AIT ##

Figure (4.13)

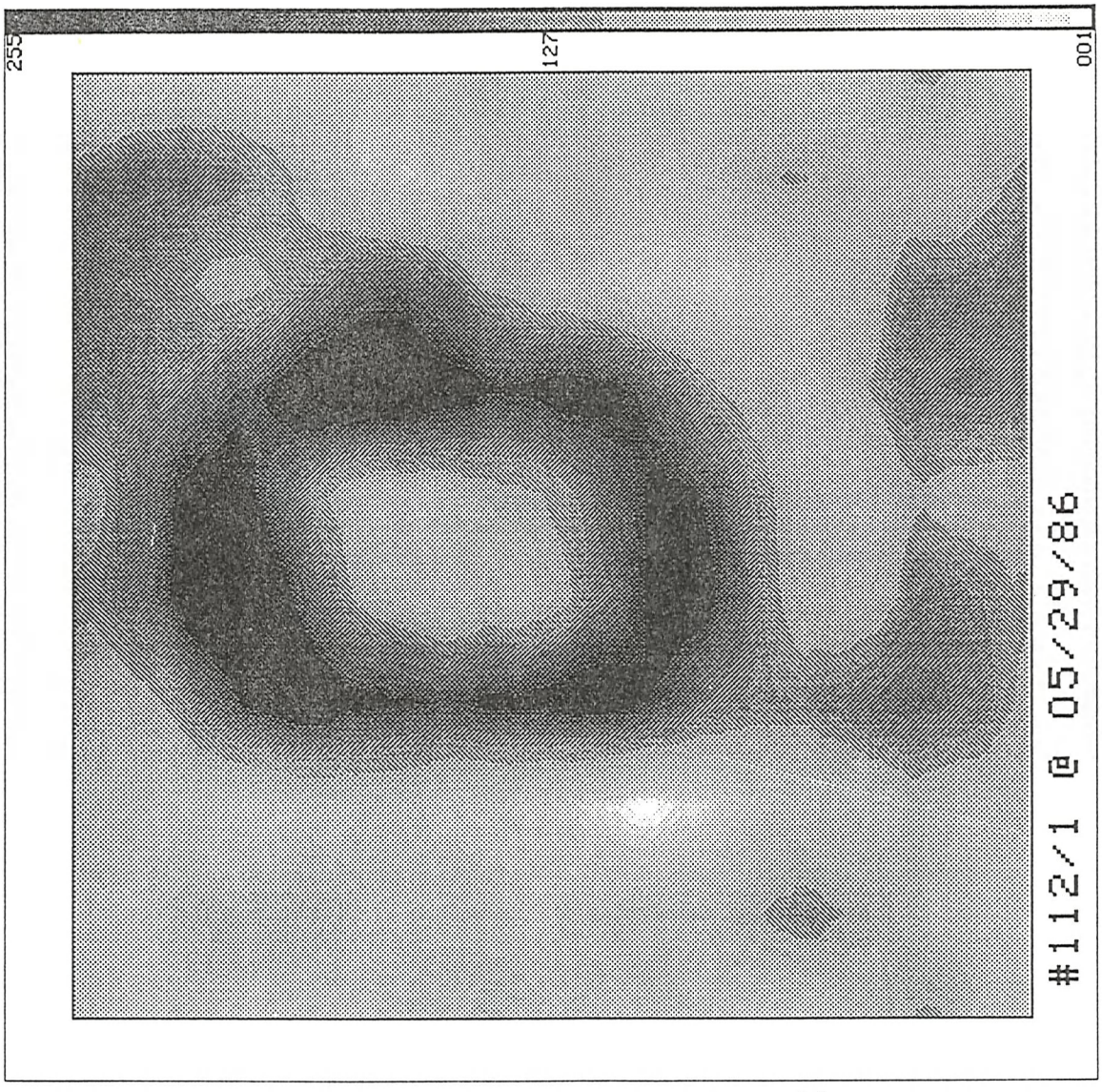

137Cs extended source image : simple deconvolution ## ZEBRA – preAIT ##

4.8 Comparison of ZEBRA telescope with current experiments.

ZEBRA telescope is a very encouraging experiment. It has demonstrated its ability of generating high quality images. This could lead to an enormous amount of data in this branch of astronomy and hence a better understanding of the universe. Table (4.1) gives the comparison of ZEBRA telescope with some of the current experiments such as; GRIP (Gamma Ray Imaging Payload, Althouse et al 1987) , DGT (Directional Gamma Ray Telescope, Dunphy et al 1987) and COMPTEL (Max-Plank Institute's Compton Telescope, Diehl 1988).

Table(4.1)
The Comparison of the ZEBRA telescope with some of the current experiments.

	ZEBRA	GRIP	DGT	COMPTEL
Energy Range(MeV)	0.2-10	0.03-5	0.16-9.3	0.1-30
Angular Resolution	61' * 56'	0.6°	16 * 24	1°
Field of View	8° * 9°	20°	15° * 23°	-
Energy Resolution at 1 MeV. FWHM %	9	7	13	10
Point Source Locability	1 arc min	3 arc min	1°	1°

Chapter 5

5 The performance of ZEBRA detectors.

5.1 Introduction.

In this chapter the theoretical consideration and the experimental performance of both position sensitive and anticoincidence detectors are described and the performance of other units related to the detection of gamma ray photons are evaluated. Also factors that affect resolution and system stabilization are discussed. A full detail of all of these is given bellow.

5.2 The position sensitive detectors.

5.2.1 Theoretical consideration of positional location of gamma ray photons.

If a gamma ray photon of energy E_γ interacts in a position sensitive detector at a distance of (x) from the midpoint of the bar as shown in fig (5.1), then the photomultiplier output signal at one end (E_L) can be described by :

$$E_L = E_\gamma . (\frac{P}{E_o}) . e^{-\alpha(L/2+x)} \qquad (5.1)$$

Similarly the signal at the other end (E_R) can be described by

$$E_R = E_\gamma . (\frac{P}{E_o}) . e^{-\alpha(L/2+x)} \qquad (5.2)$$

where;

α, is the light attenuation coefficient per unit length in each direction.

L, is the length of the bar.

P, is the probability of a light quanta produced at one end of the bar will generate a photoelectron in the nearby photomultiplier.

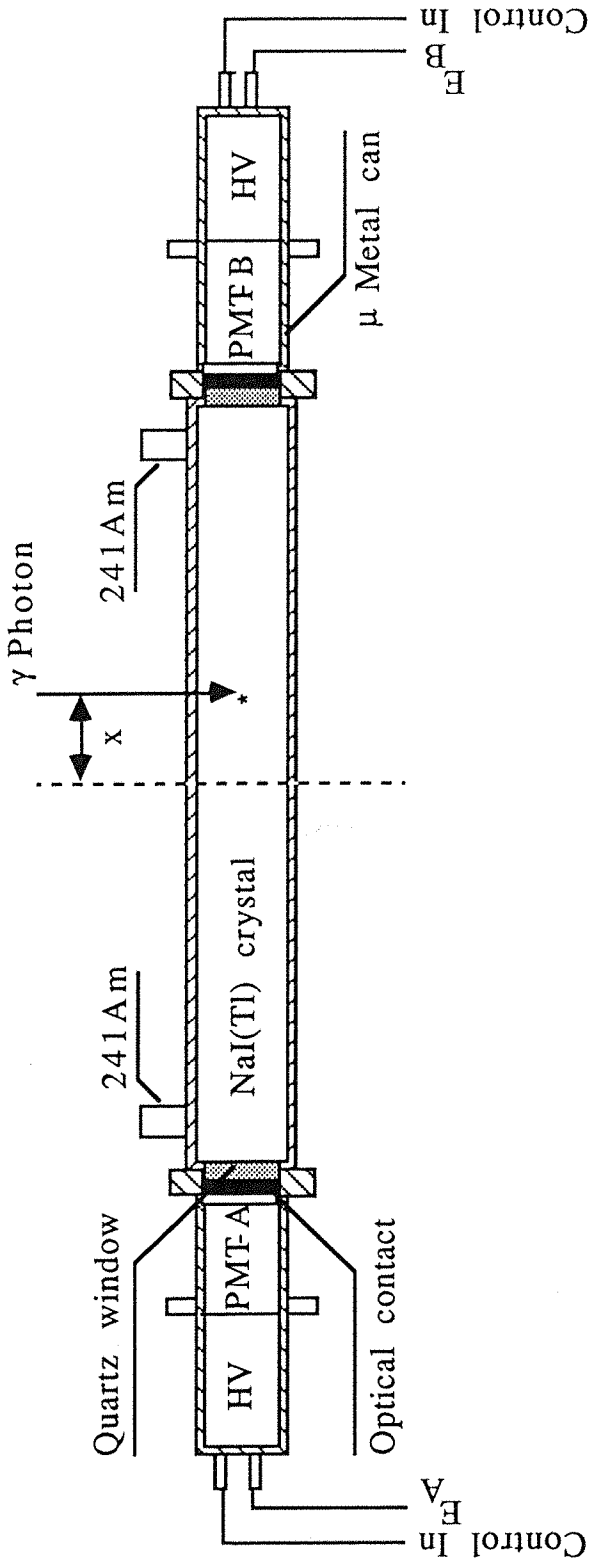

Figure(5.1) A position sensitive detector unit

E_o, is the energy required to emit a light quanta from the sodium iodide crystal per keV.

Dividing (5.2) by (5.1), the position of interaction of an event can be determined and described by :

$$x = \frac{ln\,(E_R/E_L)}{2\alpha} \qquad (5.3)$$

To evaluate the error in the position, it has been assumed that the error in $(E_L \text{ and } E_R)$ are Poissonian and can be expressed by :

$$\delta x = \frac{1}{2\alpha.\sqrt{E_\gamma.P/E_o}}.\, e^{\alpha L/4}.\, \sqrt{e^{\alpha x}+e^{-\alpha x}} \qquad (5.4)$$

To evaluate an optimum attenuation coefficient for each bar, equation (5.3) must be integrated with respect to (L) and then differentiated with respect to (α). The result of this operation must be then equated to zero ant this leads to an optimum value of :

$$\alpha L = 2.9 \qquad (5.5)$$

ZEBRA position sensitive detectors were ordered from BICRON Corporation (U.S.A.) to match this attenuation specification.

5.2.2 Theoretical consideration of spectral resolution.

The energy deposited on a position sensitive detector as a result of the interaction of a photon at a distance of $(x)cm.$ from the mid point can be obtained from the multiplication of equation (5.1) and (5.2). The result is given by :

$$E_\gamma = e^{\,\alpha L/2}\,.\,\sqrt{E_L.E_R}\,.(\frac{P}{E_o}) \qquad (5.6)$$

and the standard error in the energy (E_γ) can be expressed by :

$$\delta E_\gamma = \left(\frac{e^{\alpha L/4}}{2P/E_o}\right) . \sqrt{E_\gamma.(P/E_o).} \sqrt{e^{-\alpha x}+e^{\alpha x}} \qquad (5.7)$$

5.2.3 Departure from the ideal case.

So far only the theoretical calculations of the interaction position of an event and the deposited energy have been considered. Experimentally it has been found that the position sensitive detectors do not have the same attenuation coefficient in both directions, which means two different values of (α) must be used in all calculations. Therefore the signal outputs from both photomultiplier tubes must be described by :

$$E_L = E_\gamma . \left(\frac{P}{Eo}\right) . e^{-\alpha_L(L/2+x)} \qquad (5.8)$$

$$E_R = E_\gamma . \left(\frac{P}{Eo}\right). e^{-\alpha_R(L/2-x)} \qquad (5.9)$$

where (α_L) *and* (α_R) are the attenuation coefficients from left to right and right to left receptively.

This difference in (α) values was found to be of the order of 2% over a sample of 10 bars. This difference is presumed to be due to the method of treatment of the crystal surfaces.

After the re-arrangement of equation (5.1)and(5.2) to (5.8)and(5.9), the position of location of an event can be described by:

$$x = \frac{ln\,(E_R/E_L)\,-L/2(\alpha_L-\alpha_R)}{(\alpha_L+\alpha_R)} \qquad (5.10)$$

and the F.W.H.M. position resolution can be described by :

$$\delta x = \frac{1}{(\alpha_L+\alpha_R)} . \sqrt{E_\gamma . Po/E_o} . \sqrt{(e^{\alpha_L(L/2+x)} + e^{\alpha_R(L/2-x)})} \qquad (5.11)$$

The same correction is required to the calculation of the energy and the final version can be expressed by :

$$E_\gamma = (e^{L/4\ (\alpha_L+\alpha_R)} . e^{-x/2(\alpha_R-\alpha_L)} . \sqrt{E_L . E_R} .)(\frac{P}{E_o}) \qquad (5.12)$$

and the error in the calculation of (E_γ) can be described by :

$$\delta E_\gamma = (e^{L/4(\alpha_L+\alpha_R)} . e^{x/2(\alpha_R-\alpha_L)})(\frac{2P}{E_o}) . \sqrt{E_\gamma . (P/E_o)} . \sqrt{e^{-\alpha_L(L/2+x)} + e^{-\alpha_R(L/2-x)}}$$

$$(5.13)$$

5.2.4 Light attenuation along the detectors.

The surface of the position sensitive detectors have been treated in such away that the light intensity is attenuated along the bar. According to the ordering specification, the attenuation of the scintillation light must have a roll off function within the range of a minimum 100:10, and a maximum 100:8 over the central 50cm. of the position sensitive detector.

To evaluate the performance of these detectors, a 12 way analog to digital convertor controlled by a PDP 11/24 CAMAC system was employed. The tests were performed using a collimated ^{137}Cs (662 keV) source directly above the detectors. A typical experimental light attenuation along a position sensitive detector (serial no. DX-508) is shown in fig(5.2). These experimental data points, for a

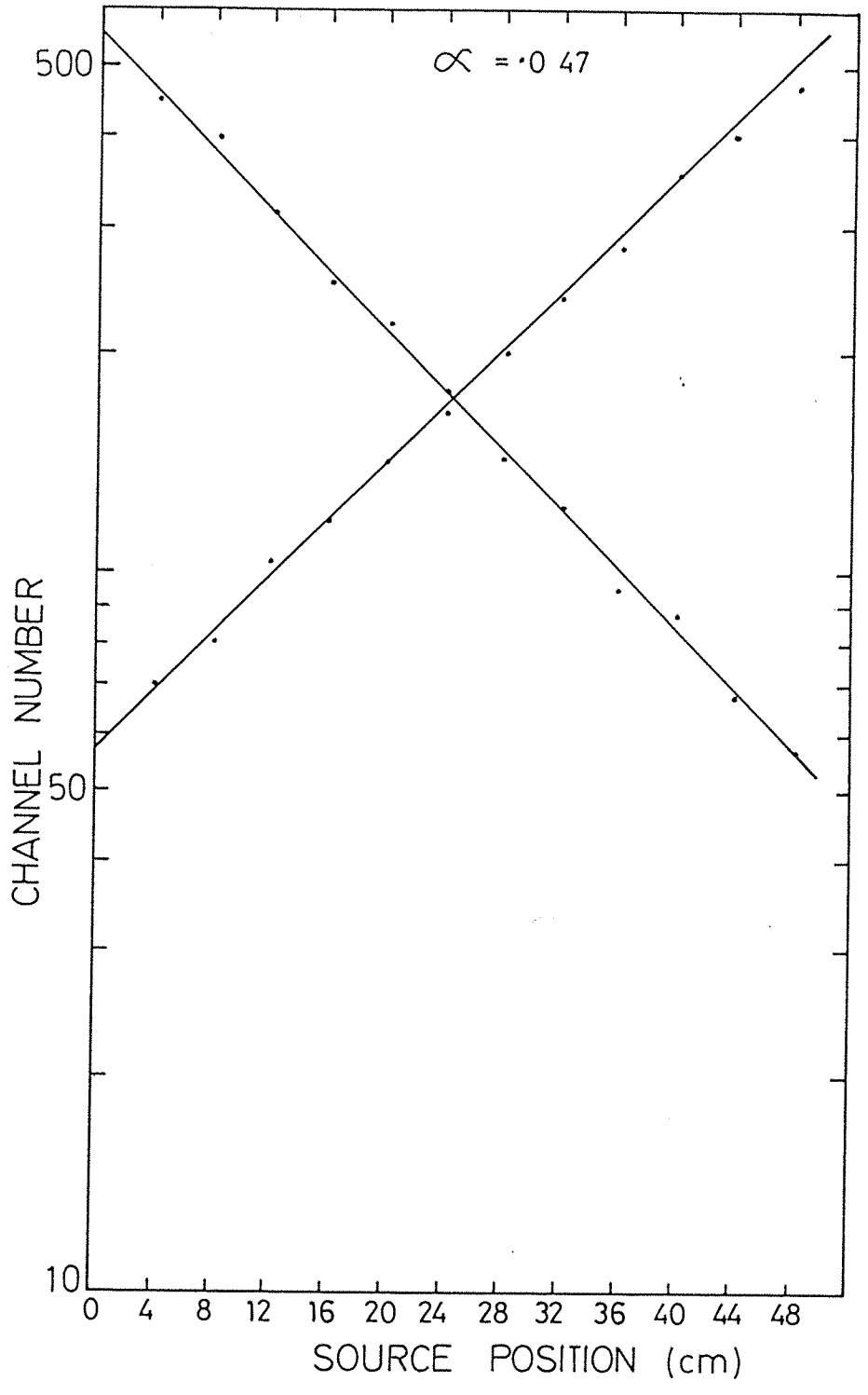

Figure (5.2) The light attenuation curve along one ZEBRA position sensitive detector.

sample of 10 detectors, were fitted using a least square method. Table(5.1) shows the attenuation coefficient obtained. The maximum deviations from the straight lines were also calculated. The average value of α was found to be 0.27-0.25 which is within the optimum specification range.

The light collection efficiency increase for events which occur close to the photomultiplier tubes. This is due to the fact that the probability of photons reaching the nearby photocathode without attenuating at the surface is grater. This leads to a large error in the position using the e^{-x} relationship. The extent of this problem was, however, reduced by using a slightly degraded reflection compound on the crystal surface near the ends of the bar.

5.2.5 Calibration of position sensitive detectors.

The position sensitive detector have been calibrated using a computer controlled data acquisition system based on a PDP 11/23 (Boella et al 1986). This system is able to position a collimated gamma ray source at any desired point above the bar to an accuracy of 0.1 mm.

The first stage of the calibration employed a ^{137}Cs source to normalize the gain of the two photomultiplier tubes to a few percent of their final values. The energy and position of each event was calculated. Then the source was moved to the next position and the same procedure was repeated. This data and the spectrums of each tube was accumulated in the memory of the computer and later dumped to magnetic tapes.

This data was analyzed to calculate the attenuation coefficient along the bar in each direction. Also the energy and the position resolution as a function of position were calculated. The result of a typical position sensitive detector is given in fig.(5.3) which compares the theoretical and experimental energy and position resolution versus position. Table (5.2) shows the energy and position resolution for a sample of (9) position sensitive detectors. The average energy resolution for a ^{137}Cs source at the centre of the bar is 9.7% and the average position resolution is 1.93cm..

Table (5.1)
The attenuation coefficients for 10 position sensitive detectors with the maximum deviation from the from the fitted data.

Bar Serial No.	Attenuation Coefficient cm^{-1}	(αL)Value	Maximum Deviation%
DJ-292R	αL = 0.04820	2.70	5.2 @ 52cm
	αR = 0.04715	2.64	4.7 @ 4 cm
DJ-293R	αL = 0.04472	2.50	5.5 @ 2 cm
	αR = 0.04364	2.44	2.8 @ 54cm
DJ-294R	αL = 0.04783	2.68	4.8 @ 2 cm
	αR = 0.04668	2.61	3.8 @ 54cm
DJ-295R	αL = 0.04803	2.69	2.3 @ 2 cm
	αR = 0.04862	2.72	4.8 @ 54cm
DJ-296R	αL = 0.04744	2.66	2.1 @ 2 cm
	αR = 0.04833	2.71	3.4@ 54cm
DJ-297R	αL = 0.05267	2.95	2.4 @ 8 cm
	αR = 0.05177	2.90	4.7 @ 53cm
DJ-289R	αL = 0.04911	2.75	3.9 @ 52cm
	αR = 0.04931	2.76	5.5 @ 2 cm
DI-587R	αL = 0.04822	2.70	2.6 @ 2 cm
	αR = 0.04782	2.68	2.7 @ 32cm
DI-588R	αL = 0.04703	2.63	1.3 @ 52cm
	αR = 0.04868	2.73	4.2 @ 54cm
DI-964R	αL = 0.05038	2.82	3.5 @ 2 cm
	αR = 0.04936	2.76	2.3 @ 2 cm

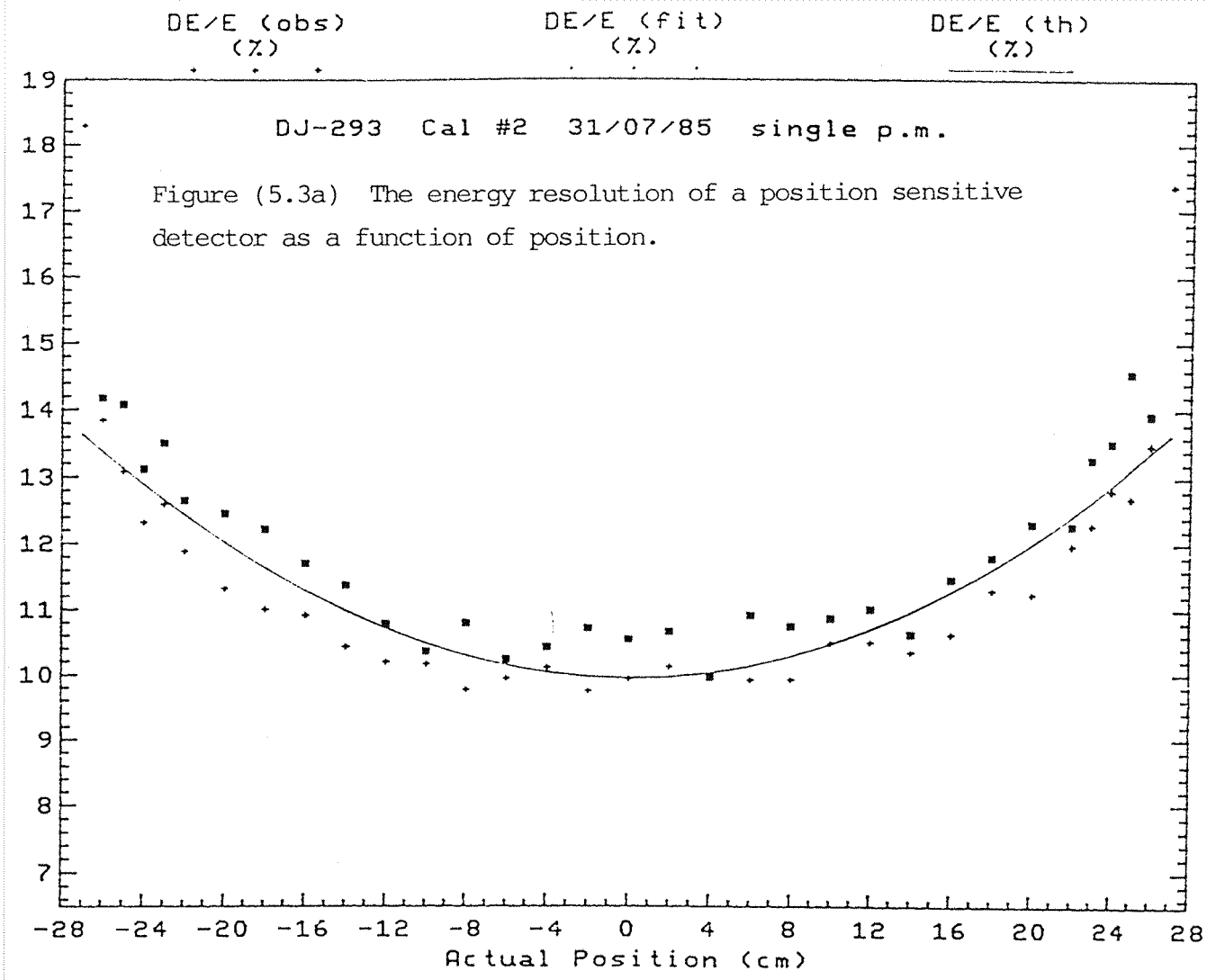

Figure (5.3a) The energy resolution of a position sensitive detector as a function of position.

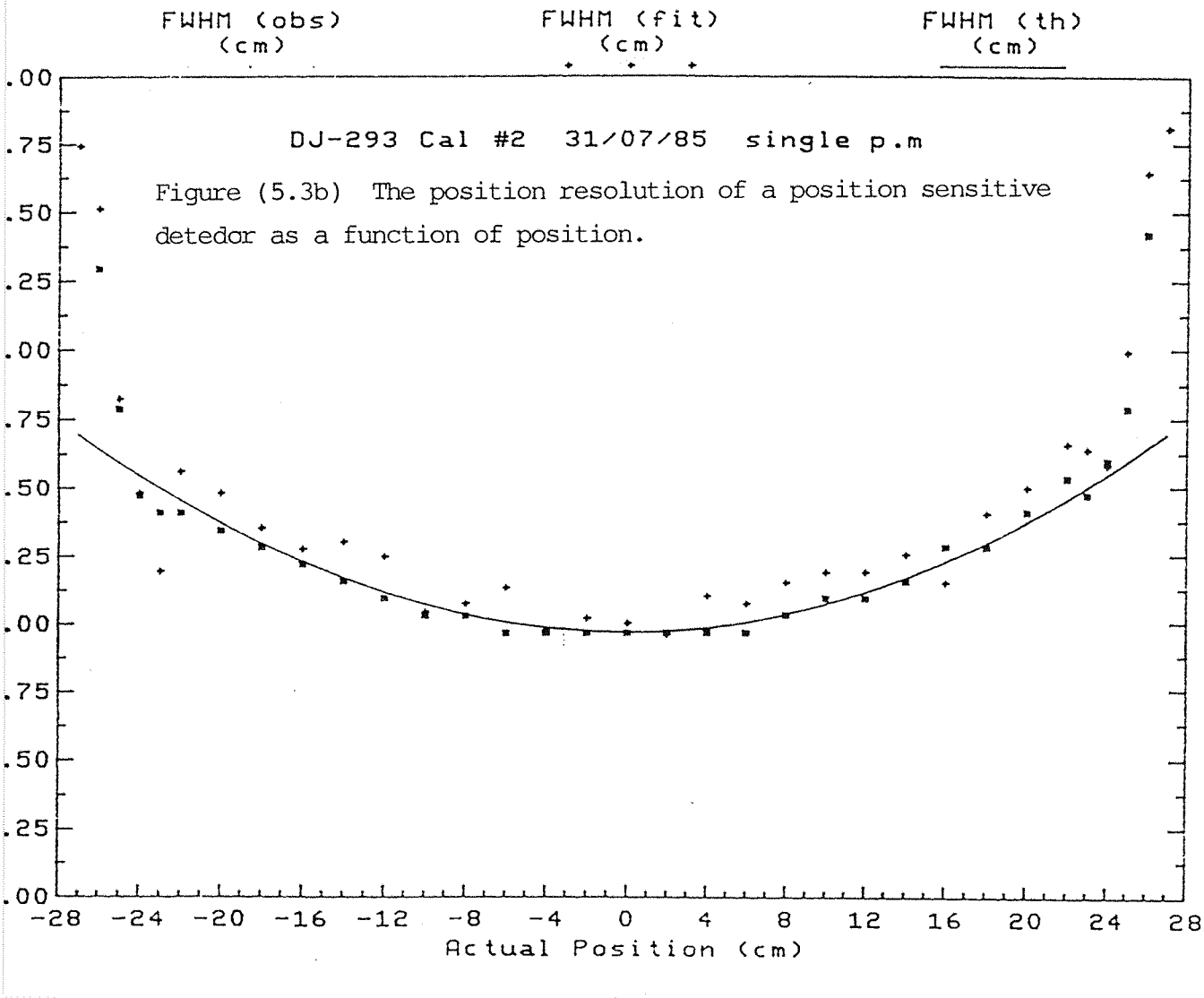

Figure (5.3b) The position resolution of a position sensitive detedor as a function of position.

Table(5.2)
The spectral resoultions of a sample of 9 position sensitive detectors using the callibration data (collimated ^{137}Cs source fixed at the centre of the bars).

Bar Serial No.	Energy Resoluiton (%) FWHM	Positional Resoultion (cm) FWHM
DP-785	9.705	2.038
DP-786	9.716	2.014
DP-788	9.462	1.931
DP-817	10.001	1.883
DP-818	9.469	1.888
DP-819	9.213	1.766
DP-820	9.355	1.873
DP-821	9.699	1.959
DP-854	11.071	2.046

Fig.(5.4) shows the attenuation of light along the bar in each direction. There is a systematic effect of the order of 1-2% in the central region of the bar and up to 5% in the last 5cm. of the ends. This is due to the deviation from the ideal case. These errors in calculating the energy and position of each event were measured and correction look-up tables were applied to the results of the calculations. However, to reduce these systematic errors, only the central 49cm. of the bar was taken in consideration of all calculations.

The ratio of the incident gamma ray energy (E_γ) to the calculated (E_{cal}) as a function of position is given in fig.(5.5). Also the difference between the calculated event position (x_{cal}) and the actual event position (x_{act}) versus actual event position is shown in fig.(5.5).

5.3 The anticoincidence detectors.

5.3.1 Light attenuation along the detectors.

No attenuation along the detectors were required for this type of NaI crystals but the best that the manufacturers could produce was an attenuation of 3:1.

The experimental evaluation of the light attenuation along these detectors were achieved by using a collimated ^{137}Cs source. The signals were passed to a multichannel analyzer through amplifiers. A typical light attenuation of an anticoincidence bar (serial no. DJ-566R) is shown in fig.(5.6).

5.3.2 Calibration of the anticoincidence detectors.

The anticoincidence detectors were calibrated in the same way of the position sensitive detectors. First the computer controlled data acquisition system, mentioned earlier, was used to normalize the two photomultiplier tubes to a few percent of their final values. Again the energy and position of each event was calculated. The only difference between calibrating an anticoincidence bar and a

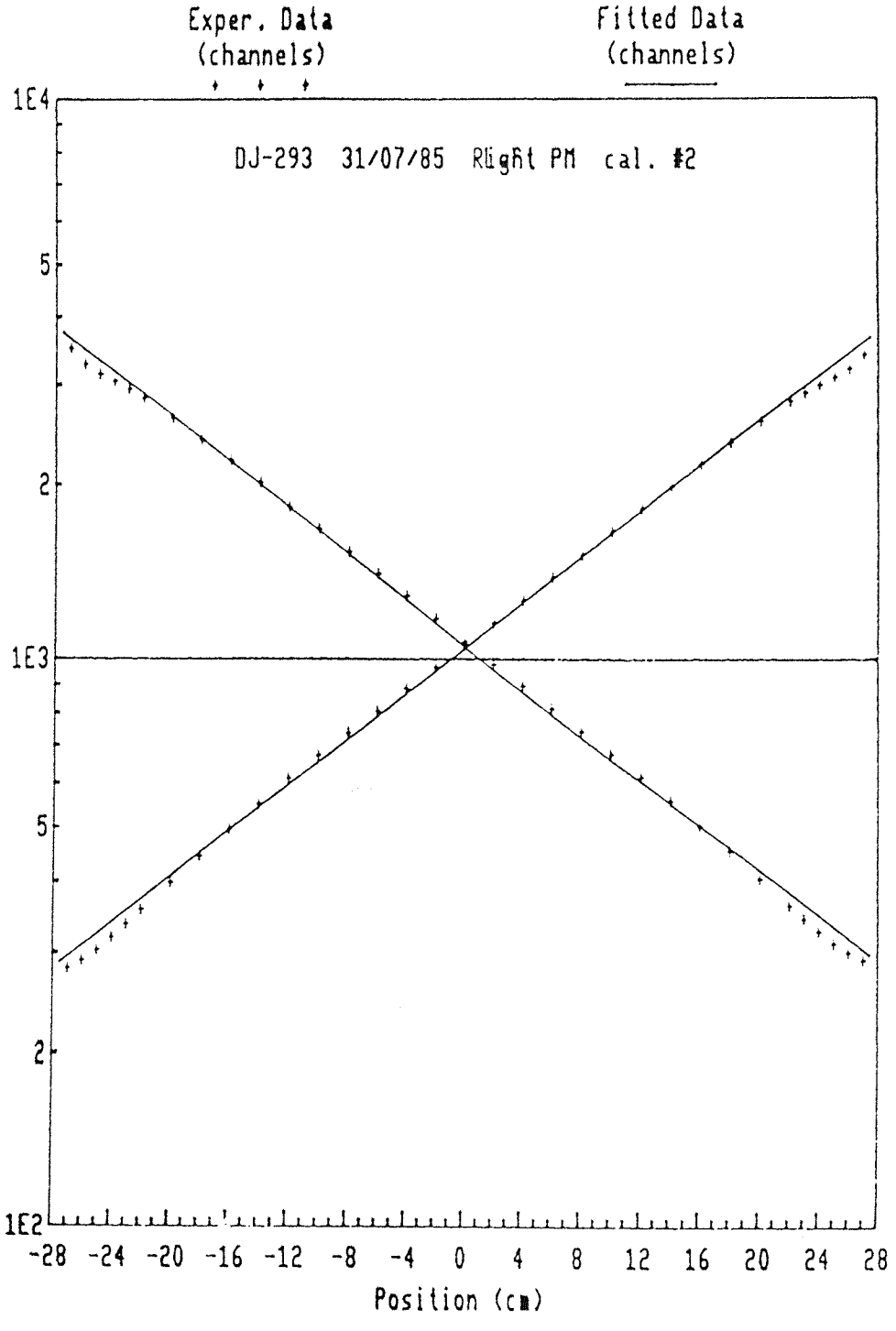

Figure (5.4) The light attennation curves as a function of position in both directions down a position sensitive detector.

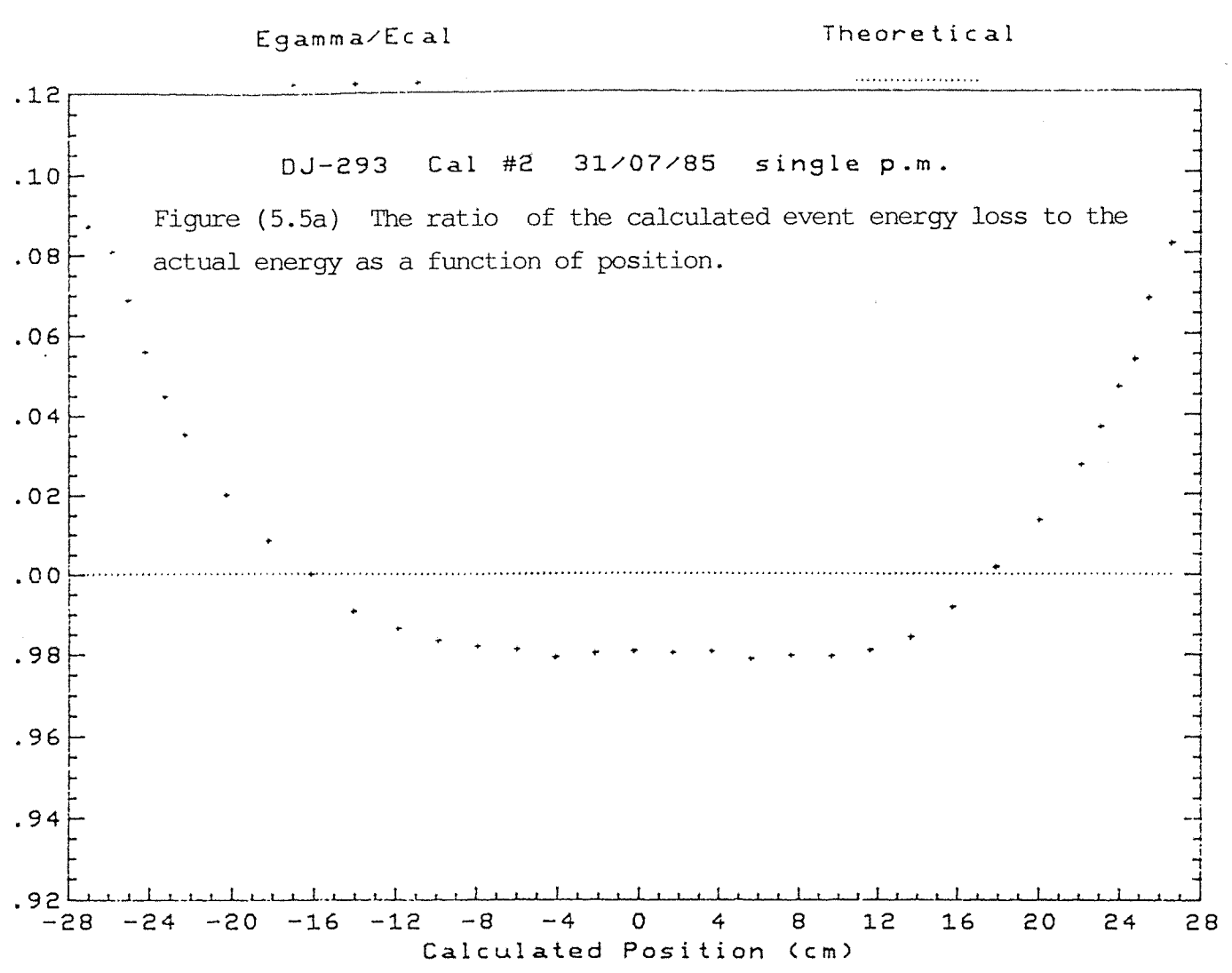

Figure (5.5a) The ratio of the calculated event energy loss to the actual energy as a function of position.

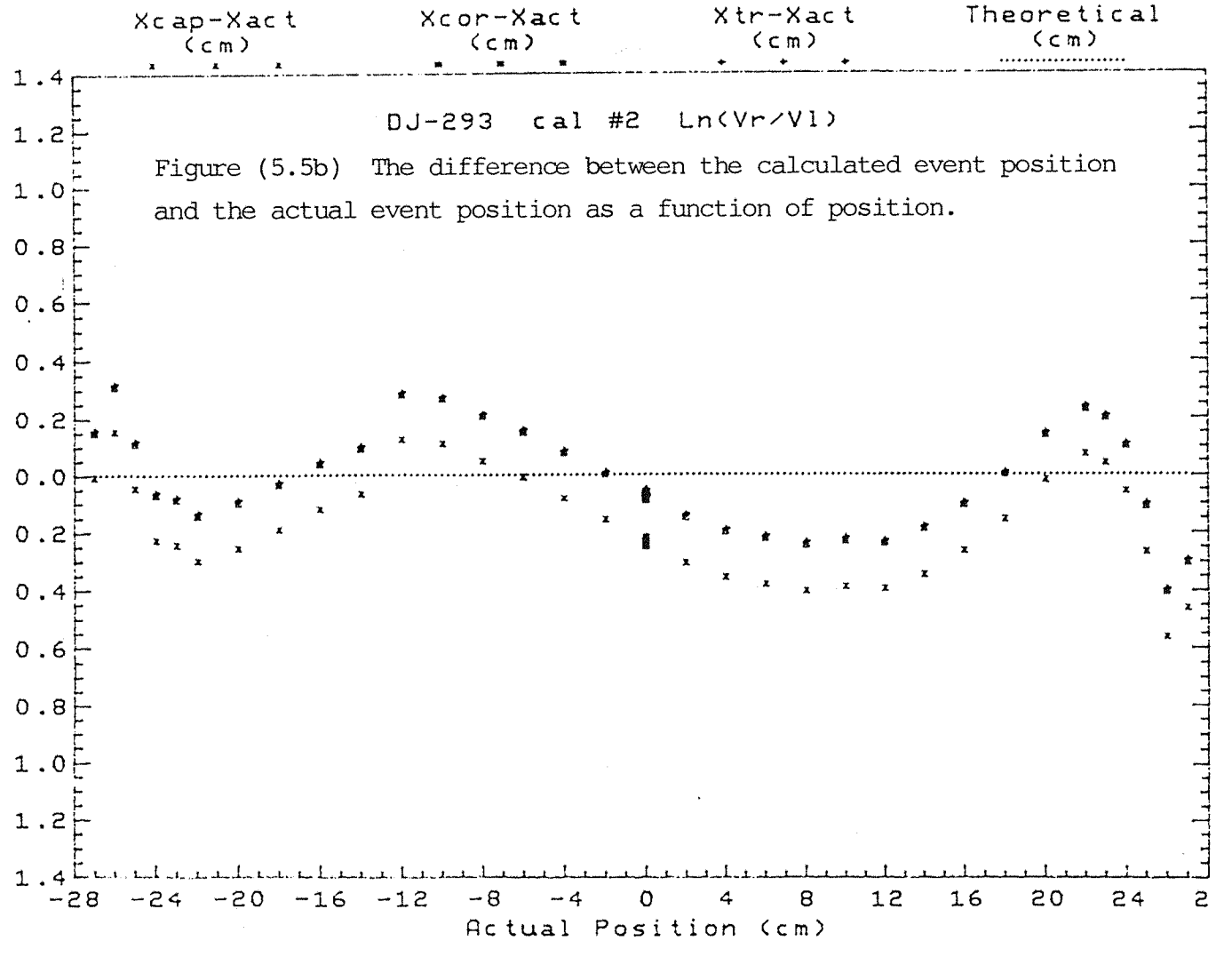

Figure (5.5b) The difference between the calculated event position and the actual event position as a function of position.

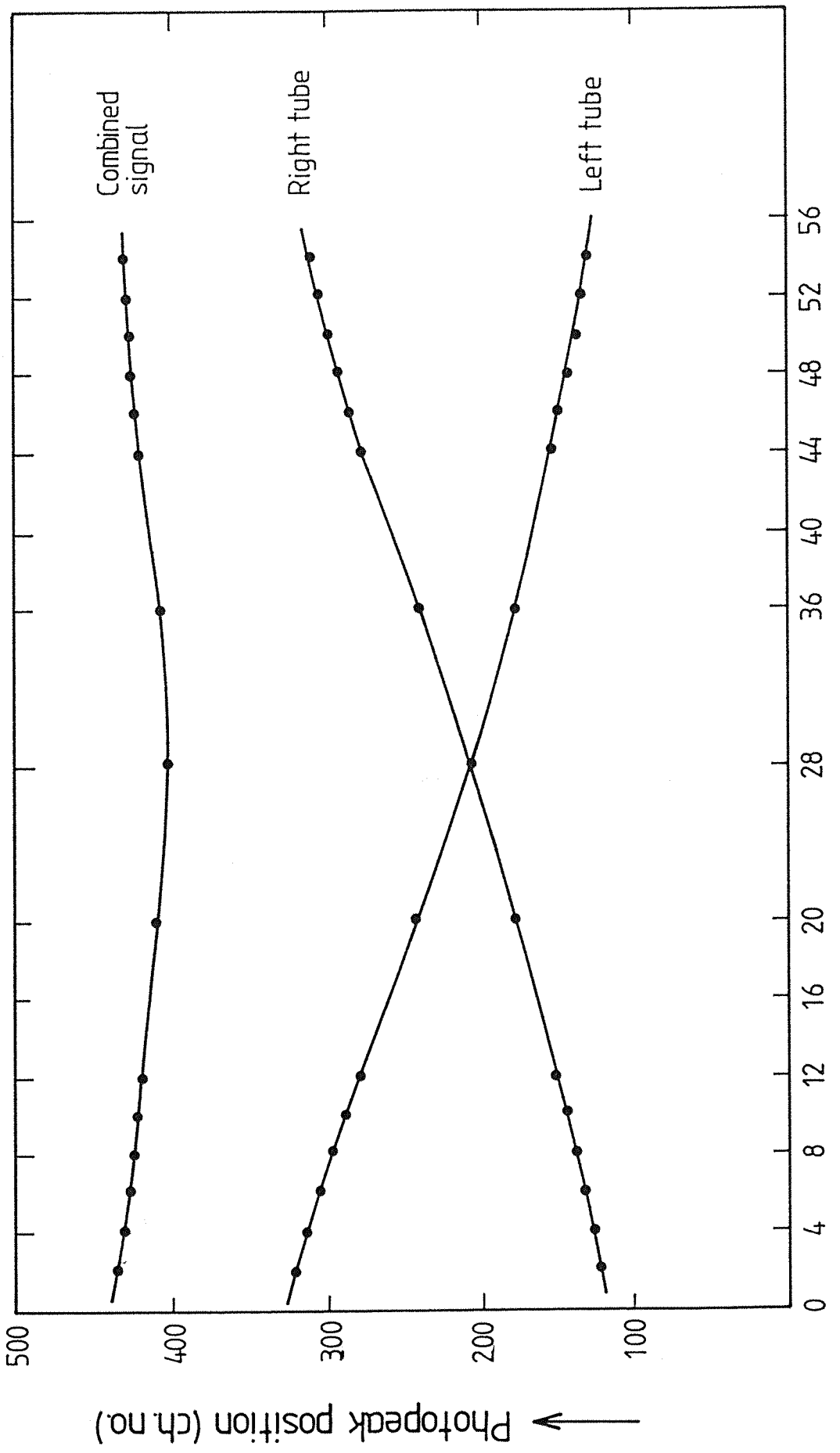

Figure (5.6) The light attunation curve for an anticoincidence bar of ZEBRA telescope.

position sensitive one was that fewer positions along the bar were used. The data was analyzed and the energy and position resolutions were also calculated as a function of position.

5.4 Factors affecting resolution.

There are many factors which effect the pulse height spectrum of scintillators. These effects have been studied theoretically and experimentally by many authors(e.g. Wright 1954 , Prescott and Takhar 1963 ..etc.). Briefly these factors are :

(i) The emission of photons by the scintillator: There is a statistical variation in the number of photons per scintillation due to the non-uniform distribution of activator ions and the crystal defects. Also successive particles may lose different amounts of energy in the scintillator due to scattering and edge effects. All these effect the number of photons emitted by the scintillator.

(ii)The collection of photons by the photocathode: Since the scintillations occur in different positions along the crystal bar, the light collection efficiency depends on the position of the scintillation. To reduce the spread of the spectrum distribution, light pipes or optical contacts have been employed to achieve this aim. In ZEBRA's case many tests have been performed to find the best optical contact which produce an optimum spectrum (details are given in section 5.6).

(iii)The emission of photoelectrons by the photocathode: The number of photoelectrons emitted from the photocathode due to each scintillation statistically varies from one cathode to another and from one point to another in the same cathode. Cathodes also emit thermal electrons which play a role in the variation of the pulse-height distribution.

(iv) The collection of photoelectrons and the multiplication process in the dynode chain: The emitted photoelectrons from the cathode must reach the first stage of the dynode structure. These photoelectrons can be easily deflected from their path by magnetic fields. The Earth's magnetic field is large enough to achieve this.

Therefore, it is necessary to have a high voltage between the cathode and the first dynode without increasing the tube's noise. This voltage will not only reduce the deflection of the photoelectrons but also increases the number of secondary emission and this will improve the resolution automatically. In the case of the ZEBRA experiment, the photomultiplier tubes mounting countainers are made of *μ–metal* to reduce the effect of extraneous magnetic fields.

5.5 The photomultiplier tubes and their performance.

The spectral resolution of a detector is highly dependant on the spectral sensitivity of the photomultiplier tubes. Therefore it is essential to employ tubes with high quantum efficiency and whose output remain linear over the dynamic range of the scintillator crystal.

The pulse height spectrum of a photomultiplier tube depends on few factors. First of all the initial number of photoelectrons emitted by the photocathode after the occurrence of the scintillation in the crystal. Secondly, the electron gain, which depends on the geometry, number and efficiency of dynodes.

The photomultipliers coupled with the ZEBRA detectors are HAMAMTSU R878-01 tubes. These tubes have very high resolution due to the =100% collection efficiency of photoelectrons from the cathode by the first dynode. It was also found that the light output of these tubes remain linear over the dynamic range of the telescope. These results and more of the characteristics of these tubes are given by (Gil 1987).

5.6 The selection of optimum optical contact.

It is highly essential that the emitted light from the crystal scintillator must not be absorbed by the crystal itself. Although the detectors are coupled optically with the potomultiplier tube window, a large quantity of light will be critically reflected. This light must be returned to the crystal and directed to the exit once

again. This aim can be achieved by grinding the crystal surface so the light can be returned to the window at a suitable angle within the critical angle (Siegbahn 1955).

The method of joining the crystal with the photomultiplier tube window using an optical interface is a successful method. In this way the critical angle can be increased which leads to a reduced amount of light that needs to be recirculated in the crystal.

In the following sections a full description of the test for selecting an optimum optical for ZEBRA is given with a discussion of the results.

5.6.1 Test configuration and results.

A series of tests were performed on a NaI position detector and photomultiplier tubes to evaluate the optimum pulse height resolution. Several types of material were used as the interface between the NaI crystal and the tube. The interface material tested were Eccosil 2cn, Silicone fluid, RTV-2 silicone rubber VP7612 and Air gap.

The first part of the tests carried out using both sides of the detector. Analyzing each event in coincidence and looking at the pulse height distribution through a PDP 11/24 CAMAC system computer as show in fig.(5.7). A collimated ^{137}Cs source was used as a standard reference. The optical interface material which was used were :

(i) Silicone fluid, refractive index 1.403 at 25°C..

(ii) Eccosil 2cn, refractive index 1.408 at 25°C..

(iii)Air gap 2.35 mm thickness.

The data obtained shows that the energy and position resolutions in the centre of the bar are as follow :

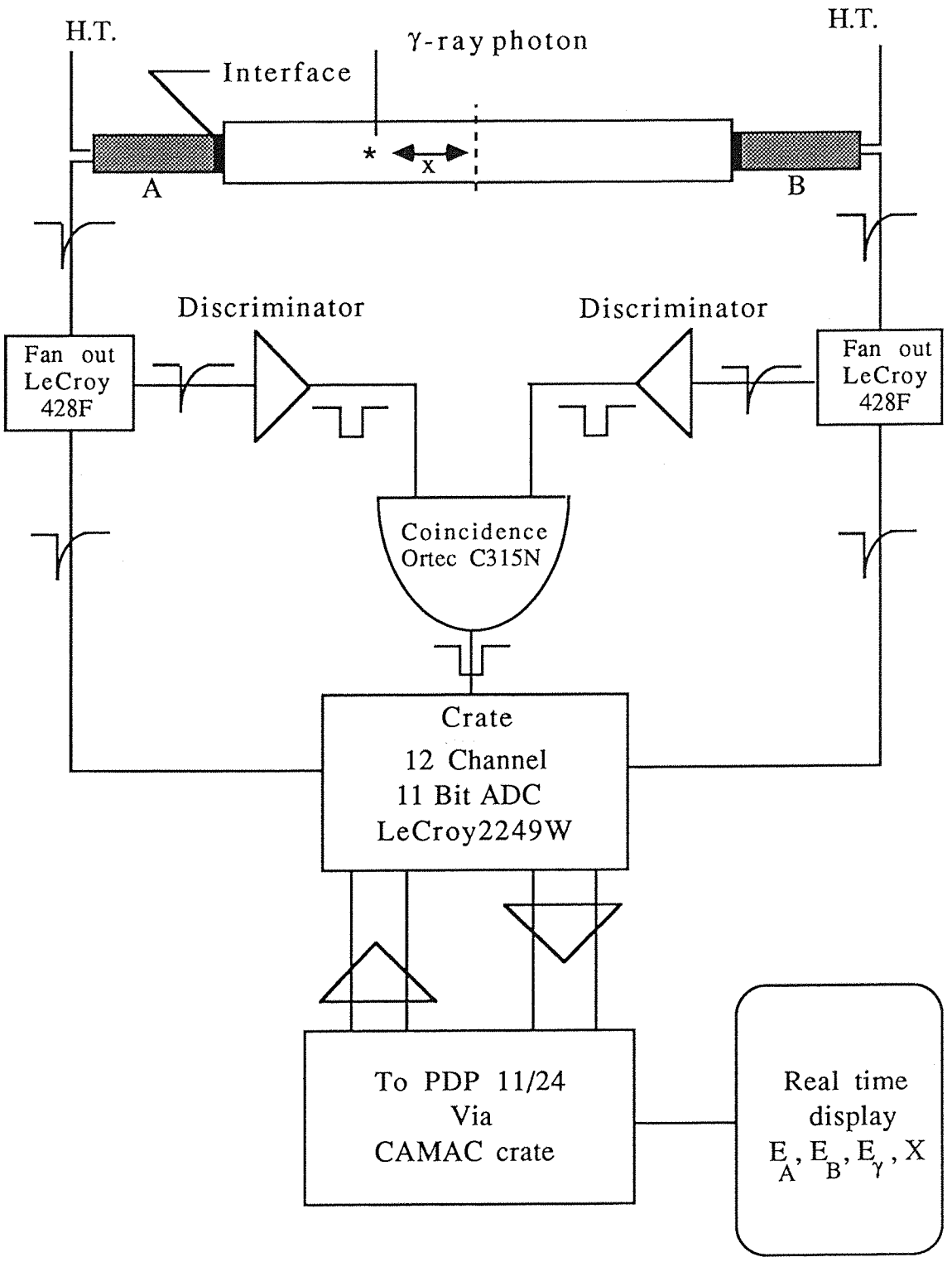

Figure(5.7) A block diagram of the system used for the optical contact tests

	Optical joint	Energy resolution % F.W.H.M.	Position resolution cm. F.W.H.M
(i)	Silicone fluid	11.60	2.1
(ii)	Eccosil 2cn	12.93	2.4
(iii)	Air gap	14.31	2.8

Fig.(5.8) and (5.9) illustrate the comparison of the position and energy resolutions along the bar for the ^{137}Cs source for the three interfaces use.

Fig.(5.10) shows the energy and position spectrum for a collimated ^{137}Cs source (28cm.) from the left. The energy spectrum is windowed around the photopeak.

The second part of the tests used one tube of an anticoincidence bar (serial no. DJ-580R). The signal being analyzed in a multichannel analyzer as shown in fig.(5.11). Once again a collimated ^{137}Cs source was used as a reference source and placed 20cm. from the end of the bar. The interface materials used and the data obtained from the tests are listed in table (5.3).

5.6.2 Discussion of results.

The results of these tests indicate that the second best material after the silicone fluid, which is not usable for a flight, is RTV-2 silicone rubber VP7612.

Figure (5.8).

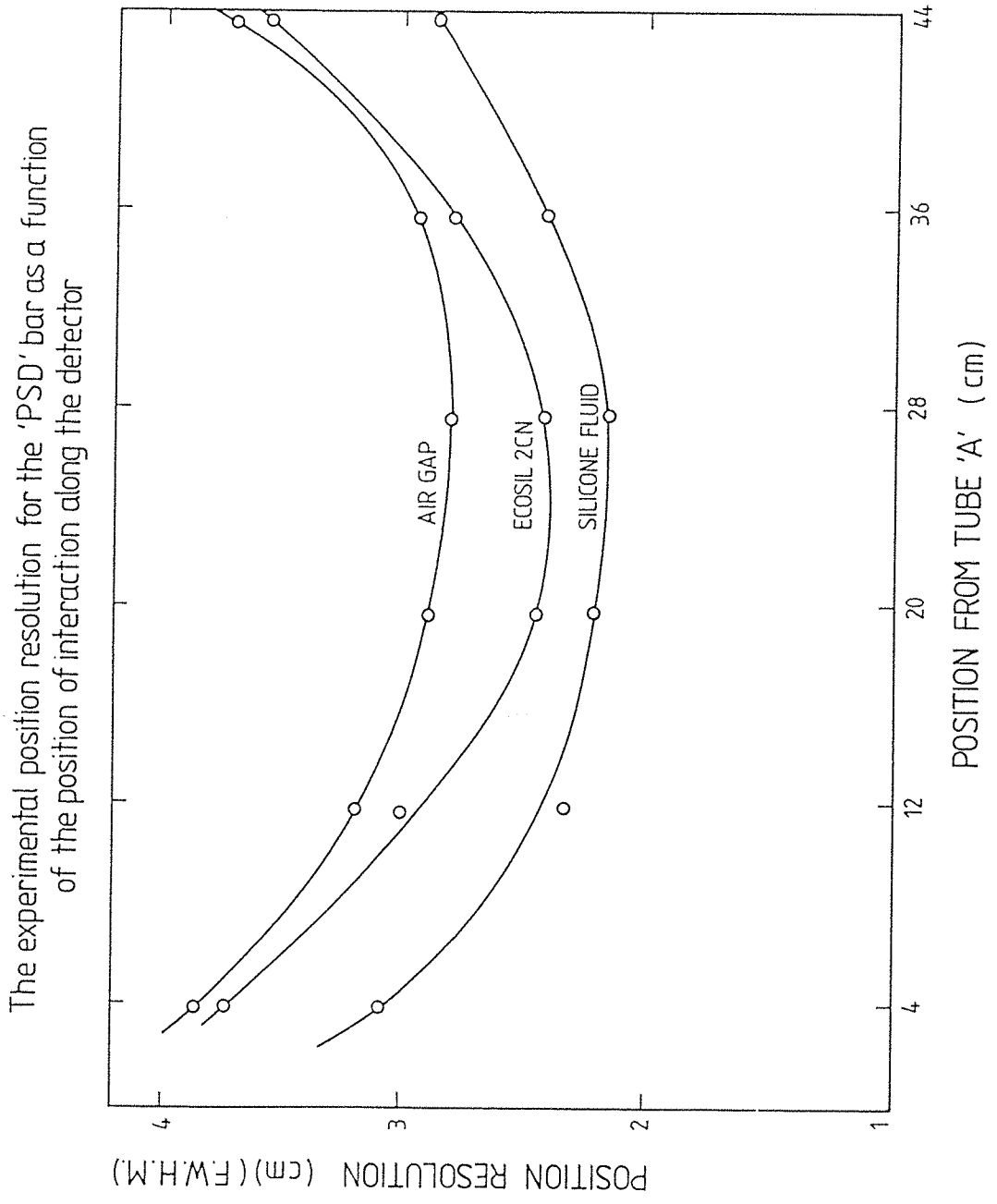
The experimental position resolution for the 'PSD' bar as a function of the position of interaction along the detector
POSITION RESOLUTION (cm)(F.W.H.M.)
POSITION FROM TUBE 'A' (cm)
AIR GAP
ECOSIL 2CN
SILICONE FLUID
1
2
3
4
4
12
20
28
36
44

Figure (5.9).

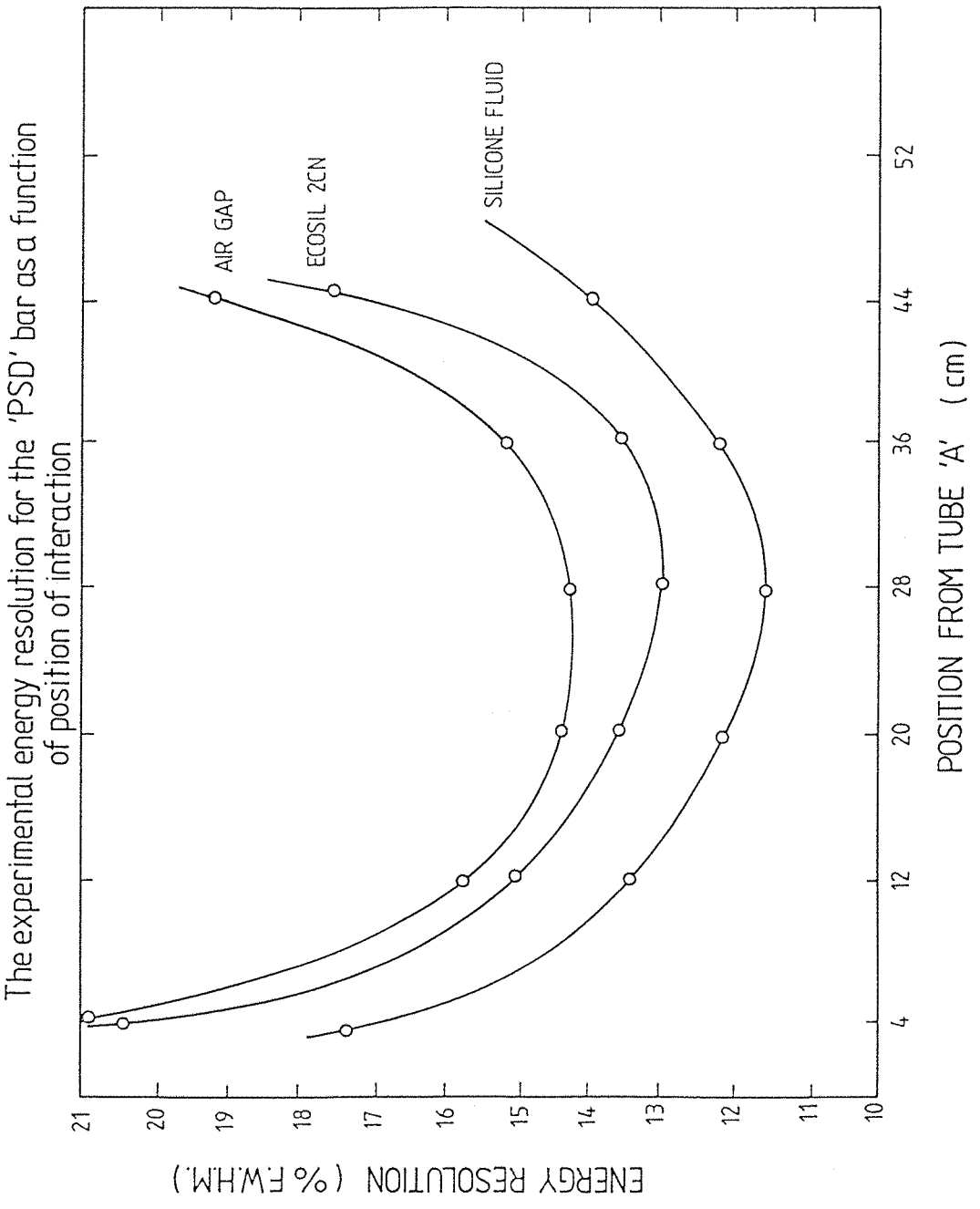
The experimental energy resolution for the 'PSD' bar as a function of position of interaction
AIR GAP
ECOSIL 2CN
SILICONE FLUID
ENERGY RESOLUTION (% F.W.H.M.)
POSITION FROM TUBE 'A' (cm)
21
20
19
18
17
16
15
14
13
12
11
10
4
12
20
28
36
44
52

Figure (6.10)

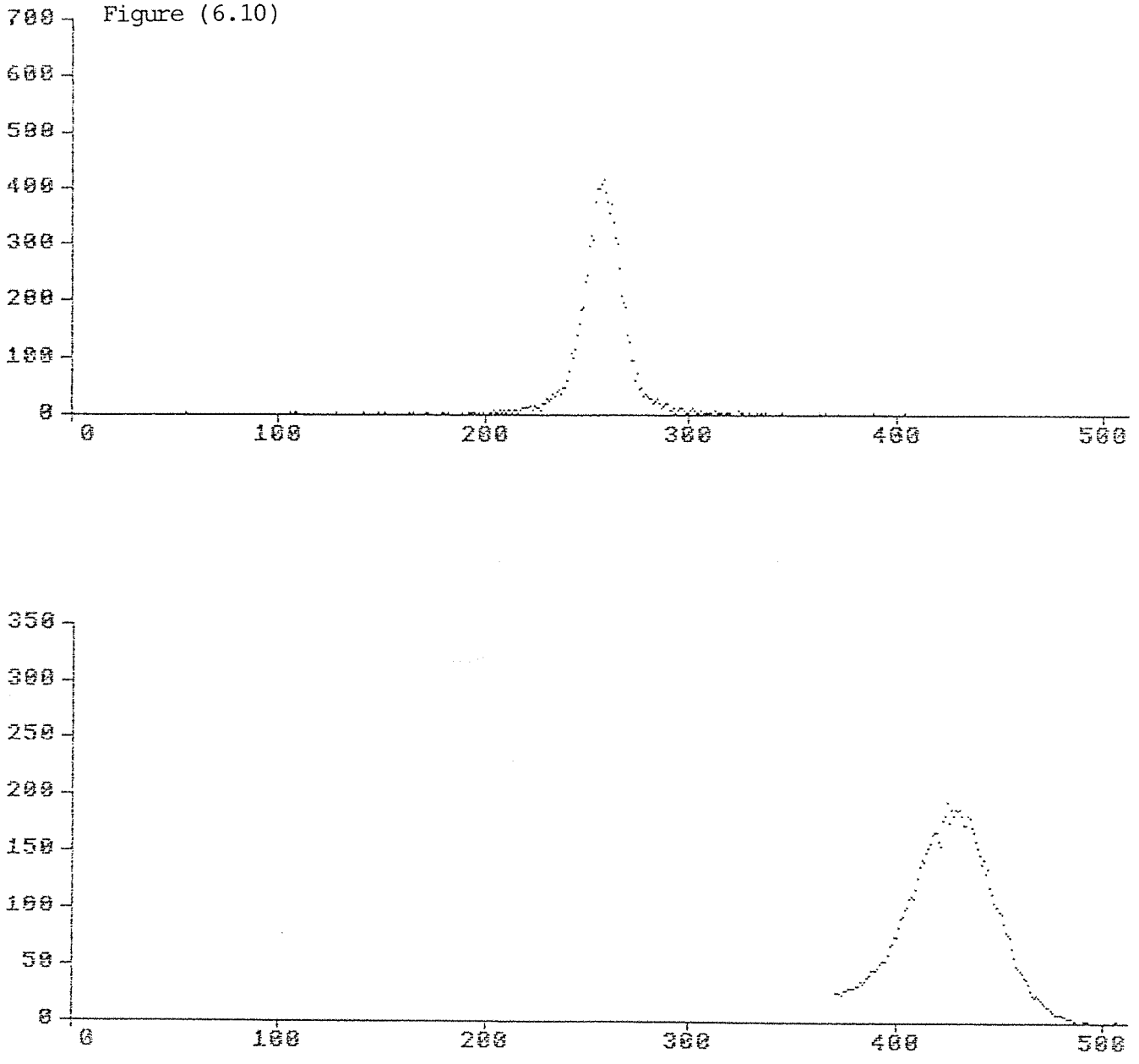

Figure (5.10) The energy and position specrums for a collimated Cs^{137} source in the center of ZEBRA bar.

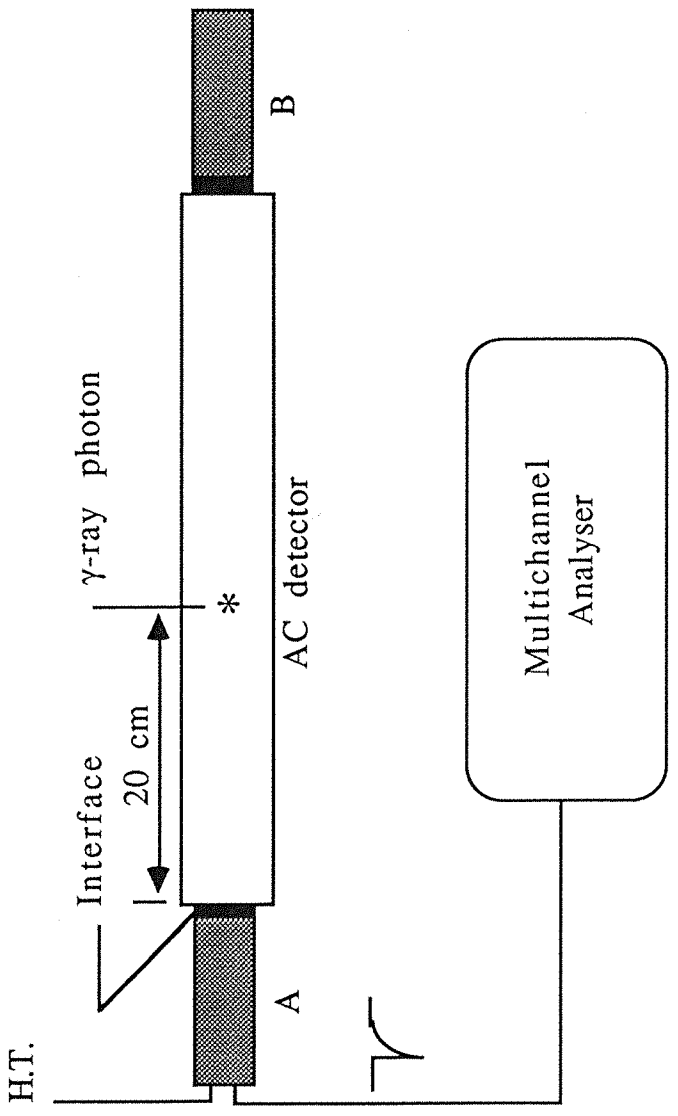

Figure(5.11) The experimental set up for the second part of the optical contact test

Table (5.3)
The interface materials used for the optical contact tests and their corespondent enrgy resolution

Optical Joint	Energy Resolution FWHM %
1. Silicone fluid.	10.68
2. RTV-2scilicpne rubber VP7612.	10.71
3. Eccosil 2cn pouring in a ring mould.	11.20
4. Eccisil 2cn disk.	12.04
5. Air gap white wishers of 2.35 mm thickness.	13.83
6. Air gap black washers of 3.70 mmthickness.	14.25
7. Air gap with a grinded crystal surface using emery cloth P360.	15.70
8. Air gap with a grinded crystal surface using emery cloth P320.	16.68
9. Air gao with a grinded crystal surface using emery cloth P280.	17.04
10. Air gap with a grinded crystal surface using glass paper M2 (grit no.70).	16.36
11. Air gap with a grinded crystal surface using glass papaer S2 (grit no.40).	14.59
12. Using Eccosil 2cn disk with a grinded crystal surface using glass papar S2 (grit no.40).	13.31
13. Using Eccosil 2cn disk with a grinded crystal surface using glass paper S2 (grit no.40).	11.75

5.7 Factors affecting the stabilization of photon interaction on a position sensitive detector.

A series of tests have been performed on a position sensitive detector to evaluate system stabilization parameters. These were operational stabilization parameters for the tubes, amplifiers and the crystal.

5.7.1 Test configuration and results.

The first test was to determine weather the photopeak position of the energy spectrum of a gamma ray interaction in a detector is time variable from the moment the units are switched on. The output signal of the tubes were treated as illustrated in fig.(5.12). Table (5.4) shows a change of up to 5% in the photopeak position in roughly three hours period (fig.5.13 a and b).

The second part of the tests was to determine weather the tubes are responsible to this shift or the amplifiers. Therefore, in this particular test, the tubes and the multichannel analyzer were left running over night while the amplifiers were switched on the following day. This enabled us to determine the effects in th photopeak position due to the running of the amplifiers. Table (5.5) shows a change of 1% in 3 hours (fig.5.14 a and b).

The final part of the tests were to investigate the effect on changing the temperature of the crystal on the photopeak position. Table (5.6) clearifie no significant shift of the peak with temperature. The change is negligible within the range of -3°C. of room temperature(25°C.)(fig.5.15).

5.7.2 Discussion of results.

The results of these tests shows that for a telescope flight, any calibration tests or imaging tests, the detection plane should be run for at least 3 hours before taking data so stabilization can occur. It was also found that temperature differential has no effect on the photopeack position of an energy spectrum.

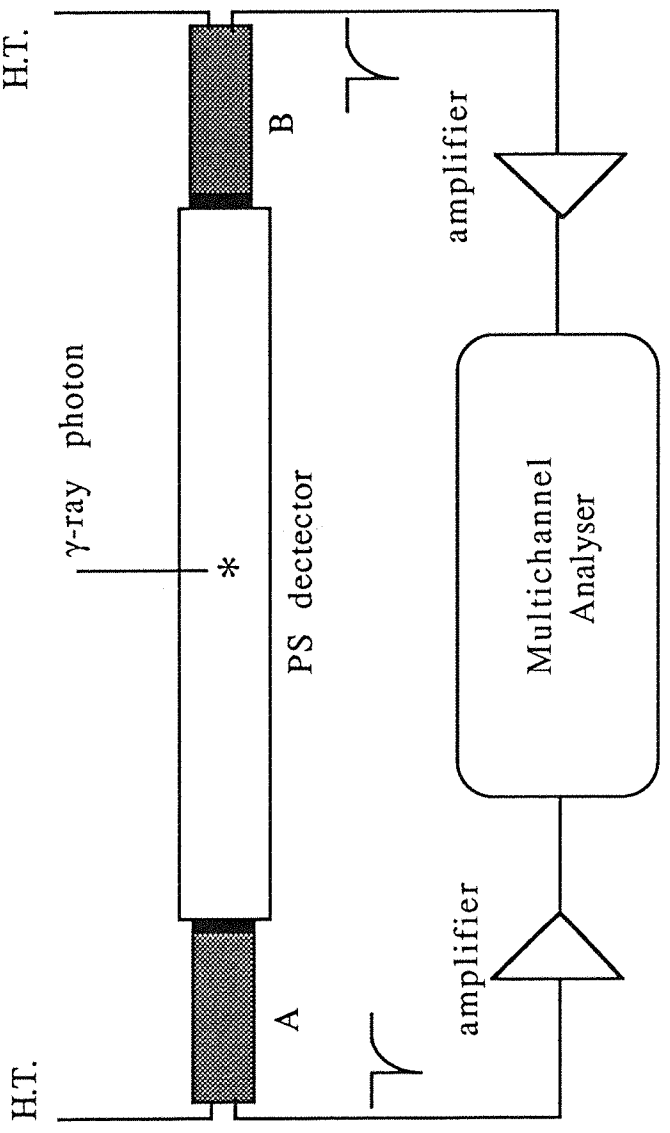

Figure(5.12) The laboratory test arrangment used for the evaluation of factors affecting system stabilization

Table (5.4)
The variation of photopeak position with time.

Tube Side	Moniter Voltage	Time (h)	Photopeak Position ch.no.
Left	2.5	0.00	488
Right	2.5	0.00	618
Left	2.5	0.30	478
Right	2.5	0.30	615
Left	2.5	2.15	470
Right	2.5	2.15	599
Left	2.5	2.30	464
Right	2.5	2.30	598
Left	2.5	3.00	464
Right	2.5	3.00	599
Left	2.5	3.30	464
Right	2.5	3.30	600
Left	2.5	4.00	464
Right	2.5	4.00	600

Figure (5.13a)

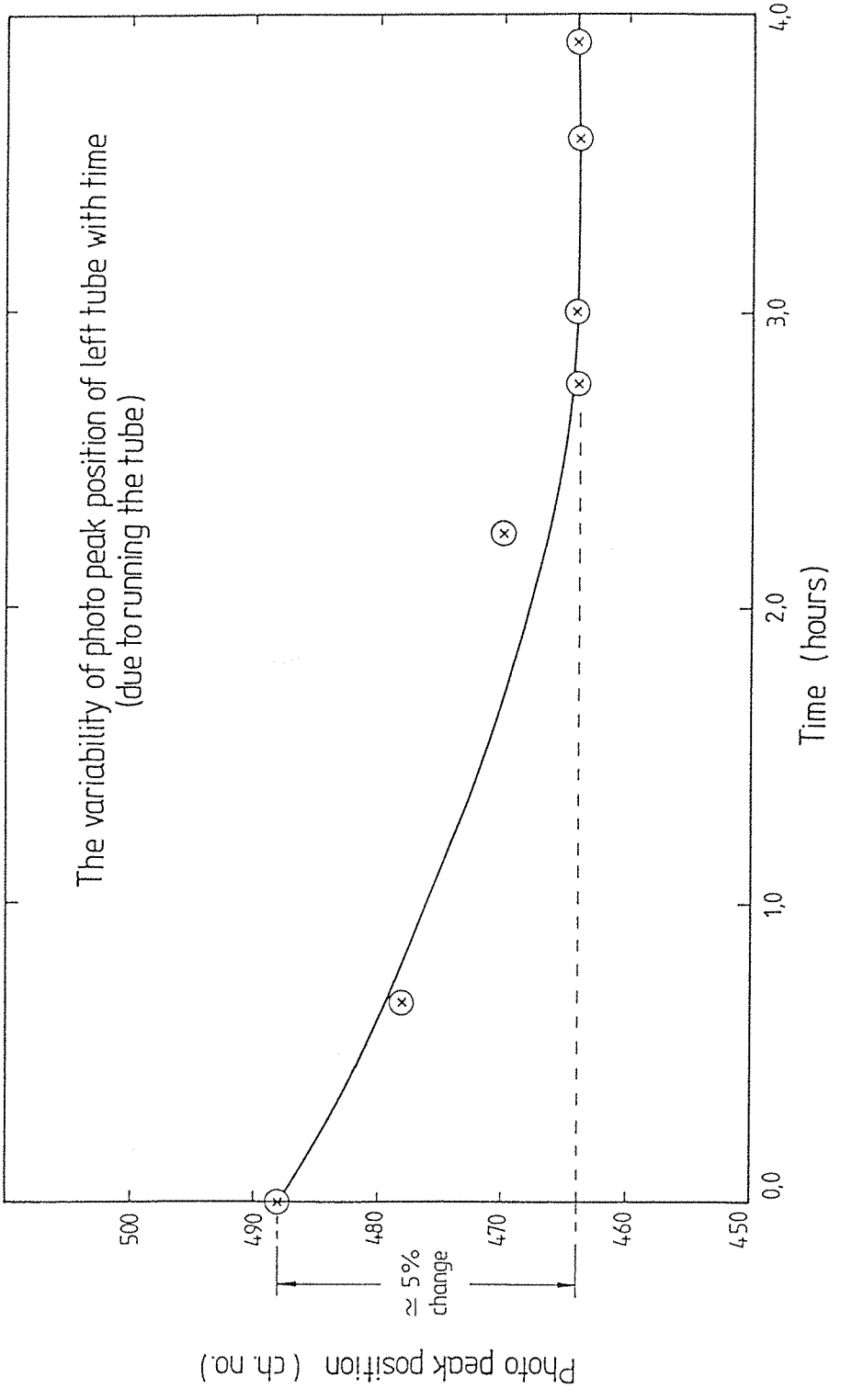
The variability of photo peak position of left tube with time
(due to running the tube)
Photo peak position (ch. no.)
Time (hours)
500
490
480
470
460
450
0,0
1,0
2,0
3,0
4,0
≃ 5% change

Figure (5.13b).

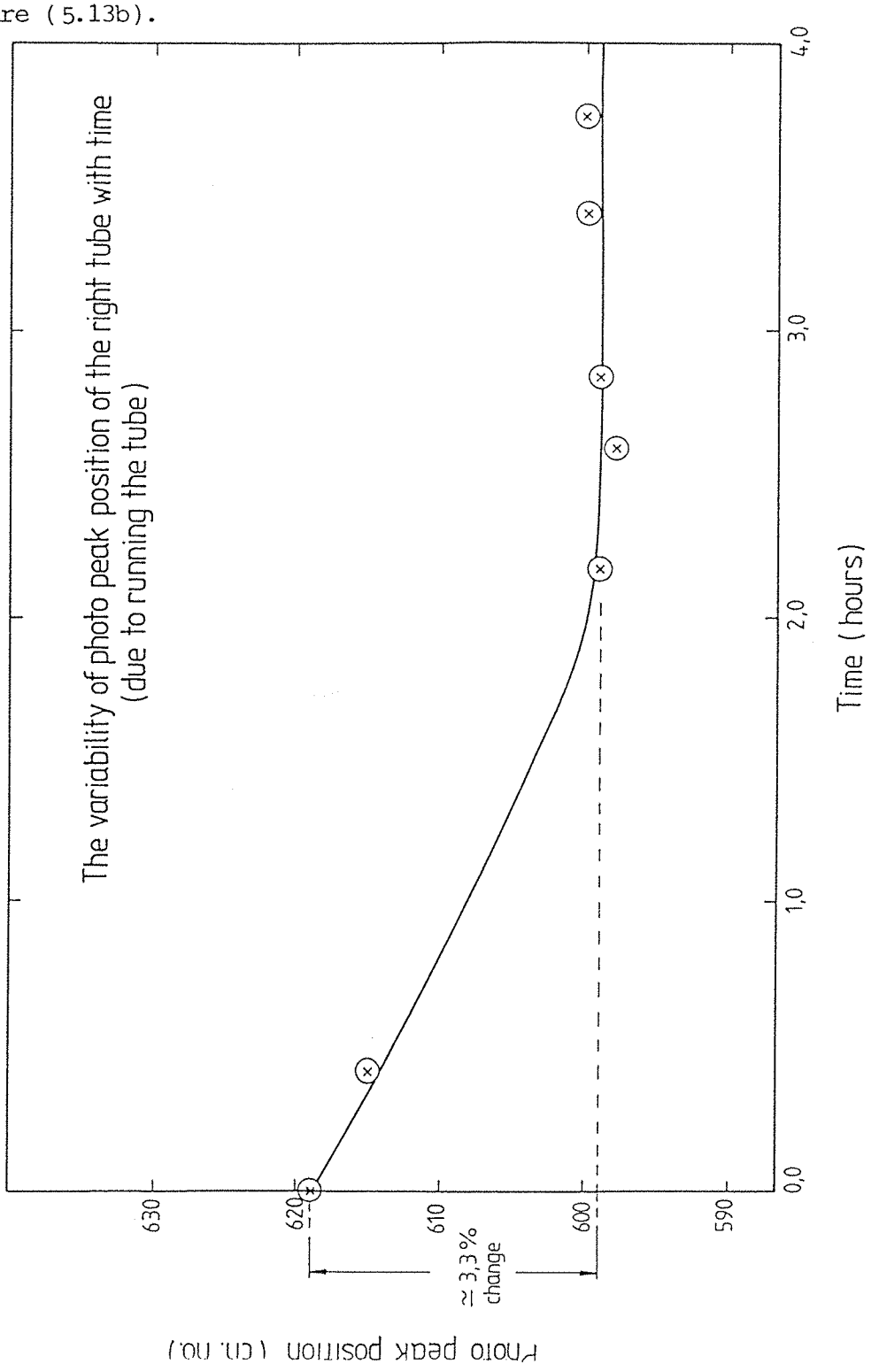
The variability of photo peak position of the right tube with time
(due to running the tube)
Photo peak position (ch. no.)
Time (hours)
630
620
610
600
590
0,0
1,0
2,0
3,0
4,0
≃ 3,3 %
change

Table 5.5
The variation of phpotopeak position with tiome due to running amplifiers.

Tube Side	Moniter Voltage	Time (h)	Photopeak Position ch.no.
Left	2.5	0.00	604
Right	2.5	0.00	466
Left	2.5	0.15	604
Right	2.5	0.15	466
Left	2.5	0.45	603
Right	2.5	0.45	465
Left	2.5	1.15	603
Right	2.5	1.15	462
Left	2.5	2.00	601
Right	2.5	2.00	461
Left	2.5	2.15	600
Right	2.5	2.15	460
Left	2.5	2.45	600
Right	2.5	2.45	460
Left	2.5	3.15	600
Right	2.5	3.15	460

Figure (5.14a).

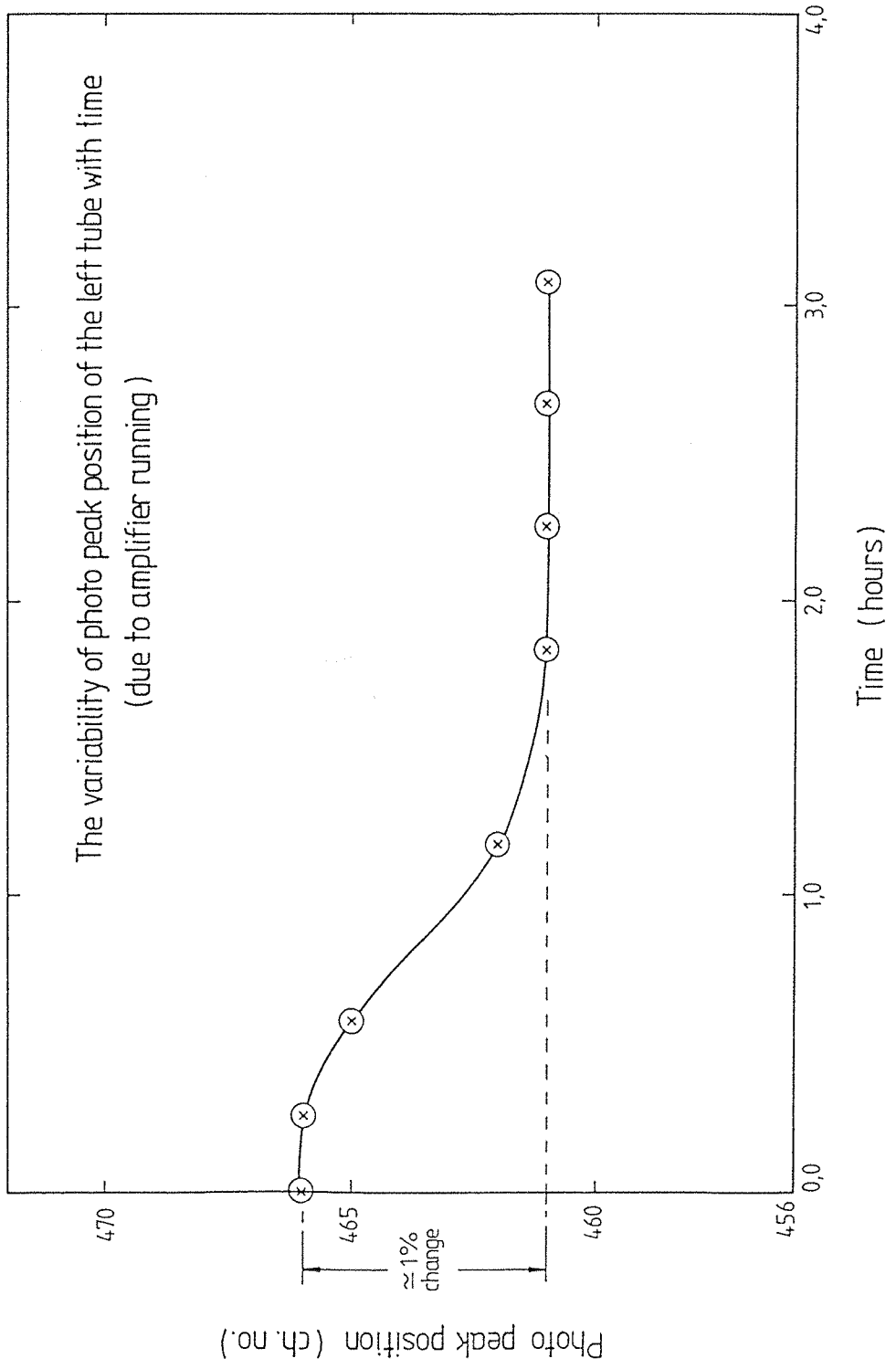
The variability of photo peak position of the left tube with time
(due to amplifier running)
Photo peak position (ch. no.)
Time (hours)
470
465
460
456
0,0
1,0
2,0
3,0
4,0
≃1% change

Figure (5.14b).

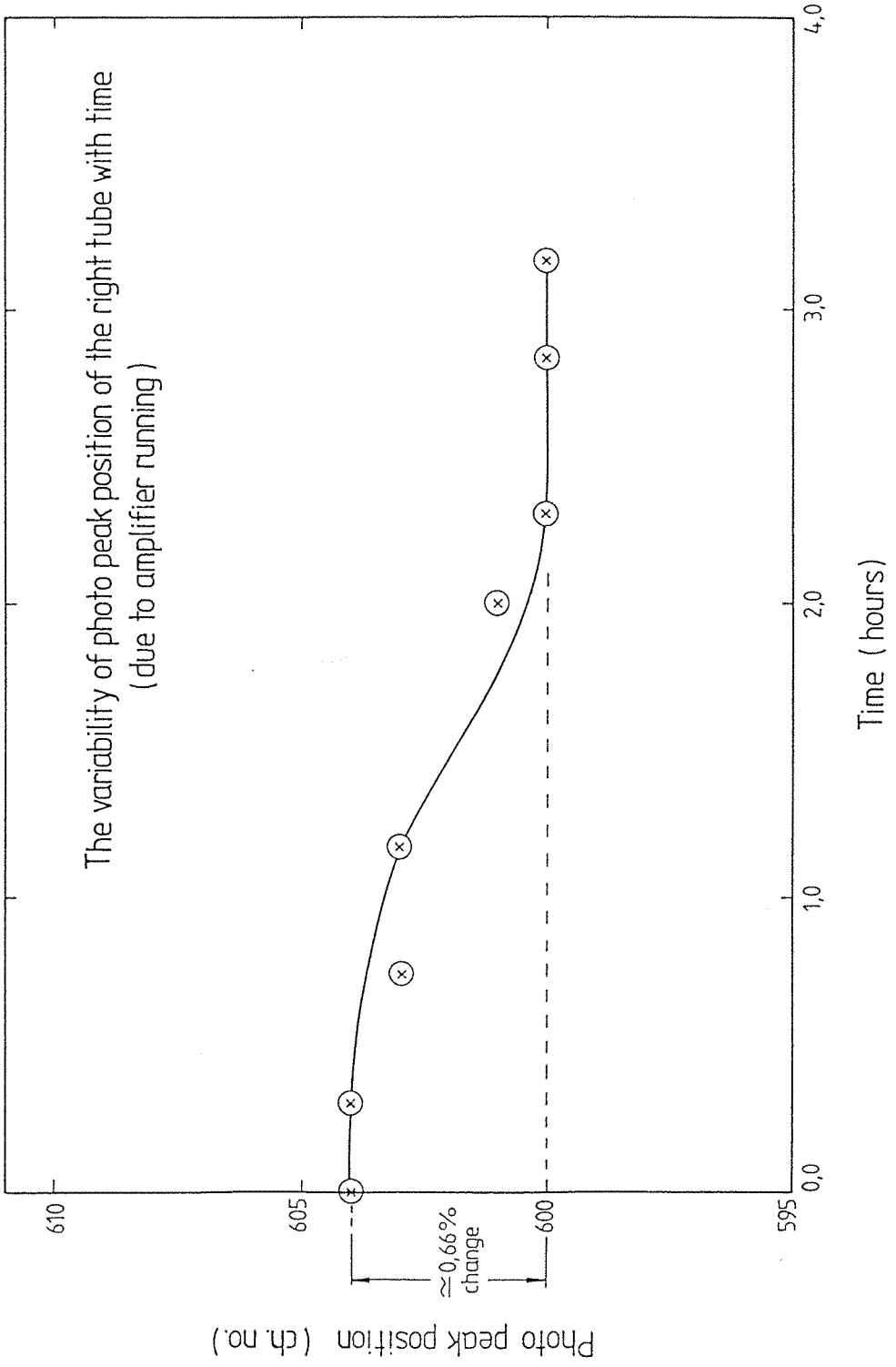
The variability of photo peak position of the right tube with time
(due to amplifier running)
Photo peak position (ch. no.)
Time (hours)
610
605
600
595
0,0
1,0
2,0
3,0
4,0
≃0,66% change

Table (5.6)
The variation of the photopeak position with time due to tempreture differentioal.

Tube Side	Tempreture (°C)	Time (h)	Photopeak Position ch.no.
Left	26.7	0.00	456
Right	26.7	0.00	601
Left	26.3	0.30	456
Right	26.3	0.30	602
Left	25.8	1.20	456
Right	25.8	1.20	602
Left	25.4	1.45	456
Right	25.4	1.45	602
Left	24.9	2.45	457
Right	24.9	2.45	602
Left	24.4	3.00	457
Right	24.4	3.00	603
Left	24.1	3.15	457
Right	24.1	3.15	603
Left	23.7	3.45	457
Right	23.7	3.45	603
Left	23.6	4.15	457
Right	23.6	4.15	602
Left	22.2	7.00	455
Right	22.2	7.00	602

Figure (5.15).

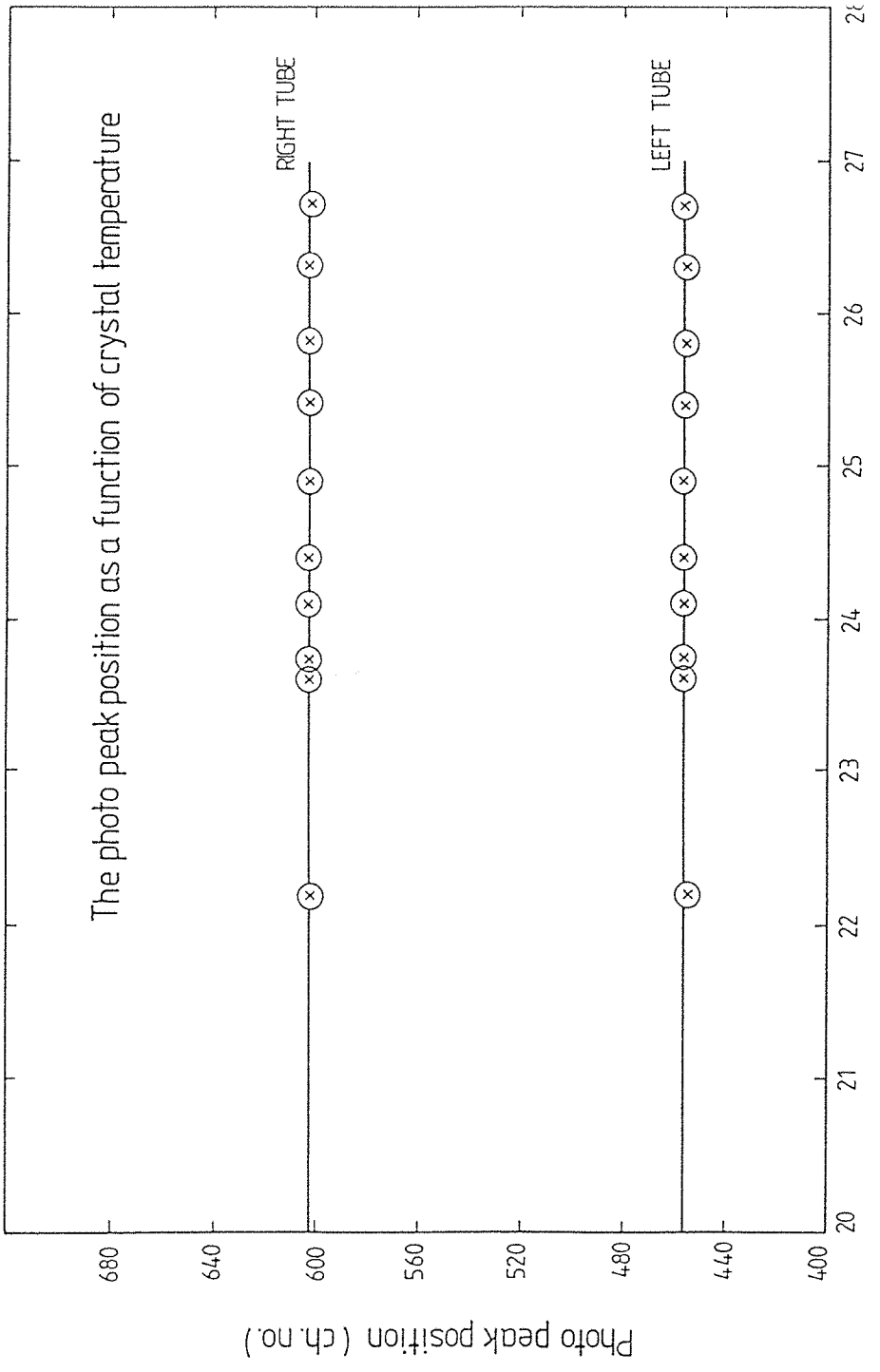
The photo peak position as a function of crystal temperature
RIGHT TUBE
LEFT TUBE
Photo peak position (ch.no.)
Temp (°C)
680
640
600
560
520
480
440
400
20
21
22
23
24
25
26
27

5.8 Conclusion.

The remarkable performance of ZEBRA detection plane has been shown to be very close to the expected from the theoretical consideration.

The results of the optical test led to the choice of an optimum interface which gives an exceptionally good energy resolution. It is also clear from section (5.7) that the stability of the position sensitive detectors is essential and to have a stable detection plane, the system must be run for not less than 3 hours.

Also it was shown that small systematic errors arise from assuming the ideal case for the exponential attenuation along the bars. These errors can be reduced by calculating them from the calibration of the detection plane and by the use of look-up tables operating on the data after the calculation of the energy and position and the energy of each event. It has been decided to implement the look-up tables on-board in flight electronics.

Chapter 6

6 The prediction and measurements of the ZEBRA telescope sensitivity.

6.1 Introduction.

The sensitivity of a telescope is limited by the number of photons detected from an astronomical object and the background level from the vicinity of that particular object. In the case of gamma ray astronomy, the photon flux is quite low compared with the intensity of photons from sources in the rest of the electromagnetic spectrum.
The nature of gamma ray photons, particularly their penetration power, make observation in the desired energy range, (0.2-10.0)MeV, a bit awkward.
The sensitivity of a gamma ray telescope is dependent upon a number of parameters such as , large sensitive detection area, long integration period, high detection efficiency, effective shielding system and low background level.
The first two parameters are dependent upon the mechanical arrangement of the telescope. The rest of the parameters for the case of ZEBRA telescope have been discussed in this chapter in detail. In addition to that the expected sensitivities of the telescope for continuum and line emission have been evaluated.

6.2 Background noise level.

Only the contribution to the detector background has been considered as the background noise level for ZEBRA telescope. The contribution to the background due to the existence of the mask has been ignored since it is fixed (4m.) away from the detection plane.
The main contributions to the background noise level in the ZEBRA imaging telescope are:

1. Gamma ray induced background.
2. Neutron induced background.
3. Cosmic ray effects.

All these contributions have been calculated by (Charalambous et al 1984). The evaluated background takes the following form :

$$\frac{dN}{dE} = 200\ E^{-2} \quad ph\ cm^{-2}\ s^{-1}\ keV^{-1} \qquad (6.1)$$

6.3 The anticoincidence system.

The most effective way to reduce the intensity of Compton scattering and the photon escape process in an observed pulse height spectrum is to surround the main detector with an efficient anticoincidence shield. The function of the shield is to detect all the escaped photons. At the same time it works in anticoincidence with the main detector. The system also function to reduce external background radiation such as cosmic rays.
In the case of ZEBRA telescope, each position sensitive detector is shielded by the two adjacent detectors and by the anticoincidence bars from below.
To evaluate the performance of the ZEBRA shielding, a series of tests were performed. The results of these tests are discused in the following sections.

6.3.1 Laboratory assessment of ZEBRA shielding.

6.3.1.1 Test configuration.

A block of six detectors were assembled, three position sensitive detectors on top and three anticoincidence detectors below. The objective of the test was to evaluate the performance of the anticoincidence system for the top central detector. Data from these detectors were acquired via a CAMAC system and afterward processed in a PDP 11/24 computer (fig.6.1).

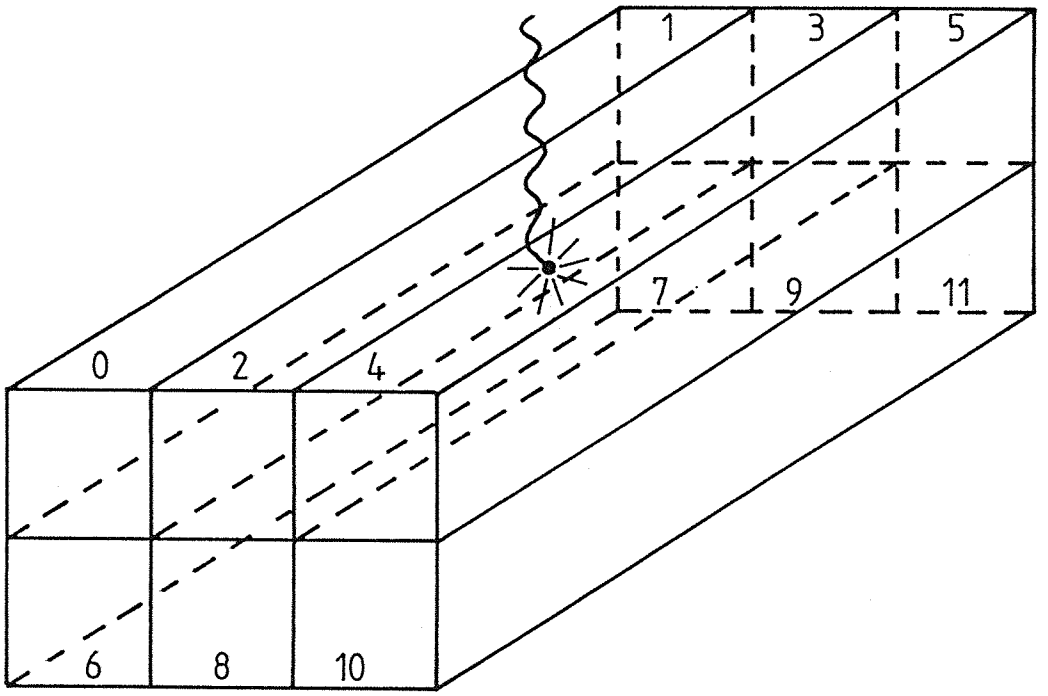

Figure (6.1) The arrangement of the six detectors used for the assessment of ZEBRA shielding.

A number of gamma ray sources such as, ^{137}Cs, ^{22}Na, ^{60}Co, ^{88}Y and an $^{241}Am/Be$ were set above the centre of the central detector to achieve the aim of the test.

A collimated ^{137}Cs source was used to calibrate the system. Three different positions were chosen (centre of the detector, + and - 15cm. from the centre). The data was analyzed and the system was calibrated.

The main test was carried out using the mentioned gamma ray sources fixed at (1m.) above the central detector. A typical ^{137}Cs source spectrum is shown in fig.(6.2a).

The test of the $^{241}Am/Be$ neutron source is an interesting case. Neutrons are absorbed in NaI crystals by the following two process :

$$^{23}Na + {}_{o}n^{1} \text{ ----------> } ^{24}Na \qquad (6.2)$$

$$^{127}I + {}_{o}n^{1} \text{ ----------> } ^{128}I \qquad (6.3)$$

The two products ^{24}Na *and* ^{128}I which are produced by the neutron capture shown above, have two different half-lives of 15 hours and 25 minutes respectively. This leads to an easy separation of the two process. The cross-section of the ^{23}Na for the neutron capture is inversely proportional to the velocity of the neutrons therefore, the neutron flux can be determined from the ^{24}Na activity.

Fig.(6.2 b) shows the gamma ray spectrum of the $^{241}Am/Be$ neutron source . This spectrum features two peaks. Their calculated energy are (1374±37)keV and (1736±42)keV. These are corresponding to the energy peaks of (1368)keV and (1732)keV according to GAMMA RAY CATALOUGE.

6.3.1.2 Shielding quality.

The comparison between the shielded and unshielded spectra is of very high interest. This comparison will show the quality of the shielding system for the imaging telescope.

The effect of this shielding is highly dependent on the system rejection for Compton scattering photons. The answer to this

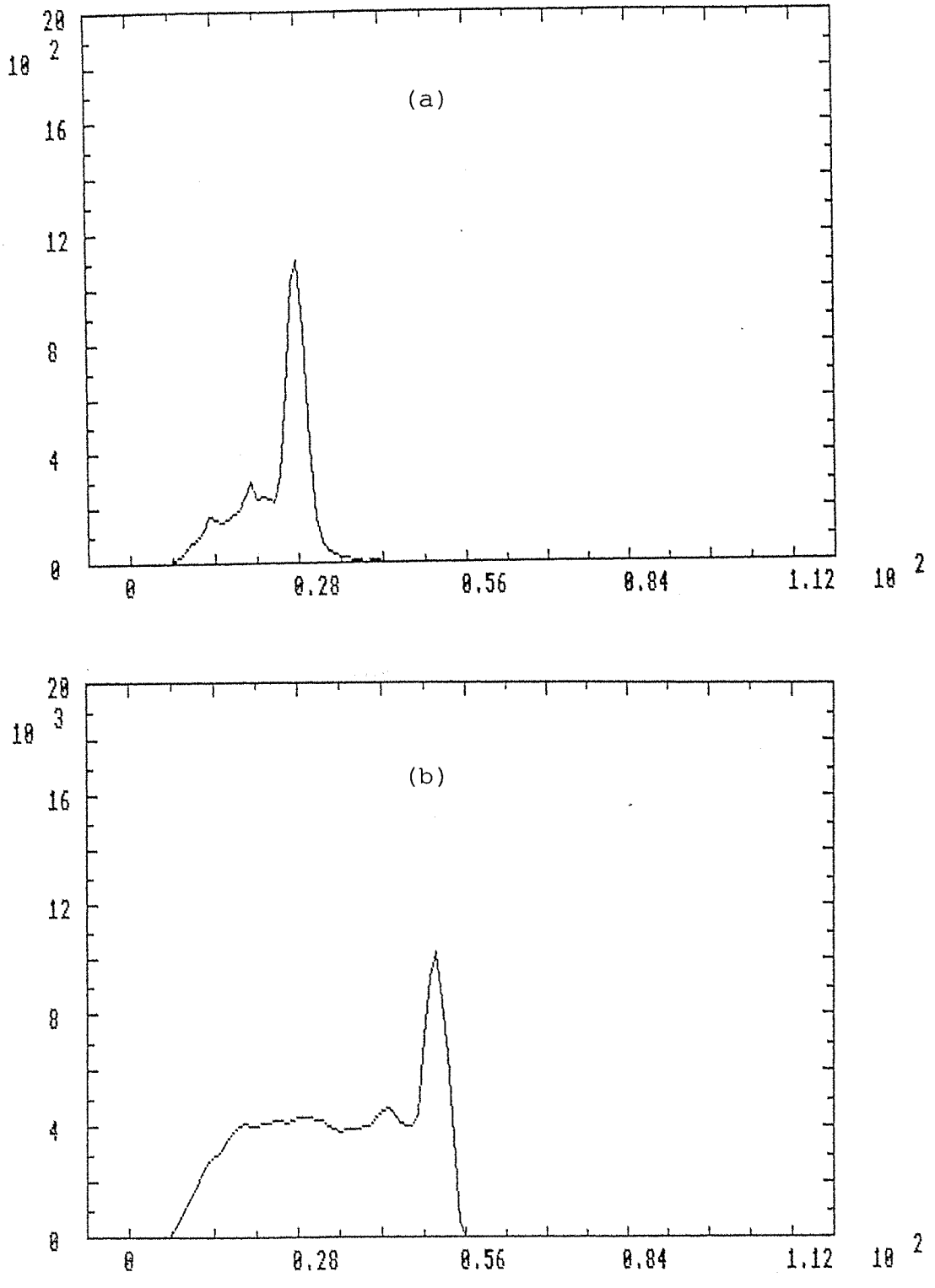

Figure (6.2a, b) The energy spectrum of (a) Cs^{137} source, (b) Am/Be neutron source.

query was given when the shielded and unshielded data of a collimated ^{137}Cs source fixed at 46cm. above the desirable detector was subtracted. The result is given in fig.(6.3). This curve represent the number of rejected Compton scattered photons versus energy. It is clear that the rejection is substantial at low energies and decreases when it get closer to the photopeak region. The quality of the shielding was further expressed when the shielded and unshilded spectra of the ^{137}Cs source were compared as shown in fig.(6.4). The same method was applied to the ^{22}Na source. The results are given in fig.(6.5) and (6.6).

6.3.2 Peak-to-total ratio.

The photofraction, or the peak-to-total ratio, is a key parameter in describing the response of a gamma ray detector. This quantity is defined as the ratio of interactions in which the incident gamma ray photons are totally absorbed to the incident photons that interact and do not lose their entire energy. This parameter was evaluated for a ZEBRA detector at three different positions along the bar (-15cm., 0cm., +15cm.). The result is given in fig.(6.7).

6.3.3 Energy resolution characteristics.

The energy resolution of the instrument is a function of energy of the incident photons. This parameter was determined and given in section (4.7.1). Here we investigate the variation of the energy resolution of the instrument according to source position. The energy resolutions of a collimated ^{137}Cs source, fixed at different positions away from a position sensitive detector was evaluated. The result is given in fig.(6.8). This curve shows that the energy resolution reaches saturation and is not effected by the source position after about (50cm.) away from the detector.

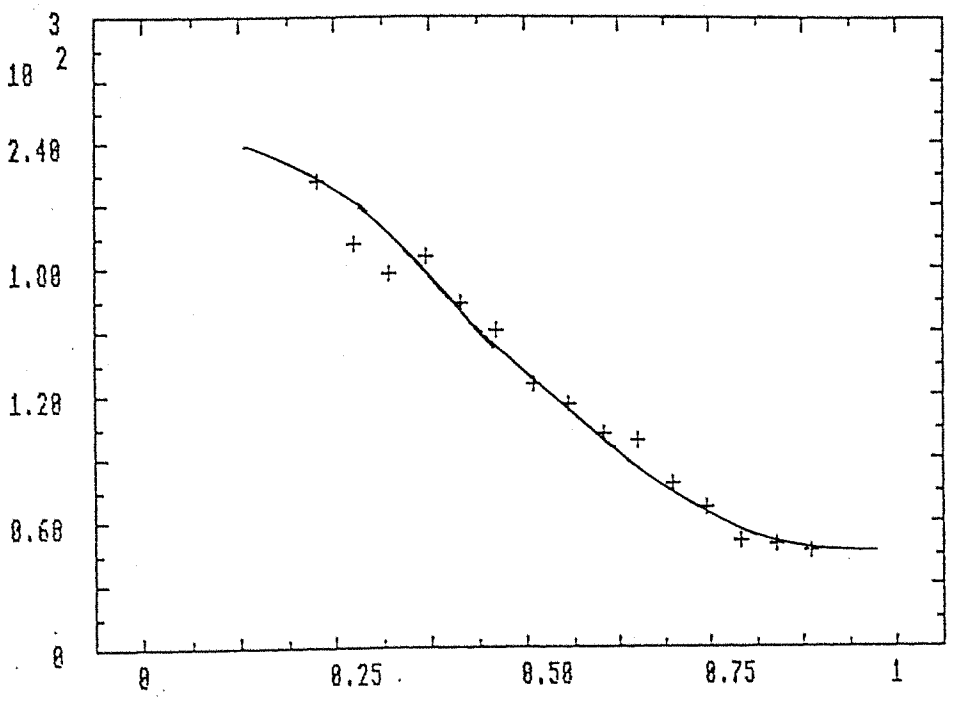

Figure (6.3) The system's refection of compton scattering photons as function of energy for Cs^{137} source.

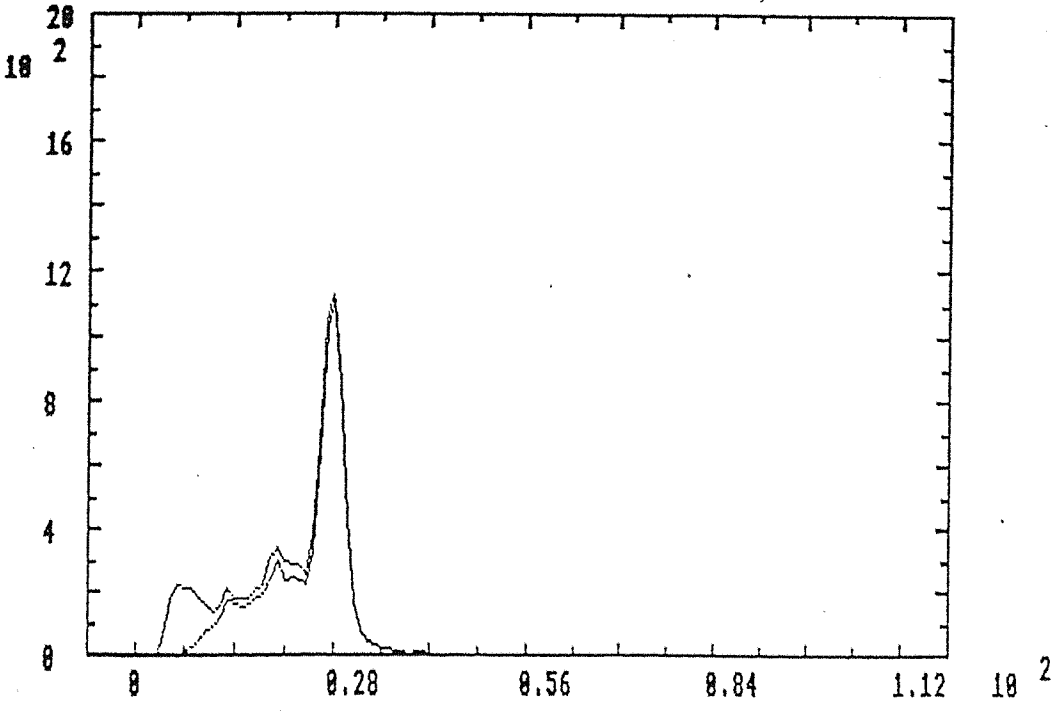

Figure (6.4) The comparison of the shielded and unshielded Cs^{137} source spectrums.

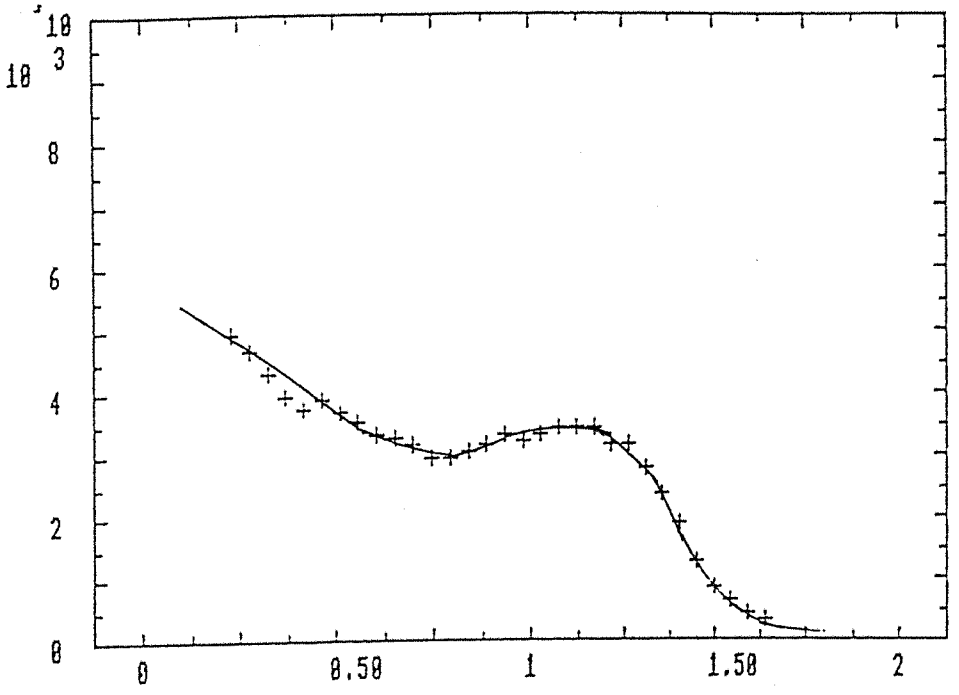

Figure (6.5) The system's reflection of compton scattering photons as function of energy for Na^{22} source.

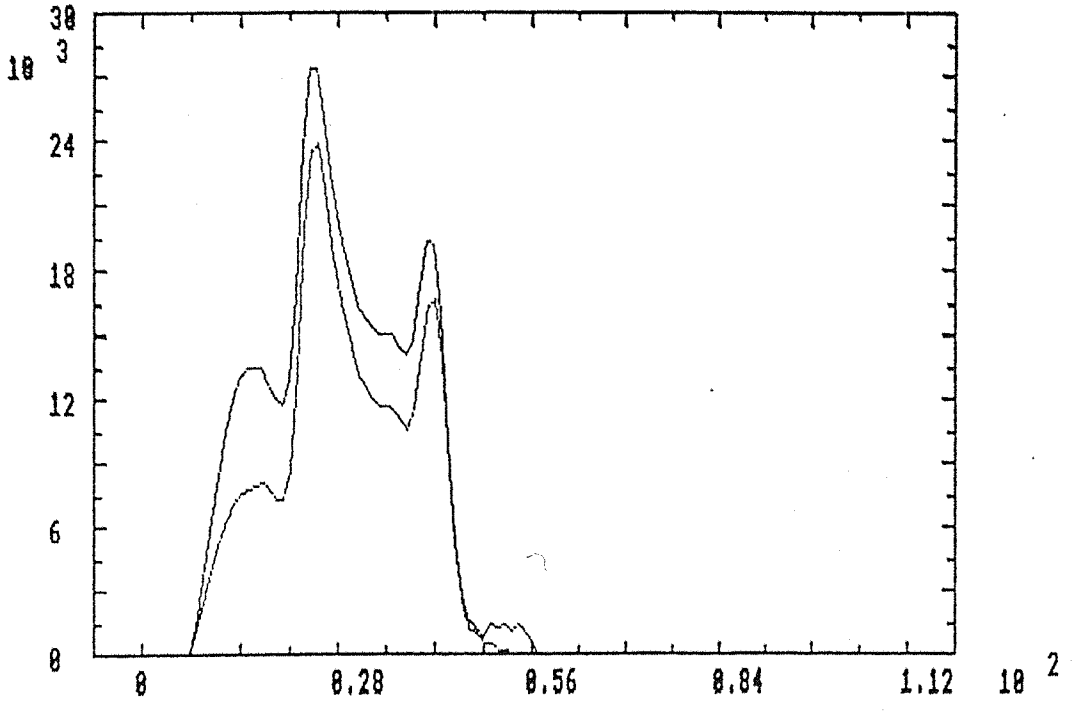

Figure (6.6) The comparison of the shielded and unshielded Na^{22} source spectrums.

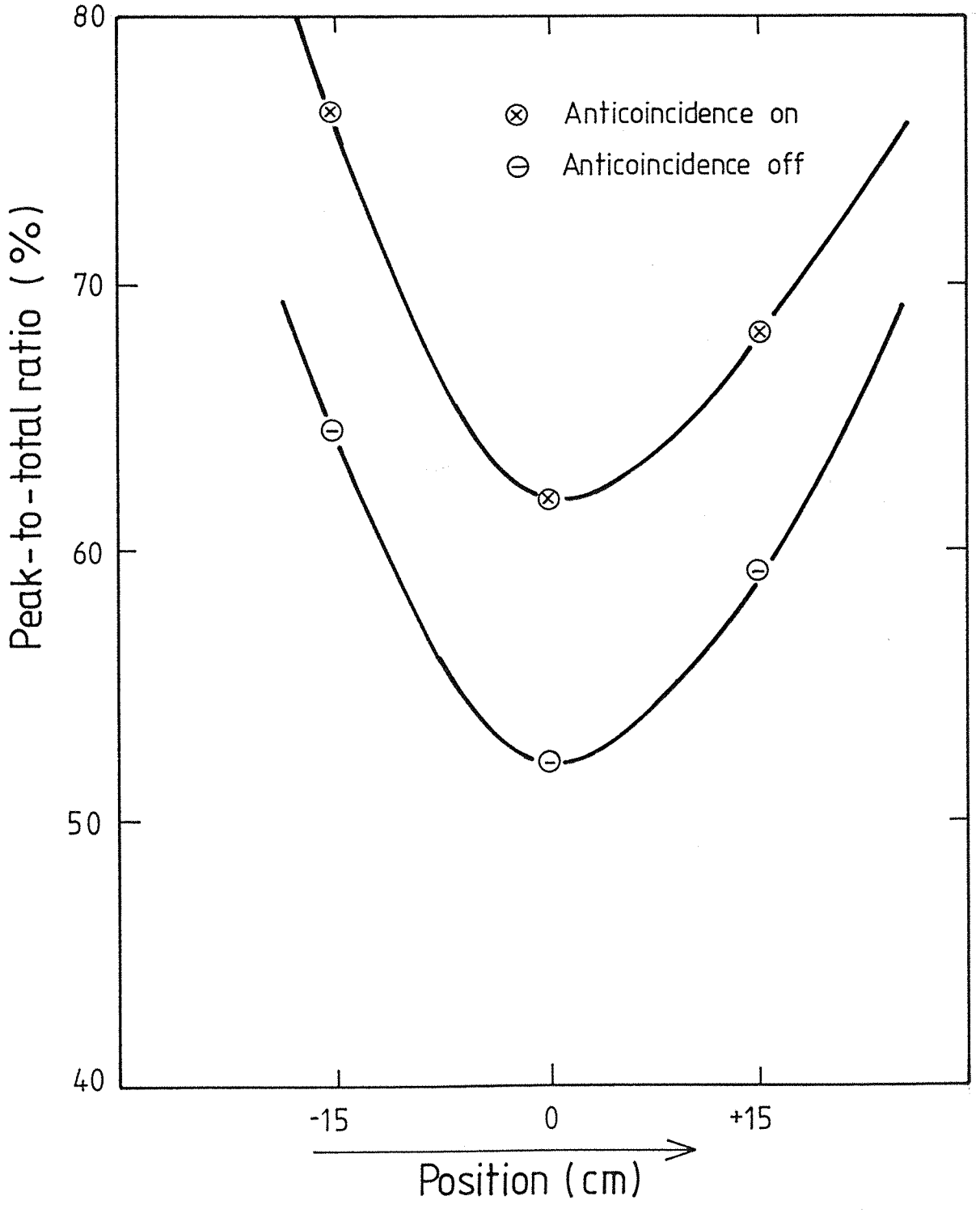

Figure (6.7) (Peak-to-total ratio) vs (Position) for a collimated Cs^{137} source immediatly above the NaI crystal.

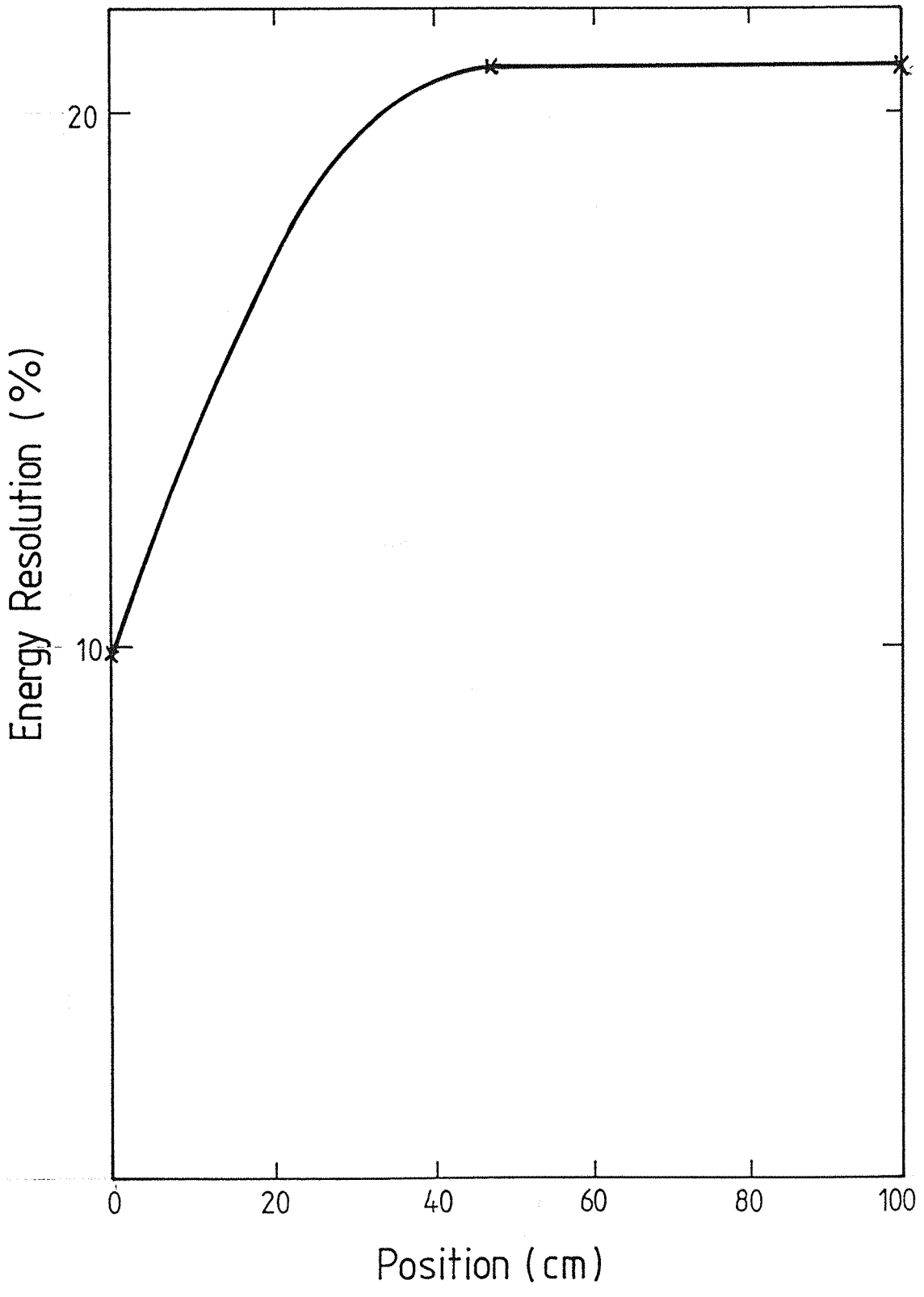

Figure (6.8) The energy resolution vs source position above the cental bar.

6.3.4 Test for the escape photons resulting from pair production.

If a gamma ray photon with energy $(E_\gamma > 2m_oc^2)$ interacts within a detector, the pair production probability increases strongly with energy. Under such circumstances, a positron-electron pair is created from which the positron will annihilate with an electron and emit two photons of (511) keV. One or both of these photons can leave the detector and interact in the adjacent detector. The performance of the ZEBRA detectors were evaluated for this .
A test was performed on the configuration of fig.(6.1) using a collimated ^{228}Th source $(E_\gamma = 2.6\ MeV)$. An energy window of (1.022 MeV) was set for the Nth detector and one of (0.511 MeV) for the rest of the detectors. Fig.(6.9 a) shows the position peak of the Nth detector. There is no indication for the existence of position peaks for the $(N-1)^{th}$ and $(N+1)^{th}$ detectors (fig.6.9 b,c). This confirm that each detector is triggering in anticoincidence to the adjacent detector. Fig.(6.9 d,e) shows the position peaks for the $(C-1)^{th}$ and $(C+1)^{th}$ detectors. It indicates that photons with energies more than 0.511 MeV have been detected by these two particular bars. This demonstrates that the produced positrons by the pair-production have annihilated and gamma rays of 511keV are liberated. Some of these photons from the N^{th},$(C-1)^{th}$ and $(C+1)^{th}$ detectors escaped and interacted in the Cth detector therefore, a pseudo position peak appear as shown in fig.(6.9 f).
The conclusion of this test is that there is the possibility of the telescope to be operating in the pair-production mode which is an additional to the imaging and timing modes described in section (4.4.2).

6.4 The ZEBRA gamma ray detection efficiency.

The detection efficiency can be expressed as the ratio of the detected gamma ray photons to the total number of incident photons. A Monte-Carlo calculations of the response of the detection plane of ZEBRA telescope to gamma ray photons as well as experimental evaluations are given below. The two results are compared and discussed here. The experimental tests were

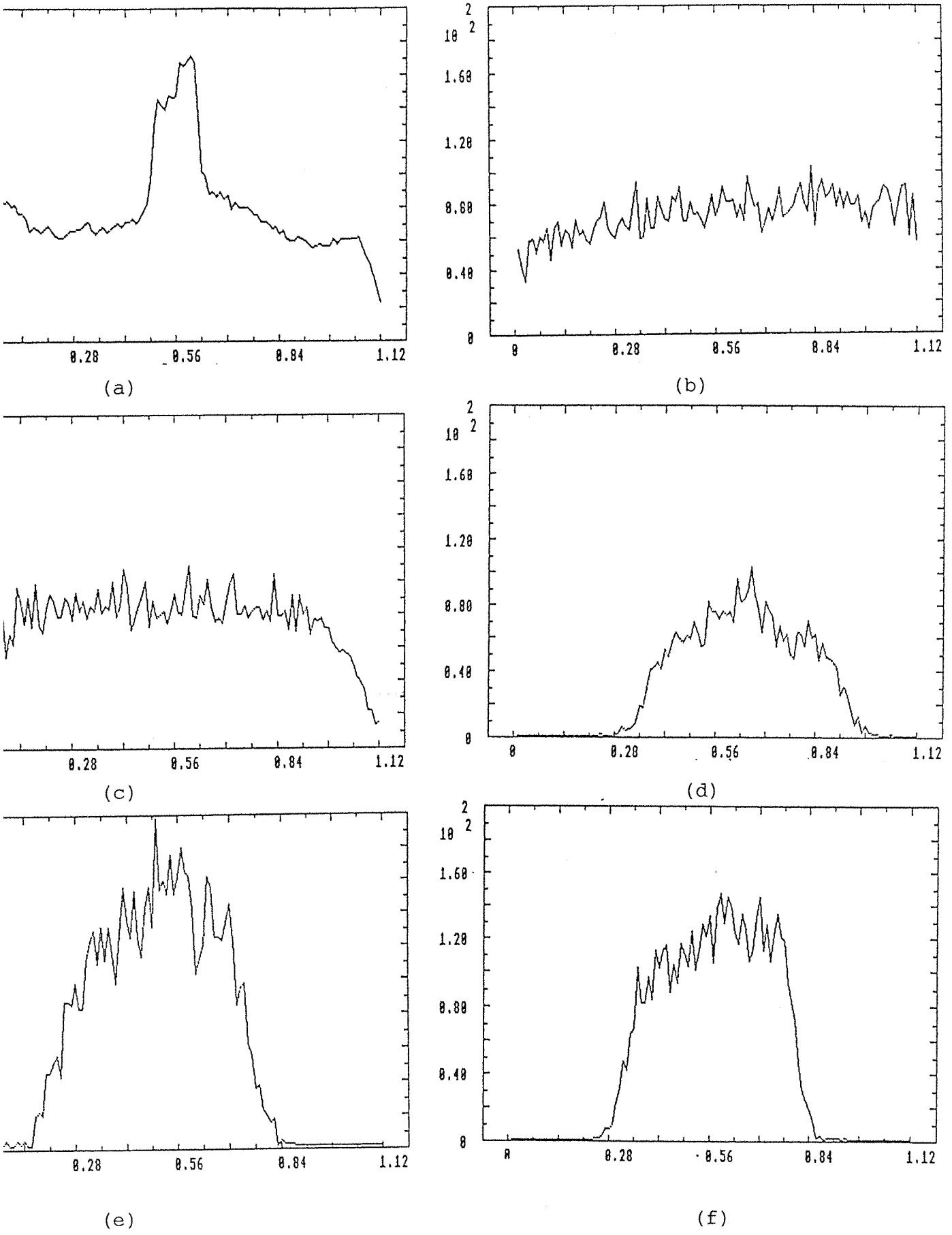

Figure (6.9) The peak positions for all the six bars used in the shielding experiment.

achieved as a part of the final assembly and integration tests of the experiment in its last stage before flying.

6.4.1 Simulation studies of the detection efficiency.

The Monte-Carlo simulation code employed to evaluate the expected detection efficiencies of ZEBRA is given by (Nataluci et al 1986). The detection module is given in fig.(6.10). The threshold of the position detectors were set to (180 keV) while the anticoincidence detectors were set to (80 keV).
The Monte-Carlo simulation has taken three interaction process into account; the photoelectric effect, the Compton scattering and the pair-production. It has also assumed that a monochromatic parallel beam of ($2*10^5$) photons are perpendicularly incident onto the upper surface of the detection plane.
The efficiencies of the detection plane as a function of energy were calculated. Also the peak-to-total ratio values were calculated. These results are compared with the experimental data here.

6.4.2 Experimental evaluation of the detection efficiency.

A series of tests were carried out to evaluate the response of the ZEBRA detection plane such as the detection efficiency and the photofraction. The method of the tests and the results are demonstrated bellow.

6.4.2.1 Measurements Method.

In order to minimize the room scattering problem and calculate the response of the detection plane properly, the following method was used. A block of lead was employed as an anticollimator fixed at a distance of (1.5m.) away from the centre of the detection plane (A beam of laser was used for the alignment). A schematic diagram of the test is shown in fig.(6.11). The idea was to block the field of view of the detection plane from any direct gamma ray

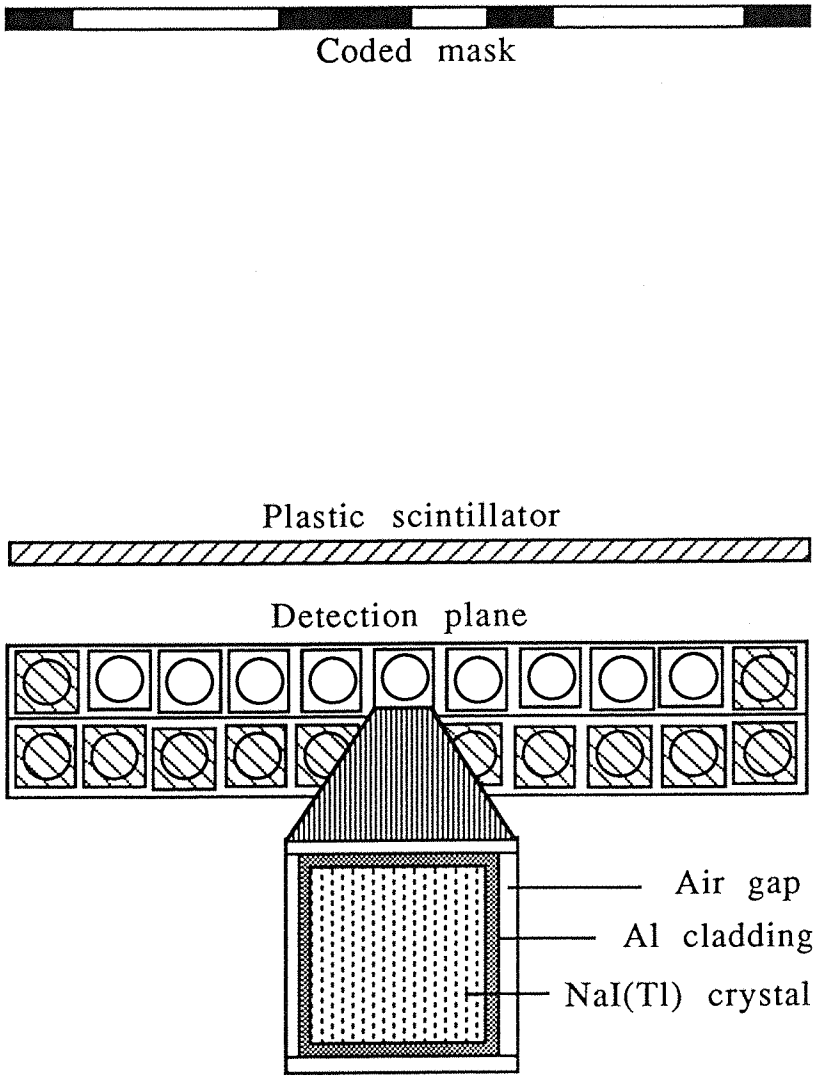

Figure(6.10) A schematic view of the ZEBRA detection plane model used for the Monte-Carlo simulation of the detection efficiencies (from Nataluci et al 1986)

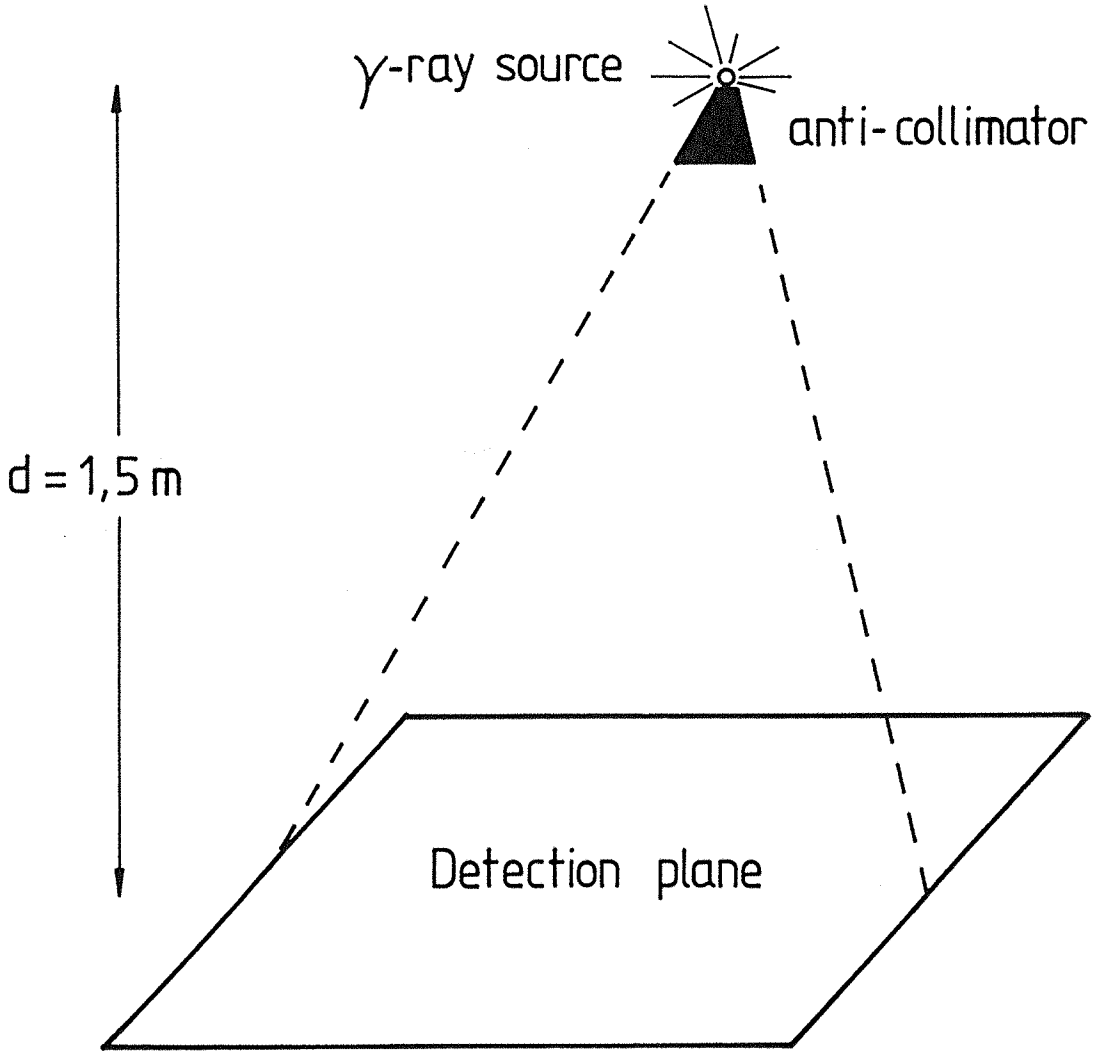

Figure (6.11) A schematic diagram of the detection efficiency evaluation test.

photons so the amount of scattered photons by the surrounding of the detection plane can be evaluated.
The full detection plane was illuminated using four different gamma ray sources; ^{137}Cs, ^{22}Na,^{54}Mn and ^{203}Hg. Four sets of data were taken :

1. Background measurement without the presence of the lead block *(B)*.
2. Background measurement with the presence of the lead block *(B+L)*.
3. Source measurement with the presence of the lead block (B+L+X).
4. Source measurement without the presence of the lead block *(B+X+S)*.

The combination of these data sets define the, background level, the amount of scattered photons and the net flux of photons that incident into the detection plane ;

* 2-1 = The difference in the background level due to the existence of the lead block.
* 3-2 = The scattering from the surrounding.

* 4-3 = The net photons that incident into the detection plane.

6.4.2.2 Environment background level

To calculate the total detection efficiency, it is essential to measure the background level of the environment. This measurement was checked with and without the presence of the anticollimator block. It was found that the difference between the two data sets has no statistical significance as shown in (fig.6.13).

6.4.2.3 Scattering level.

The level of scattering from the surrounding such as the structure of the room etc. can not be ignored and must be taken into consideration. As it was expected, many gamma ray photons scattered back into the detection plane after undergoing Compton

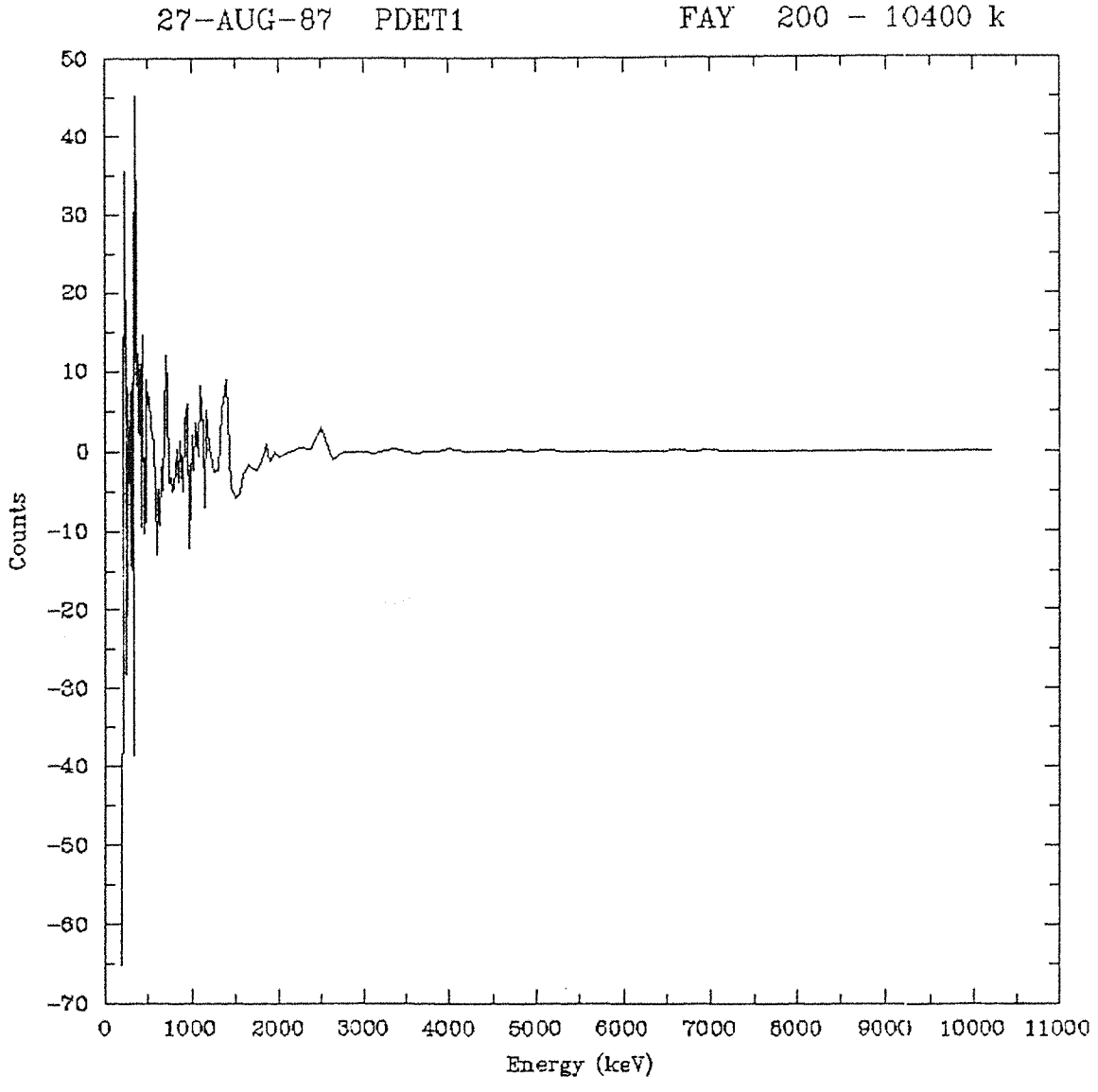

Figure (6.13) The enviromental background level with and without the presence of the anticollimator.

scattering process. A typical scattering spectrum for a ^{137}Cs source is given in fig.(6.14). Table (6.1) indicates how significant is the scattering level.

Table (6.1)

Source	Scattering level %
^{137}Cs	7
^{22}Na	8
^{54}Mn	18
^{203}Hg	0.2

*Table (6.1) The scattering level of the gamma ray sources used in the efficiency tests.

6.4.3 Total detection efficiency.

The total detection efficiency (ε_t) of a detector for gamma rays of energy E_γ can be expressed as :

$$\varepsilon_t(E_\gamma) = \frac{n_t}{n_o \Omega} \qquad (6.4)$$

where :
n_t is the total number of photons detected by the detector per sec..
n_o is the total number of photons emitted by the source per sec..
$4\Pi\Omega$ is the solid angle subtended by the detector at the source.

The calculated solid angle for the given configuration was calculated to be $8.674*10^{-3}$ Sr.. The detection efficiency was evaluated and given in Table (6.2). This result is compared with the Monte-Carlo simulation and depicted in fig.(6.15).

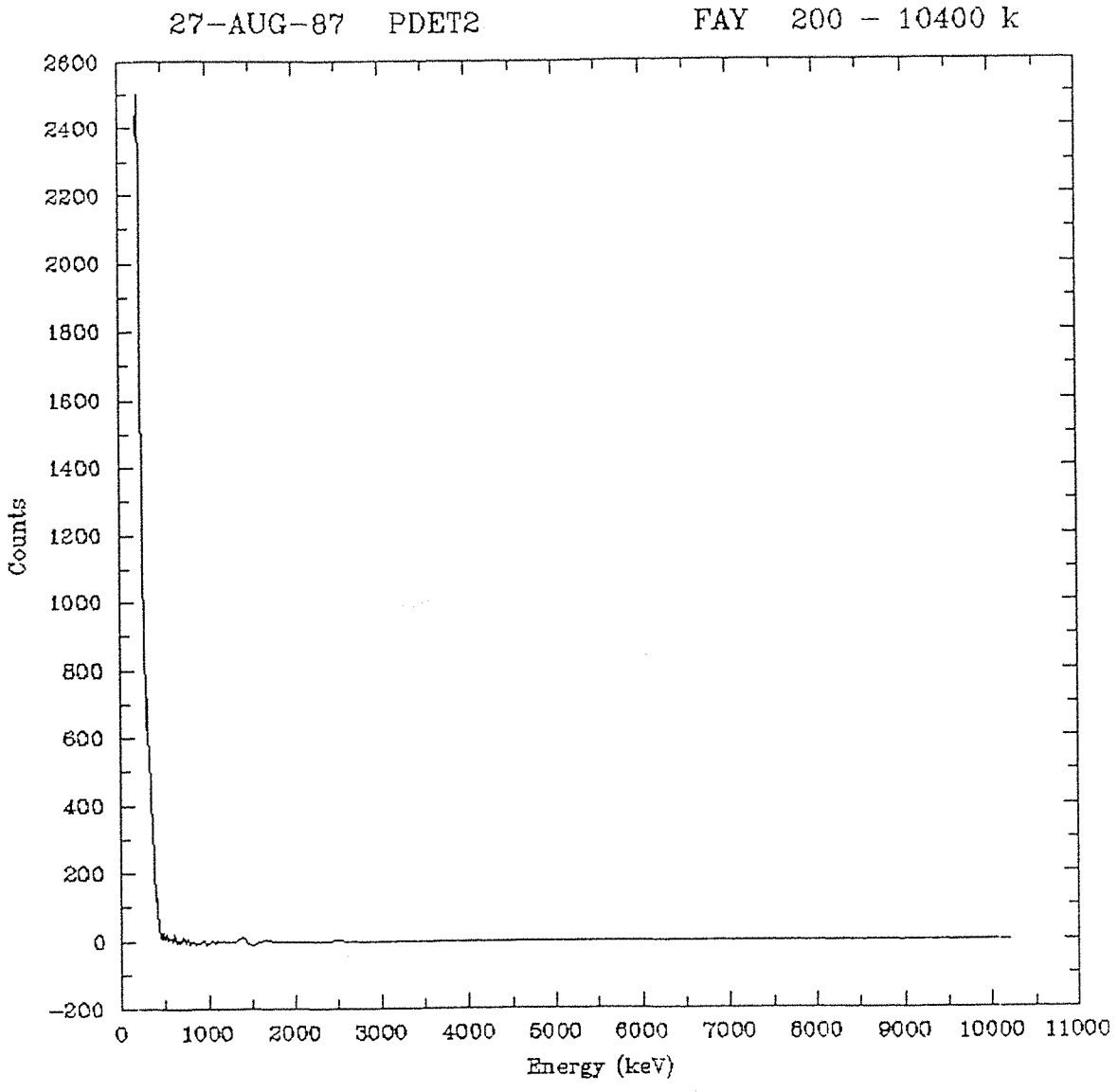

Figure (6.14) A typical scattering spectrum for a ^{137}Cs source.

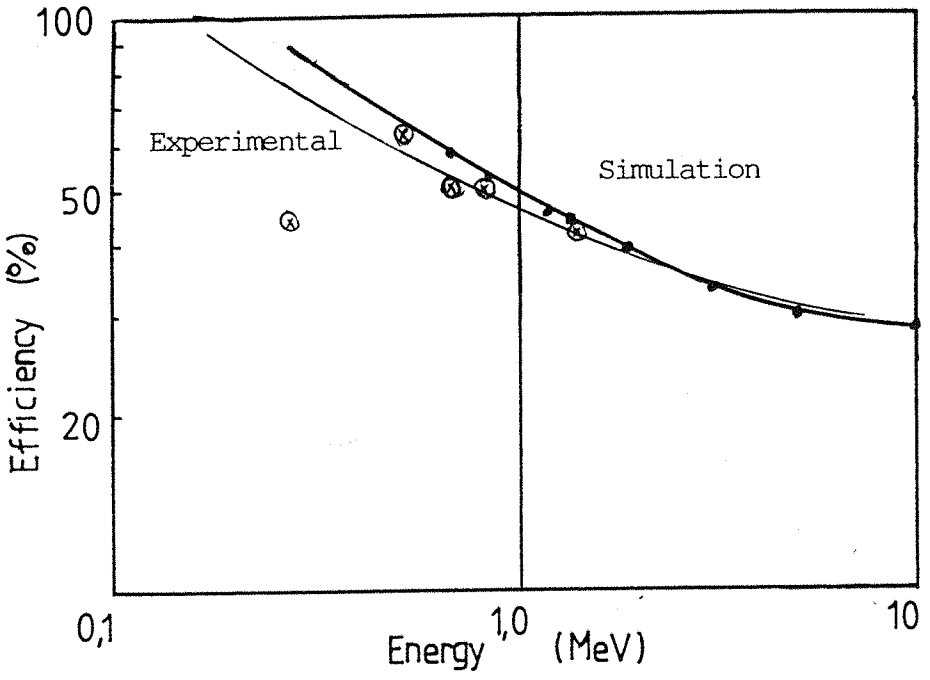

Figure (6.15) The comparison of the Monte-Carlo simulation with the experimental results.

Table (6.2)

Source	Efficiency %
^{137}Cs(662 keV)	49±2
^{22}Na(511 keV)	63±2
(1275 keV)	42±2
^{54}Mn(835 keV)	51±2
^{203}Hg(279 keV)	42±2

Table (6.2) The detection efficiencies of the ZEBRA telescope for different gamma ray sources.

The results of this test, with the exception of the ^{203}Hg source, is fairly compatible with the Monte-Carlo simulation data. The errors are in the order of less than 10% and this is understandable. The case of the ^{203}Hg source has given unexpected results from the beginning. The difference between the simulation and the experimental data was large (roughly 30% worse). This was found to be due to a combination of few factors. First, the background of all the nine position sensitive detectors was searched and it was found that at least five of them were set to about (235 keV) energy threshold instead of (200 keV) (fig.6.16). This obviously has a comparatably larger effect on decreasing the efficiency for relatively lower energy gamma ray source such as ^{203}Hg(279 keV). It is clear from table (6.2) that this factor did not contribute a great deal in decreasing the efficiency of higher energy sources. A second factor that could have contributed to this decrease is the destabilized deadtime of the experiment. The dead time could have changed during taking data without notice, and hence reduced the amount of detected photons. Finally, the over estimation of the photon flux emitted by the source due to the uncertainty of its flux (-3.7% as declared by the suppliers) could have also contributed to this problem.

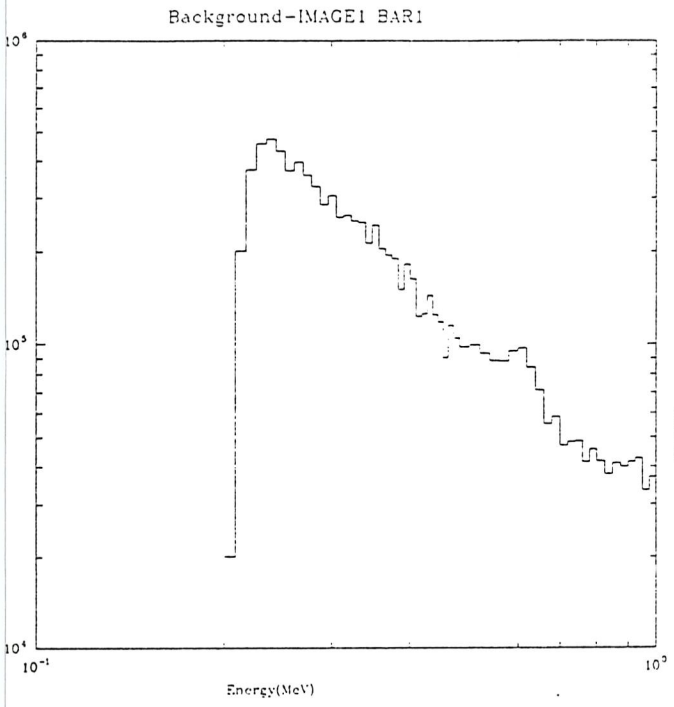
Background-IMAGE1 BAR1
Energy(MeV)

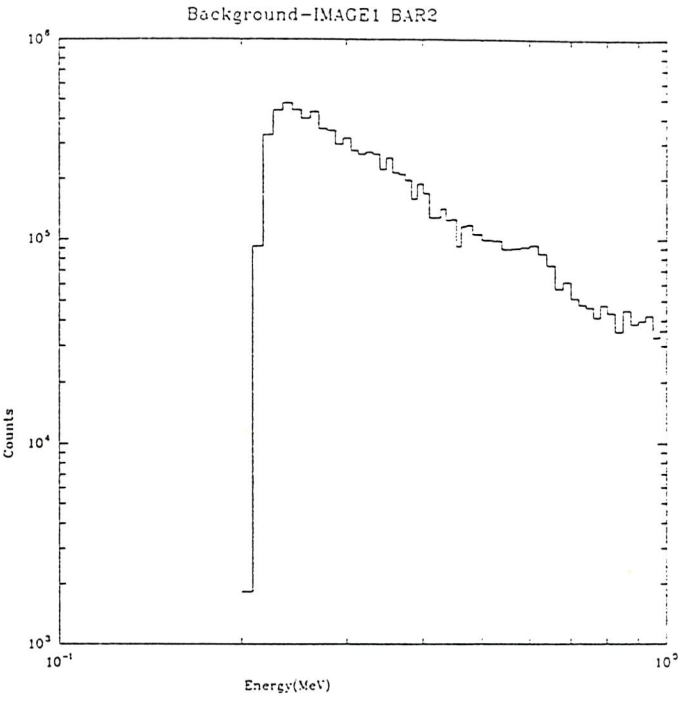
Background-IMAGE1 BAR2
Counts
Energy(MeV)

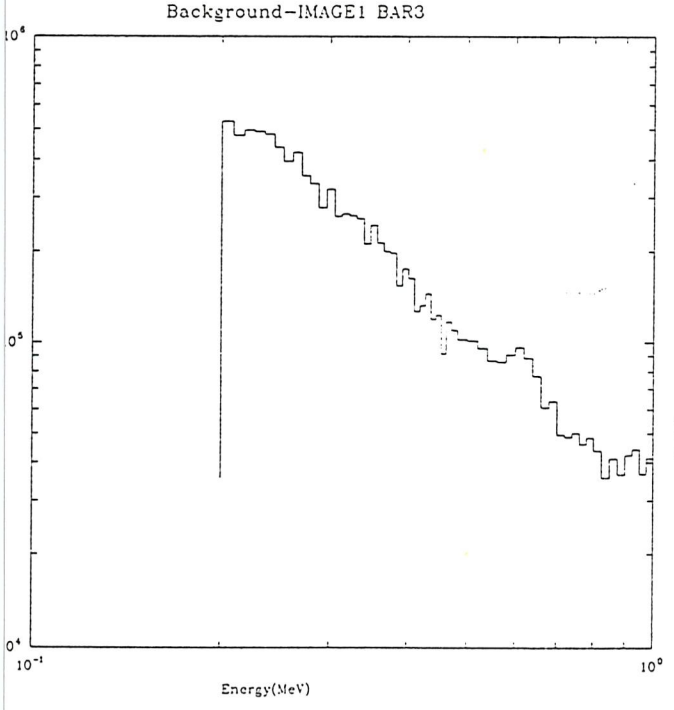
Background-IMAGE1 BAR3
Energy(MeV)

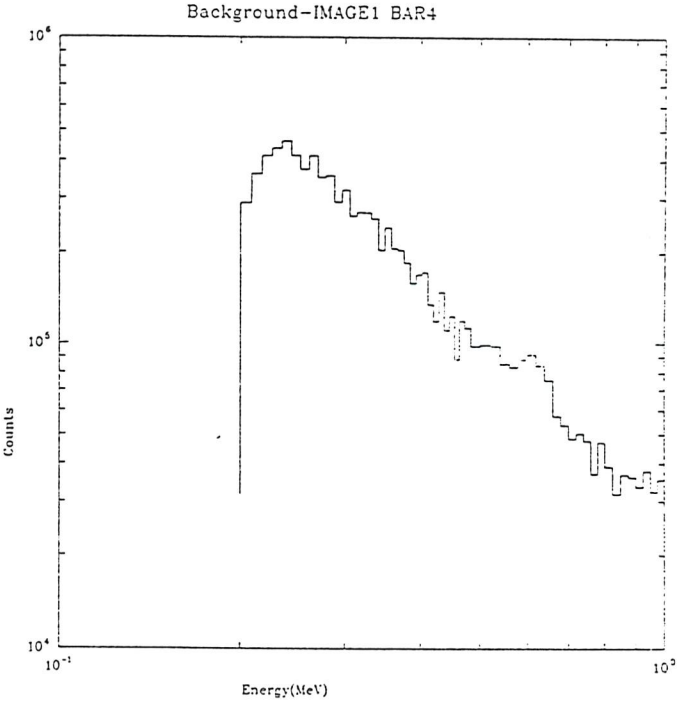
Background-IMAGE1 BAR4
Counts
Energy(MeV)

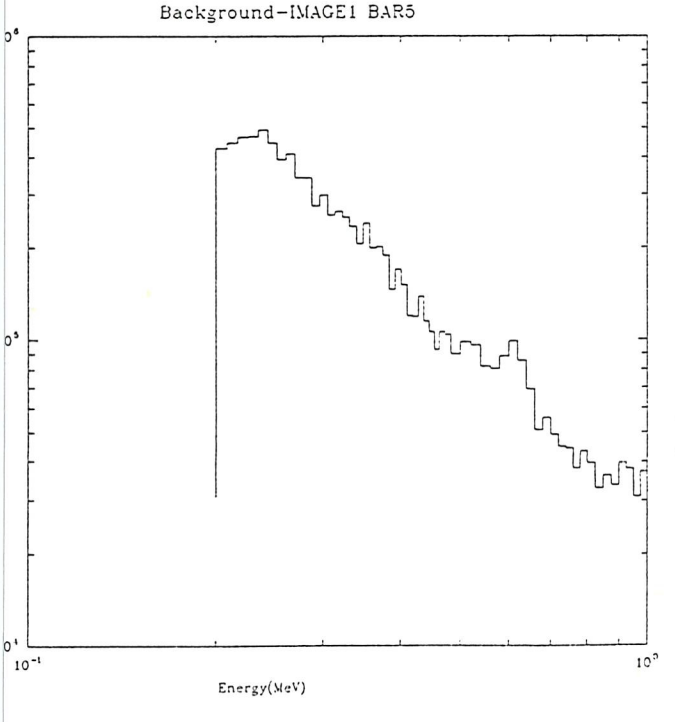
Background-IMAGE1 BAR5
Energy(MeV)

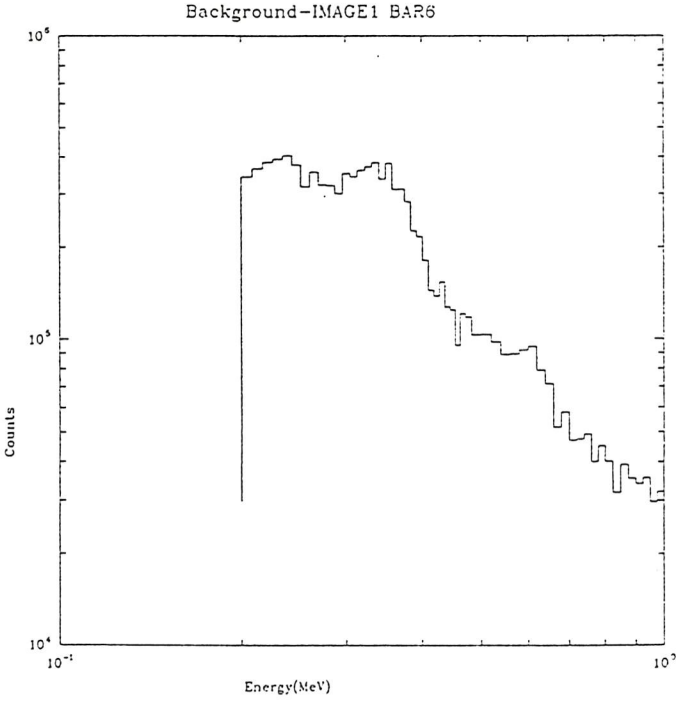
Background-IMAGE1 BAR6
Counts
Energy(MeV)

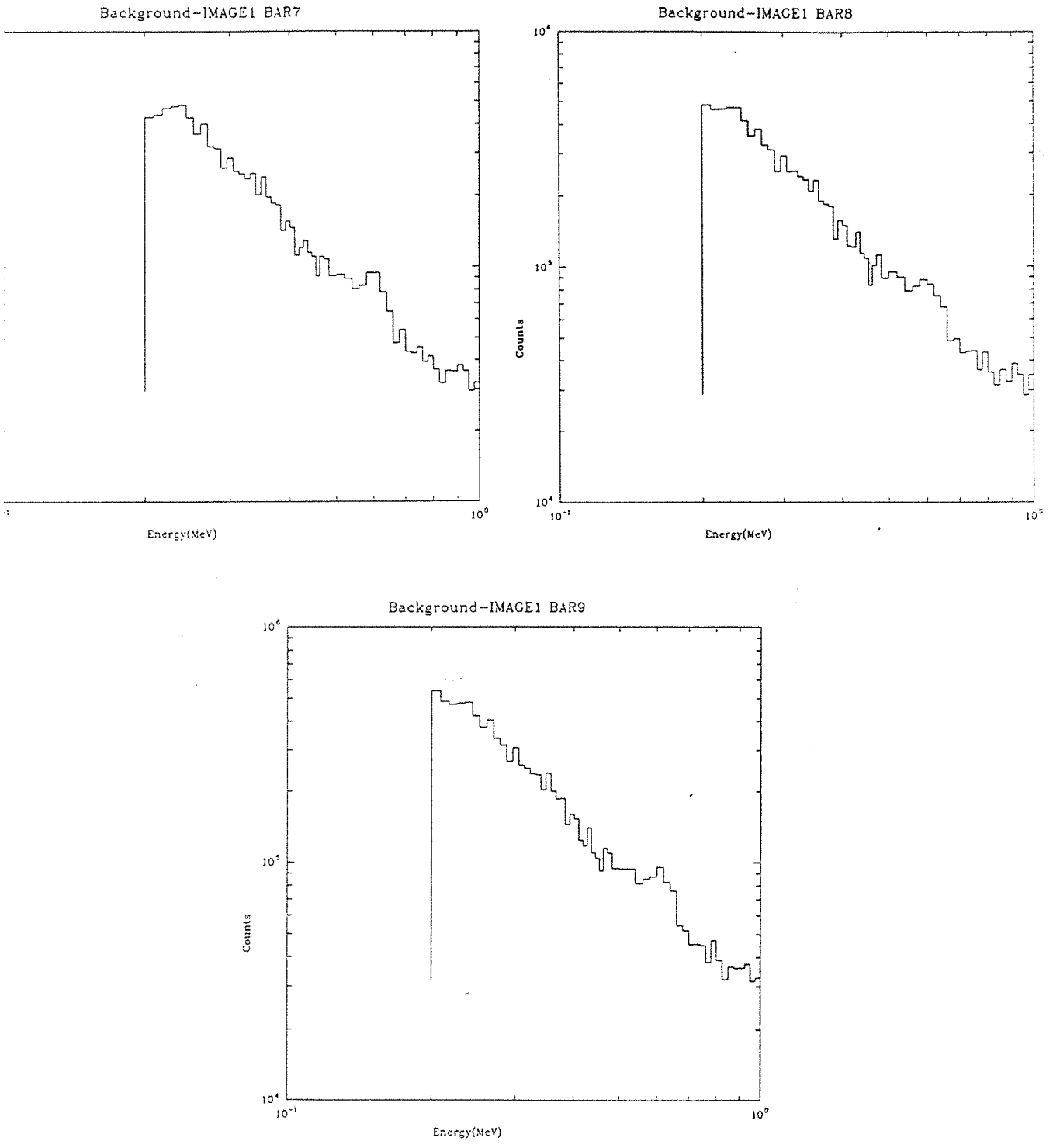

Figure (6.16) The threshold set-up of all nine position sensitive detectors .

6.5 The sensitivity of the ZEBRA telescope.

The sensitivity of the telescope to continuum and discrete gamma ray line emission was calculated at the (1σ) level with an integration period of ($2*10^4$)sec.. The continuum sensitivity curve was compared to some galactic and extragalactic sources. The time for detecting (3σ) from some of these objects was calculated. Also the line sensitivity was compared to some of the gamma ray lines previously detected from some cosmic sources. All these are given next.

6.5.1 The continuum sensitivity.

The continuum sensitivity of the ZEBRA telescope at the (1σ) level corresponding to an integration period of $2*10^4$ sec. is shown in fig.(6.17). The expression used for calculating this curve is :

$$\Phi_{min} = \frac{2\sigma}{\varepsilon}\sqrt{\frac{B(E)}{A.T.\Delta E}} \quad ph\ cm^{-2}\ s^{-1}\ keV^{-1} \qquad (6.5)$$

where :
$B(E)$ is the background level in counts.cm^{-2}.s^{-1}.keV^{-1}.
ΔE is the energy band
A is the detection area
T is the integration period
ε is the efficiency
σ is the statistical significance

The background counting rate was taken from the calculations of (Charalambous 1983) which assume that it takes the forum :

$$\frac{dN_c}{dE} = 200\ E^{-2} \quad counts\ cm^{-2}\ s^{-1}\ keV^{-1} \qquad (6.6)$$

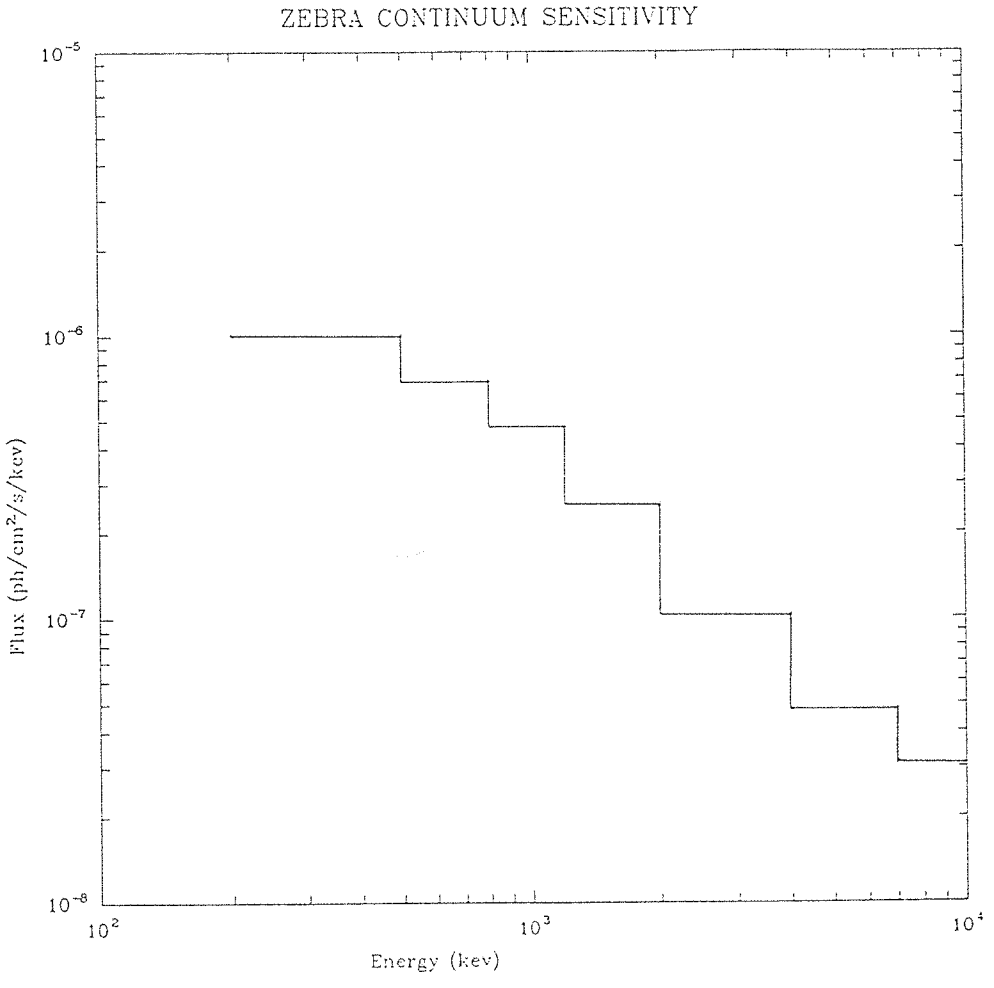

Figure (6.17) The sensitivity of ZEBRA telescope to the continuum emission of gamma ray point sources.

The detection efficiency used for the calculations based on the Monte-Carlo results given earlier.
The predicted number of (σ) from some well-known galactic and extragalactic sources, are calculated and given in table (6.3). Also the required time for the (3σ) level was calculated and given in the same table. Meanwhile table(6.4) shows the single power law used for the calculations and the references from which they were taken.
A special calculation was made for the CRAB pulsar due to its unique features. It is the only pulsar that has been observed throughout almost the entire electromagnetic spectrum. The light curve of this pulsar in the gamma ray region consists of two time peaks of equal intensities joined by an interpeak emission (Mahoney et al 1984). The sensitivity calculations, both with and without the presence of the Mask are given in table(6.5).

6.5.2 The line sensitivity.

ZEBRA line emission sensitivity for the same integration time and sigma level is shown in fig.(6.18). This curve has been derived using the expression :

$$\Phi_{min} = \left(\frac{1.3\ \sigma}{\varepsilon}\right).\sqrt{\frac{4.B(E).\Delta E}{A.T}}\ \ ph\ cm^{-1}\ s^{-1} \qquad (6.7)$$

where :
ΔE is the energy resolution of the detection plane in keV at the emission line energy.

Gamma ray lines were first observed from Solar flares (Chupp et al 1973). Since then, lines have been reported from the galactic centre, transient events and some extragalactic sources. Table (6.6) shows the line sensitivity of ZEBRA experiment for some of the detected gamma ray lines such as, the (511keV) annihilation line and the (1.8MeV) of the ^{26}Al from the galactic centre.

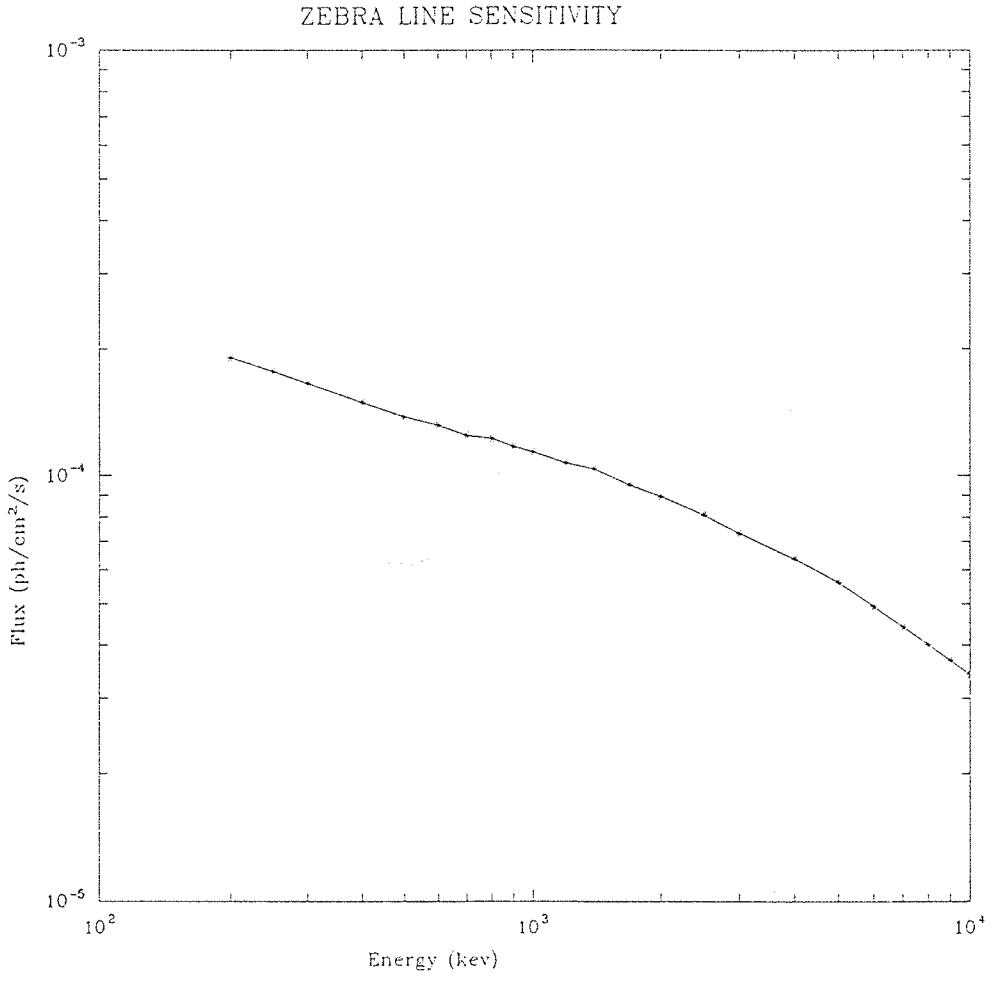

Figure (6.18) The sensitivity of ZEBRA telescope to gamma ray emission from discret line (1σ , 2 x 10^4 s).

6.6 Conclusion.

The results of the shielding experiment are very encouraging. Many photons that contribute to the intensity of the Compton distribution in the pulse height spectrum were rejected by the anticoincidence system. The conclusion of the shielding quality is shown in fig.(6.4) and (6.6).

The photon detection efficiency results were also quite promising. The comparison of these results with the simulation data did not show a great deal of difference.

Finally, all these have contributed to the prediction of a very sensitive telescope which could detect a large number of very interesting galactic and extragalactic gamma ray sources.

Chapter 7

7 A satellite development of the ZEBRA telescope : GRASP.

7.1 Introduction.

The GRASP telescope (Gamma Ray Astronomy with Spectrometry and Positioning) is a proposed future astronomy mission designed to operate as a high resolution spectral imager in the gamma ray energy range of the electromagnetic spectrum. The design cover the photon energy range from 15 keV to more than 100 MeV with a spatial resolution of about (1 arc min.) and a fine spectral analysis ($\lambda/\Delta\lambda$ = 1000) of any gamma ray line features in the spectra. This experiment with its long mission lifetime is capable to study as much as 1000 of astronomical objects.

This design comprises a coded mask and a position sensitive detector plane. The detection plane is a combination of Caesium Iodide(Tl) scintillators and Germanium solid state detectors arranged into an overall position sensitive matrix array. The CsI elements, which are a major part of the position sensitive detector, provide a high efficient active shield for the solid state detectors (Bignami et al 1987).

A schematic view of the GRASP telescope is shown in fig.(7.1) and the performance parameters are given in table(7.1). The CsI array is capable to generate high quality images of gamma ray continuum emission.

As the sensitivity of the CsI array to gamma ray line emission is very good (better than 10^{-5} ph.cm^{-2}.s^{-1}.), it is capable to locate line sources quite accurately with a spectral resolution of ($E/\Delta E$ = 10). The quality of the images generated by the Germanium is not so good but have an excellent spectral resolution. The combined data can provide a percise origin and a fine spectral structure.

To reduce the photon induced background in the CsI, a 3cm. thick CsI veto counter is surrounding the CsI imager plane. The shielding system is completed by an active collimator placed on top

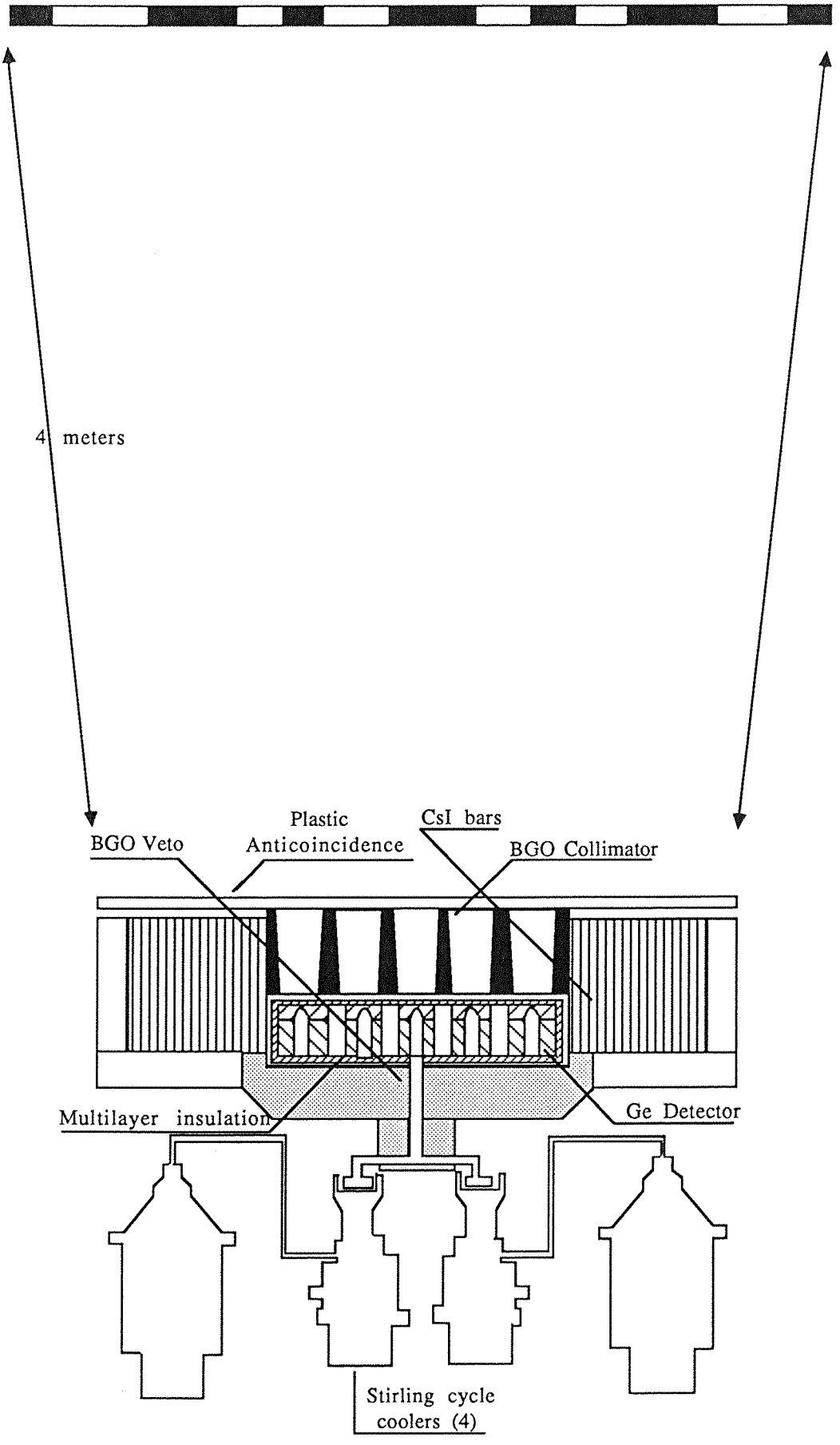

Figure(7.1) A schematic diagram of the GRASP telescope

Performance parameter	Ge array	CsI array
Energy range	15 keV–10 MeV	300 keV–100 MeV
Detection area	550 cm^2	2500 cm^2
Spectral resolution ($E/\Delta E$ at 1 MeV)	10^3	20
Field of view	6° FWHM	6° FWHM
Typical point source location capability	3′	1′
Temporal resolution	0.1 s	0.1 ms
Line detection sensitivity at 1 MeV		
(a) 3σ in 10^5 s	2×10^{-5} photons cm^{-2} s^{-1}	3×10^{-5} photons cm^{-2} s^{-1}
(b) 3σ in 10^6 s	6×10^{-6} photons cm^{-2} s^{-1} (narrow line, width <1 keV)	10^{-5} photons cm^{-2} s^{-1} (broad line, width 20 keV)
Continuum sensitivity		
(a) 3σ in 10^5 s	3×10^{-7} photons cm^{-2} s^{-1} keV^{-1}	2×10^{-9} photons cm^{-2} s^{-1} keV^{-1}
(b) 3σ in 10^6 s	10^{-7} photons cm^{-2} s^{-1} keV^{-1} (at 100 keV, bandwidth 100 keV)	6×10^{-10} photons cm^{-2} s^{-1} keV^{-1} (at 10 MeV, bandwidth 5 MeV)

Table (7.1) Summary of GRASP detector characteristics.

of the Ge detector and a thick scintillator veto arrangement on the bottom.

7.2 The Germanium spectrometer.

This part of the detection plane comprises two different kinds of detector elements. The first part is a planar type hyperpure Ge detectors constructed to detect photons with energy< 100 keV and to localize their interaction position.
The second part is a coaxial hyperpure Ge detectors for the detection of photons with a medium energy (100keV-10MeV).

7.2.1 The planar array.

Each of the planar array detectors has a dimension of $(5.5*5.5*1)cm^3$, with strips ruled on the top and the bottom 1cm. apart as shown in fig.(7.2). There are 10 preamplifiers, 5 on the top and 5 on the bottom which operate to localize the interaction within 1cm.. There will be no difference whether a p-type or n-type Ge is employed since electrons and holes are travelling roughly the same distance in both cases.

7.2.2 The coaxial array.

The major contribution to the background in the energy level of few hundred keV to few MeV is due to the radioactivity generated inside the detector. Gehrls 1985, came to a conclusion that the main source of background noise is related to the decays inside the detector which is due to the activation of the elements that constitute the crystal.
In the Ge detectors, at energies above 200 keV, gamma ray photons can be absorbed by multiple spatially separated interactions which consist of one or more Compton scattering followed by a photoelectric absorption. Meanwhile the β^- decay of proton and neutron induced radionucleids in the Ge has a short path of few mm.. The first interaction has been considered as a multiple-site and the second interaction as a single-site.

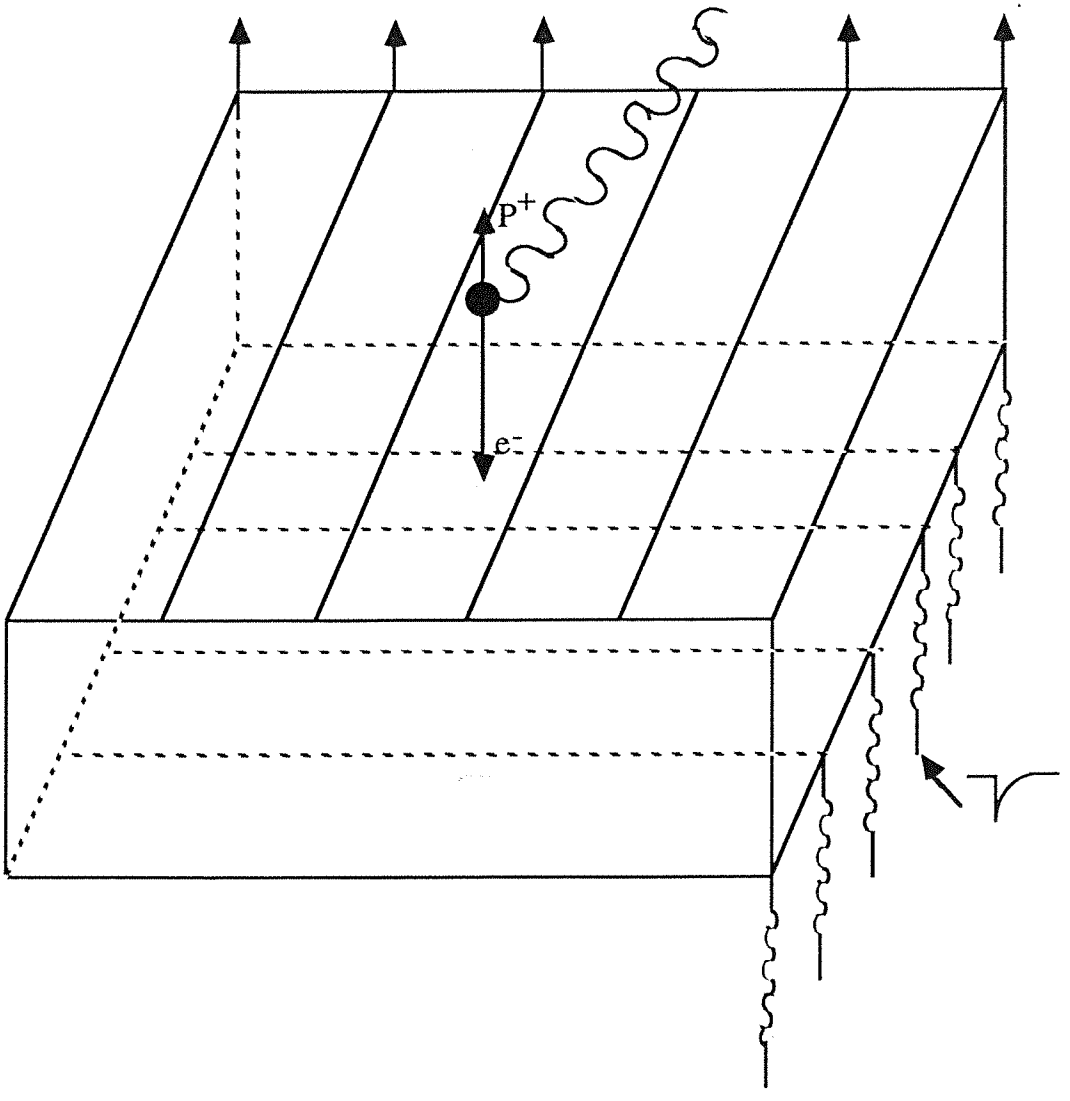

Figure(7.2) The operation principle of a planar strip detector. The liberated electron - hole pairs resulting from the interactions of gamma ray photons which are collected at the upper and lower electrodes ; therby localizing the position of interaction

Fig.(7.3) shows the type of gamma ray photon interactions which possibly occur in the Ge array. Interaction type-1 is a single-site event leaving its entire energy in the upper part detector. Case-2 is a multiple-site event with loosing some energy in the upper detector and the rest in the lower detector. While in case-4 the photons traverse the upper detector without suffering any energy lose and stops in the lower layer suffer a single Compton scattering followed by a photoelectric absorption. Finally, in case-3, the photon has left some of its energy in one Ge detector and the remaining in another detector and this type of events are rejected.
The background level can be reduced by about an order of magnitude if a technique can be used to distinguish between single and multiple-sites. This eventually improve the sensitivity of the experiment significantly.
The GRASP team are trying to achieve this aim by one of the following three techniques :

1. Detector segmentation.
2. Multi-layer planar.
3. Pulse shape discrimination.

Any of these techniques will reject about 95% of the single-site events and accept more than 80% of the multiple-site interactions. Meanwhile the β^- decay will be eliminated in any cases.

7.3 Caseium Iodide imaging detectors.

This part of the detection plane is constructed from a 3-dimensional array of gamma ray detectors which are capable to locate and measure the energy deposited by the photon interactions in the CsI detectors. The overall CsI position sensitive detectors comprise a stack of bars (approximate dimensions are 13.5*13.5*150 mm^3.).
These bars (about 100 of them) are based around the central Ge array and are acting as an active shield of (15cm.) thickness for the Ge array.
The cross section of these bars matches the sensitive central area of the photodiodes and has a maximum light collection efficiency. The length of these bars has been chosen to be 15cm. to provide the

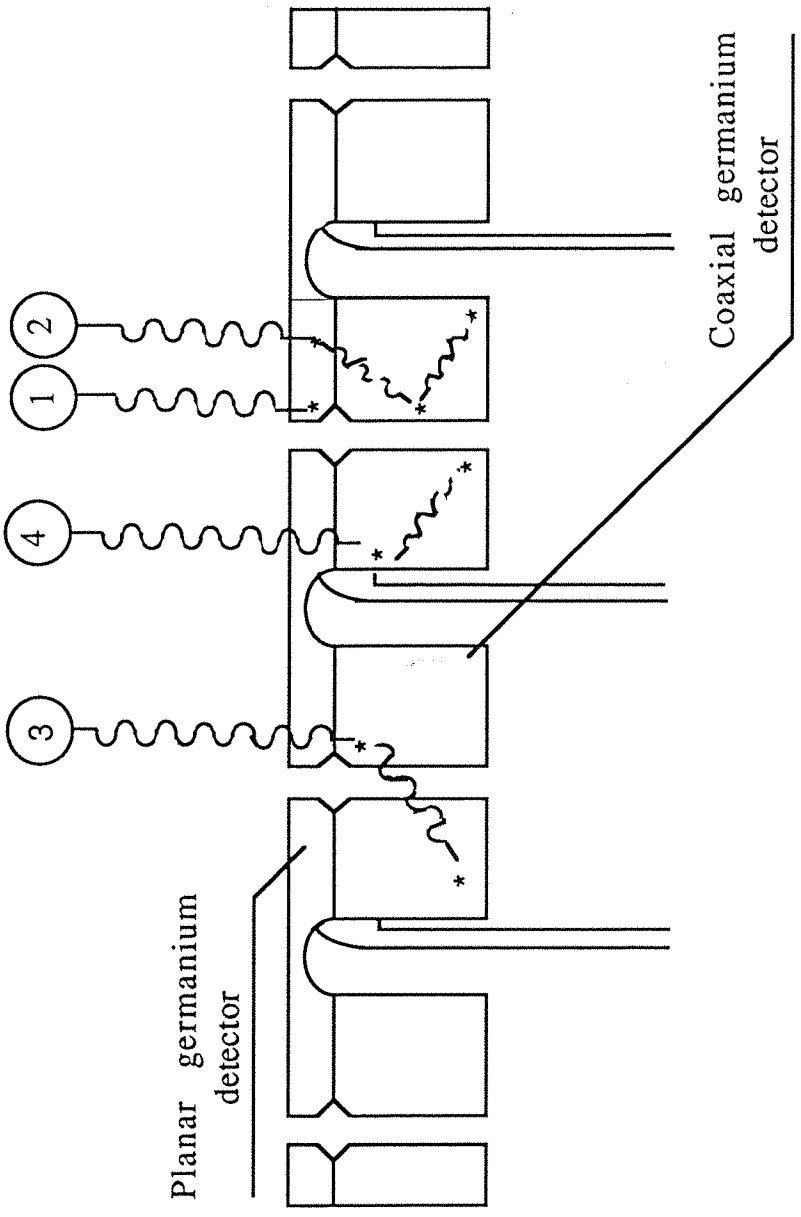

Figure(7.3) Gamma ray photon interactions in the germanium array

required thickness of the veto shielding for the Ge array. At the same time the width of the bars has been chosen to be 13.5mm. to provide a resonable pixel size which matches the Ge element and the employment of coded mask to generate images of the sky at (arc min.) level.

The CsI bars are viewed by pin photodiodes and these diodes are connected to low level noise amplifiers built specially for this purpose. Each bar is optically isolated from the adjacent units.

In this experiment, photodiodes have been chosen instead of photomultipliers for many reasons :

1. They do not present any significant attenuation of gamma rays.
2. They are uneffected by magnetic field changes.
3. They do not require a high voltage power supply to run.
4. They are small and light.

The surface of the CsI crystals has been treated in such away to give an attenuation light signal as a function of distance along the bar.

The attenuation of light signals along the bars can be given by :

$$E_1 = \left(\frac{E_\gamma}{E_o}\right) . P . e^{-\alpha(L/2+x)} \qquad (7.1)$$

$$E_2 = \left(\frac{E_\gamma}{E_o}\right) P . e^{-\alpha(L/2-x)} \qquad (7.2)$$

where :

L is the length of the bar.

x is the distance from the midpoint of the bar.

$E\gamma$ is the energy deposited at the bar.
Eo is the required energy to emit a light quantum in the detector per keV energy deposited.
P is the total possibilities that a light quantum produced at one end generate a photoelectron in the nearby photocathode.

Thus the position of interaction can be given as :

$$x = \frac{1}{2\alpha} \ln(E_2/E_1) \qquad (7.3)$$

and the error as :

$$\Delta x = \frac{e^{\alpha L/4}.\sqrt{e^{\alpha x}+e^{-\alpha x}}}{2\alpha.\sqrt{E_\gamma.(P/E_o)}} \qquad (7.4)$$

The energy deposited is :

$$E_\gamma = e^{\alpha L/2}.\sqrt{E_1.E_2}.(\frac{E_o}{P}) \qquad (7.5)$$

and the error is :

$$\frac{\Delta E_\gamma}{E_\gamma}(F.W.H.M.) = 2.35\ \Delta x \qquad (7.6)$$

7.3.1 The performance of the CsI detection units.

The experimental arrangement of the evaluation of the CsI bar performance is shown in fig.(7.4). The signals from the amplifiers are processed by a CAMAC system in conjunction with a Vax computer. A typical roll-off curve of one of the bars is shown in fig.(7.5)(Dean et al 1987). The gamma ray photons derived from a collimated ^{137}Cs source. The attenuation coefficient of this particular bar is $(\alpha = 0.1)$. A wide range of (α) values are obtainable experimentally which is very helpful to design detectors with optimum positional resolution.
The estimated spectral values which can be supplied by the GRASP

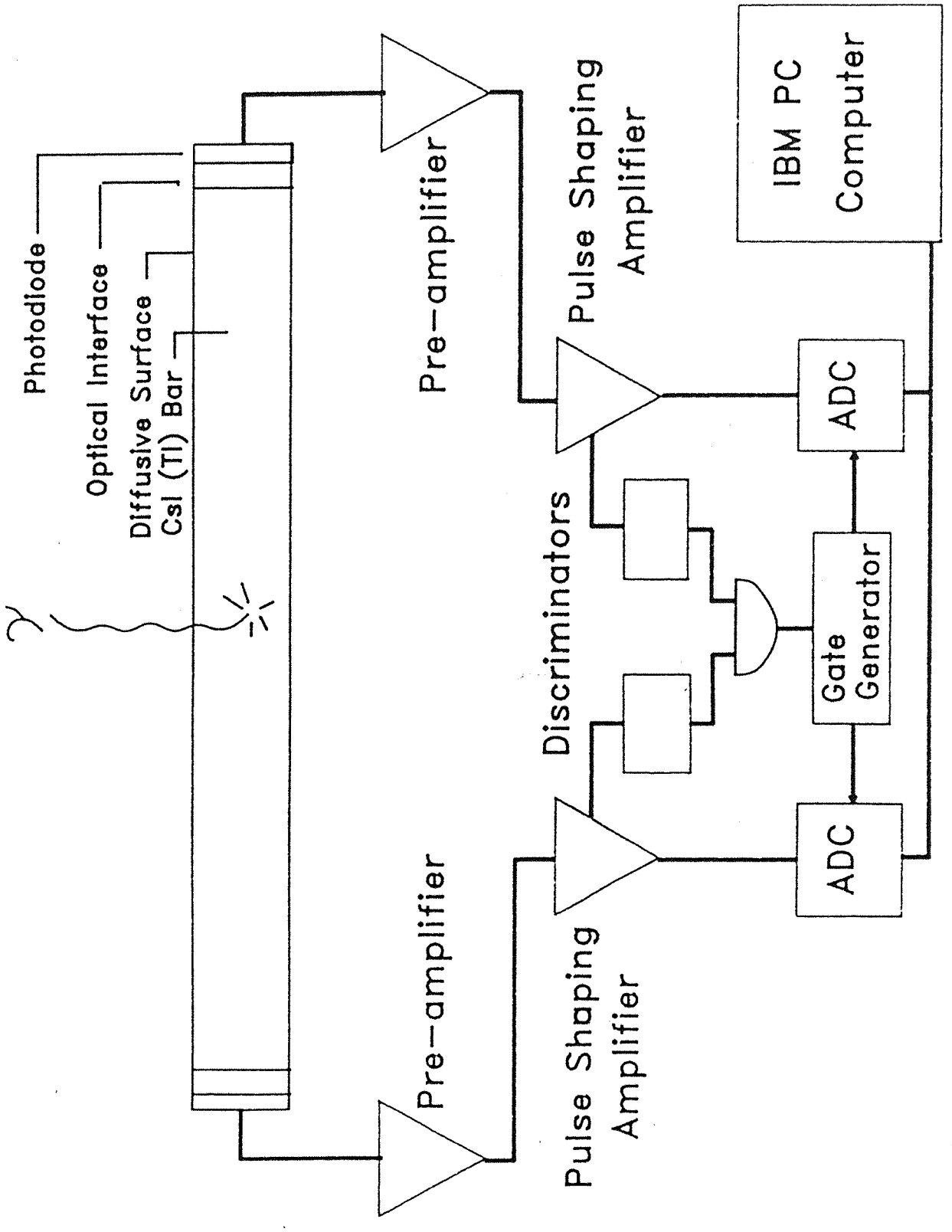

Figure (7.4) Experimental arrangment of the CsI detector test.

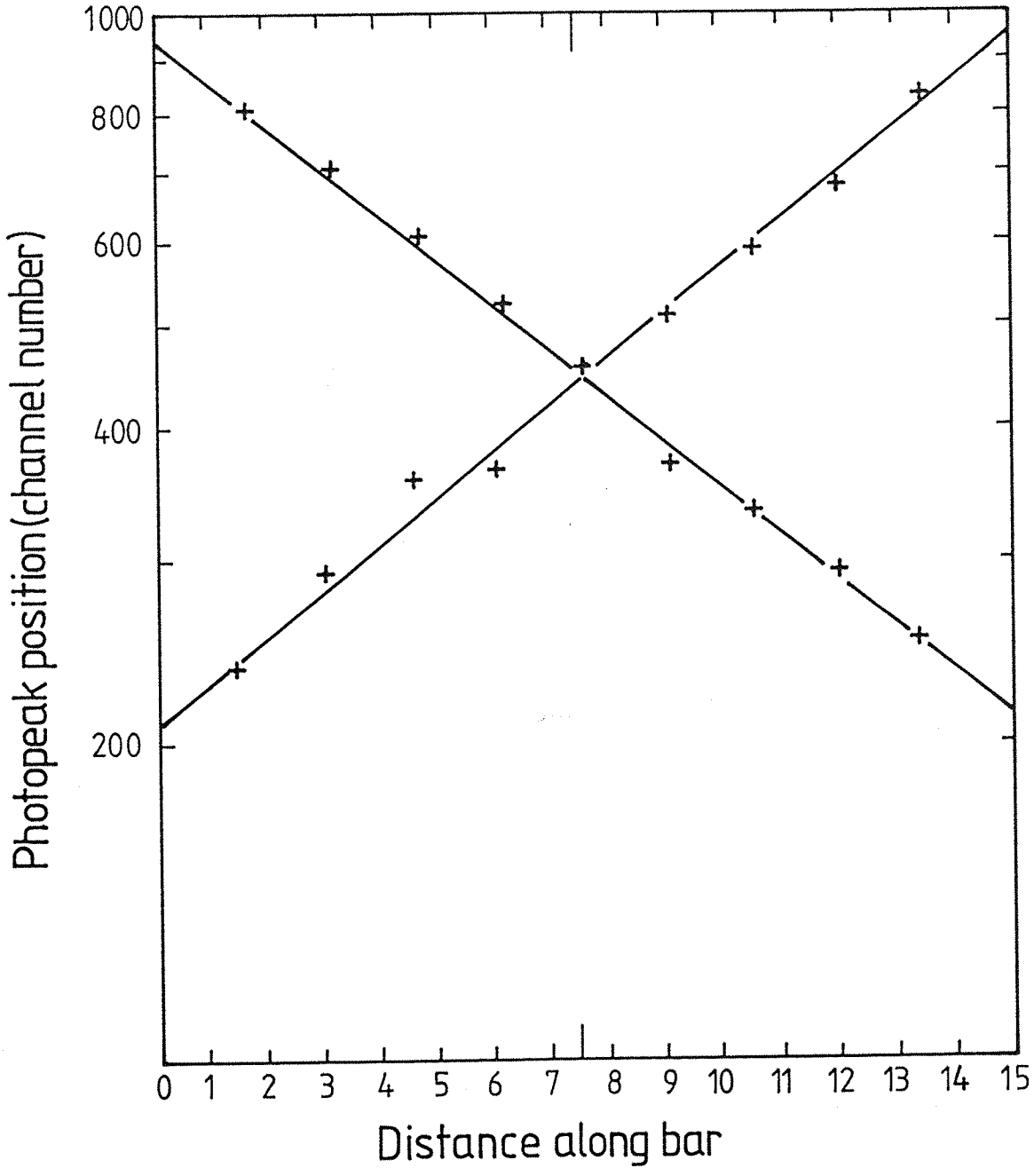

Figure (7.5) The light attenuation curve for CsI bar.

geometry are :

$$\Delta x = 0.8\text{-}1.5 \text{ cm. F.W.H.M.}$$
$$\frac{\Delta E}{E} = 7\text{-}10 \text{ \% F.W.H.M.}$$

at gamma ray energy of (1 MeV) and (α) values of (0.05-0.1).
The ^{137}Cs spectrum taken from this arrangement is shown in fig.(7.6). The performance of the CsI/photodiode combination will not degrade in the radiation environment. Fig.(7.7) shows this performance over the range of (-40°C.) to (+40°C.) with a near constant performance.
The detection efficiency of the telescope over the working energy range is close to unity as shown in fig.(7.8). Also the absorption efficiency is given in the same diagram.

7.4 The veto system.

This system is designed to reduce the background noise level produced by the undesired gamma ray photons, also to suppress the effect of the interaction of charged particles on the system.
The Ge solid state spectrometer is shielded mainly by the CsI detectors and partially by the arrays of the CsI counters. The collimator's aperture has been chosen in some way to reduce the contribution of cosmic gamma ray diffuse component of the background at energies up to 100 keV.
Since the CsI imager supply continuum and broad line sensitivity at energies above few hundred keV, it does not require a thick veto system. At this level, the major contribution of the background is the neutron induced events (Charalambous et al 1985). Therefore the 3cm. thick CsI veto counters that surround the CsI imager has been optimized to reduce the background level.
The last part of the veto system is the plastic anticoincidence counter which designed to eliminate the effect of the charged particle specially low energy electrons.

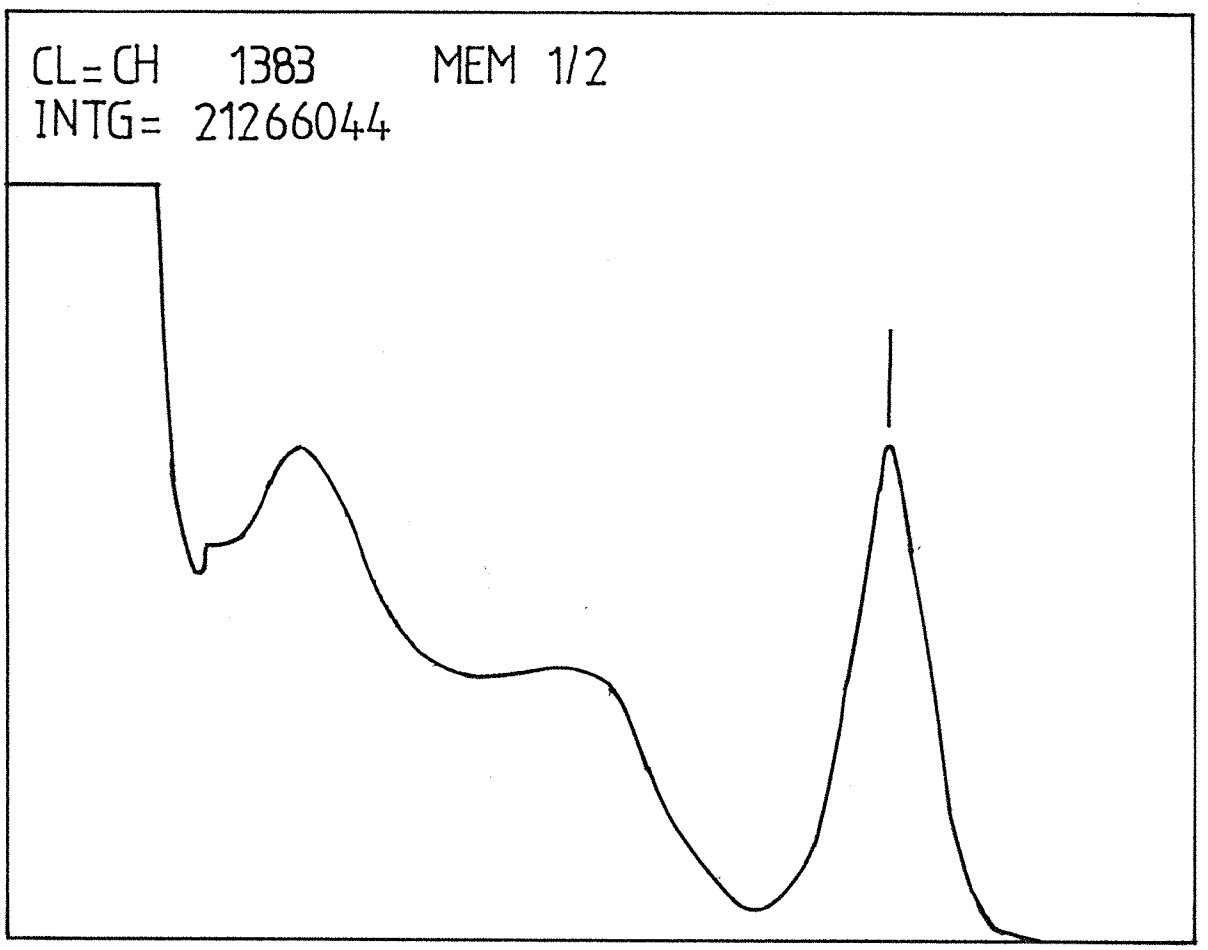

Figure (7.6) A typical ^{137}Cs source spectrum from the combination of CsI/Photodiode.

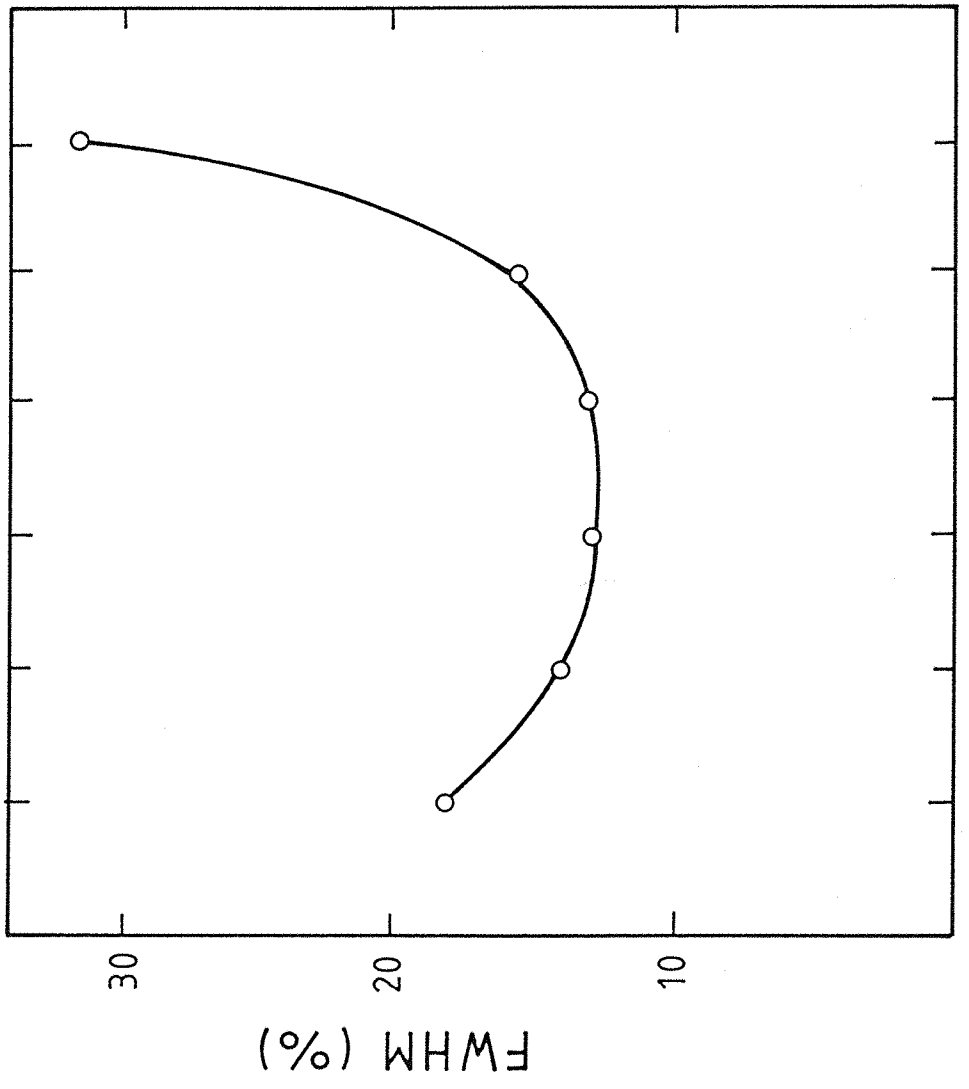

Figure (7.7) The energy resolution of the CsI bar as a function of temperature.

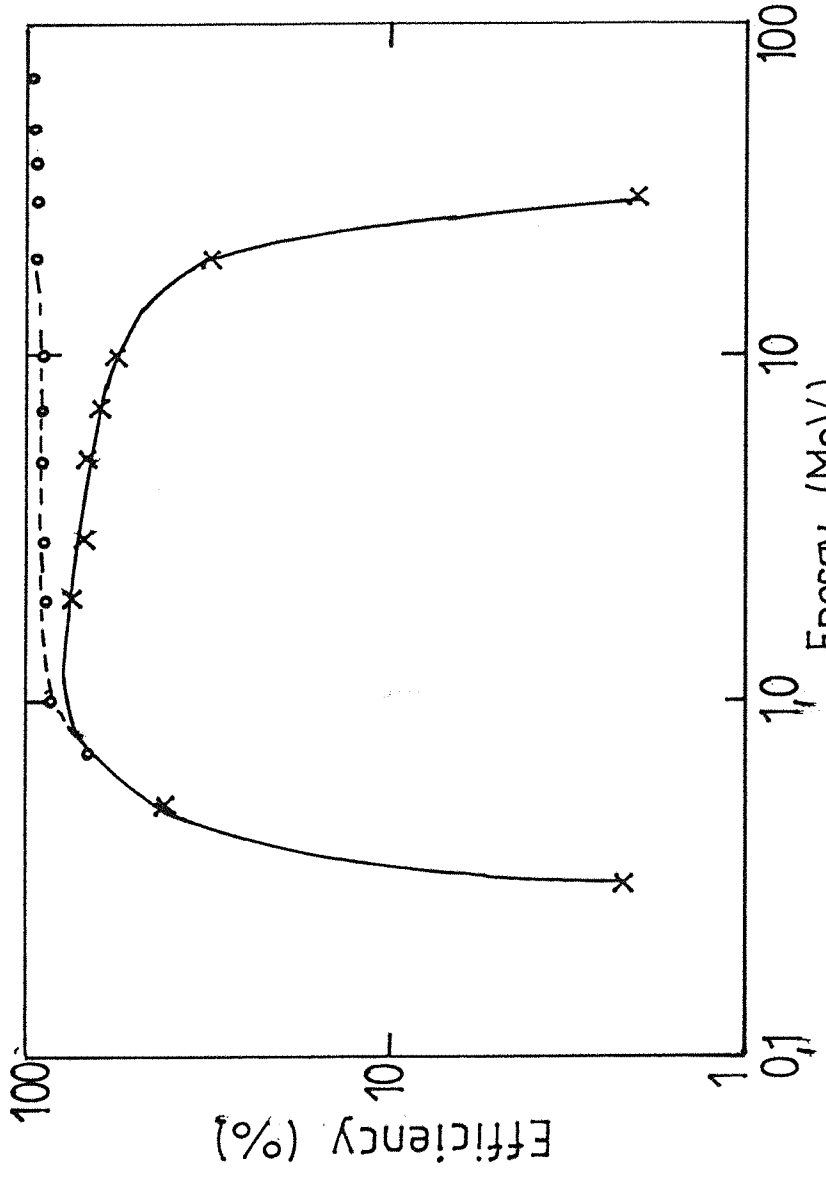

Figure (7.8) The detection efficiency of the CsI detection plane as a function of energy.

7.5 The coded mask.

Coded aperture mask technique has an enormous role in producing high quality images of gamma ray sources at the present time. This technique has increased the possibility of designing gamma ray telescopes with a large detection plane, wide field of view, fine angular imaging capacity and the ability of simultaneous monitoring of source flux and background counts. The latter aspect is extremely important in gamma ray astronomy due to the existence of many desirable weak sources to be detected.
The GRASP telescope will employ the latest technique in coded aperture mask which is a rotating hexagonal uniformly redundant arrays mask.
The introduction of rotating masks which periodically replace mask pattern by anti-mask pattern, will improve the endurance to spatial and time variation in the detector background noise (Coock et al 1984).
Some possible patters for the GRASP mask is shown in fig.(7.9). The basic mask pattern elements size is related to the CsI element size which is matched to the size/positional resolution of the Ge detector.
The substance of the mask elements will be a high-Z material such as Tungsten with a thickness of about 2cm.. The mask will be mechanically supported by a honeycomb structure which is >80% transparent for photons with energy more than 15 keV. The rotation time of the mask will be about 1-10 minutes.
Good quality images can be produced by the Ge and CsI detectors. The quality of the images can be improved by the combination of the two data sets.

7.6 The electronics system.

This system consists of two sets of (Front End Electronics-FEE) and (Digital Processing Electronics-DPE) units. One for the CsI detectors and one for the Ge detectors. Both units transfer their information to one (Data and Telecomand Interface Electronics-DTIE) which is consequently transfer the data to the (Data and Telecommand Bus) as shown in fig.(7.10).
The FEE contains the preamplifiers, amplifiers, analog thresholds,

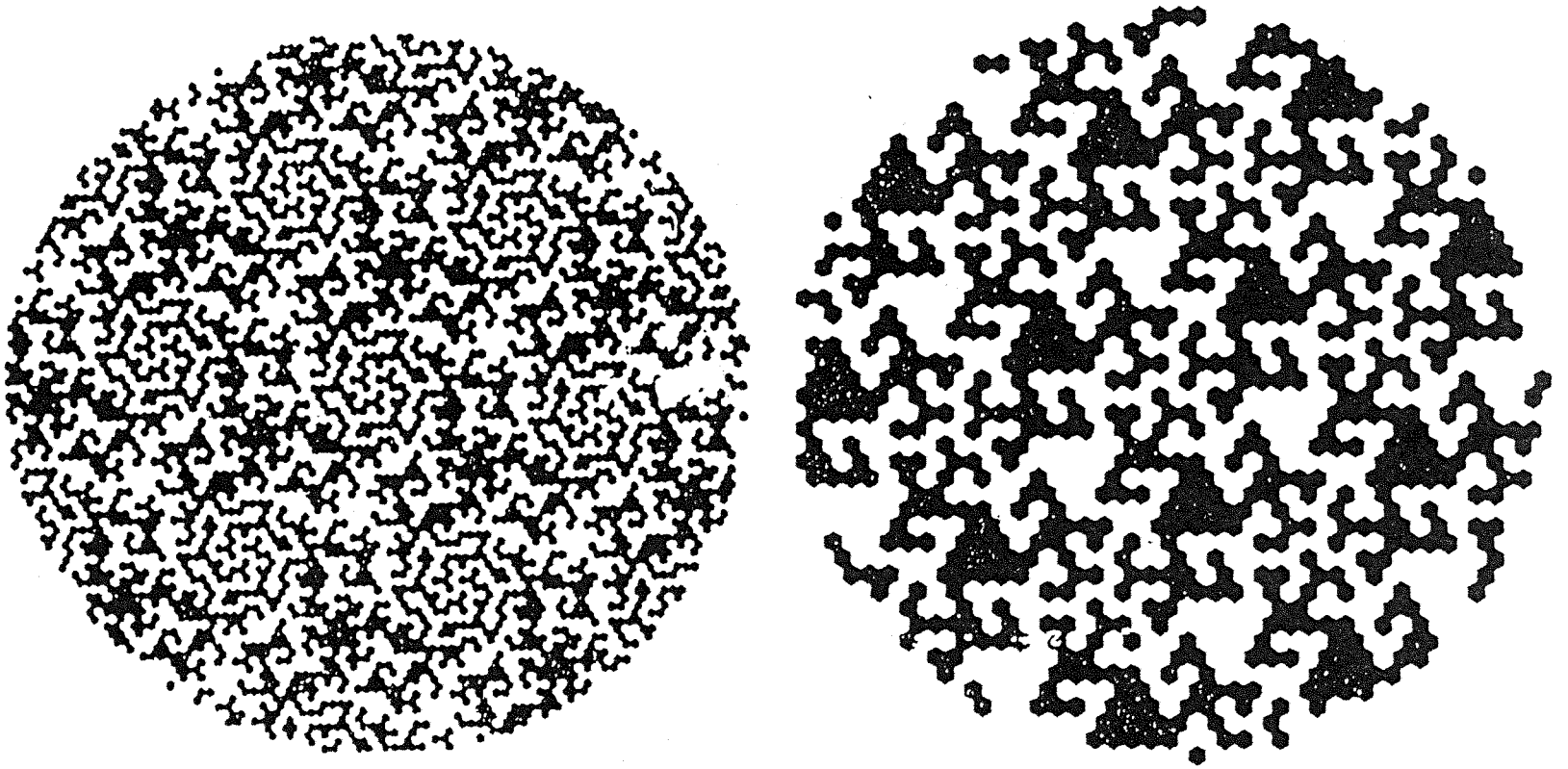

Figure (7.9) Some examples of uniformly redundant array coded aperture masks.

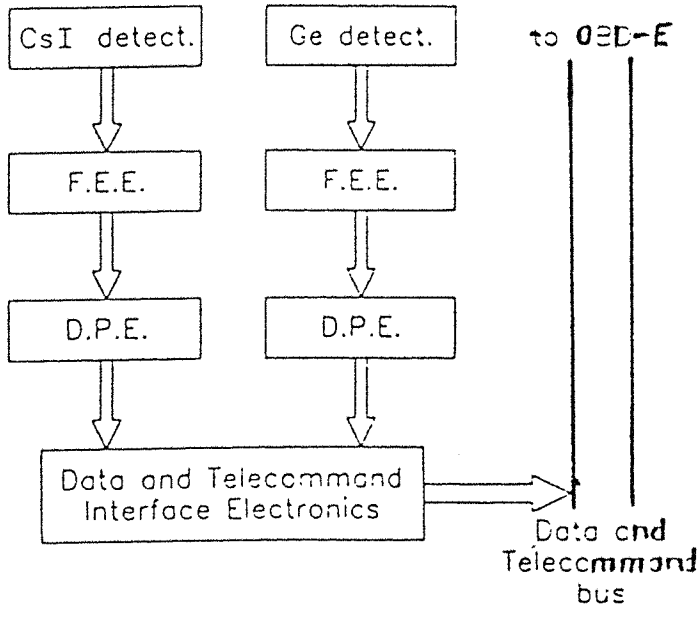

Figure (7.10) The electronics system of the GRASP telescope.

basic coincidence circuits and analog to digital conversion circuits. The FEE is divided into sub-divisions,each division is responsible for receiving data from a stack of bars typically 100 of them (this only in the case of the FEE of the CsI detectors) and then transfer the data to the DPE. A similar arrangement has been employed for the FEE of the Ge detectors.
The DPEs have several functions such as; receiving data from the FEEs and select the desirable events, controlling thresholds,recognition of mode of interaction, timing and generating House-keeping data (e.g. event-rate meters,dead time counters..etc). The DTIE receive data from the two DPEs, organize and then transfer them to the (On-Board Data Handling Electronics Electronics-OBDHE) via the command and the data bus. A detailed description of the GRASP telescope is given by (Bignami et al 1988).

7.7 Background and sensitivity calculations.

7.7.1 Background level.

The background estimation for the CsI detectors is based on the results of the Monte-Carlo studies and experimental tests done at Southampton University to evaluate the background of the ZEBRA and SIGMA projects. Charalambous et al 1985 have determined the various background components in low energy gamma ray telescopes. While the estimation for the background level in the Ge detectors is based on both balloon and satellite experiments (Geherls 1985, Pasciesas et al 1983, Mahoney et al 1980).
The following components are contributing to the background level of the CsI detectors :

1. Cosmic diffuse photons that enter the forward aperture.
2. Gamma rays which locally produced by the interaction of gamma ray photons with the material of the space-craft.
3. Events generated from the neutrons produced throughout the body of the experiment and the space-craft.
4. Spallation generated within the detectors.

Meanwhile, the components that dominate the background level in

the Ge detectors are :

1. Cosmic diffuse photons which enter the front aperture.
2. Cosmic diffuse photons which pass through the CsI detectors and counters.
3. Events generated from neutrons, such as elastic neutron scattering and β^- decay.
4. Spallation products and inelastic neutron scattering within the Ge detectors which consequently generate radioactive isotopes and hence gamma ray lines.

7.7.2 Sensitivity calculations.

The GRASP continuum sensitivities as shown in fig.(7.11) are corresponding a (3σ) significance of 10^5 and 10^6 seconds integration times. The calculations are based on the formula given in section (6.5.1).
Up to 500 keV, the Ge detectors are used to supply the main continuum sensitivity while the CsI arrays provide the rest of it.

The line sensitivities of the telescope for the same integration times are given in fig.(7.12 a,b) and the formula used for the calculations is given in section (6.5.2).

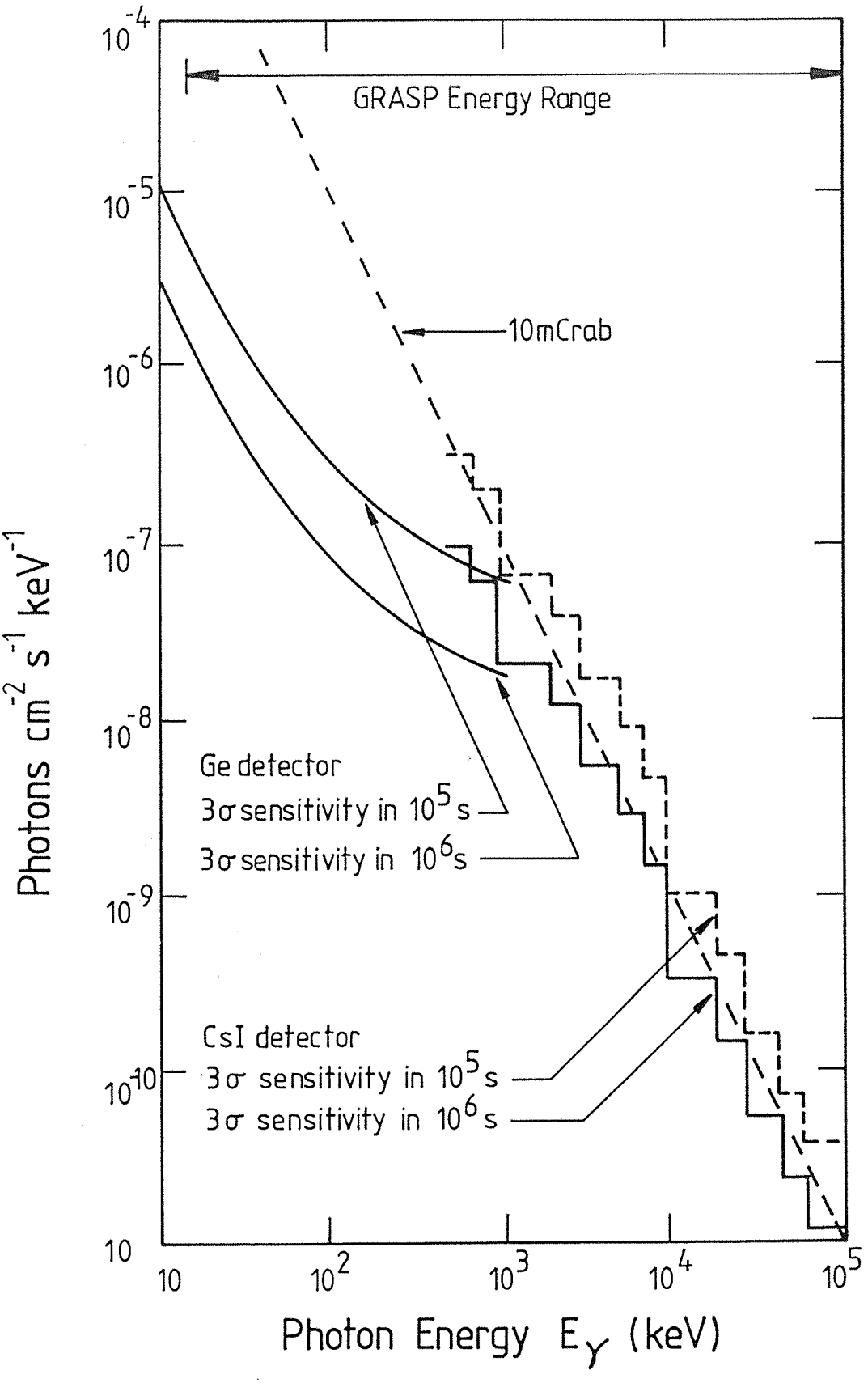

Figure (7.11) The continuum sensitivity of the GRASP tele scope.

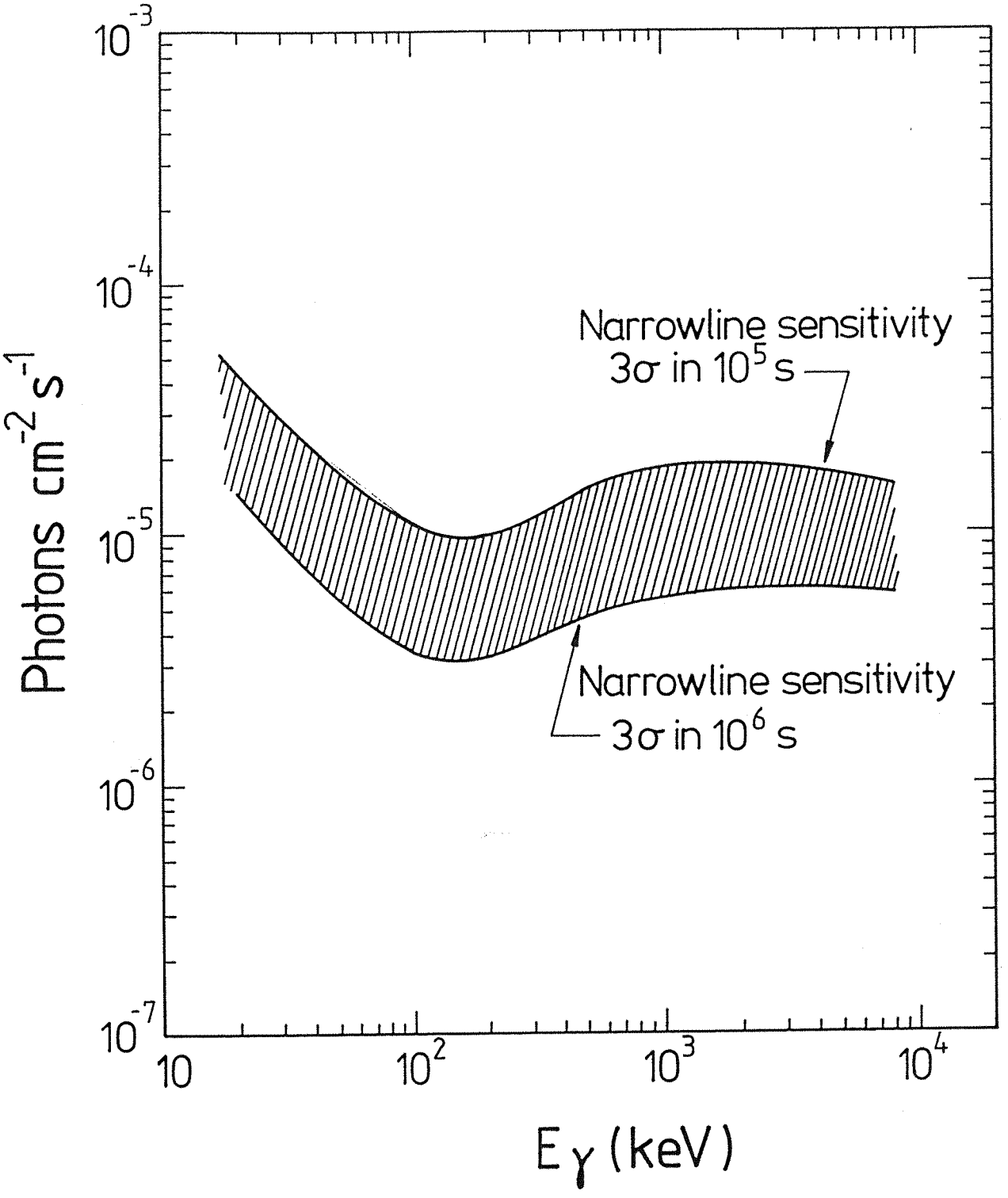

Figure (7.12b) The narrowline sensitivity of the GRASP telescope.

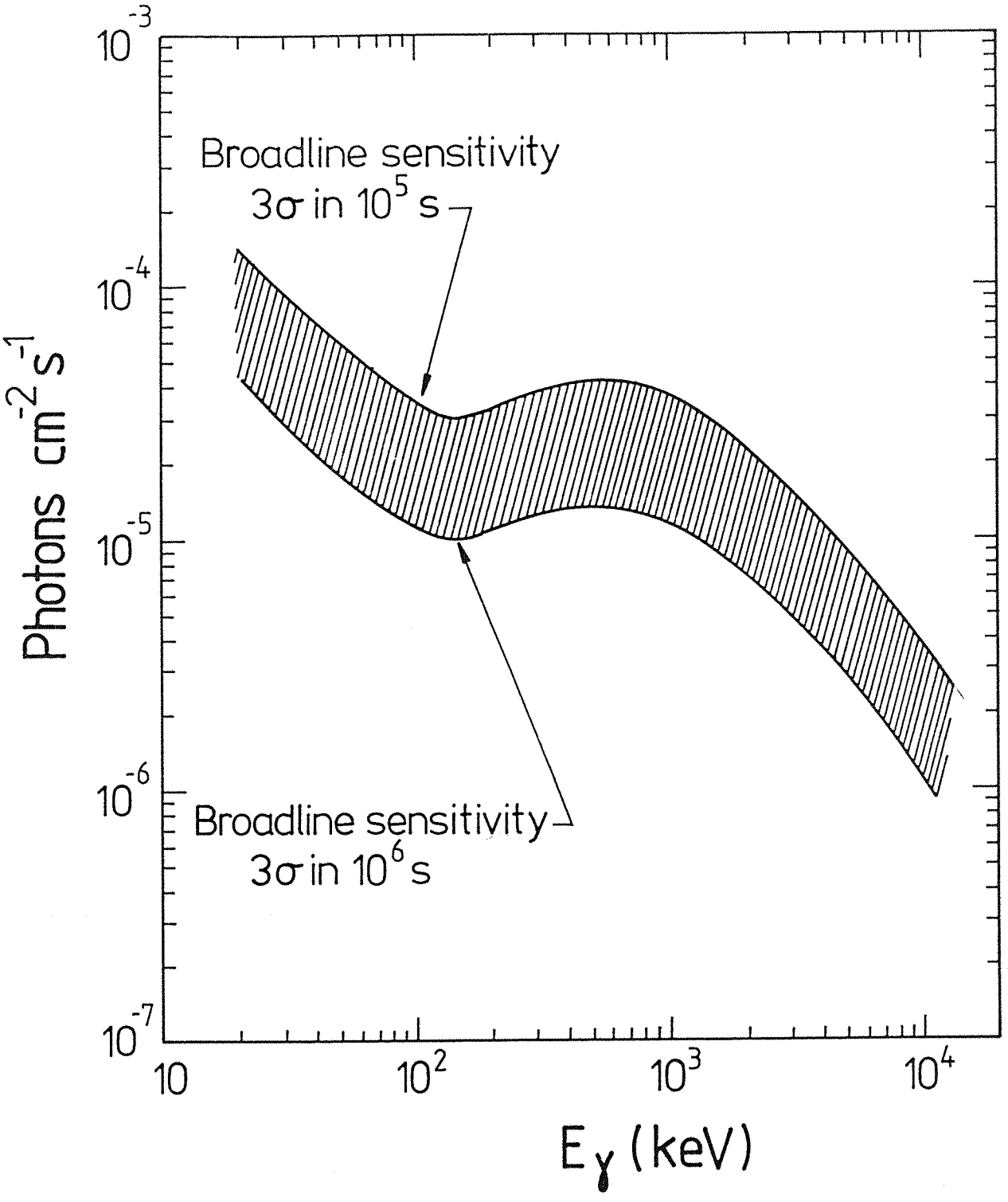

Figure (7.12a) The broadline sensitivity of the GRASP telescope.

References :

Ables,J.G., *Proc.Astron.Soci.*, 4(1968)172.
Aitken,G. et al, *J.Opt.Soc.Am.*, 71(1981)759.
Althouse,W.E. et al, *19th Int.Cosmic Ray Conf.*, 3(1985).
Althouse,W.E. et al, *20th Int. Cosmic Ray Conf.*, (1987).
Archer,N.P. et al, *Nucl.phys.*, 83(1966)241.
Ayre,C.A. et al , *Mon.Not. R.Soc.*, 205(1983)285-295.
Baker,R.E. et al, *Nucl.Inst.meth.*, 158(1979)595-604.
Bassani,L. and Dean,A.J. *Space Sci. Rev.*, 35(1983)367-398.
Beuermann,K.P., *J.Geophys.Res.*, 76(1971)4291-4310.
Bennet,K. et al, *Astron.Astrophy.*, 61(1977)279-284.
Bignami,G.F., et al, *Space Sci.Inst.*, 1(1975)245-268.
Bignami,G.F. and Morfil,G.E., *Astron.Astrophy.*, 87(1980)85-87.
Bignami,G.F. et al, *Astron.Astrophy.*, 93(1981)71-75.
Bignami,G.F. and Hermsen,W., *Ann.Rev.Astron.Astrophy.*, 211(1983) 67-108.
Bignami,G.F. et al, *Nature*, 310(1984)464-469.
Bignami,G.F. et al, *IEEE Tran.Nucl.ScI.*, NS-34(1987)31-35.
Bignami,G.F. et al, *Space Sci. Rev.*, 49(1988)157-171.
Bildsten,L. and Zurck,W.H., *Ap.J.*, 329(1988)212-224.
Boella,G. et al, *Il Nuovo Cimento*, 7C(1984)805-839.
Boella,G. et al, *IEEE Tran.Nucl.Sci.*, 33(1986)755-758.
Bowyer,C.S. et al, *Ap.J.*, 161(1970)L1.
Brown,C.M., *J.App.Phys.*, 45(1973)1806.
Butler,R.C. et al, *Nucl.Inst.Meth.Phys.Res.*, 221(1984)41-44.
Butler,R.C. et al, *19th Int.Cosmic Ray Conf.* LA Jolla,USA, (1985)322-325.
Caroli,E. et al, *Space Sci.ReV.*, 45(1987)349-403.
Charalambous,P.M., *Ph.D.Thesis*,Southampton Univ., 1983.
Charalambous,P.M. et al, *Nucl.Inst.Meth.Phys.Res.*, 221(1984)56-59.
Charalambous,P.M. et al, *Nucl.Inst.Meth.Phys.Res.*, 221(1984)183-186.
Charalambous,P.M. et al , *Nucl.Inst.Meth.*, A238(1985)533-541.
Chupp,E.L., *Gamma ray astronomy*, D.Redel Publishing Company, Boston USA, (1976).
Clayton,D.D., *Gamma ray astrophysics*, Edt. by Stecker,F.W. and Trombka,J.I.,NASA SP-339, (1973).
Cook,W.R., *IEEE Tran.Nucl.Sci.*, NS31(1984)771-755.

Crannell,C.J. et al, *Positron annihilation in Solar Flares*,NASA-x-682-75-167,Godard space flight centre, (1975).
Dean,A.J. and Ramsden,D., *Phil.Trans.R.Soci.*,London, A301(1981) 557-602.
Dean,A.J. et al, *IEEE Tran.Nucl.Sci.*, NS34(1987)62-65.
Dicke,R.H., *Ap.J.*, 153(1968)L101.
Diehl,R., *Space Sci.Rev.*, 49(1988)85-106.
Dunphy,P.P. et al, *Nucl.Inst.Meth.* (1987).
Evans,R.D., *The Atomic Nucleus*, McGraw-Hill book company,(1955).
Fabian,A.C. and Rees,M.J., *X-ray Astronomy, COSPAR advancer in space exploration, 3 ,edt. Baity,W.A. and Peterson,L.E., Pergamom Press,* (1980).
Farman,M. and Hardie,J., *COSPAR*:Ref.JASR 10.4.5.(1986).
Fenimore,E.E. and Cannon,T.M., *App.Opt.*, Vol.17,No.3(1978)337-347.
Fenimore,E.E. and Cannon,T.M., *Opt.Eng.*, 19(1980)283.
Fictel,C.E. et al , *Ap.J.*, 198(1975)163-182.
Fichtel,C.E. and Trombka,J.I., *Gamma ray astrophysics*,NASA SP-453, (1981).
Finger,M.H. and Prince;T.A., *Proc.19th Int.cosmic Ray Conf.* India, 8(1985).
Fleming,J.S. and Goddard, *Nucl.Inst.Meth.Phys.Res.*, 221(1984)242.
Gehrels,N., *NASA,TM86162*, 1985.
Gil,A., *Ph.D. Thesis,* Southampton Univ., 1986.
Ginzburg,V.L., *Astrophy.Space.Sci.*, 1(1968)1.
Ginzburg,V.L., *Elementary processes for cosmic ray astrophysics*, Gordon and Breach publishing company,New York (1969).
Grumplinger and Sconfelder,V., *Nucl.Inst.Meth.* (1979).
Hall,R.D. et al, *Ap.J.*, 210(1976)631-641.
Hartman,R.,et al, *Proc.18th Int.Cosmic Ray Conf.*, 8(1983)16-18.
Hayles,R.I., *Ph.D. Thesis*,Southampton University, (1982).
Hillier,R., *Gamma ray astronomy*, Clarendon Press-Oxford, (1984).
Johnson,W. et al, *Ap.J.*, 172(1972)L1-L7.
Johnson,W.N. and Haymes,R.C., *Ap.J.*, 184(1973)103-125.
Kelley,G.G. et al, *Nucleonics,* 14(1956)53.
Klebesadel,R.W. et al, *Ap.J.*, 182(1973)L85-L88.
Kniffen,D.A. et al, *Nature* , 251(1974)397-399.
Leventhal,M., et al, *Ap.J.*, 216(1977)491-502.
Leventhal,M. et al, *Ap.J.* , 225(1978)L11-L14.

Leventhal,M., *13 th Texas symposium on relativistic astrophysics*, (1987)382.
Ling,J.C. et al, *Ap.J.*, 231(1979)896-905.
Lovett,R., *Ph.D. Thesis*, Southampton Univ. (1973).
MacCallum,C.J. et al, *Ap.J.*, 317(1987)877-880.
Mahoney,W.A, *Nucl.Met.Inst.*, 178(1980)363.
Mahoney,W.A. et al , *Ap.J.*, 286(1984)575-585.
Manchanda,R.K., et al, *Ap.J.*, 252(1982)172-178.
Matz,S.M. et al, *Nature*, 331(1981)416-418.
Mayer-Hasselwander et al, *Astron.Astrophy.*, 105(1982)164-175.
Mazets,E.P. et al, *Asrtophy. Space Sci.*, 82(1982)261-282.
McConnel,M.L., et al, *20th international Cosmic ray confrence*, 1987.
Mckechnie,S.P., *Proc.18 th Int.Cosmic Ray Conf.*, 8(1983)16.
Natalucci, et al, *Proc.2nd European Simulation Congress*,Belgium, (1986)484-489.
Pasciesas, *Nucl.Inst.Meth.*, 216(1983)261.
Pollock,A.M.T. et al, *Astron.Astrophy.*, 146(1985)352-362.
Prantzos,N. et al , *Ap.J.*, 307(1986)324-331.
Prescott,J.R. and Takhar,P.S., *IEEE Tran.Nucl.Sci.*, NS-941962)'.
Ramaty,R. and Lingenfelter,R, *Ap.J.*, 213(1977)L5-L7.
Ramaty,R. et al, *Ap.J.(Supplement)*, 40(1979)487-526.
Ramaty,R; and Lingenfelter,R.E. , *Nature*, 278(1979)127-132.
Rybicki,G.B. and Lightman,A.P., *Radiative processes in astrophysics*, John Wiley and sons publishing company, (1979).
Said,S.S., *J.Phys.G.*, 8(1982)383.
Sacher,W., and Schonfelder,V., *Ap.J.*, 279(1984)817-826.
Sale,R.G., *Ph.D. Thesis*, Bristol Univ., (1970).
Schonfelder,V. and Litchi, *Ap.J.*, 191(1974)L1-L5.
Schonfelder,V. et al, *Ap.J.*, 217(1977)306-319.
Schonfelder,V. et al, *Ap.J.*, 240(1980)350-362.
Schonfelder,V. et al, *Astron.Astrophys.*, 110(1982)138-151.
Share,G.H. et al, *Ap.J.*, 326(1988)717-732.
Siegban,*Alpha,Beta and gamma Spectroscopy*, 1955.
Skinner,J. et al, *Nature*, 330(1987)544-547.
Stecker,F.W., *Nature*, 22(1969)865.
Stecker,F.W., *Cosmic gamma rays*,NASA SP-249, (1971).
Stecker,F.W., *Origin of cosmic rays*,Edt. by Osborne,J.L. and Wolfendale,A.W., (1974).
Strickman,M.S. et al, *Ap.J.*, 253(1982)L23-L27.

Swanenburg,B.N. et al, *Ap.J.*, 243(1981)L69-L73.
Teegarden,B.J. and Cline,T.L., *Ap.J.*, 236(1980)L67-L70.
Thompson,D.J. et al, *Ap.J.* , 213(1977)252-262.
Vedrenne,G., *New Instr.Space Astron.*, Edt. by Van Der Hucht and Vaiara, Pergamon,Oxford and New York, (1978)151.
Villa,G. et al, *IEEE Tran.Nucl.Sci.*, NS-34(1987)26-30.
Von Ballmos,P. et al, *Ap.J.*, 312(1987)134-142.
Walraven,G. et al, *Ap.J.*, 202(1975)502-510.
Winkler,P.E. and White,A.E., *Ap.J.*, 199(1975)L139-L142.
Wills,R.D. et al, *Phil.Tran.Roy.Soc.* London, A301(1981)537.
Wills,R.D. et al, *Non Solar Gamma Rays*, Cospar symp., Edt. by Coswick,R. and Wills,R.D., *Adv.Space Explore*, 7(1980)43.
Woods,J.W. et al, *IEEE Trans.Nucl.Sci.*, NS-22(1975).
Worrall,D.M. et al, *Ap.J.*, 232(1979)683-688.
Wright,G.T., *J.Sci.Inst.*, 31(1954)462.
Zyskin,Y.L. and Mukanov,D.B.,*Conference paper, 18th I.C.R.C. Banhalore,1,122,Sov.Astron.Letters*, 9(1983)177-180.